Investigation of the Microwave Effect

By

Karl Hossbach

A Doctoral Thesis submitted in partial fulfilment of the requirements for the award of Doctor of Philosophy of Loughborough University

November 2014

Acknowledgement

I want to thank Prof. Binner, who gave me the opportunity to work on this project and supported me throughout the project.

Additionally, I am indebted to all the people from LMCC, especially Mr John Bates for his co-operation concerning electron microscopy. Many thanks to all the staff and students from Department of Materials for their help and support. Special thanks to all the members of the ceramic research group for helping me with my experiments.

I am grateful for the help of Keith Dinsdale with the mercury porosimetry at Nottingham University.

Further, I want thank my family, who supported me when I had problems with this project.

Karl Hossbach

November 2014

Abstract

Over the past decades, microwave sintering has been investigated, and the effects of microwave sintering have been demonstrated, however there is still uncertainty as to what is causing the enhancements known as the “microwave effect”.

For a better understanding of the “microwave effect”, the effect of microwaves on the pore size distribution during densification has been investigated for submicron-sized zinc oxide (ZnO), which was sintered with conventional heating and varying amounts of microwave power but always maintaining exactly the same time-temperature profile. Initially, the density of the sintered samples was measured and compared; this proved that the densification of the hybrid sintered samples was increased and that the higher the level of microwaves used, the more it enhanced the densification. After this, the porosity was investigated through the use of nitrogen adsorption analysis, mercury porosimetry and Field Emission Gun Scanning Electron Microscopy (FEGSEM). Initially, it was found that sintering with microwaves reduces pores faster than for conventional sintering as expected. However, the experiments also revealed that the mechanisms of the reduction in the porosity were not different for microwave sintering compared to conventional sintering. When the porosity was compared at equivalent densities, it was observed that there was no significant difference, either in terms of the amount of porosity or the microstructure development. Since the structural development was the same for both conventional and hybrid sintering, it was concluded that the cause for the enhancement of the densification was enhanced diffusion caused by an additional driving force induced by the microwave field.

The investigation of the solid-state reaction between zinc oxide and alumina was designed to investigate whether the diffusion associated with reactions was also enhanced by the use of microwaves. Therefore, zinc oxide and alumina samples were reacted as diffusion couples using conventional and hybrid heating, the latter with varying amounts of microwave power. The analyses of the reaction layer using FEGSEM showed an increase in the reaction product layer thickness when hybrid heating was used, with a higher level of microwaves yielding more growth. These

results supported the view that the enhanced reaction rates were caused by enhanced diffusion, again caused by an additional driving force induced by the microwave field. For both the densification and reaction cases, the most likely additional driving force is considered to be the ponderomotive effect.

List of Figures

List of Tables

Abbreviation

BSE	back-scattered electrons
BSE-SEM	back-scattered electrons scanning electron microscopy
EDS	energy-dispersive X-ray spectroscopy
FEGSEM	Field Emission Gun Scanning Electron Microscopy
OFT	optical fibre thermometers
PC	pure conventional sintering
tan δ	loss tangent
TD	theoretical density
x W hybrid	hybrid sintering with an amount of x W of microwaves
xYSZ	x% yttria stabilized zirconia

1 Introduction

The aim of this project is to provide a better understanding of the “microwave effect”. The latter is generally understood to mean the enhancement of the mass transport and solid-state reaction rates during the processing of materials. This includes accelerated kinetics for a wide range of processes, e.g. lower sintering or reaction temperatures [1-12]

The concept of the “microwave effect” has been investigated for a long time and over a wide range of materials, including polymers [1-3], powder metals [4-6], glasses [7-9] and ceramics [10-12]. For the latter, the effect of microwaves has been demonstrated for sintering [13-15], annealing [16, 17], solid-state reactions [18-20], and others. Examples for this effect are reduced processing temperature [16, 17], shorter reaction times [13, 21, 22] and increased densification for microwave sintering, particularly in the intermediate sintering stage [23-25].

There have been many attempts to explain the microwave effect. The theories about its origin range from reduction of the activation energy [16], to changes in the pre-exponential factor [26], to different structural development [16] and the creation of an additional driving force [27]. A reason for the variety of theories is precisely because of the wide range of materials and processes that have been examined. For ceramics in particular, the situation is confused by the fact that much of the research has been undertaken using different furnaces for conventional and microwave heating [10, 16] and the question of the accuracy of the temperature measurement during microwave sintering. The latter also sparked an argument if the ‘microwave effect’ was a genuine effect or an artefact due to the problem of temperature measurement [28].

In his PhD-thesis, “Determination of the physical basis behind the ‘microwave effect’”, Wang [29] reinvestigated the microwave effect, but using a single cavity and improved temperature measurement techniques to sinter his samples using both conventional and hybrid heating and with exactly the same heating cycle for both conditions. His work provided an answer for the problem of temperature measurement in a microwave field and confirmed that the microwave effect exists and that samples heated via hybrid heating have, in most cases, a higher density

than conventionally heated samples produced with the same temperature-time profile in the same furnace cavity. The work also demonstrated, unsurprisingly that the more a ceramic coupled with microwaves the greater the effect observed. These experiments were continued by using dilatometer measurements for ZnO and 3 mol% yttria partially stabilised zirconia (YSZ) by Lorenz [30] and Hossbach [31] to extend these results to other properties.

Even before Wang's work there were attempts to find out which of all the theories could be true. The first clear indications were achieved by two independent research groups, who were the first one to utilize hybrid heating [32, 33]. Freeman et al. [32] demonstrated the effect of microwaves on the flow of a current through sodium chloride crystals. Wroe and Rowley [33] demonstrated the dependence of the enhanced densification on the usage of microwaves. Both groups designed their experiments in ways that a difference in temperature between their conventional and hybrid heating investigations was avoided. Wroe and Rowley used a hybrid furnace that allowed the simultaneous use of conventional and microwave heating. In comparison Freeman et al. design their experiment in a way that the use of microwaves did not raise the temperature. Therefore, all of their findings could be linked directly to the effect of the microwaves. The results of these experiments support the theory about the additional driving force via ponderomotive forces [27]. This theory had further strengthened by the demonstration of directional diffusion in a linear microwave field by Whittaker [34].

Most of the other theories have been rejected by this time. The mounting indications have led to the theory about the ponderomotive force, which suggest that microwaves create a directional flow of diffusion in the present of grain boundaries as semi-penetrably boundaries, to the main explanation of the microwave effect. However the theory about the different structure development, where the use of microwave sintering leads a larger remaining amount of open porosity at higher densities, suggested by Janney et al. [16] seemed to be overlooked.

The current attempt at achieving an improvement in the understanding of the "microwave effect" has been achieved by a detailed investigation of microwave sintering and a comparison with conventional sintering. The pore size distribution and

the microstructure has been investigated during the densification of zinc oxide (ZnO) under a range of heating conditions, including conventional and hybrid heating, the latter involving the combination of conventional and microwave heating. In addition, the solid-state reactions of ZnO/MgO and alumina (Al_2O_3) have been investigated using the same approach.

2 Literature Review

2.1. Green Forming

Green forming is an important step in the production of ceramics because powder has to be turned into the correct shape for the component before it can be sintered and the final product is created. Further, any defect introduced in this processing step into the “green product” can usually not be eliminated during the following processing steps [35].

Green Forming – dry route

The most commonly used techniques for the compaction of dry powder (<2 wt% water) and semidry powder (~5 – 20 wt% water) are uniaxial pressing and isostatic pressing [36].

Uniaxial pressing

Because of its rapid production with high tolerances, uniaxial pressing is the most widely used green forming route in the ceramics industry. The processes of filling the powder into the die, compaction through applied pressure and ejection of the compact contribute to the advantages of uniaxial pressing and enable a high degree of automation, see Figure 1. However, there also some disadvantages to the process. Firstly, because of the confinement of the die the potential shapes that can be produced are limited. Further, because of friction along the dies walls during the compaction phase pressure variation can occur and can lead to defects [36, 37].

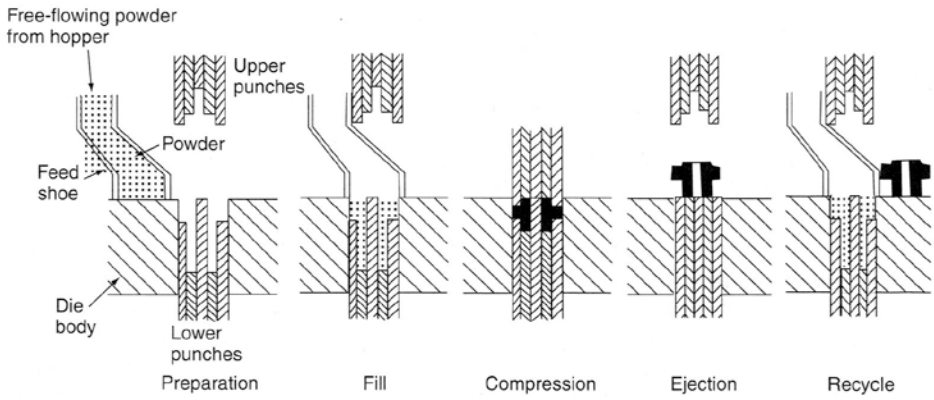

Figure 1 Schematic illustrating automated uniaxial pressing [37]

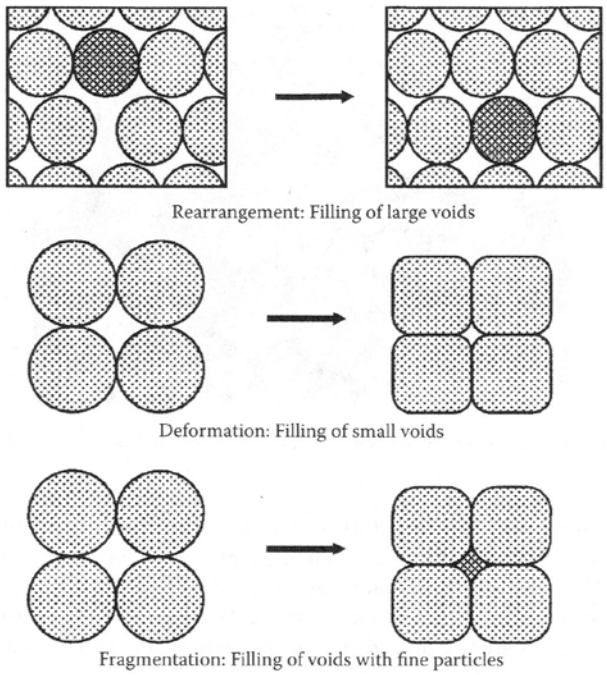

Figure 2 Schematic diagram showing the stages of granule compaction [36]

Due to the high degree of automation for die pressing, the flow behaviour of the powder is very important because a rapid uniform filling of the die has to be achieved since it affects the packing homogeneity of the green body. This means that powders are typically granulated to improve their flow behaviour. The strength of the granules affects the pressing process however. During the compaction phase, Figure 2, the granules first rearranged to fill large voids. As the compaction continues the granules deform and small voids are reduced. This rearrangement of the granules is important because large packing flaws of the die filling are eliminated through the rearrangement phase. These flaws lead to density differences in the green body and cracking during sintering [36, 37]. Low-density, weak granules then fracture, filling the

small voids with powder particles, leading to higher densities. In contrast, hard granules can shield neighbouring softer granules from exposure to the maximum pressure, leading to pore clusters. This intergranular porosity is difficult to remove during sintering and can lead to serious defects in the final product.

Isostatic pressing

The basic processing steps during isostatic pressing are the same as for die pressing. At first the powder is poured into a flexible mould, typically a rubber bag though this can vary depending on the type of isostatic pressing. After this, as for die pressing, the powder is compacted before it is ejected. The compaction is realised by a uniform hydraulic pressure that allows a higher degree of compaction to be achieved so that the green densities are higher and more homogenous than for die pressing, see Figure 3. This leads to improved results during subsequent densification. Isostatic pressing can be divided into 2 types, wet-beg and dry-bag pressing, see Figure 4 [36, 37].

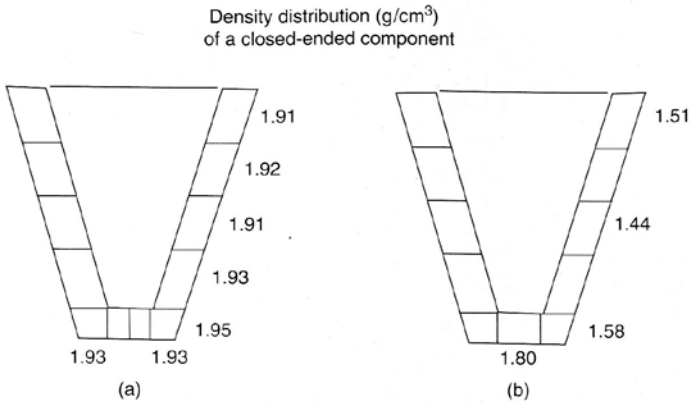

Figure 3 Improvement in green density uniformity of a thin-wall crucible achieved by (a) isostatic pressing and (b) die pressing [37]

In dry-bag isostatic pressing a double-walled flexible mould is typically used. After the compaction, only the inner bag containing the compact is removed. This allow for fast production. In contrast, for wet-bag pressing the powder filled mould is directly in contact with the pressure fluid and so time is needed to allow the fluid to drain before the green body can be removed. The dry-bag process is therefore easier to automatize and generally faster, whilst the wet-bag process usually offers improved tolerances. A potential problem for isostatic pressing is achieving an even filling of

the mould, especially for complex shapes where it can be difficult to distribute the powder evenly [36, 37].

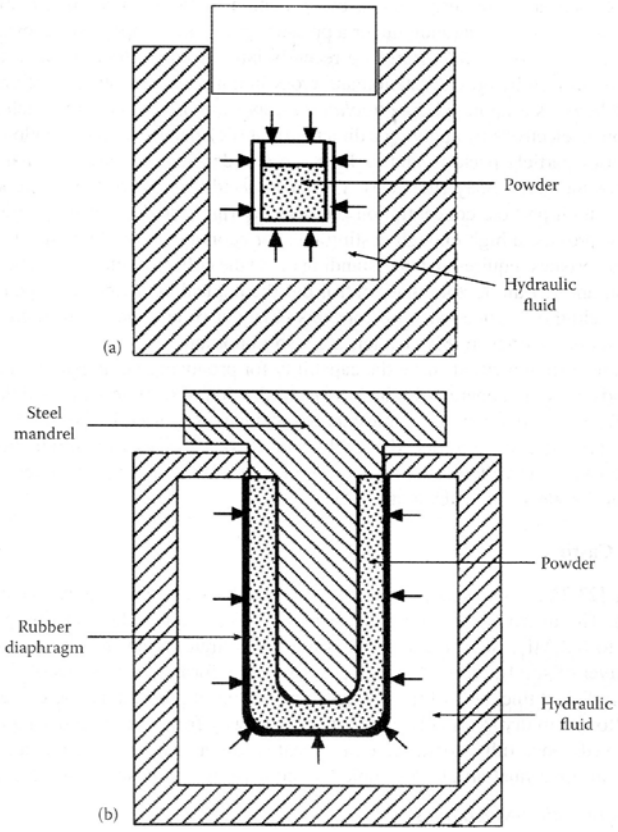

Figure 4 Two modes of isostatic pressing: (a) wet-bag pressing and (b) dry-bag pressing [36]

Green forming – wet route

Colloidal processing of ceramics

An advantage of colloidal processing over green forming via pressing is the potential to achieve lower defect densities and more uniform microstructures. This is possible because wet forming is typically based on the sedimentation of individual particles, rather than the forced compact of granules. During the sedimentation process there is the opportunity for particles to adjust their position to achieve green microstructures with a low incidence of defects. The key to success, however, is very largely controlled by controlling the rheology of the suspension that is used. First, the particles cannot be too large or rapid sedimentation will lead to an unstable

suspension. Another important factor for the stability of colloidal system is the total interparticle potential energy, V_{total}, which can be expressed as [36, 38, 39]:

$$V_{total} = V_{vdW} + V_{elect} + V_{steric} + V_{structural} \quad (2.1)$$

where V_{dvW} is the attractive potential energy due to long-range van der Waals interactions between the particles, V_{elect} the repulsive potential energy resulting from electrostatic interactions between like-charged particle surfaces, V_{steric} the repulsive potential energy resulting from steric interaction between the particle surfaces (typically coated with adsorbed polymeric species that act as dispersants), and $V_{structural}$the potential energy resulting from the presence of nonadsorbed species in solution that may either increase or decrease suspension stability. The various types of stabilisation are schematically illustrated in Figure 5.

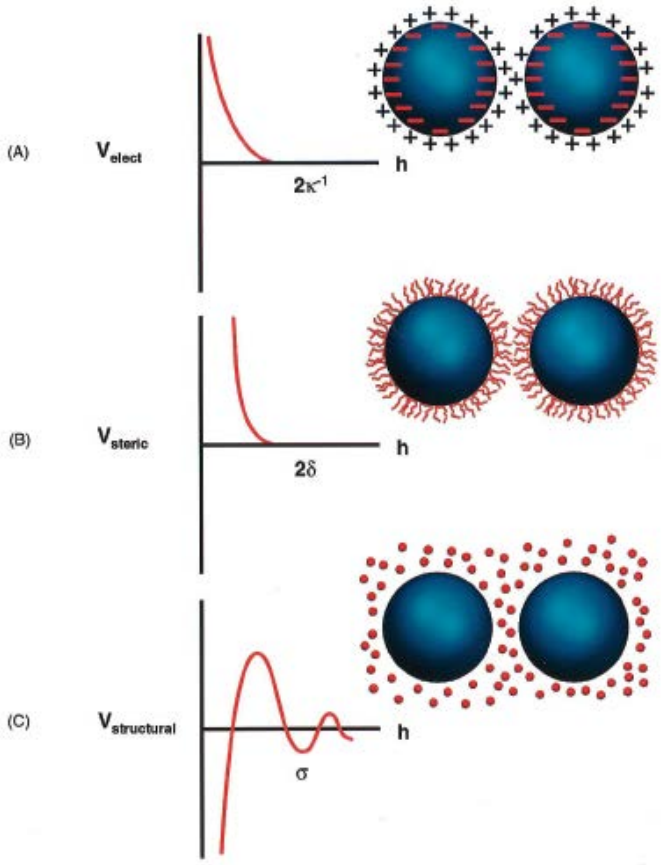

Figure 5 Schematic illustration of the interaction potential energy and relevant length scales for (A) electrostatic, (B) steric, and (C) structural contributions, where k-1 is the effective double-layer thickness, δ the adlayer thickness, and σ the characteristic size of species resulting in ordering within the interparticle gap. [39]

For the production of ceramics from colloidal systems, the most commonly used methods are slip casting and tape casting though all of the casting techniques are based on the removal of the liquid to consolidate the suspended particles [36, 37].

Slip casting

For slip casting, a mould of microporous plaster of Paris is prepared and the slurry (slip) poured into the mould, see Figure 6. The capillary suction pressure (~0.1 – 0.2 MPa) of the mould leads to a flow of liquid from the slurry into the mould. As the liquid is removed from the slurry, the solid particles of slurry settle along the mould walls and create the cast or cake. Once, the required thickness is reached the surplus slip is poured out and the cast dried. As the mould and the cast are drying the cast normally shrinks away from the mould and so can be removed easily. The process is very good for producing complex-shaped components, including hollow bodies, but can also be used for simple shapes [36, 37].

As indicated earlier, the preparation of the slip is vital for the slip casting process; it should not be too sensitive to slight variations in solid content or chemical composition and also needs to be stable for a long periods to allow for storage. Further, the viscosity should be low enough so that the mould can be filled completely and the solid content should be high enough to ensure reasonable casting rates. If the casting process is too slow variation in the cast thickness and density, due to settling, are possible. The cast formed can also be ‘flabby’ due to trapped liquid medium within it. In contrast, if the cast is formed too fast, it results in a lack of control of the wall thickness and the cast is often brittle. Additionally, it has to be ensured that no air becomes trapped inside the cast (from entrained air or chemical reactions that form bubbles) since entrapped bubbles will remain in the cast and become potentially critical defects in the final product [36, 37].

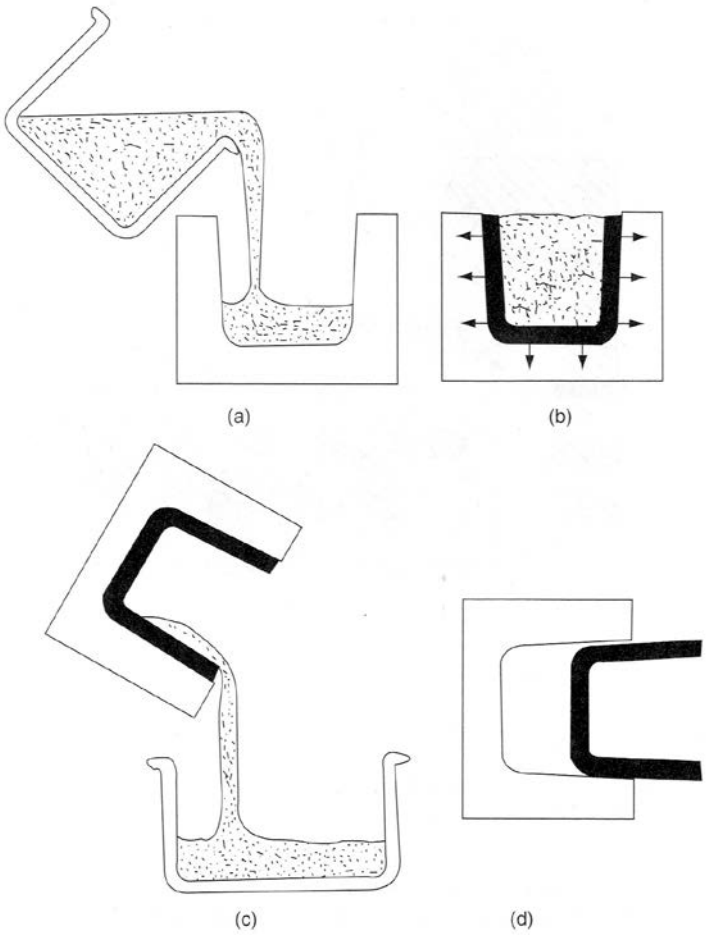

Figure 6 Schematic illustrating the drain-casting process, (a) Fill mould with slip, (b) mould extracts liquid, forms compact along mould walls, (c) excess slip cast drained, and (d) casting removed after partial drying [37]

Tape casting

In contrast to slip casting, where the liquid of the slurry is removed by the capillary suction of the mould, for tape casting drying occurs via evaporation. This is possible because the slurry is spread under the control of a blade as a thin layer, between ~10 µm to ~1 mm thickness, onto a surface that is typically a moving acetate sheet, see Figure 7. As the solvent evaporates, the particles are left behind as a tape. After drying, the tape is removed from the carrier surface and cut into pieces for further processing or can be stored on take-up reels. Tape casting is ideal to produce large quantities of thin tape at low cost. However, the slurry required for this production is a carefully adjusted mixture of particle, solvent and a combination of additives, up to 50 vol%, such as binder, plasticizer, dispersant, wetting agent and antifoam agent. This

combination needs to be optimised for every specific tape casting slurry. Also, there are high requirements for the binder, viz. [36, 37]:

1) Allows the formation of a tough but flexible film when dry;
2) Volatilises to a gas when heated or burns off without leaving residual carbon or ash;
3) Remains stable during storage, especially with no change in molecular weight;
4) Soluble in an inexpensive, volatile, nonflamable solvent.

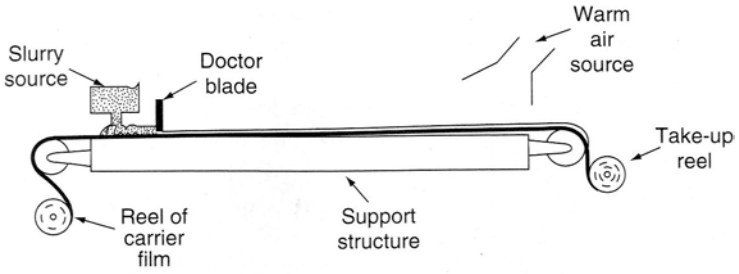

Figure 7 Schematic illustrating the doctor blade tape-casting process [37]

2.2 Solid State Sintering of Ceramics

2.2.1 General

Sintering is one of the most common processes involved in the fabrication of ceramics. Almost all ceramic bodies have to be sintered at high temperatures to attain densification and produce the required microstructures. These microstructures, which are influenced by the size and shape of the grains, the amount, size and distribution of the pores, and the nature and distribution of any second phases, determine the properties of ceramics [37].

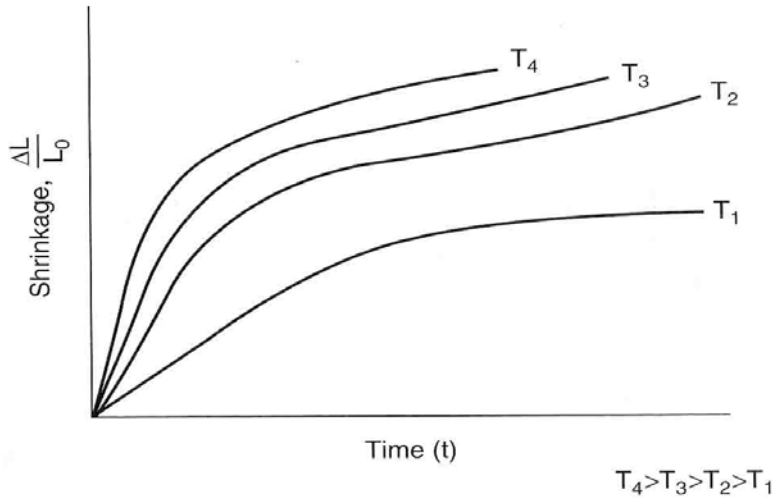

Figure 8 Schematic diagram of sintering curves showing the effect of temperature and time [37]

Densification is a normal output of sintering of ceramics; particles change shape to increase their contact area with neighbouring particles reducing porosity through grain growth and boundary movement. The reduction of the free energy of systems is an important part of sintering and it is characterised by material transport. This matter transport, diffusion, is activated and sustained by energy as heat, from the outside of the ceramic system. The diffusion can be accelerated, for example, by increasing the sinter temperature T_{sinter}, Figure 8 [37].

Normally for a single phase system $T_{sinter} \approx 0.5 \ldots 0.95\ T_{melt,}$ where T_{melt} is the absolute melting temperature of the material [40].

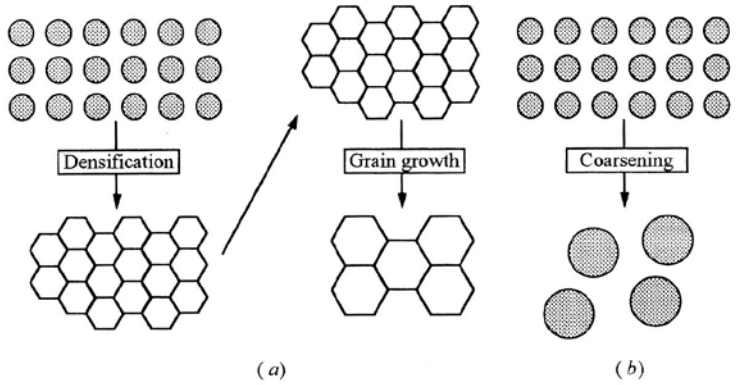

Figure 9 Two different paths to lower the free energy of a collection of particles (a) Sintering (densification and grain growth lead to shrinkage of the compact) (b) Coarsening (growth of large grains while smaller are eliminated, no shrinkage occurs) [41]

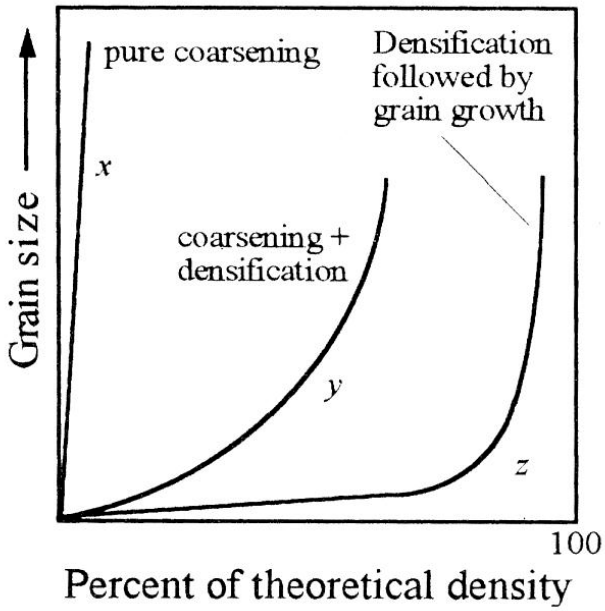

Figure 10 Grain size versus density for densification (curve z) and coarsening (curve x) [41]

Coarsening is an alternative route to reduce the free energy of systems, Figure 9, and leads to an increase of the average grain size. Further, coarsening increases the pore and grain size with time and does not allow the centre of particles to move closer together. The increase of grain size is achieved by the movement of atoms across curved grain boundaries, from the inside to the outside of the curvature, leading to the elimination of the smallest grains [41].

The process of densification and coarsening often occurs parallel and at a given temperature the fastest mechanism dominates. Therefore, the majority of sintering curves resemble curve y in Figure 10. Even in the best case, coarsening occurs at the final stages of the sintering, curve z, resulting in it being almost impossible to reduce any remaining porosity with further heating [41].

2.2.2 Driving Force for Sintering

A lowering of the free energy of the system is an accompaniment of sintering, as with all other irreversible processes. The cause, for this lowering of the free energy, is

described as the driving forces for sintering; the main forces are often the curvature of the particle surface, an externally applied pressure and a chemical reaction [42].

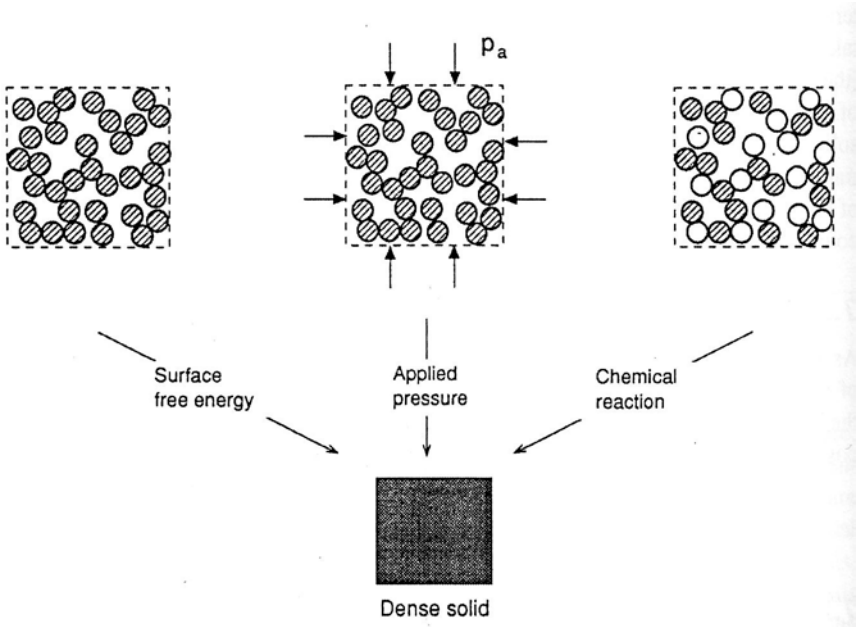

Figure 11 The three main driving forces for sintering [42]

The surface curvature

The curvature of the particle surface is the main driving force, when no eternal pressure is applied and no chemical reaction is present. Assuming 1 mole of powder consists of spherical particles with a radius r. The number of particles *N* is

$$N = \frac{3M}{4\pi r^3 \rho} = \frac{3V_m}{4\pi r^3} \tag{2.2}$$

Where ρ is the density of the particles, which are assumed to contain no internal porosity, *M* is the molecular weight, and V_m is the molar volume [42].

The surface area of the system, S_A, of particles is

$$S_A = 4\pi r^2 N = \frac{3V_m}{r} \tag{2.3}$$

Thus, the surface free energy associated with the system of particles E_s is

$$E_s = \frac{3\gamma_{sv} V_m}{r} \quad (2.4)$$

Where γ_{sv} is the specific surface energy. The surface free energy provides motivation for sintering. E_s represents the decrease in surface free energy of the system if a fully dense body is produced from the mole of material [42].

As equation 2.3 indicates, the change of a particles surface is driving the reduction of the free energy and with it sintering. Therefore, the curved surfaces of the particles play an important role in the sintering, because the curvature of the particle surfaces add an additional force to the effective stress on atoms under the surface [36]:

$$\sigma = \gamma_{sv} \left(\frac{1}{R_1} + \frac{1}{R_2}\right) \quad (2.5)$$

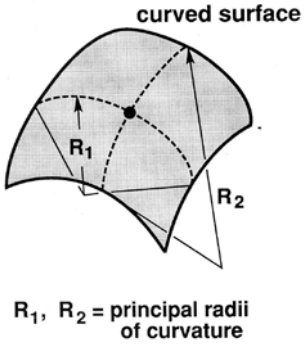

Figure 12 The curvature at any point on a curved surface [43]

For a “concave” surface the effective stress is negative, because the atoms are in compression. The curvature of a “convex” surface is defined as positive and its atoms are less tightly bound to their neighbours. Therefore they will be more like to escape into the gas phase. [41].

External applied pressure

The external applied pressure is main contributor to the driving force, when the pressure is applied over a significant part of the heating process and in the absence

of the chemical reaction. The contribution of the external applied pressure to the driving force is much greater than the surface curvature (more than 20 times) [37, 42].

The work, W, applied to the system by the external pressure:

$$W = p_a V_m \tag{2.6}$$

Where p_a is the applied pressure and V_m is the molar volume [42].

Chemical reaction

Chemical reactions are also a possible source for the driving force for sintering. The decrease in free energy, G, accompanying a chemical reaction can be calculated by:

$$\Delta G = -RT \ln K_{eq} \tag{2.7}$$

Where R is the gas constant (8.3 J/mol), T is the absolute temperature and K_{eq} is the equilibrium constant for reaction [42].

The decrease of the free energy in the system is significantly greater for a chemical reaction than for the external applied pressure. This would mean that it is a great possibility to minimize the free energy of a ceramic system. However, the control of the microstructure is extremely difficult when a chemical reaction occurs. Therefore, a chemical reaction is rarely deliberately used as driving force for the sintering of advanced ceramics [42].

Sinter additives

Sinter additives are in general ‘impurities’, which are deliberately mixed into the ceramic mixture to fulfil a certain function, for example [41]:

- To form a liquid phase (explained in section 2.1.5). These impurities are capable of creating low-temperature eutectics and enhancing the sintering

kinetics. Only very small amount of these impurities is required to achieve an effect.

- To reduce the evaporation rate and lower the surface diffusion and with it suppressing coarsening.
- Reduction of the grain boundary mobility and hence reducing grain growth, for example, by ‘pinning’ the grain
- Enhancement of diffusion by identifying the rate-limiting ion and adding the proper dopant

In this project, no sinter additives were used to ensure that the observed effects on the samples were only caused by the use of microwaves.

2.2.3 Diffusion in Solids

Defects

Atomic diffusion is essential for sintering to occur, with the driving forces for atomic movement coming from high surface energies, curved grain boundaries and chemical potentials. However, the rate of diffusion is controlled by the imperfections, or defects, in the crystal structure since these, in turn, affect the ability and speed with which atoms can move and hence the rate at which processes such as sintering and grain growth can occur [42].

The presence of defects in crystalline solids can be explained by structural reasons, as the arrangement of atoms/ions in crystal is not ideal when all lattice sites are occupied, and by chemical reasons, as the variation of the valence of atoms can cause a deviation of the inorganic compounds from the fixed composition. These defects can be divided into three groups: point defects, line defects and planar defects [42].

Point defects, Figure 13, are a lattice point and its immediate vicinity that is not occupied by the proper ion or atom that is needed to preserve the long-range periodicity of the structure and its immediate vicinity. Missing atoms or vacancies,

interstitial atoms occupying the interstices between atoms and substitutional atoms sitting on sites that would normally be occupied by another type of atom are all point defects [42].

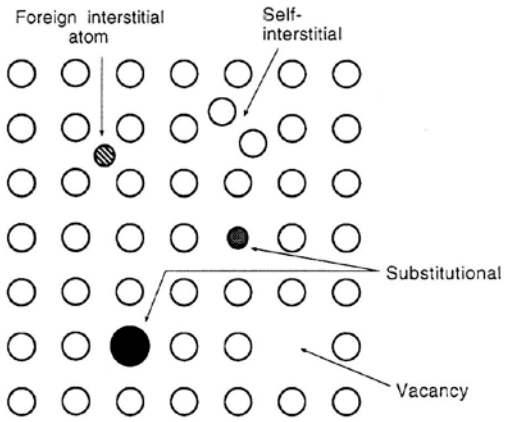

Figure 13 Point defects in an elemental solid [42]

Intrinsic and extrinsic defects are both point defects types. The reasons for the existence of extrinsic defects are the presence of impurities in the host crystal while intrinsic defects involve the transfer of atoms from the regular lattice sites, as shown Figure 13. The Schottky defect, Figure 14, and the Frenkel defect, Figure 15, are two of the most common types of intrinsic defects in ionic crystals. The movement of a cation and an anion from their lattice sites to an external surface creates vacancies and is called Schottky defect. At the surface, the cation and anion form extra perfect crystal. The Frenkel defect is the cation, which leaves its regular position in the lattice site and occupies an interstitial site, and the result is a vacancy [42].

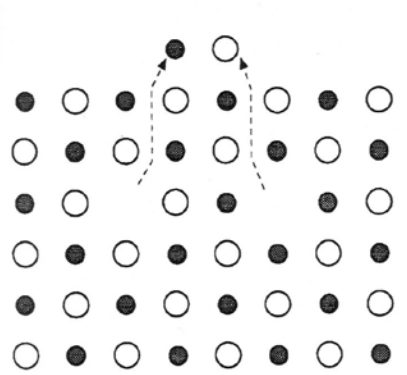

Figure 14 Schematic diagrams illustrating Schottky defect [42]

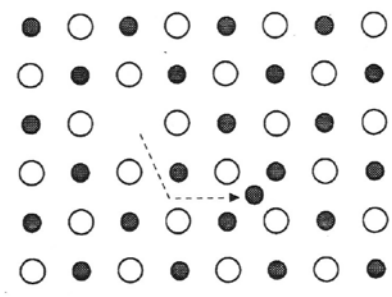

Figure 15 Schematic diagrams illustrating Frenkel defect [42]

Displacements in the periodic structure of the lattice in a certain direction are defined as line defects and referred to as dislocations. These displacements separate the crystal into a slipped and unslipped part and the boundary between these two parts is called dislocation line. The dislocations are called edge dislocation, Figure 16a, when the dislocation boundary is perpendicular to the direction of the slip, and screw dislocation, Figure 16b, when parallel to the direction of the slip [44].

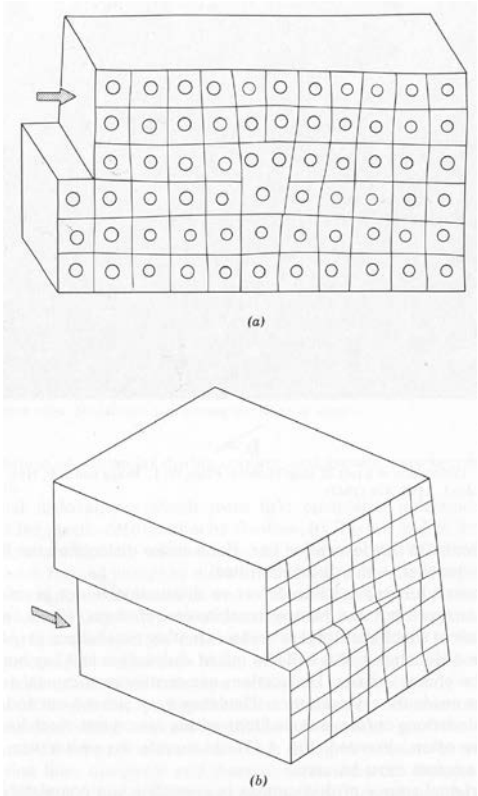

Figure 16 (a) Pure edge and (b) pure screw dislocation [45]

Planar defects are stacking faults, internal interfaces (e.g. grain boundaries) and free surfaces [42].

The presences of defects as vacancies and interstitial atoms are requirements for the diffusion mechanisms of vacancy and interstitial diffusion. Further defects reduce the required energy to move atoms, because is easier for an atom to into a vacancy than to move another atom. An interstitial atom does not required energy to leave its lattice place and only needs it for its movement through the lattice [44].

Fick's first and second laws

An important process in ceramic sintering is the transport of matter in which the diffusing species include atoms, ions and molecules. The gradients in the concentration cause the movement of the diffusing species. The concentration can be considered as a function of distance and time. Fick's first and second laws describe the diffusion process:

$$J = -D\nabla C \tag{2.8}$$

and

$$\frac{dc}{dt} = D\frac{d^2c}{dx^2} \tag{2.9}$$

Where *J* is the vector with components and represents the number of diffusing species crossing unit area. *D* is the diffusion coefficient. *C* is the concentration [42].

The conclusion of Fick's first law is that the flux of the diffusing species is proportional to the concentration gradient and occurs in the direction of decreasing concentration. The concentration in Fick's first law is independent of time. This means that concentration gradient is a driving force for the diffusion of species [42].

Fick's second law describes the change in concentration as a function of time and it can be derived from his first law and an application of the principle of the conservation of matter [42].

As said before concentration differences are required for matter transport via diffusion. During the sintering of ceramics one of the concentration gradients is the defect concentration. For example compared to a flat surface, the vacancy

concentration is lower for a convex surface, because vacancies are “pushed out“ of convex surfaces to minimise the surface. In contrast the concave surface is stretched out and has a higher vacancy concentration than a flat surface. This significant difference in the vacancy concentration will lead according to Fick’s law to flux of vacancies from the concave to the convex surface. This vacancy will start also a counter flow of atoms from the convex to the concave surface. The resulting matter transport will continue until the convex and concave surfaces are reduced to a flat surface [42].

The differences in the concentration, which enable the matter transport described above, are not the only potential driving forces for the atoms to act. Further driving forces could be pressure, electrical potential and so on. All these different forces describe collectively as gradient in the chemical potential [42].

Mechanisms of diffusion

The path of the matter transport and diffusion along the major paths is determined by the different types of the defect. Lattice diffusion, surface diffusion and grain boundary diffusion are mechanisms of diffusion; each provides a different path of atom movement and since each provides a different degree of ease the kinetics are also different [42].

Lattice Diffusion

The movement of point defects through the bulk of the lattice is lattice diffusion and is referred to as volume diffusion or bulk diffusion. The type of defect (vacancy or interstitial) determines if the lattice diffusion occurs by vacancy mechanism or interstitial mechanism [42].

Vacancy mechanism:
The change of position between an atom and a vacancy is defined as vacancy mechanism, Figure 17a. The movement of the vacancy is opposite to that of the atom.

Interstitial mechanism:

Interstitial mechanism is the movement of an atom, if it is small enough, from one interstitial site to one of the neighbouring interstitial sites, Figure 17b.

Interstitialcy mechanism

Interstitialcy mechanism is the movement of interstitial atoms when the distortion of the lattice is too large for interstitial diffusion. This leads to a change of position between an interstitial atom and an atom on a regular site, Figure 17c. For this the two do not need to be the same type of atom [42].

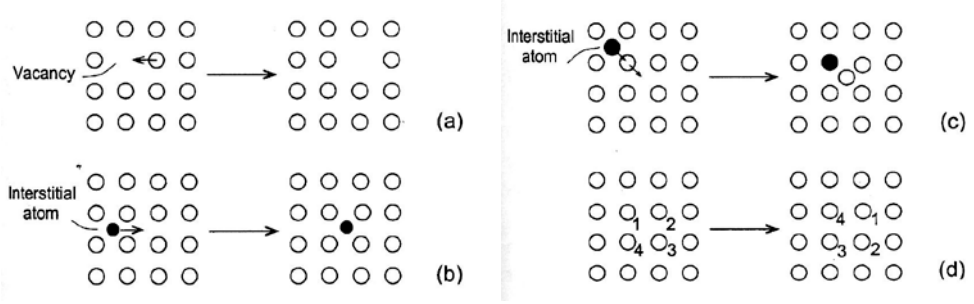

Figure 17 Mechanisms of lattice diffusion (a) vacancy mechanism, (b) interstitial mechanism, (c) interstitialcy mechanism and (d) ring mechanism [42]

Direct exchange or ring mechanism:

The ring mechanism, Figure 17d, is the direct exchange of place of several atoms by rotating in a circle. This mechanism does not require any defects. Further this mechanism is improbable in ionic solids, because the created momentarily distortion causing electrostatic repulsions which lead large energy changes [42].

Grain boundary diffusion

The movement of atoms or vacancies in the boundaries between the crystal grains in polycrystalline materials is the definition of grain boundary diffusion. The activation energy for grain boundary diffusion is generally less than that for lattice diffusion. The reason for this is that the atoms on the grain boundaries have fewer neighbours than the atoms involved in lattice diffusion. The grain boundary diffusion can consequently be more rapid than lattice diffusion because of the lower activation energy of the grain boundary and the highly defective nature. For a relatively constant grain

boundary thickness, the fraction that is occupied by the grain boundary in the material increases with decreasing grain size. The rate of grain boundary diffusion is therefore dependent on the grain size [42].

Surface diffusion

The movement of atoms or vacancies in a thin surface layer is surface diffusion. Since the atoms in this region have the lowest number of neighbours, surface diffusion has the lowest activation energy. Another reason for this low activation energy is that the atoms are less tightly bound in comparison with the other mechanisms [42].

As said the beginning of this section, these diffusion mechanisms have a different degree of easing the kinetics. The surface diffusion has the highest diffusion coefficient and lowest activation energy among the mechanisms of diffusion, because the surface atoms have fewer neighbours and less tightly bonded. Therefore the diffusion coefficients and the corresponding activation energy for lattice diffusion D_l, grain boundary diffusion D_{gb} and surface diffusion D_s are increasing in the order $D_l < D_{gb} < D_s$ and $Q_s < Q_{gb} < Q_l$. Because of the lower activation energy surface diffusion will be more likely at lower temperature. At higher temperature the importance of the surface diffusion will drop, because grain boundary or even lattice diffusion will be available as soon as the energy is in the system to activate the diffusion mechanisms [42].

Mechanisms of sintering

The matter transport via diffusion along definite paths, called mechanisms of sintering, is needed for sintering to occur. These sintering mechanisms are the means for the transport of matter from region with high chemical potential, referred to it as source, to a sink, which is the region with low chemical potential. Figure 18 and Table 1 show the 6 different sintering mechanisms, which are all responsible for the bonding and neck growth between the particles. These mechanisms can be divided into densifying and nondensifying mechanism as only some of them achieving densification and shrinkage. [42].

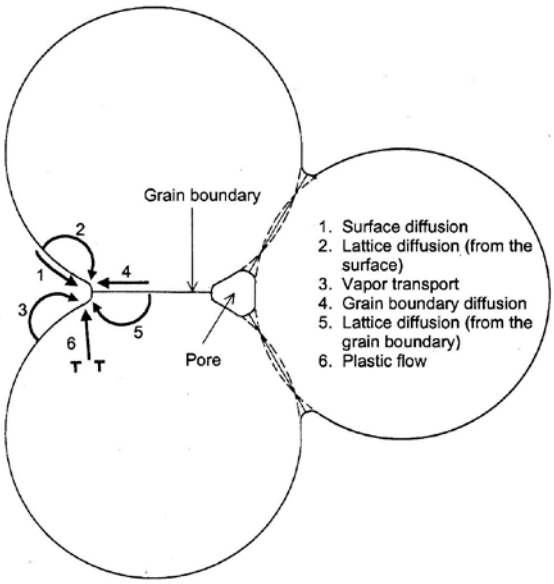

Figure 18 Mechanisms occurring during sintering [42]

Table 1 Overview of sintering mechanisms [42]

Mechanism	Source of matter	Sink of matter	Densifying	Nondensifying
Surface diffusion	Surface	Neck		X
Lattice diffusion	Surface	Neck		X
Vapour diffusion	Surface	Neck		X
Grain boundary diffusion	Grain boundary	Neck	X	
Lattice diffusion	Grain boundary	Neck	X	
Plastic	Grain boundary	Neck	X	

As Figure 18 and Table 1 show, all previous described diffusion mechanisms are part of sinter mechanism. However two of the diffusion mechanisms, surface and grain boundary diffusion, lead to opposing results, because only the grain boundary diffusion will lead to densification, while the surface diffusion is a nondensifying mechanism. The lattice diffusion is an ambivalent mechanism, because depending on its source, it can be either a densifying mechanism, source is the grain boundary, or when the source is the surface a nondensifying mechanism. For the densification of ceramic grain boundary and lattice diffusion are important, because the plastic flow is more common for the densification of metal powders [42].

The nondensifying mechanisms are responsible for the reduction of the curvature of the neck surface, which leads to a reduced driving force for sintering and with it a reduced rate of densification [42].

2.2.4 Densification in Three Sintering Stages

Sintering is a densification and grain growth process. The densification is the removal of the porosity from the ceramic green body. If the pores change shape without an increase in density, coarsening will take place. Sintering has three steps, namely, an initial stage, an intermediate stage and a final stage [35].

Table 2 shows the main parameters and densification processes in the three sintering stages.

Table 2 Main parameters in the three sintering stages [35, 42]

Stage	Microstructure feature	Density range
Initial	**Particle surface smoothing and rounding of pores** **Grain boundaries form** **Open pores neck formation and growth** **Porosity decreases < 12 %**	**Up to 0.65**
Intermediate	**Intersection of grain boundaries** **Shrinkage of open pores** **Significant decrease of the mean porosity** **Equilibrium pore shape with continuous porosity**	**0.65 – 0.90**
Final	**Closed pores intersect grain boundaries** **Closed pores containing kiln gas form when density ≈ 92 %** **Pores shrink to a limited size or disappear** **Pores larger than grains shrink relatively slowly** **Equilibrium pore shape with isolated porosity**	**> 0.90**

Initial stage

The initial phase is characterised by rapid neck growth via diffusion, vapour transport, plastic flow, or viscous flow and the removal of large initial differences in surface

curvature. The primary densification mechanism for this stage is shrinkage via neck growth [42].

The model for this stage consists of two equally sized spheres in contact, referred to as the two-sphere model, as shown in Figure 19.

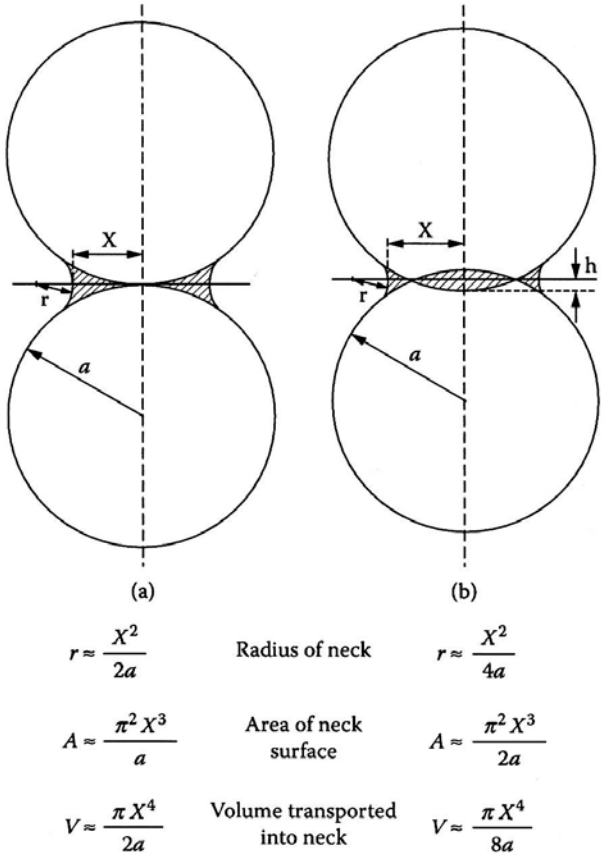

Figure 19 The two-sphere model (a) the non-densification mechanism and (b) the densification mechanism [42]

The neck formation stage is another name for the initial stage of sintering, as shown above. The curvature difference between the particle surface and that of the neck is the driving force for the initial powder to compact as discussed in section 2.1.2. The possible diffusion mechanisms are surface diffusion, lattice diffusion from the surface, lattice diffusion from the grain boundary, vapour transport and viscous flow [42].

Grain Boundary Diffusion

The flux of the atoms into the neck is [42]

$$J_a = \frac{D_v}{\Omega}\frac{dC_v}{dx} \tag{2.10}$$

Where D_v is the vacancy diffusion coefficient, Ω is the volume of an atom or vacancy, and dC_v/dx is the vacancy concentration gradient (in one dimension). The volume of the matter transport into the neck per unit time is

$$\frac{dV}{dt} = J_a A_{gb} \Omega \tag{2.11}$$

Where A_{gb} is the cross-sectional area over which diffusion occurs. $A_{gb} = 2\pi X \delta_{gb}$, when it is assumed that the grain boundary diffusion occurs over a constant thickness δ_{gb}. X is the radius of the neck. Combining Eq. (2.10) and (2.11) and substituting A_{gb} gives

$$\frac{dV}{dt} = D_v 2\pi X \delta_{gb} \frac{dC_c}{dx} \tag{2.12}$$

The one-dimensional solution can be used, because the neck radius increases radially in a direction orthogonal to the centre line of the spheres. $dC_v/dx = \Delta C_V/X$, if the vacancy concentration is constant between the neck surface and centre of the neck. ΔC_v is the difference in vacancy concentration the neck surface and centre of the neck. It further assumed that the vacancy concentration at the neck centre is equal to that under a flat, stress-free surface C_{v0}.

$$\Delta C_v = C_v - C_{v0} = \frac{C_{v0}\gamma_{sv}\Omega}{kT}\left(\frac{1}{r_1} + \frac{1}{r_2}\right) \tag{2.13}$$

Where r_1 and $r_2$are the two principal radii of the curvature of the neck surface and it is assumed that $X \gg r$. Substituting into Eq. (2.11)

$$\frac{dV}{dt} = \frac{2\pi D_v C_{V0} \delta_{gb} \gamma_{sv} \Omega}{kTr} \tag{2.14}$$

The relation for V and r given in Figure 19b and assuming the grain boundary diffusion coefficient D_{gb} equal to $D_v C_{v0}$ is

$$X^5 dX = \frac{16 D_{gb} \delta_{gb} \gamma_{sv} \Omega a^2}{kT} \tag{2.15}$$

After integration and application of the boundary conditions $X = 0$ at $t = 0$ Eq. (2.15) becomes

$$\frac{X}{a} = \left(\frac{96 D_{gb} \delta_{gb} \gamma_{sv} \Omega}{kT a^4}\right)^{1/6} t^{1/6} \tag{2.16}$$

The linear shrinkage is the change in length ΔL in relation to the original lengthL_0.

$$\frac{\Delta L}{L_0} = -\frac{h}{a} = -\frac{r}{a} = -\frac{X^2}{4a^2} \tag{2.17}$$

Where h is half the interpenetration distance between the spheres. Using Eq. (2.16) to obtain

$$\frac{\Delta L}{L_0} = -\left(\frac{3 D_{gb} \delta_{gb} \gamma_{sv} \Omega}{2kT a^4}\right)^{1/3} t^{1/3} \tag{2.18}$$

A more general form to express the neck growth and shrinkage is

$$\left(\frac{X}{a}\right)^m = \frac{H}{a^n} t \tag{2.19}$$

$$\left(\frac{\Delta L}{L_0}\right)^{m/2} = -\frac{H}{2^m a^n} t \tag{2.20}$$

Where m and n are numerical exponents which depend on the sintering mechanism and H is a function that contains the geometrical and material parameters of the powder system, Figure 20.

Figure 20 Plausible Values for the Constants Appearing in Equation 2.19 and 2.20 for the Initial Sintering Stage [36]

Mechanism	m	n	H[b]
Surface diffusion[a]	7	4	$56D_s\delta_s\gamma_{sv}\Omega/kT$
Lattice diffusion from the surface[a]	4	3	$20D_l\gamma_{sv}\Omega/kT$
Vapor transport[a]	3	2	$3p_0\gamma_{sv}\Omega/(2\pi mkT)^{1/2}kT$
Grain boundary diffusion	6	4	$96D_{gb}\delta_{gb}\gamma_{sv}\Omega/kT$
Lattice diffusion from the grain boundary	5	3	$80\pi D_l\gamma_{sv}\Omega/kT$
Viscous flow	2	1	$3\gamma_{sv}/2\eta$

[a] Denotes nondensifying mechanism, i.e., $\Delta L/L_0 = 0$.

[b] D_s, D_l, D_{gb} are the diffusion coefficients for surface, lattice, and grain boundary diffusion. δ_s and δ_{gb} are the thicknesses for surface and grain boundary diffusion. γ_{sv} is the specific surface energy. p_0 is the vapor pressure over a flat surface. m is the mass of an atom. k is the Boltzmann constant. T is the absolute temperature. η is the viscosity.

Intermediate stage

This stage starts when the pores reach their equilibrium shapes which is determine by the surface tension and interfacial tensions. The porosity is still continues and situated along the grain edges. The reduction of the pore volume is the densification mechanism for this stage. Thereby the pores are shrinking until the reduction of their cross section reaches a critical point where the pore getting unstable and pinch off and get isolated. Therefore this stage covers the major part of the sintering, because in general the pores are first isolated when the theoretical density reaches around 90 % [42].

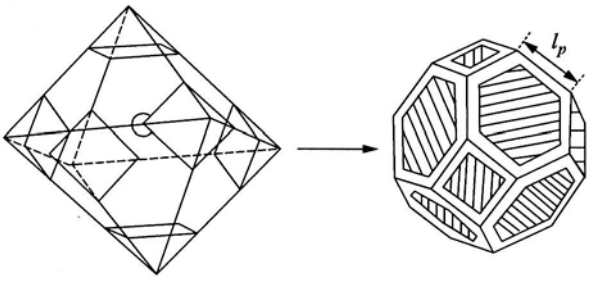

Figure 21 Sketch illustrating the formation of a tetrakaidecahedra from a truncated octahedron [36]

A space-filling array of equal-sized tetrakaidecahedra with cylindrical porosity along its edges is the idealized model and unit cell for this stage. A tetrakaidecahedra is an octahedron at whose corners a pyramidal shape is cut off. The resulting structure is a tetrakaidecahedra and has 36 edges, 24 corners and 14 faces (8 hexagonal and 6 square). The volume of a tetrakaidecahedra is

$$V_t = 8\sqrt{2}l_p^3 \tag{2.21}$$

Where l_p is the length of a tetrakaidecahedra edge. As said before the pores in this stage are situated along the tetrakaidecahedra edges as cylinder with a radius r and are shared between 3 neighbouring tetrakaidecahedra. The total pore volume for unit cell is

$$V_p = \frac{1}{3}\left(36\pi r^2 l_p\right) \tag{2.22}$$

The porosity for the unit cell, V_p/V_t is

$$P_c = \frac{3\pi}{2\sqrt{2}}\left(\frac{r^2}{l_p^2}\right) \tag{2.23}$$

Since it is assumed that the geometry of the pores is uniform. The chemical potential at every pore surface is equal. This reduces the sintering mechanisms to grain boundary and lattice diffusion as the nondensifying mechanisms cannot operate under these assumption

Lattice diffusion

The flux per unit length of the cylinder is

$$\frac{J}{l} = 4\pi D_v \Delta C \tag{2.24}$$

Where D_v is the vacancy diffusion coefficient and ΔC is the vacancy concentration difference between the pore (source) and the boundary (sink).

For lattice diffusion, assuming: 1) the convergence of the flux to the boundary does not qualitatively change the flux equation with respect to its dependence on the pore radius; 2) the width is equal to the pore diameter; 3) the flux is increased by a factor of 2 due to the freedom of the vacancy diffusion flux to diverge initially, then the densification rate is determined by the diffusion mechanisms, grain size and temperature. The smaller the grain size, the higher the densification rate [42].

These assumption change Eq. (2.24) into

$$J = 2(4\pi D_v \Delta C)2r \tag{2.25}$$

Since each of the 14 faces of a tetrakaidecahedra is shared by 2 grains the volume flux per unit cell is

$$\frac{dV}{dt} = \frac{14}{2} J = 112\pi D_v \Delta C \tag{2.26}$$

The 2 principal radii of the curvature for the cylindrical pore are r and ∞, so that ΔC is

$$\Delta C = \frac{C_{v0}\gamma_{sv}\Omega}{kT_r} \tag{2.27}$$

Substituting into Eq. (2.26) and putting $D_l = D_v C_{v0}$, where D_l is the lattice diffusion coefficient

$$dV = \frac{112 D_l \gamma_{sv}\Omega}{kT} dt \tag{2.28}$$

The integral of dV is equal to the porosity given by Eq. (2.22)

$$\int dV = 12\pi r^2 l_p \Big]_{r_0}^{r} \tag{2.29}$$

Combined with Eq. (2.28)

$$r^2]_r^0 \approx -10\frac{D_l\gamma_{sv}\Omega}{l_p kT}t\Big]_t^{t_f} \tag{2.30}$$

Where t_f is the time when the pore vanishes. Dividing both sides of this equation by l_p^2 and evaluating the integrand yields

$$P_c \approx \frac{r^2}{l_p^2} \approx \frac{10D_l\gamma_{sv}\Omega}{l_p^3 kT}(t_f - t) \tag{2.31}$$

This equation is only order-of magnitude calculation, because of all the assumptions that had been made. As soon as the pore are pinched off and isolate this model cannot be applied [42].

$P = 1 - \rho$ describes the relation between porosity P and relative density ρ can be used to express Eq. (2.31) in terms of densification rate. After differentiating with respect to time,

$$\frac{d}{dt}(P_c) = -\frac{d\rho}{dt} \approx -\frac{10D_l\gamma_{sv}\Omega}{l_p^3 kT} \tag{2.32}$$

l_p equal grain size G

$$\frac{1}{\rho}\frac{d\rho}{dt} \approx \frac{10D_l\gamma_{sv}\Omega}{\rho G^3 kT} \tag{2.33}$$

Grain boundary diffusion

The flux equations for the grain boundary diffusion, using the same geometrical model as for the lattice diffusion, are

$$P_c \approx \frac{r^2}{l_p^2} \approx \left(\frac{2D_{gb}\delta_{gb}\gamma_{gb}\Omega}{l_p^4 kT}\right)^{2/3} t^{2/3} \tag{2.34}$$

Using the procedure described above, Eq. (2.34) can be described as

$$\frac{1}{\rho}\frac{d\rho}{dt} \approx \frac{4}{3}\left[\frac{D_{gb}\delta_{gb}\gamma_{sv}\Omega}{\rho(1-\rho)^{1/2}G^4kT}\right] \quad (2.35)$$

Final stage

If the process cannot be controlled carefully in this stage then exaggerated grains separated from pores can occur within some regions of the microstructure [35]. This stage starts as soon as the pore is pinched off and isolated at the grain corners. Ideal for this stage is that the porosity continues to shrink until it disappears [42].

The geometric model for this stage again array of equal-sized tetrakaidecahedra. However, this time the porosity no longer situated along the edges. Instead at every corner are equal-sized spherical pores. This means that every tetrakaidecahedra has 24 pores and every neighbouring 4 tetrakaidecahedra. The pore volume for a single tetrakaidecahedra is

$$V_p = \left(\frac{24}{4}\right)\left(\frac{4}{3}\right)\pi r^3 \quad (2.36)$$

The porosity in a single tetrakaidecahedra is

$$P_s = \frac{8\pi r^3}{8\sqrt{2}l_p^3} = \frac{\pi}{\sqrt{2}}\left(\frac{r^3}{l_p^3}\right) \quad (2.37)$$

By choosing the thick-walled spherical shell of solid material around a single pore of the radius r is possible to create a more convenient unit cell. The density of the unit cell is equal to the density of the powder system and the outer radius of the shell is defined as b.

$$\rho = 1 - \left(\frac{r}{b}\right)^3 \quad (2.38)$$

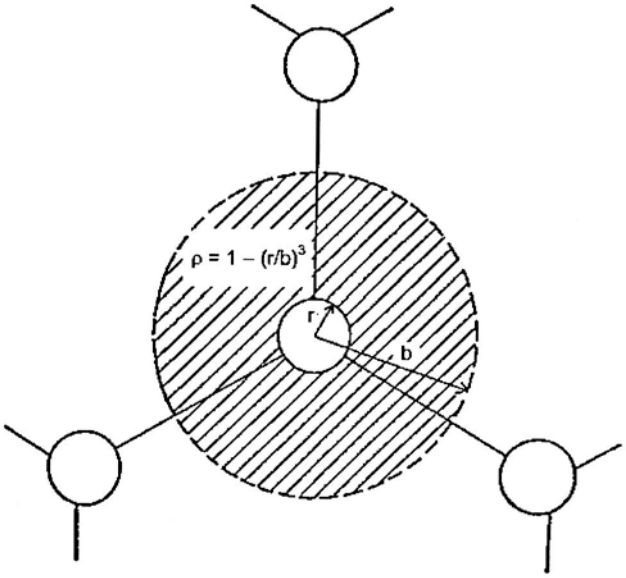

Figure 22 A porous solid during the final stage of sintering can be modelled by constructing a spherical shell centred on a single pore. The outer radius b is chosen such that the density of the shell matches that of the porous solid. [42]

The densification rate equations for the lattice and grain boundary diffusion in the final stage are [46]

$$\frac{1}{\rho}\frac{d\rho}{dt} = \frac{40}{3}\left(\frac{D_l\Omega}{G^2kT}\right)\left(\frac{2\gamma_{sv}}{r}\right) \tag{2.39}$$

$$\frac{1}{\rho}\frac{d\rho}{dt} = \frac{15}{2}\left(\frac{D_{gb}\delta_{gb}\Omega}{G^3kT}\right)\left(\frac{2\gamma_{sv}}{r}\right) \tag{2.40}$$

The densification rate depends on the diffusion mechanisms, grain size and temperature [47].

2.2.5 Grain Growth in Sintering

Grain growth is an integral, but generally undesired, part of sintering. There are two types of grain growth: normal and discontinuous or abnormal, which is called secondary recrystallization or cannibalistic grain growth. In normal grain growth, Figure 23a, the grain size distribution is relatively narrow and has a fixed distribution shape throughout growth. In abnormal grain growth, a few large grains eventually

consume all the smaller grains, Figure 23b. The strength, creep, electrical and magnetic properties of the ceramics are controlled by the grain distribution and grain size. Therefore, control of the final grain size is necessary [42].

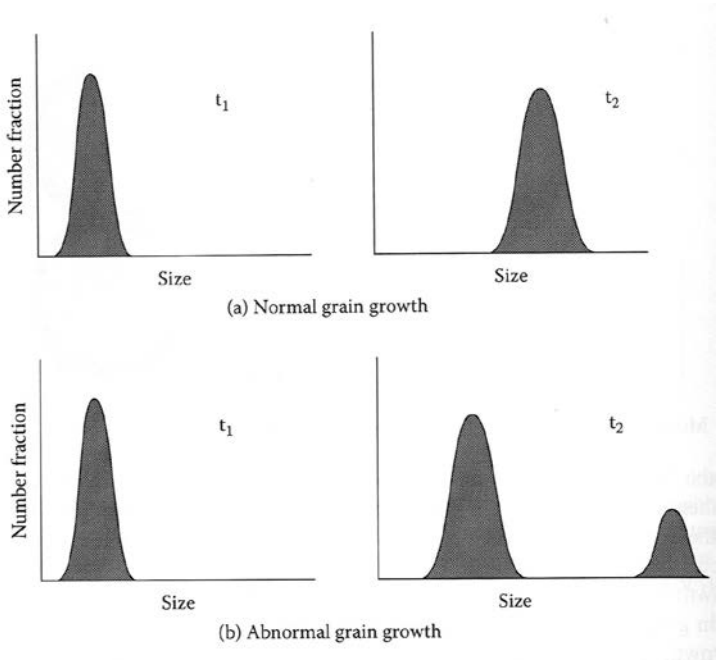

Figure 23 Grain size distribution for (a) normal grain growth and (b) abnormal grain growth [42]

Normal grain growth

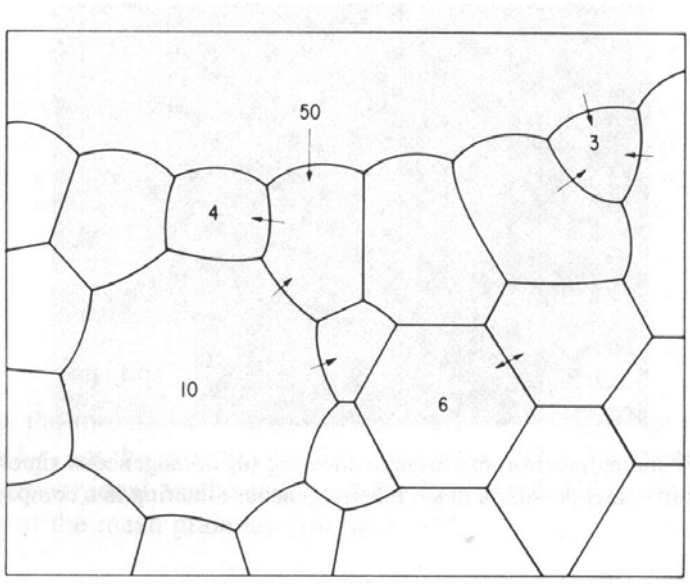

Figure 24 The model of the movement of grain boundaries [47]

A model of the migration of a grain boundary due to atom transport driving forces caused by the difference in surface curvature was presented by Burke and Turnbull [47]. This is shown in Figure 24.

As discussed in section 2.1.2, the curvature of the particle surface forms part of the driving forces for sintering. It is also the reason for grain growth. In the 2-dimensional case, the equilibrium angle is 120°, which corresponds with 6 sided grains. In this case, their sides are straight and they are neither shrinking nor growing. If a grain has less than 6 sides than its sides are convex and, since the grain boundaries move towards their centre of curvature, the grains shrink. Grains with more than 6 sides have concave surfaces and, hence grow. As the average grain size is increasing, shrinking grains are losing sides until they reach the minimum of 3 sides and start to disappear, Figure 25. All this results in the reduction of the free surface energy in the system, because when atoms move from a convex into a concave surface, they reduce their free energy, Figure 26 [45, 48].

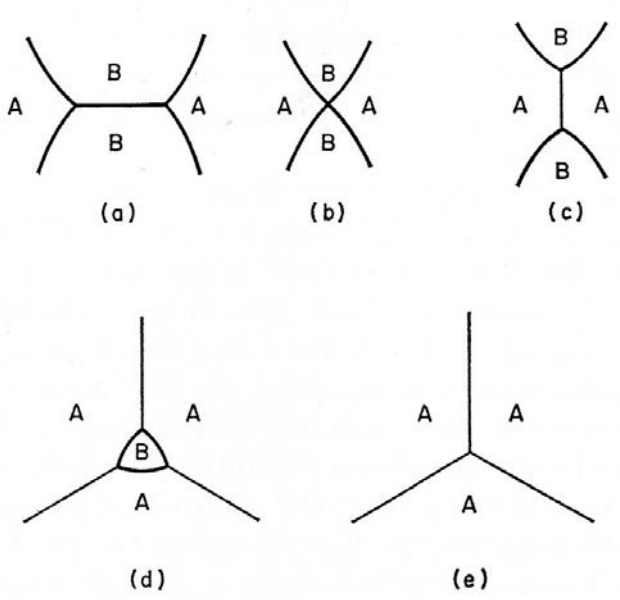

Figure 25 Change of grain size (a), (b) and (c) grain B loses sides and shrinks as grain A grows and gains side for B; (d) and (e) disappearance of grain B [48]

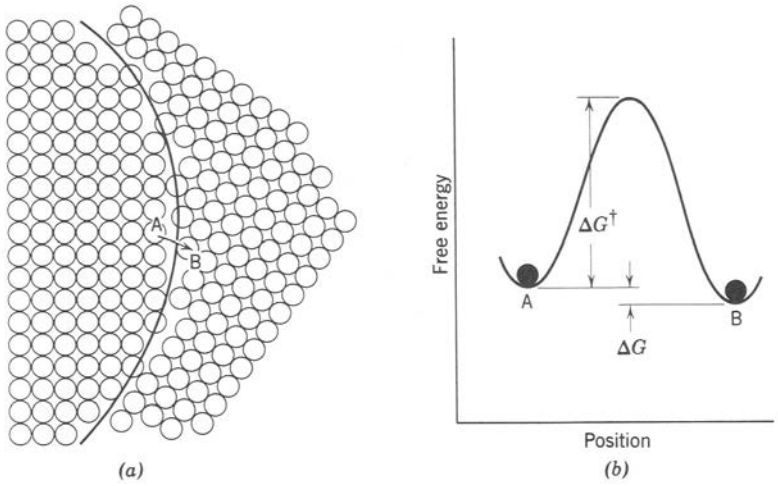

Figure 26 (a) Structure of grain boundary and (b) energy change for atom jump [45]

Abnormal Grain growth

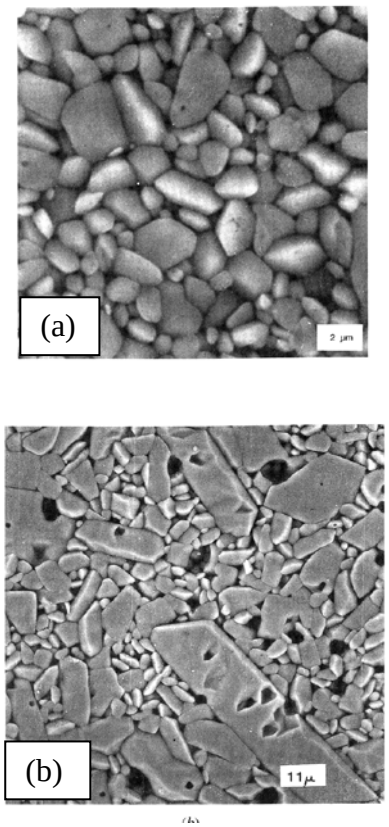

Figure 27 (a) Normal grain growth and (b) abnormal grain growth [35]

Some very large grains can occur in a fine-grained matrix during ceramic sintering, Figure 27. They are a result of abnormal or runaway grain growth in which the large grains have a much faster growth rate than the fine-grained matrix. These grains are

referred to as abnormal grains. There two explanations for the development of these abnormal grains. One is that the presences of impurities, which are acting as sinter additives, create a liquid phase, as discussed in section 2.1.2, and when recrystallizing create the large grains. The other explanation is that these abnormal grains have more sides than their neighbours, Figure 24. The result of this situation is that the curvature of the side, which the surrounding grains share with these large grains, is increased. Hence the surface radius of the small grains is smaller towards the abnormal grains and result in an increase of the growth rate of the abnormal grain compared towards grains with fewer sides [45].

2.2.6 Pore reduction during sintering

As described earlier, the reduction of porosity, which can be divided into different categories (Table 3), is part of the densification of ceramics during sintering and starts, as shown in Table 2, in the initial phase of sintering [42].

Table 3 Classification of the pores according to their size (diametre or width) [42]

Category	Pore size / nm
Micropores	<2
Mesopores	2 – 50
Macropores	>50

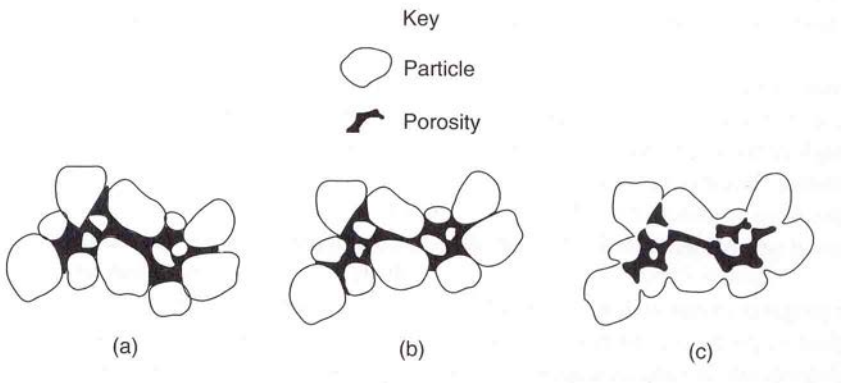

Figure 28 Changes that occurs during the initial stage of sintering. (a) Starting particles, (b) rearrangement, and (c) neck formation. [37]

The first sintering stage involves rearrangement of particles to increase the number of points of contact and the neck formation at the contact points between each particle. This reduces the pore volume, but, as shown in Figure 28, the influence is small compared to the reduction in the intermediate stage, Figure 29, because in this sintering phase the shrinkage of the ceramic is equal to the reduction of the porosity. During this sintering the open porosity will be removed or converted into closed porosity, a process that continues until all open porosity is lost. After this, the closed porosity is removed, Figure 30. However, whether the final porosity can be removed completely depends on several factors. First of all, how rapid the grain growth is and whether the pores become isolated, which makes it very difficult to remove them. The reason for this, is that the paths for the matter transport become much longer and this leads to a decrease in the diffusion rate, Figure 31. Therefore it would be necessary to increase the sintering time to achieve high densities. However this increases the risk of abnormal grain growth and does not necessarily lead to a fully dense sintered sample, because air or gas can be trapped inside a pore. The latter is another reason for the difficulty in achieving the complete removal of the porosity inside a sample, because as the pore shrinks and the entrapped gas will be compressed. This continues until the pressure of the compressed gas is high enough to prevent pore elimination [35, 37, 42, 48].

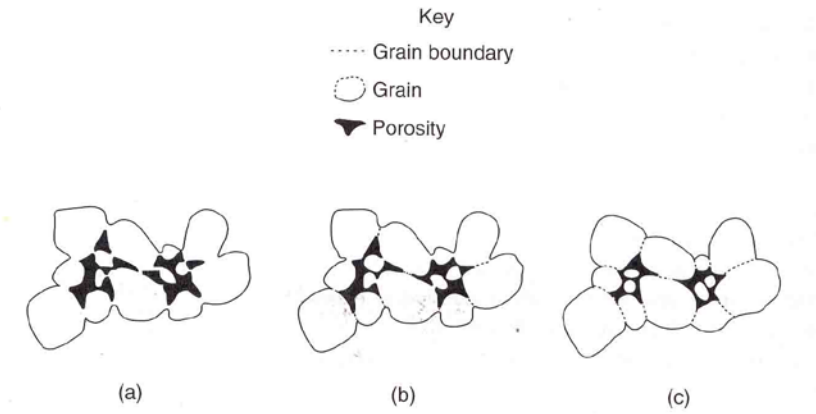

Figure 29 Changes that occurs during the second stage of sintering. (a) Neck growth and volume shrinkage, (b) lengthening of grain boundaries, and (c) continued neck growth and grain boundary lengthening, volume shrinkage, and grain growth [37]

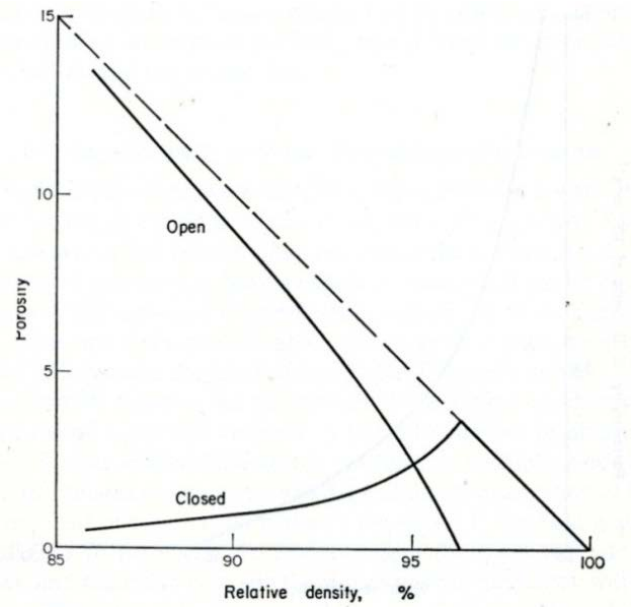

Figure 30 Variation of the open and closed porosity during sintering [48]

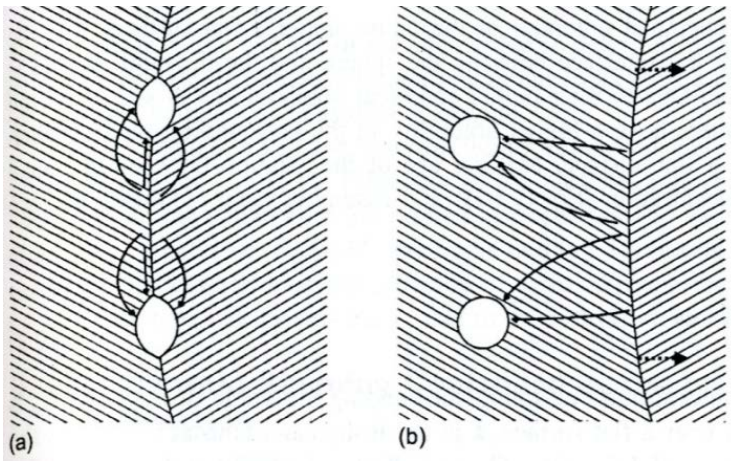

Figure 31 (a) Densification mechanism for porosity attached to a grain boundary (Arrows indicate paths for atom diffusion) (b) Densification mechanism for porosity separated from a grain boundary (solid arrows indicate paths for the atom diffusion, and dashed arrows indicate the direction of boundary migration [42]

As for the densification, the reduction of the free energy is the driving force for a pore to shrink. However, the decrease in the free energy is not the only effect created when a pore shrinks. Since the shrinkage of a pore increases the grain boundary area, which leads to an increase in the free energy. Therefore, the reduction in the free energy from pore shrinkage needs to be greater than the increase due to the increasing grain boundary and an equilibrium shape of pores with a dihedral angle Ψ can be defined by [42]

$$\cos\frac{\Psi}{2} = \frac{\gamma_{gb}}{2\gamma_{sv}} \tag{2.41}$$

Where γ_{gb} and γ_{sv} are the interfacial energy of the grain boundary interface and at the pore surface.

When the dihedral angle is known than it is possible, in two dimensions, to determine the critical pore coordination number, N_c:

$$\Psi = (180N_c - 360)/N_c \tag{2.42}$$

The critical pore coordination number is defined as the number of surrounding grain N for which the side of the pore are straight and the pore is stable. If the number of surrounding grains is smaller than N_c than the pore surface is convex and the pore shrinks. Further, if the pore surface is concave, $N > N_c$, than the pore grows, Figure 32 [42].

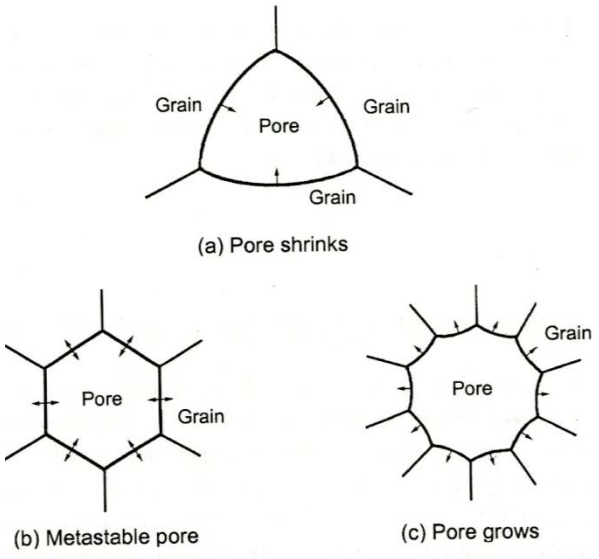

Figure 32 Pore stability in the two dimension for a dihedral angle of 120° [42]

2.2.7 Alternative Sintering Methods

Solid-state sintering is not the only possibility to produce ceramics. Hot pressing and hot isostatic pressing are sintering techniques which based on the use of an external pressure to increase the driving force for sintering. The induced additional driving force only enhances the densification, the sintering mechanisms remain unchanged. In some case ceramic are sintered via liquid-phase sintering, which requires the formation of a liquid phase during sintering and therefore follows different mechanisms compared to solid-state sintering.

Hot Pressing and Hot Isostatic Pressing

Hot pressing is used for the densification of samples with high degree of covalent bonding such as SiC, and Si_3N_4 and ceramic matrix composites. The enhanced densification rate leads to higher density and reduced grain size and can also be used to reduce the sintering temperature or time. The reduction of the sintering temperature is helpful if the sample will decompose at higher temperature or has volatile components. In addition, the potentially reduced grain size will improve the mechanical properties of the sample, because these properties are maximized with small grain sizes at high densities [37, 42].

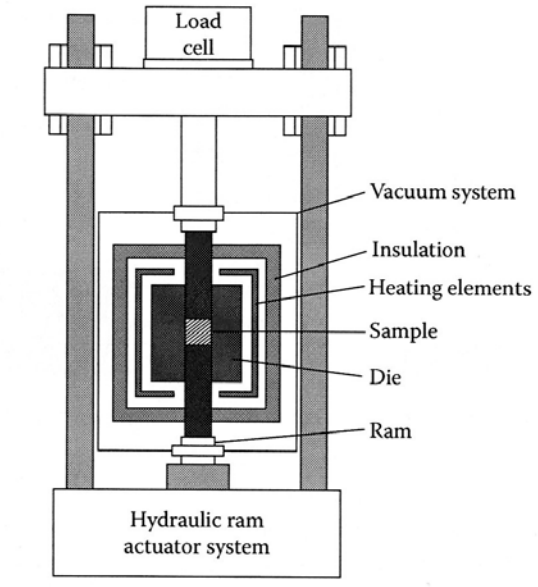

Figure 33 Schematic of a Hot Press [36]

Best description for hot pressing is die pressing at high temperature which could be called “pressure sintering”. Figure 33 shows a basic setup for a hot press. Since the sample is die pressed at sintering temperature, the die needs to withstand these temperatures and should not interact with the material to be pressed. The most common die material is graphite. Therefore the furnace needs to be evacuated or filled with inert gas to prevent the oxidation of the graphite [37].

As described in section 2.1.2 an applied pressure is one of the driving forces for densification and exceeds the effect of the curvature of the particle surface. This acceleration of the densification is achieved by the rearranging of particles to improve packing and increased contact stress between the particles. This stress leads to an increase of the chemical potential of the atoms in the grain boundaries. However atoms on the pore surfaces are not affected. The one sided increase of the chemical potential will increase the potential difference and with it the driving force for densification. The densification rate equation is

$$\frac{1}{\rho}\frac{d\rho}{dt} = A\left(\frac{\Omega}{G^m kT}\right)\left(\frac{\alpha\gamma_{sv}}{r} + p_a\phi\right) \tag{2.43}$$

where p_a the hydrostatic component of the applied stress, A is a constant depending on the geometrical model, m is an exponent depending on the diffusion mechanism, α is a constant depending on the geometry of pore and ϕ is the stress intensification factor, a geometrical factor accounting for the effective stress on the grain boundary being greater than the applied stress because of the presence of porosity in the body [42].

Table 4 Values for the constants appearing in the Densification Rate Equation (Eq. 2.43) [42]

Mechanism	Intermediate stage	Final stage
Lattice diffusion	A = 40/3; m = 2; α = 1	A = 40/3; m = 2; α = 2
Grain boundary diffusion	A = 95/2; m = 3; α = 1	A = 15/2; m = 3; α = 2

In a solid with relative density ρ and randomly distributed spherical pores, ϕ is given by

$$\phi = 1/\rho \tag{2.44}$$

Hot pressing achieves several processing and property advantages compared to pressureless sintering [37]:

- Reduction of processing time
- Possible reduction of grain growth, when densification temperature is reduced
- Minimization of porosity and grain growth lead to higher strength
- Improved high-temperature properties through possible reduction of the amount of sintering aids
- Possibility to avoid usage of binders or other organic additives by starting with a loose powder

The main limitation for the use of hot pressing is the shape capability. As for die pressing, hot pressing can produce easily only flat plates, blocks or cylinders. More complicated shapes are beyond the range of hot pressing without machining, because of application of uniaxial pressure [37].

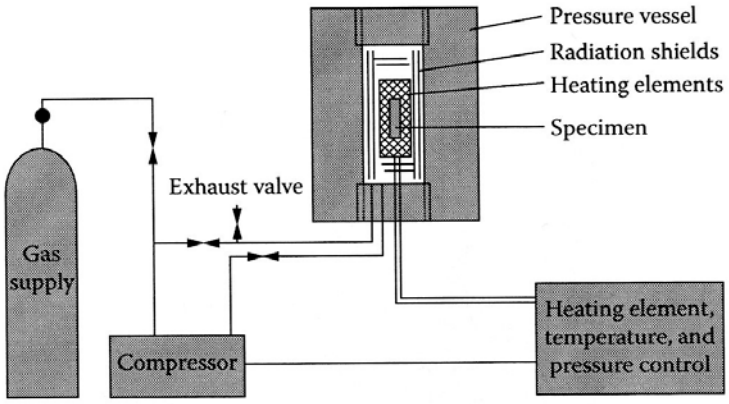

Figure 34 Schematic of Hot Isostatic Press [36]

Hot Isostatic Pressing (HIP) allows pressure to be applied from multiple directions and hence overcomes the limitation of the shape capability for hot pressing. The fundamental principal of HIP is the same as for cold isostatic pressing. For HIP the

sample needs to be evacuated and sealed in a gas-impermeable envelop. The material for this envelop can be glass, tantalum or other metal, depending of the sintering temperature. This envelopment is required because if any high-pressure gas leaks into the sample and creates an equalization of the pressure, densification will not occur.

Liquid-phase sintering

Liquid-phase sintering is typically used for ceramics with a high degree of covalent bonding such as Si_3N_4 and SiC, which are difficult to densify by solid-state sintering. Further it is used when solid-state sintering is too expensive or the required fabrication temperature is too high [42].

The advantage of liquid-phase sintering compared to solid-state sintering is a faster densification. This occurs because the liquid phase reduces the friction between the particles and the introduction of capillary forces leads to the dissolution of share edges and all together leads to a faster rearrangement of solid particles. The rapid particle rearrangement is not to the only difference with solid-state sintering. The presence of the liquid phase also increases the numbers interfaces, liquid/vapour γ_{lv} and liquid/solid γ_{ls}, Figure 35, and the surface energy. Another important parameter is behaviour of the liquid at a solid surface, because if the liquid forms a bead and sits in the free space of the porosity than the resulting sintering will be less advantages of the presence of a liquid phase. Therefore the degree of wetting is important and can be quantified by the equilibriums angle θ which is formed between the solid and the liquid. For the equilibrium all the forces are balanced

$$\gamma_{sv} = \gamma_{ls} + \gamma_{lv} \cos\theta \tag{2.45}$$

For wetting it is the preferred the value for γ_{sv} is high and that the values for γ_{ls} and/or γ_{lv} are low. Further if the contact is between 0 and π/2 the system is wetting [41]. Additives can be used to alter the wetting behaviour. Further the contact angle will be lowered when the temperature is increase, because the solubility of the liquid will be increased.

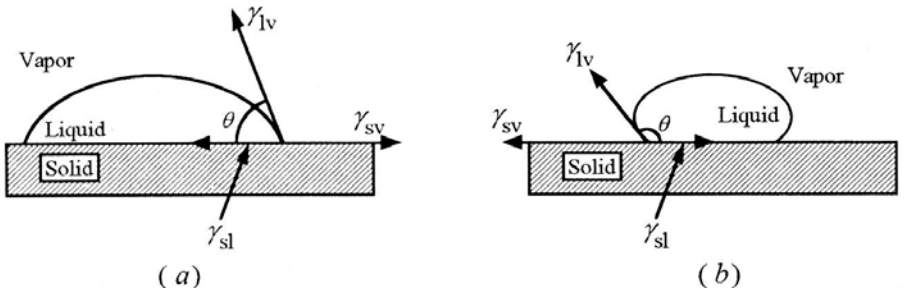

Figure 35 (a) Wetting system showing forces on the liquid drop (b) Nonwetting system with $\theta > 90°$ [41]

Wetting is important for liquid-phase sintering, because the liquid has the potential to completely penetrate the grain boundaries. This is important for the development of the microstructure, because grain boundary penetration has the potential to breaking up agglomerates. The required condition for a thick liquid film to penetrate and separate grains is $\gamma_{gb} > 2\gamma_{ls}$, which means that equilibrium dihedral angle ψ, Figure 36,

$$\gamma_{gb} = 2\gamma_{ls} cos\frac{\psi}{2} \tag{2.46}$$

must be 0 [41].

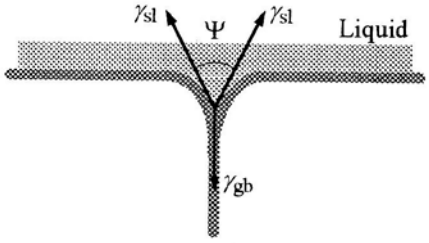

Figure 36 Equilibrium dihedral angle between grain boundary and liquid phase [41]

The presence of solids and liquids leads to surface tensions which create capillary forces. These forces, together with the lubrication potential of the liquid, are a reason for the fast rearrangement of particles and densification, because the capillary forces lead to strong attractive forces between neighbouring particles. There are 2 origins for the attractive forces: first the force resulting from curvature of the meniscus and its pressure differential across it and secondly the component of the liquid/vapour surface energy normal to the two surfaces [41].

The sintering mechanisms for liquid phase sintering utilise a liquid from a melting solid, which will wet and penetrate between grains, create attractive forces between them and pull them together. In combination with the lubrication effect of the liquid, 3 successive mechanism are responsible for the sintering, Figure 37.

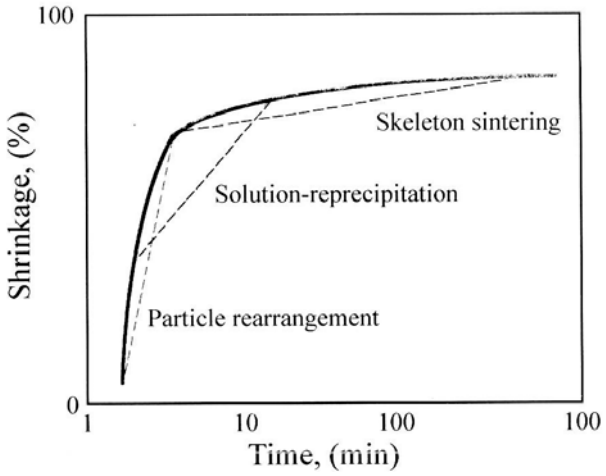

Figure 37 Time dependence of the shrinkage evolution as a result of the mechanisms [41]

Particle rearrangement is the first mechanism. Capillary forces and liquid filling the porosity are used the rearrange the particles and to achieve densification. As this is a very rapid process, it is possible to achieve 100% density almost instantaneously if the liquid flows and the finer pores between the particles are filled with liquid [41].

The following mechanism is solution reprecipitation. The capillary forces are not only attractive forces between particles; they lead to an increase in the chemical potential of atoms at point of contact compared to atoms in areas without contact. The chemical potential difference between the 2 types of atoms is given as:

$$\mu - \mu_0 = kT \ln \frac{a}{a_0} = \Delta P \Omega_{MX} \tag{2.47}$$

$$\Delta P = \frac{\gamma_{lv}}{\rho_2} \tag{2.48}$$

Where ΔP is the pressure across the curved surface, a is the activity of the solid in the liquid at the point of contact, and a_0 is the same activity under no stress. At the

contact points atoms are dissolved because of the chemical potential gradient. These dissolved atoms are lead away from the area between the 2 particles through the liquid phase. The result of this is shrinkage and densification. The diffusion in liquid is far higher (order of magnitude) then for those in solid, which is a reason why the densification kinetics are much faster for liquid-phase sintering than for solid-state sintering. However this advantage can only be used as long as the solid is soluble into the liquid which is doing the wetting [41].

The last stage is solid-stage sintering, because liquid phase sintering stops as soon as a rigid skeleton is formed. The change to solid-stage sintering reduces the rate of shrinkage and densification significantly [41].

Liquid-phase sintering is more economical than solid-state sintering, because it is more forgiving in term of packing and of course much faster. Therefore most of the commercial ceramics are liquid-phase sintered unless the required application cannot tolerate the presence of a glassy phase, e.g. ceramic insulators [41].

2.3 Solid-State Reaction

2.3.1 General

Solid-state reactions are very common in the production of powders of complex oxides such as titanates, ferrites and aluminates. Therefore solid-state reactions are widely researched and may be divided into several subsections such as heterogeneous reactions, and reactions in a single-phase system or reactions in a powder bed and the reaction within compacted bodies, which could be polycrystalline as well as single crystalline [36, 49]. This review is focused on the general aspect of solid-state reactions in multiphase systems of compacted bodies, the spinel formation and the zinc aluminate spinel ($ZnAl_2O_4$) and magnesium aluminate spinel ($MgAl_2O_4$) in particular.

The simplest case for a solid-state reaction is the reaction of two solid materials, A and B, into a solid reaction product, C. These starting materials can be single element or complex compounds and are initially in contact with each other. As the

reaction proceeds, the precursors will be separated by a growing layer of the reaction product, Figure 38. Therefore, transport of atoms, ions or molecules, by several possible mechanisms through the phase boundary and reaction product, is necessary to continue the reaction [36]. The transport mechanisms are the same as described in section 2.1.3 for the sintering of ceramics. The growth of a product layer by a diffusion-controlled reaction is defined by

$$y^2 = Kt \tag{2.49}$$

Where *y* is the thickness of the reaction layer, *K* is the practical reaction rate constant and *t* is the reaction time [49].

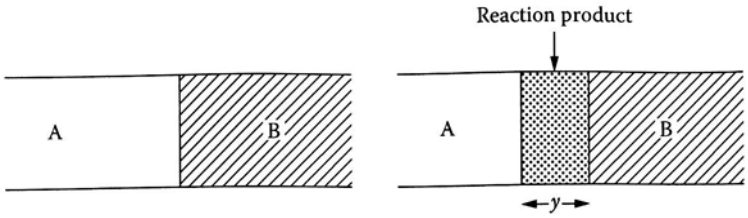

Figure 38 Schematic of solid-state reaction [36]

The difference in the free energy between the reactants and the reaction product is the driving force for the reaction, section 2.1.2. The reaction entropies will be small as long as the reactants are crystalline solids. Solid-state reactions are exothermal reactions. However, in a good approximation, isothermal conditions can be assumed, as long as the reactants are single crystals or compact bodies, because the reaction interface is small and the reaction rate is slow. This results in a low heat production per unit time. If the reactants are powders then a large reaction interface is available and isothermal conditions cannot be assumed. The exothermic reaction in this case has the potential to result in self-heating of the particles, which would increase the reaction rate and lead to an accelerated heat production in a rapid spiral [49].

If A and B are binary compounds in a ternary system then phases in the reaction product lie in the Gibbs triangle on the line joining A and B, see Figure 39. Within this quasi-binary system, the solid-state reaction will continue until at least one of the reactants is consumed. If the reaction is interrupted externally before this point than the reaction product will contain all possible phases along the line joining A and B [49].

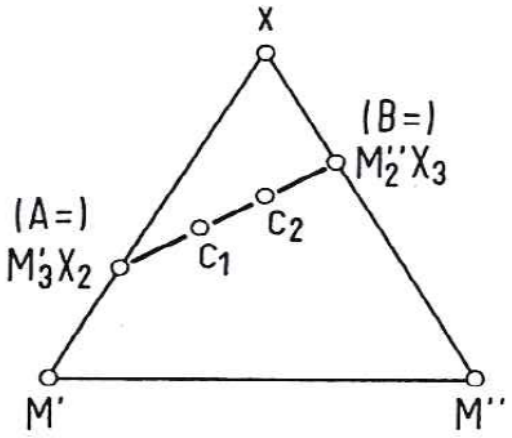

Figure 39 Gibbs triangle for ternary system M'- M''- X. The quasi-binary line $M'_3X_2M''_2X_3$ is drawn with the product phases C_1 and C_2 [49]

2.3.2 Spinel Formation

Spinel formation has been investigated for almost 100 years [50]. Because the industrial interest and time spent on the investigation the spinel reaction has thoroughly investigated [49]. Spinel has the composition AB_2O_4, where A is a divalent or tetravalent ion and B is divalent or trivalent ion, depending if it is a 2-3-spinel or 4-2-spinel. Possible reaction mechanisms are shown in Figure 40. These can be subdivided into 3 different mechanism groups [36]:

1) Transport of O_2 molecules through the gaseous phase and electrons through the product layer to ensure electroneutrality (Figure 40 a and b)
2) O-ions are stationary, while cations are transported via counter diffusion (Figure 40 c)
3) Diffusion of cations and oxygen ions through the product layer (Figure 40 d and e)

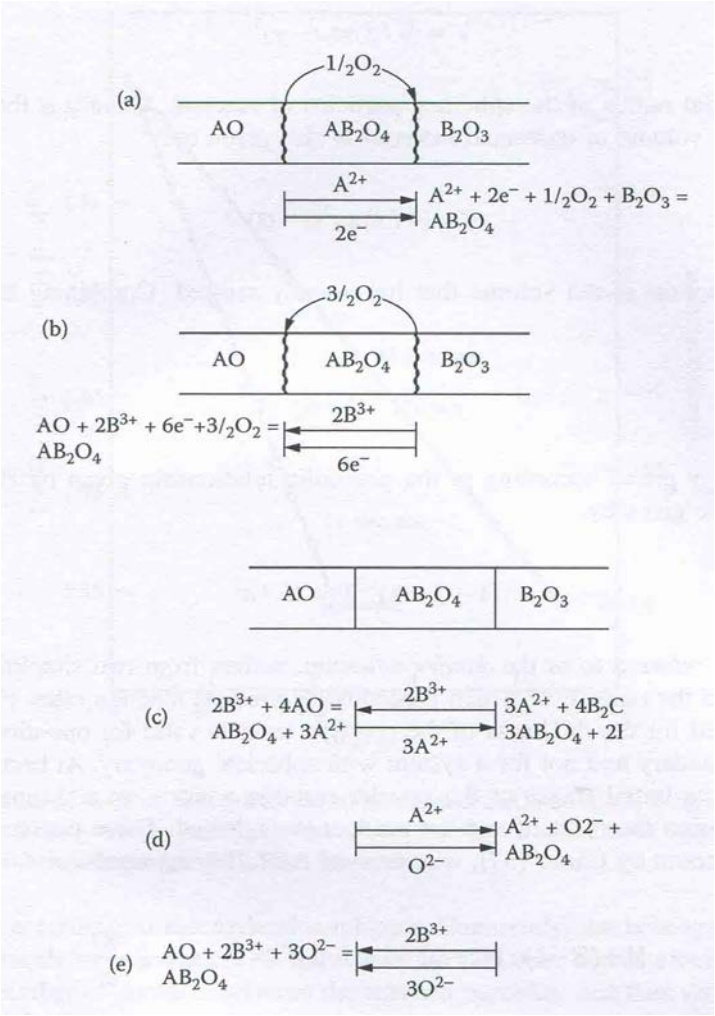

Figure 40 Reaction mechanisms for spinel formation [36]

However, there is a wide difference of the diffusion coefficients of the different ions. Therefore the 3rd group of the reaction mechanisms can be neglected as the diffusion of oxygen ions is rather slow compared to the cations. Further, the 1st group of the mechanisms is unimportant if ideal contact is achieved, because, again, the transport of the oxygen molecules is slow. Therefore, the counter-diffusion of cations is probably the only remaining reaming reaction mechanism if ideal contact is maintained at the phase boundaries so that no gas phase can enter [49].

Zinc Aluminate Spinel

For more than 80 years, the reaction of ZnO and Al_2O_3 has been investigated; it yields $ZnAl_2O_4$, Figure 41. Further, $ZnAl_2O_4$ is stable until its melting point at 1950°C,

where a considerable vaporization of ZnO occurs, and its eutectic point at 1720°C and 83 mol% ZnO, Figure 42.

Even after this long time of investigation of the reaction of ZnO and Al_2O_3, there is still uncertainty about the reaction mechanism. On one side there is evidence that the reaction to $ZnAl_2O_4$ is controlled by the diffusion of zinc ions through the product layer. However, this seems to only occur as long as the reaction is not occurring between powders, because in the latter case the reaction mechanism is changed from solid-state to a gas-solid reaction [36].

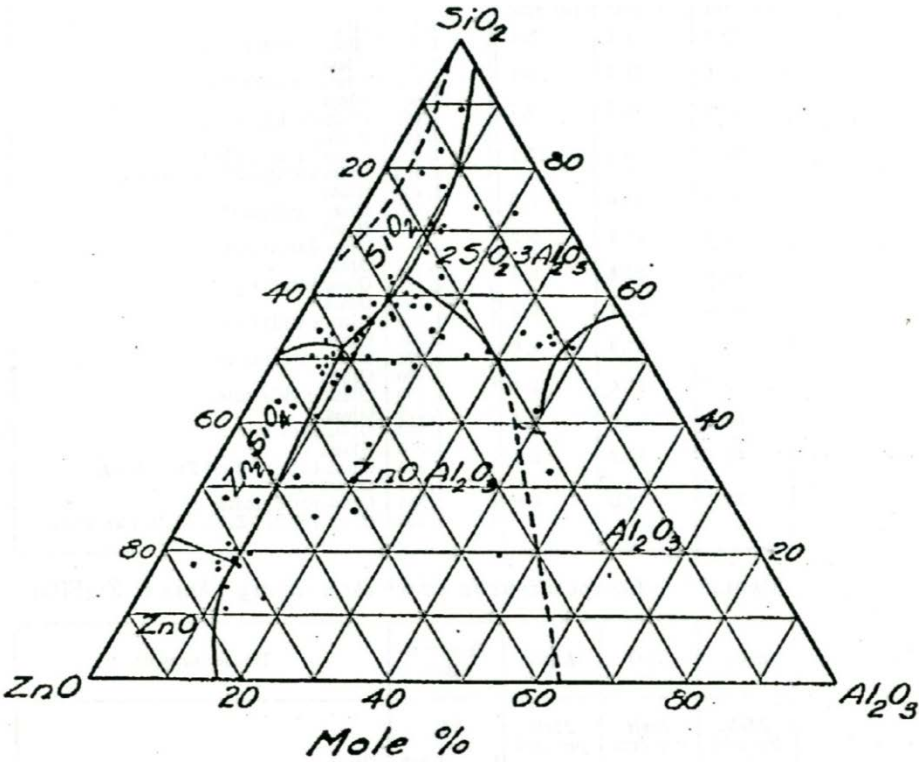

Figure 41 Phase diagram for the system ZnO-Al_2O_3-SiO_2 [51]

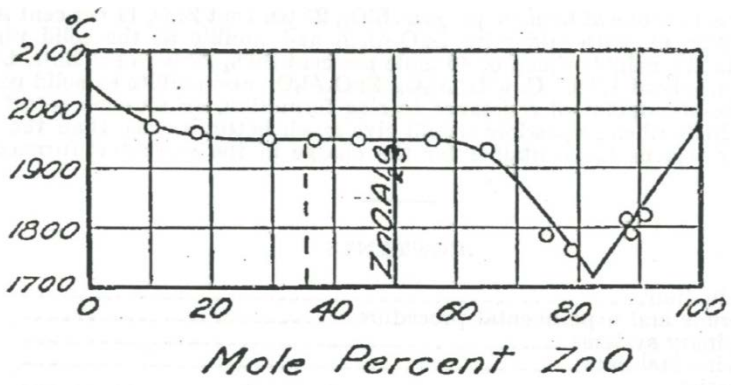

Figure 42 Melting curve for the system ZnO-Al_20_3 [51]

Bengtson and Jagitsch [52] investigated the kinetics of the zinc aluminate spinel formation. They used the method of placing platinum markers at the interface, Figure 43. The marker indicated clearly the degree of diffusion that occurred from each side, Figure 43 B and C.

After the reaction, Bengtson and Jagitsch [52] found the layer sequence $Al_2O_3/ZnAl_2O_4/Pt/ZnO$, which means that ZnO was transported through the spinel layer. However, they could not determine if the diffusion was in form of Zn- and O-ions or ZnO-molecules.

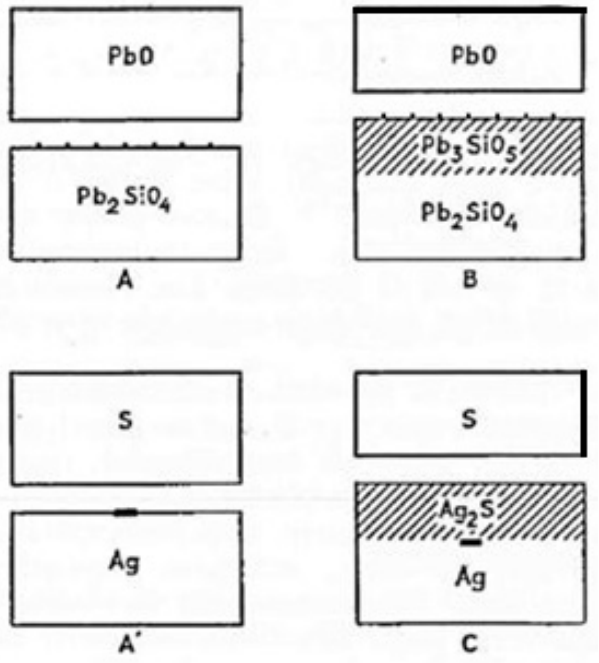

Figure 43 Method of the marked interface [52]

Lindner [53] confirmed the findings from Bengtson and Jagitsch by using radioactive Zn to trace the concentration gradient of Zn in $ZnAl_2O_4$. After the reaction, successive layers were ground off to determine the distribution of the radioactive Zn. The concentration of Zn in the spinel was constant and equal to the stoichiometric composition of the spinel. Further, no gradient was found in the concentration in the ZnO-pellet, Figure 44. Therefore, the spinel was formed at the Al_2O_3-pellet, again indicating that it was the Zn, O or ZnO that had diffused.

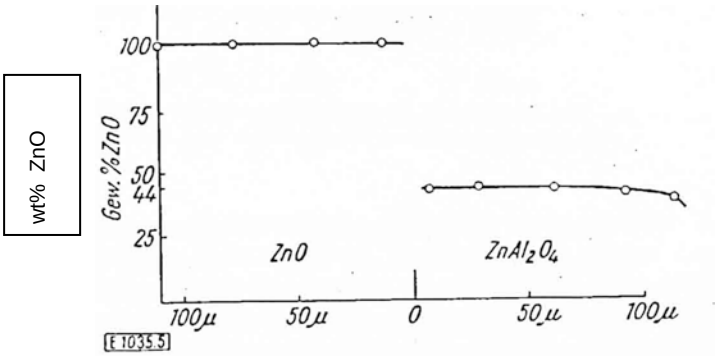

Figure 44 Concentration gradient of radioactive Zn on both sides of the initial phase boundary between ZnO and Al_2O_3 [53]

Branson [54] used Pt-markers to highlight the interface between ZnO- $ZnAl_2O_4$ and $ZnAl_2O_4$- Al_2O_3 and to establish which of the elements was diffusing through the product layer. For this the samples were heated in a range from 600° to 1200°C for 3 to 148 h. During these heat treatments the markers between ZnO and the spinel remained fixed and only the marker between spinel and Al_2O_3 moved towards ZnO. This also led Branson to the conclusion that the reaction mechanism for $ZnAl_2O_4$ was a one-way diffusion of ZnO because, with in a counterdiffusion, both markers would have moved into the $ZnAl_2O_4$. As in the experiments of Bengtson and Jagitsch [52], whose results were confirmed with these findings, it could not be determined if the movement of Zn- and O-ions or ZnO-molecules were responsible for the diffusion of the ZnO.

Further confirmation for the diffusion of ZnO into Al_2O_3 was achieved by using X-ray diffraction. For this range of the reaction time was widened so that range for 2 h to 500 h was investigated. The focus of the X-ray diffraction investigation was a temperature range from 600° to 800°C. In the temperature range 600° to 700°C (2 to 350 h reaction time) the creation of a solid-state solution was observed, because the X-ray diffraction peaks for alumina were shifted. Therefore Branson [54] concluded that ZnO diffused into the interstitial positions of the alumina and created a solid solution. In the temperature region of 700° to 800°C Branson found low-intensity peaks, which could not be identified. As the reaction was continued for 200 to 500 h in this temperature range additional undefined peaks appeared. As the formation of the solid solution was detected earlier and that the new peak lay in the general area

of an ordered spinel structure, Branson concluded that a disorder spinel structure was created. After 3 h at 800°C an ordered spinel structure was achieved.

In addition to the marker experiments and X-ray diffraction investigation, Branson [54] undertook a comparative study, where ZnO and Al_2O_3 were reacted in air and in a partial vacuum and nitrogen atmosphere. The degree of the spinel formation was drastically reduced when the oxygen was absent. Therefore, he concluded that Zn-ions were diffusing through the product layer and combining with atmospheric oxygen at the spinel-alumina interface to form spinel, Figure 45. If oxygen diffused together with Zn^{2+} through the product layer, then an absence of the atmospheric oxygen would have had no impact on the spinel reaction.

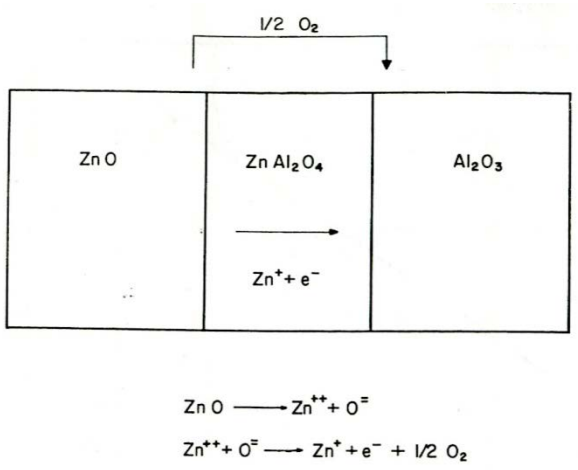

Figure 45 Schematic diagram of the solid-state reaction of $ZnAl_2O_4$ [54]

The evidence delivered by Bengtson and Jagitsch [52], Lindner [53] and Benson [54] demonstrate that the reaction to $ZnAl_2O_4$ is a one-way diffusion of Zn-ion through the spinel layer, and recombining with atmospheric oxygen to form $ZnAl_2O_4$. This reaction, Figure 45, is identical with a previous described reaction mechanism of the transport of O_2 molecules through gaseous phase and electrons through the product layer to ensure electroneutrality, see Figure 40 a.

As described earlier, the reaction of ceramic ZnO and Al_2O_3 is via a solid-state mechanism that is controlled by the diffusion of zinc ions through the product layer. However, when powder compacts are used, the reaction mechanism changes from solid-state to a gas-solid reaction. Arean et al. [55] might deliver a potential reason,

why this change occurs. They studied the temperature dependence of the kinetics and mechanism between ZnO and alumina because they found conflicting reports about the reaction mechanism for the formation of $ZnAl_2O_4$. As has been seen, they had reports that Zn-ions and electrons were transported through the spinel layer and formed spinel when combined with atmospheric oxygen at the interface of the spinel and alumina. The experiments for these reports were all done in the temperature range of 1048-1473 K. However, a conflicting report described experiments in the temperature range form 1503-1773 K, the results favoured the counterdiffusion of Zn and Al-ions through the spinel without oxygen transport. Further different activation energies (E_a) were reported, for the experiments up till 1473 K E_a = 230 kJ/mol whilst above 1503 K E_a = 361 kJ/mol. Aren et al. believed that ZnO became volatile at temperatures above 1350 K and that this could be an explanation why there would be a change in the reactions mechanisms and kinetics. Therefore they studied the formation of $ZnAl_2O_4$ in isothermal runs at different temperatures at 1173, 1273, 1373, 1573 and 1673 K with the powders as reactants. Their results showed the typical parabolic reaction for a solid-state reaction, Figure 46. However the figure also shows that the rate of the reaction is significantly increased for samples, which were heated above the 1350 K. This increase could be due to the change of the reaction mechanism.

Therefore they plotted the results as an Arrhenius plot, which demonstrated clearly there was a change in the mechanism, because the slope of the straight lines changed, Figure 47. This allowed them also to derive the activation energies, E_a = 230 kJ/mol (T < 1400 K) and E_a = 430kJ/mol (T > 1400 K) [55].

The two different values for the activation energies lead them to the conclusion that as long as the temperature was below 1400 K a true diffusion-controlled solid-state reaction was taking place. When the temperature rose above 1400 K than the volatilization of ZnO leads to a gas-solid reaction, which had an increased rate of reaction. However this type of reaction also required a higher activation energy and the measured activation energy was close to the vaporization energy (465 kJ/mol) of ZnO [55].

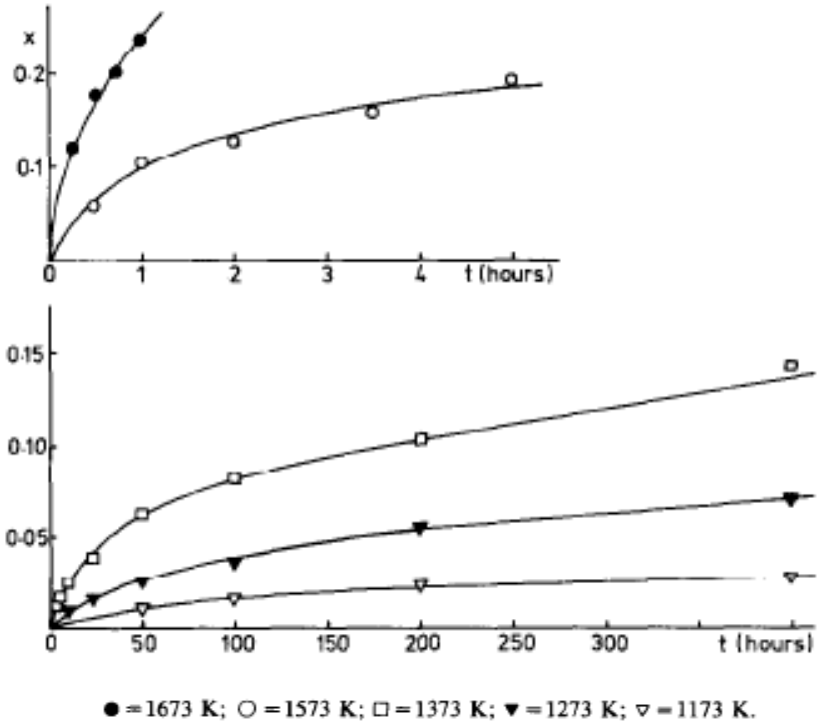

Figure 46 Fraction of reaction completed, x, as a function of time at various temperatures [55]

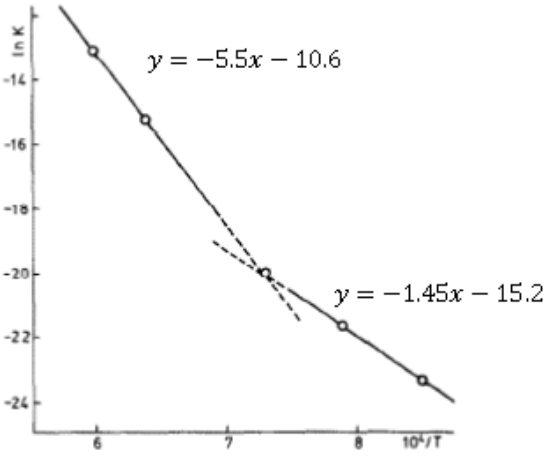

Figure 47 Arrhenius plot for the calculation of the activation energy [55]

Therefore it can be concluded that the reaction of ZnO with Al_2O_3 to $ZnAl_2O_4$ is a solid-state reaction as long as the reaction temperature remains below 1400 K. The mechanism for this reaction is that Zn-ions and electron diffuse through the spinel layer, while O_2-molecules are transported through the surrounding atmosphere to the spinel-$ZnAl_2O_4$ interface where they combine with the Zn-ion and the alumina to form the spinel. According to Arean et al. [55] the reaction of ZnO and Al_2O_3 in powder

form is also a solid-state reaction below 1400 K. The uncertainty in the earlier reports of the powder reaction could be caused by the exothermal characteristic of solid-state reactions. If the temperature in the powder bed reaction started to increase than the reaction rate was increase. This would lead to further heat production and to a spiral of increased reaction rate and heat production. During this the temperature could increase above 1400 K, which would cause the change in the reaction mechanism.

Magnesium Aluminate Spinel

For a long time the reaction of MgO and Al_2O_3 has been investigated. However compared to the reaction of ZnO and Al_2O_3, this reaction system leads to multiple reaction products, see Figure 48, and the spinel can be only created within a limited fraction range of the material system and the higher temperature. According to Bailey and Russel [56] the spinel formation starts in a higher temperature range between 925°C and 950°C. The created spinel has maximum melting point of 2135°C [57].

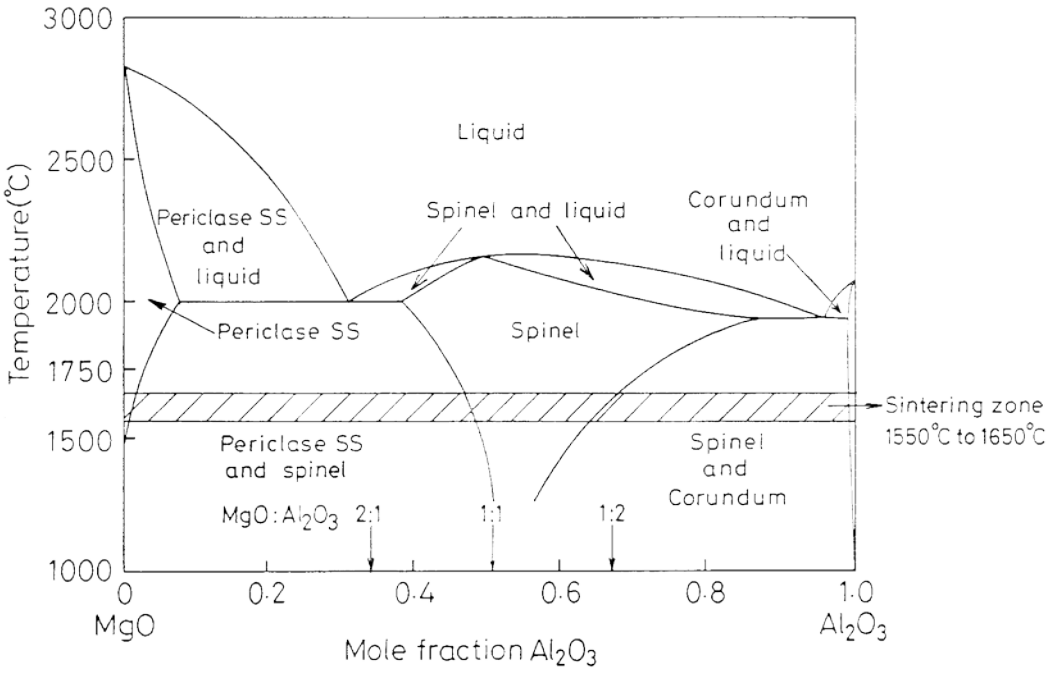

Figure 48 Phase diagram of the system MgO-Al_2O_3 and the present study on the system [58]

The high melting point of this spinel and its high strength at elevated temperature, high chemical inertness, low temperature thermal expansion and high thermal shock resistance make it an excellent refractory material for the industry. However the

production of high density and pure spinel bodies is complicated, because the spinel formation is accompanied with a volume expansion of around 8%. Therefore for industrial use, spinel bodies are produced in a two stage process. At first the spinel is created. After this the spinel is ground into powder, the ceramic body formed and sintered [57, 59].

The reaction mechanism for the spinel reaction is a counter diffusion of the Al- and Mg-ions. This was confirmed through marker experiments by Carter [60] similar to the experiments of Bengtson and Jagitsch [52]. Molybdenum wires were used as a marker material and placed between the reactants. After the reaction the samples were cross sectioned and the markers were found imbedded in the reaction product, $MgAl_2O_4$, layer. Therefore the reaction took place on both interfaces, Al_2O_3-$MgAl_2O_4$ and MgO-$MgAl_2O_4$, and it was concluded that the reaction had to be a counterdiffusion of Al- and Mg-ions.

2.4 Microwave Fundamentals and Microwave Heating

2.4.1 Characteristics of Microwaves

Microwaves have a broad spectrum of frequencies, from 0.3 to 300 GHz, Figure 49. Microwaves have similar characteristics to light waves; they are reflected by metallic objects, absorbed by some dielectric materials and transmitted without significant absorption through other dielectric materials. Microwaves travel at the speed of light in free space, Figure 50 [10].

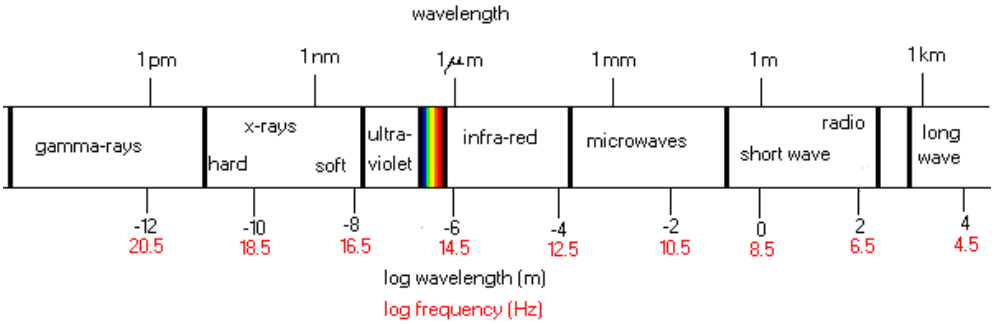

Figure 49 The electromagnetic spectrum [29]

The free space wavelength, $\lambda_{0,}$ is related to the frequency by the equation:

$$\lambda_0 = c/f \qquad (2.50)$$

Where λ_0 is the free space wavelength, *c* is the speed of light and *f* is frequency.

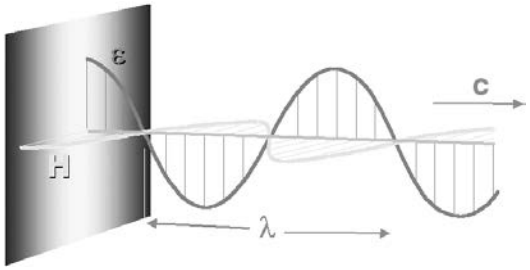

Figure 50 The propagation of the plane wave **[**29]

2.4.2 Microwave Heating

In 1945, P. Spencer [61-63] noticed that a chocolate bar in his pocket melted as he tested a magnetron. He was intrigued by this discovery and started a series of experiments, which demonstrated that a magnetron could be used heat different materials. This lead to the development of the first commercial microwave oven and opened the door for the path of microwave heating.

Microwave heating is fundamentally different to conventional heating. The latter relies on an external heat source, which creates the heat that is transported by thermal convection and radiation to the material surface. There it heats first the surface and when the temperature of the latter increases than the heat is transported towards the material core. In comparison, microwaves can penetrate a material and heat it from inside, which can lead to a volumetric heating. This direct heating of a material removes the need of heat transport from an external heat source to the material and from the surface to the core [64].

Different materials react differently when exposed to microwave radiation, Figure 51. Materials can be transparent or opaque towards microwaves or absorb them.

However, when heated above a critical temperature (T_{crit}) some materials, which were transparent at room temperature, increase their ability to absorb microwaves [10].

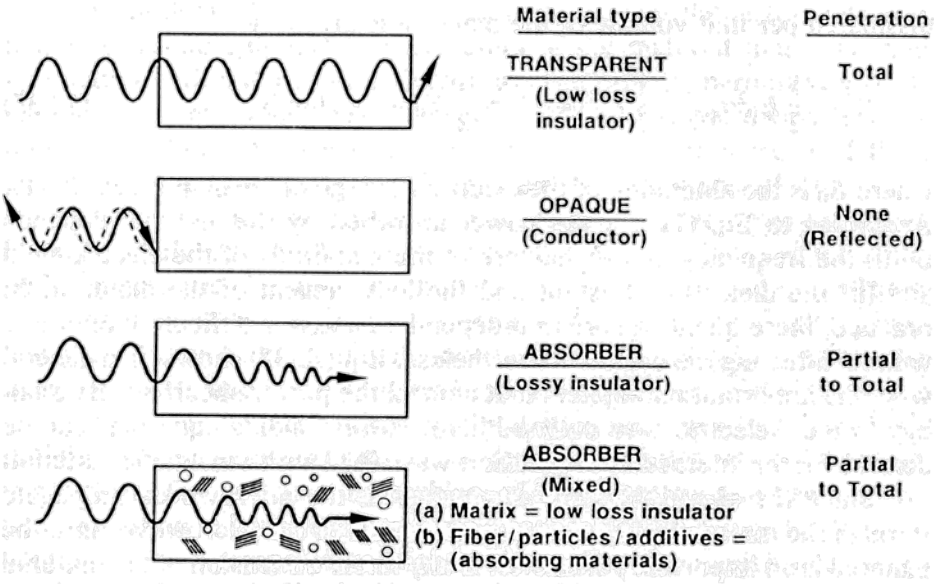

Figure 51 Schematic diagram illustrating the interaction of microwaves with materials power absorption caused by dielectric losses [10]

A materials permittivity is ε^* (Fm^{-1}) and is an indicator of the degree of the interaction/absorption of microwaves by the materials. It is composed of a real part (ε', dielectric permittivity) and an imaginary part (ε", dielectric loss factor)

$$\varepsilon^* = \varepsilon' - j\varepsilon'' = \varepsilon_0(\varepsilon'_r - j\varepsilon''_{eff}) \tag{2.51}$$

Where $j = (-1)^{1/2}$, ε_0 is permittivity of the free space ($\varepsilon_0 = 8.86 \times 10^{-12}\ \mathrm{F/m}$), ε'_r is relative dielectric constant and ε''_{eff} is effective relative dielectric loss factor [10].

When microwaves penetrate and propagate through a dielectric material, they create an internal electric field in the affected volume. This field causes the rotation of complex charges as dipoles and translational motion of free and bound charges (electrons or ions). This motion is forced onto these charges. Therefore, the inertial, elastic, and frictional forces, which are frequency dependent, create a resistance to

the induced motion. Hence the resistance reduces the electric field by causing losses, which create heat, leading to volumetric heating [10].

ε''_{eff} combines all of the loss mechanisms into a single term. However, to describe the losses, the term loss tangent (tan δ) is used, where

$$\tan\delta = \frac{\varepsilon''_{eff}}{\varepsilon'_r} = \frac{\sigma}{2\pi f\varepsilon_0\varepsilon'_r} \tag{2.52}$$

Where σ is total effective conductivity (S/m) caused by conduction and displacement currents and f is frequency (GHz).

Since microwaves are absorbed by materials and transformed into heat it is helpful to know how much power is absorbed per unit volume P (W/m³):

$$P = \sigma|E|^2 = 2\pi f\varepsilon_0\varepsilon'_r\tan\delta|E|^2 \tag{2.53}$$

Where E is magnitude of the internal field (V/m).

Equation 2.3 is the basis of microwave heating and reveals the difficulties as the absorbed power per unit volume varies linearly with f, ε'_r, tan δ and with the square E. It is also assumed that P is uniform throughout the volume and thermal equilibrium is achieved, which only occurs in rare cases. Further f, ε'_r, tan δ and E are independent of each other and E is dependent on the size, geometry and location of the material inside the microwave cavity and the design and volume of the cavity [10].

As described earlier microwaves penetrate materials and the penetration depth, D, is defined as the distance at which the initial absorbed microwave energy is reduced by a half. It is an important parameter

$$D = \frac{3\lambda_0}{8.686\pi\tan\delta(\varepsilon'_r/\varepsilon_0)^{1/2}} \tag{2.54}$$

Where λ_0 is incident or free-space wavelength.

This equation means that a greater wavelength (lower frequency) leads to a greater penetration depth. However, latter does not necessarily result in increased microwave heating, because, depending on the material properties, the internal E field created could be low [10].

Polarisation Mechanisms of Materials

It has been known for long time that materials can be heated with the use of high frequency electromagnetic waves. The heating effect usually results from the interaction of the electric field component of the wave with charged particles in the materials. The major effects responsible for this heating are conduction and polarisation [65].

Net polarisation in material can be created by the interaction of microwaves with dielectric materials. The mechanisms under pining this polarisation include like electronic, ionic, molecular (dipolar) and interfacial (space charge) polarisation. Therefore, the net polarisation, P, of the dielectric material is the sum of the contributions from each mechanism, given by:

$$P = P_e + P_i + P_m + P_s \tag{2.55}$$

Where P_e is electronic polarisation, P_i is ionic polarisation, P_m is molecular (dipole) polarisation and P_s is interfacial (space charge) polarisation [66].

Electronic Polarisation

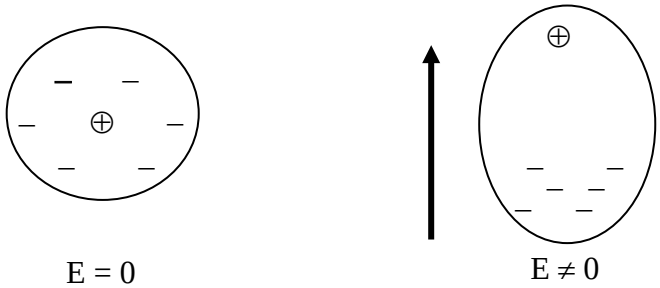

Figure 52 Electronic polarisation [66]

The reason for this mechanism is that the electron cloud can be displaced relative to its nucleus. The operational area of this effect is over most frequencies and drops off only at very high frequencies (10^{15} Hz). This mechanism is shown if the electrons are shifted from the equilibrium to the positive nuclei in the direction of the applied field (E), Figure 52 [66, 67].

Ionic Polarisation

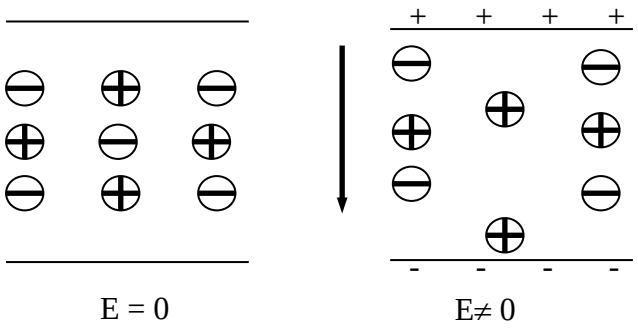

Figure 53 Ionic polarisation [66]

The displacement of positive and negative ions toward the negative and positive electrodes in an applied electrical field (E) is defined as the ionic polarisation. The result of this effect is the separation of the cations and anions relative to their equilibrium positions, Figure 53. Ionic resonance happens in the infrared frequency range (10^{12} to 10^{13} Hz) [66, 67].

Molecular (Dipolar) Polarisation

Molecules have a random orientation in a material in a normal state so that there is no net charge present. Molecular or dipolar polarisation needs an external field (E) to orientate the permanent dipoles parallel to the field, Figure 54. In some materials, this polarisation can be retained after the removal from the field until they obtain energy for the thermal activation of molecular rotation. These electrostrictive or piezoelectric materials are electrets and are the electric field analogs of magnets [66, 67].

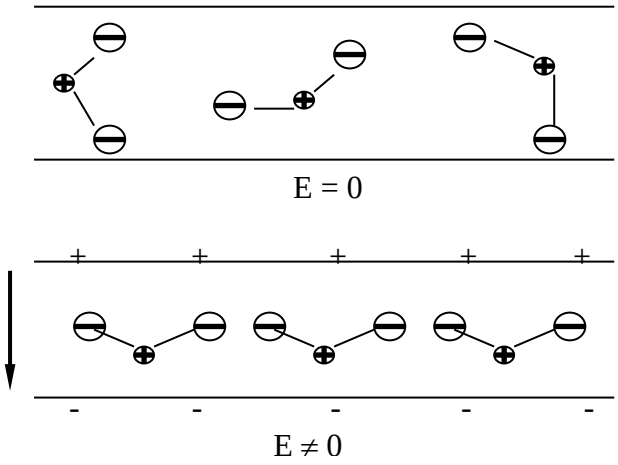

Figure 54 Molecular (dipolar) polarisation [66]

Dipolar polarisation is the reason for the majority of microwave heating effects observed in solvent systems. The difference of the electro negativities of individual atoms results in the existence of a permanent electric dipole on the molecule, such as in water. The sensitivity of dipoles to an external electrical field will lead to attempts to align with the fields by rotation. The energy required for this rotation is obtained from the field. The realignment is rapid for a free molecule, but in liquids, instantaneous alignment is disrupted by the presence of other molecules. A limit is therefore placed on the ability of the dipole to react to a field, which affects the behaviour of the molecule with respect to frequency, see section 2.4.3.

Interfacial (Space charge) Polarisation

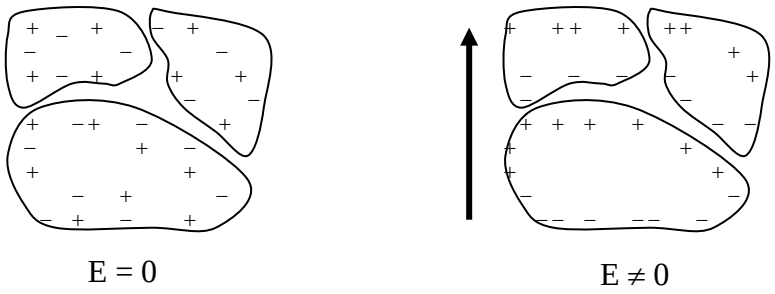

Figure 55 Interfacial (space charge) polarisation [66]

In interfacial or space charge polarisation, mobile charge carriers in a heterogeneous material are accelerated by an applied field until they are stopped by, and retained at, physical barriers. This build-up of charge specifies the polarisation of the material. Grain/phase boundaries and free surfaces are common barriers, Figure 55 [66, 67].

2.4.3 Frequency Dependence of the Different Contributions

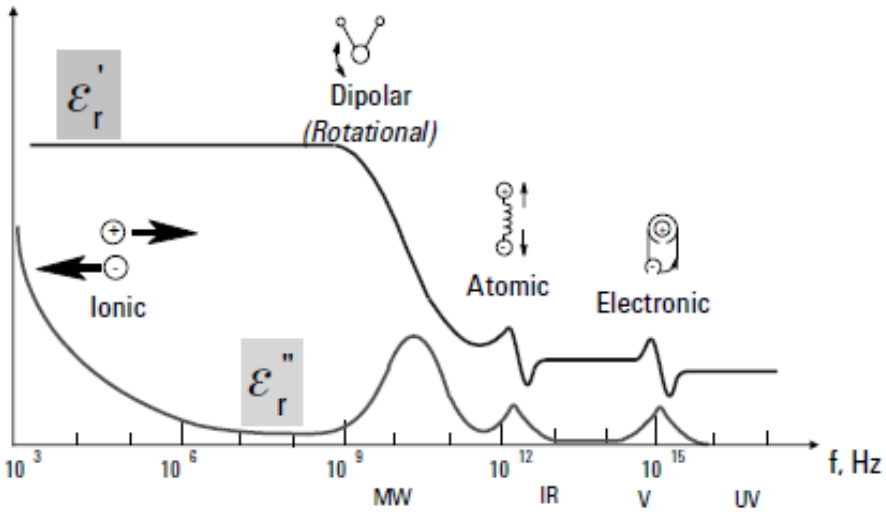

Figure 56 Frequency response of permittivity and loss factor for a typical dielectric material showing various phenomena (e' and e" are dependent on both frequency and temperature) [44]

For any material, both the real and complex permittivity will change with frequency due to the effect of the changing electric field on the movement of the dipoles. The frequency response of permittivity and loss factor is shown for a typical dielectric material in Figure 56. The figure reveals the different polarisation mechanisms that are present in the different regions of the electromagnetic spectrum [44].

Under low frequency irradiation, the dipole can react by aligning itself in phase with the electric field. Whilst the molecule creates some energy by this behaviour, and some is lost in collisions, the overall heating effect is small. At very high frequencies of the electric field, on the other hand, the dipoles do not have enough time to react to the field, and there is no rotation. Without a motion of the molecules there is no energy transfer and as a result no heating [65].

Between these two extremes, at frequencies that are approximately those of the response times of the dipoles, is the microwave region. The microwave frequency is low enough that the dipoles have time to react to the alternating field, and therefore to rotate, but high enough that the rotation cannot precisely follow the field. As the dipole reorients to align itself with the field, the field is already changing, and a phase difference exists between the orientation of the field and that of the dipole. The reason for dielectric heating is the loss of energy from the dipole in random collisions, which are causes through this phase difference [65].

The molecular dipoles in solids are no longer free to rotate as they are in liquids, but are restricted to a number of equilibrium positions, separated by potential barriers. Theoretical treatments have been derived for the behaviour that is similar to those for liquids. The simplest model for this behaviour expects that there are two potential wells separated by a potential barrier of energy W, which represents the two possible orientations of the dipole. If W tends to be extremely large, then most dipolar solids show extremely small dielectric losses. For example, water-free ice does not heat significantly under microwave irradiation [65].

2.4.4 Loss Mechanisms

Microwaves can couple by diverse mechanisms to materials, providing a whole host of methods to transfer the microwave energy in the system. The main loss mechanisms are conduction losses, dielectric losses and magnetic losses. The different mechanisms have different correlations on certain properties such as sample type, microstructure, frequency and temperature. In metallic and high conductivity materials such as semiconductors conduction losses dominate [65].

Conduction losses

Conduction losses play an important role in the microwave heating of metals, conductive materials and semiconductors. These materials can be heated through direct conduction effects, which result from an ohmic type of loss mechanism when the current flows in the material under the action of microwaves [65].

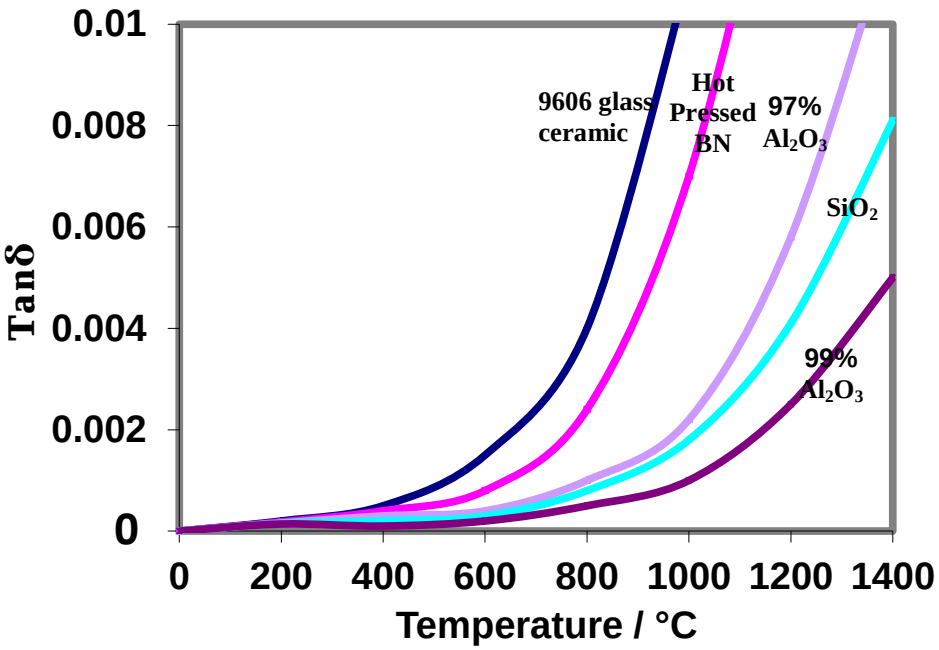

Figure 57 Temperature dependence of tan δ for a range of ceramics [10]

A large number of systems show the significance of conduction losses. The addition of dissolved salts to water markedly affects the dielectric properties as conduction increases and may become important enough to swamp the dielectric losses. On the other hand, the dielectric losses of the majority of solids arise predominantly from these conduction terms and may be strongly affected by temperature, for example, of alumina, because the donation of electrons from the O (2p) valence band into the conduction band leads to increases in the permittivity. Figure 57 illustrates this effect along with a number of other ceramic materials that demonstrate similar behaviour [10]. The dielectric loss factor and heating becomes more effective when the temperature increases [45] and dT/dt increases rapidly, as illustrated for strontium titanate and alumina in Figure 58. This can result in the temperature rising to unwanted, high levels without careful monitoring of these materials, when heated by microwave irradiation.

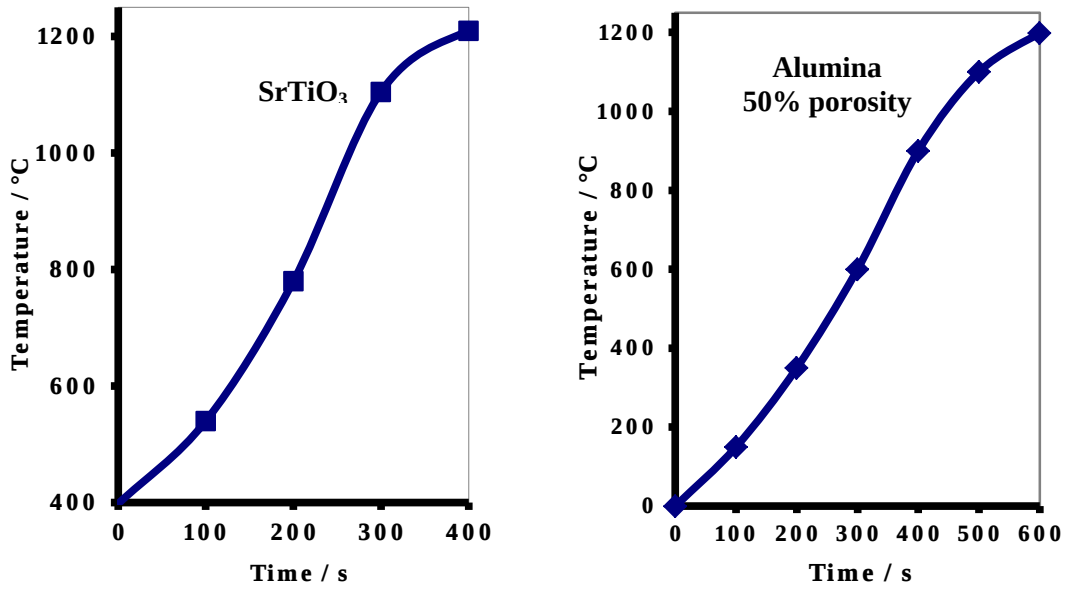

Figure 58 Thermal runaway in materials under microwave irradiation [45]

Dielectric losses

If microwaves penetrate and propagate through a dielectric material the internal field generated within the irradiated volume results in translational motion of free or bound charges such as electrons or ions and rotates charge complexes such as dipoles. The induced motions causing losses are reduced by resistance of the inertial, elastic and frictional forces. In dielectric materials, the absorption (degree of interaction) of microwaves is related to the material's complex permittivity [65].

The effective loss tangent δ is the ratio of the effective loss factor to that of the relative dielectric permittivity. Tan δ is a useful indication to show how a material interacts with the microwaves in a microwave field. Ceramics having a loss tangent lower than 0.01 can be considered as transparent to microwaves. Highly conductive materials, such as metals, will produce almost total reflection to microwaves because they are opaque/nontransparent to microwaves. Most ceramic materials have behaviour between these two extremes, thus they can absorb microwaves to varying degrees as indicated in Figure 51 [10].

Magnetic losses

Magnetic polarisation can also contribute to the heating effect observed in materials where magnetic properties exist, and a similar expression for the complex permeability of such materials can be formulated. An example of its importance is in the microwave heating of Fe_3O_4 [65].

2.5 Microwave Sintering

2.5.1 Microwave Sintering

Microwave heating has been used to sinter ceramics since the late 1960s and early 1970s and it is very different from that achieved using conventional heating furnaces. Using microwaves, the heat is generated internally by the interaction of the electromagnetic energy with the materials while in conventional furnaces materials are heated by thermal radiation [10, 68].

Microwave heating, as explained in section 2.3.2, uses the capacity of materials to absorb the microwave energy. This limits the use of microwaves, because if the material is transparent or opaque towards microwaves than microwave sintering will be difficult or even impossible to achieve [10]. However, microwave sintering can be used for a wide range of materials such as oxides, non-oxides and composites.

The most investigated materials are oxides and especially ZnO, YSZ and alumina. Liu et al. [69] sintered different mixtures of nano and coarse sized Al_2O_3 in a microwave field. They achieved a theoretical density of up to 98.5% for the microwave sintering of the 20 wt% nanometer Al_2O_3 at 1500°C for 30 min. The usage of two stage hybrid sintering allowed Binner et al. [70] to sinter 3YSZ to >99% of theoretical density whilst keeping the average grain size below 100 nm. Further investigation of oxides, especially on ZnO and YZS, were done at Loughborough University by Wang [29], Lorenz [30], Paul [71] and Hossbach [31].

Examples of these non-oxide investigations are demonstrated by the microwave assisted synthesis of Cu_2ZnSnS_4 by Kumar et al. [72]. Jones et al. [73] investigated the grain growth for microwave sintered of Si_3N_4. Qi and Yang [74] used microwave heating at prepare Mo/HZSM-5 and Cu-Mo/HZSM catalysts for the non-oxidative aromatization of methane.

The sintering of ceramic composites had been achieved by Menezes and Kiminami [75] by sintering alumina-zirconia nanocomposites within 35 min to 99% of the theoretical density. Further the microstructure of their samples was uniform and no significant grain grow was observed. Xu et al. [76] used microwave reaction sintering to produce a 20 vol% SiC reinforced $NoSi_2$ composite with a theoretical density of 91.5%. A high density $La_2Mo_2O_9$/Al2O_3 nanocomposite was successfully microwave sintered by Zhang et al. [77].

Since the mid-1990s, work has increasingly focused on the use of hybrid furnaces in which both microwave and conventional heat can be supplied simultaneously [33]. Compared to susceptors[1], this method has many advantages:

a) accurate control of input power;
b) microwave deposition in the sample body;
c) no limit on sample size.

This makes it easier to control the time-temperature profiles more precisely and the temperature profile within the ceramic. For example, it is possible to achieve a uniform temperature distribution within the sintered products by adjusting the fraction of conventional and microwave power. However, the main advantage of this approach is that it makes it easy to observe the effect of microwave power on sintering. This is impossible in systems with susceptors because not only the sintered ceramics absorb the microwave power but also the susceptors, making it difficult to estimate the fraction of microwave energy entering the sintering ceramics in a system with susceptors [33].

[1] A material with a higher dielectric loss than the material to be sintered. By absorbing more microwave energy, the susceptor is able to heat preferentially and then aid the heating of the lower loss material to be sintered. However, it is a fundamentally uncontrolled process.

2.5.2 Advantages of Microwave Sintering

Inverse temperature profile

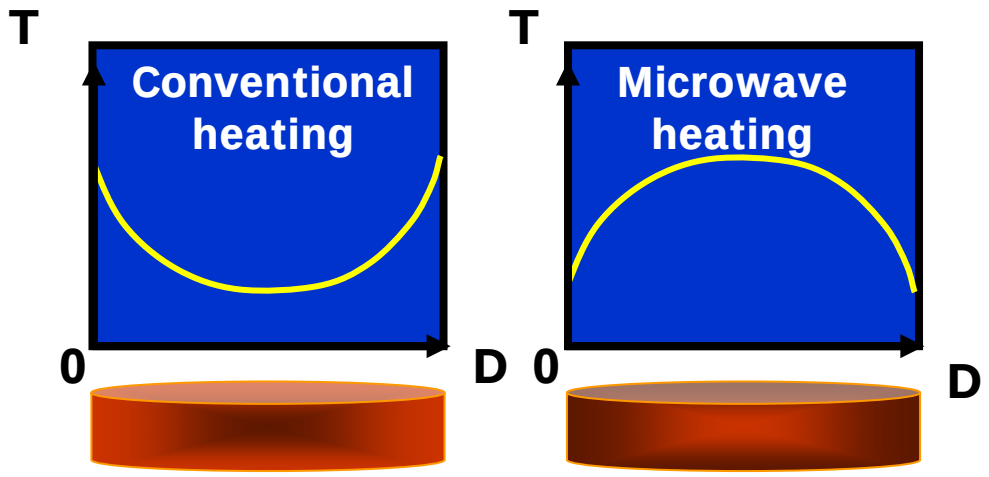

Figure 59 Schematic diagram of temperature profile during conventional and microwave heating at the begin of the heating [29]

The inverse temperature profile, Figure 59, is the fundamental difference with conventional sintering. This temperature profile is generated within the ceramic body and does not originate from an external heating source. Therefore, the internal and hence volumetric heating leads to a reversal of the thermal gradient compared to conventional heating. Hence, it yields a hotter interior than the surface while conventional heating relies on thermal conduction and radiation to transport heat from the surface of the ceramic to the centre of the body. Many factors such as power level, electric field distribution and the properties of sintered materials including heat losses, thermal and electrical conductivity, *etc.* are responsible for the magnitude of the temperature profile of microwave heating [10]. The inverse temperature profile can keep pores open from the centre of the sintered ceramic to the outside and it gives a great advantage of the microwave sintering in comparison with the conventional process. If the pores are kept open for longer in the final sintering, less gas would be trapped inside the pores. Therefore remaining porosity could be at least reduced to a minimum, because the trapped gas would have a smaller resistance towards the pore shrinkage. The acceleration of densification and the achievement of a higher final density in microwave sintering are both a result of this effect. The inverse temperature profile is good for reaction sintering that involves

the reaction of a porous solid matrix with a gas phase, e.g. YBCO high-temperature superconductors [78, 79].

Rapid heating

Volumetric heating can also lead to rapid heating providing ceramic sintering with many advantages. The temperature dependence of tan δ, as discussed in section 2.3.2, is another reason for the potential of rapid heating, Figure 60. The tan δ increases slowly, when the temperature of the ceramic increases until a critical temperature, which is different for different materials, is reached. When this critical temperature is passed then tan δ increases very quickly and with it the temperature [10].

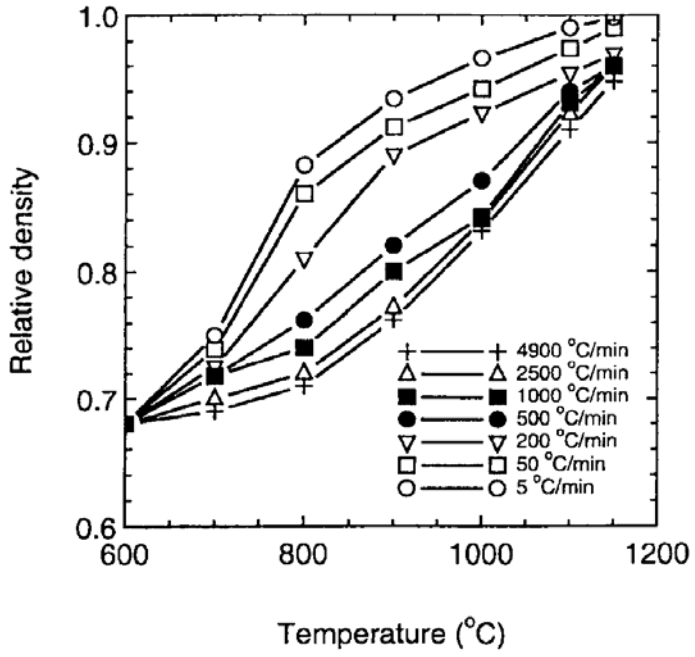

Figure 60 Relative density versus temperature for ZnO (green density = 68% TD) sintered at heating rates between 5 and 4900 K min^{-1}. All samples heated to the corresponding temperature without holding [80]

The production of ceramics with fine microstructures and with an improvement of the mechanical properties is one of the advantages [81-85]. The reason for this possibility is that the rapid heating can restrict grain growth during sintering, as demonstrated by Wang, Figure 61 [29]. An important application is to produce nano-structured ceramic and composite materials. For example, Y. Bykov, et al, obtained nano-structured titanium oxide by microwave sintering and the results showed the

micro hardness of microwave-sintered samples was higher than that of the conventionally sintered samples [86].

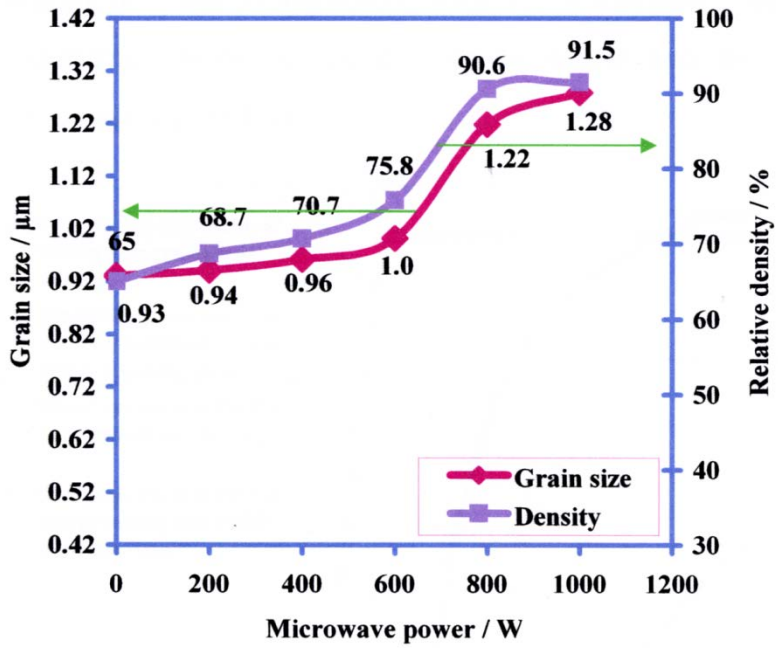

Figure 61 Grain size and density curves of (submicron) ZnO samples sintered at 680°C [29]. Note, despite the different microwave power levels, all of the samples saw exactly the same T-t profile.

Lower energy consumption and process time

Volumetric heating is the fundamental difference between microwave and conventional heating techniques. The microwaves are directly deposited in the materials so they are heated volumetrically producing greater energy efficiency, leading to less time required to sinter the materials and to lower sintering temperature, Figure 62. As a result this and the possibility of rapid heating, the energy consumption is significantly reduced [87-89].

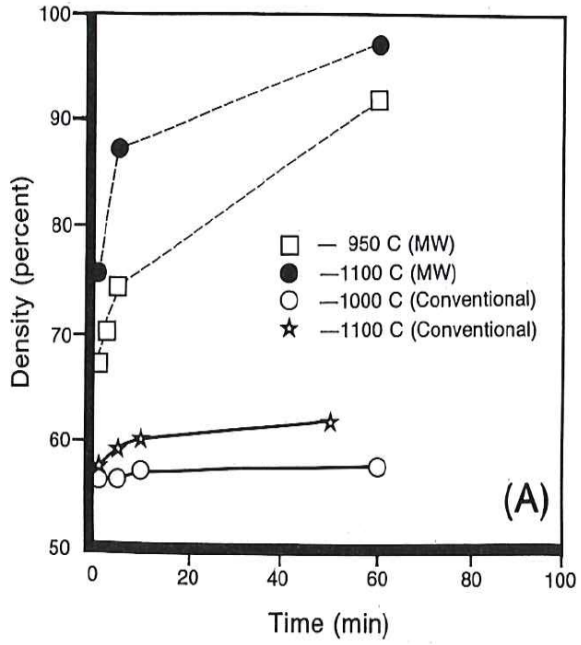

Figure 62 Enhanced densification rates for microwave sintering of alumina [87]

Selective heating

With microwave heating, there is the chance to concentrate the energy deposition in the desired region or phase in a mixture. This effect is called selective heating and is possible because materials with different dielectric losses have different microwave absorption ability. In a composite material, energy deposition concentrates in the components with high dielectric losses [10]. The efficient control over the microstructure and properties is one important application of selective heating. For example, Li et al., [90] used microwave processing to heat treat a TiC/Si_3N_4 ceramic composite and found that the strength degradation from thermal shock was substantially recovered. The mechanism of strength recovery postulated was that microwave radiation, which caused selective heating of TiC particles, enhanced the reaction of grain boundaries and resulted in the sintering of micro cracks around TiC particles.

2.5.3 Challenges that Microwave Sintering Faces

The control of microwave sintering is more complicated and difficult than that of conventional sintering. “Thermal runaway” is an uncontrolled rapid increase in the temperature of the sample. As described earlier, tan δ increases rapidly if the critical temperature is exceeded. This increase leads to higher temperature and an even faster increase in the tan δ. In the end it can lead to the melting of the sample or to the formation of local hot spots, where some regions have a much higher temperature than the rest of the sample. Reasons for this effect can include nonuniformity in the microwave field and/or the properties of the sample. The effect of the former leads to discrepancies in the energy absorption of the sample and different regions of the sample are heated at different rates. Therefore, the formation of local hot spots occurs causing differential densification and leading to cracking of the sample. A result of having the highest temperature in the centre and poor thermal transport is that the inverse temperature field can cause the same problem, producing a higher increase of the temperature than desired. In the extreme case, it can result in the sample centre melting whilst the outside of the sample is still a solid, Figure 63 [10].

Figure 63 An extreme example of thermal runaway showing the melting of an alumina ceramic from the inside out (courtesy EA Technology, Capenhurst, UK)

Another significant challenge for microwave sintering is accurate temperature measurement in the microwave field. The use of thermocouples, the most common method of measuring temperature during conventional sintering, can result in

distortion of the microwave field and so result in significant changes in the heating behaviour of the material [79]. In addition, any technique that measures the surface temperature of the sample, e.g. thermocouple or pyrometer, can result in an under-estimation of the central temperature of the sample because of the inverse temperature profile that forms during the microwave heating as described earlier. All this makes the temperature measurement more complicated than for conventional heating.

Wang [29] investigated in his work the temperature measurement problem and found that optical fibre thermometers are the best temperature measurement method, because they allow more accurate measurement than other techniques as thermocouples and pyrometers and they minimise the distortion of the microwave field.

However, despite all the investigations, it is still not known what exactly happens during microwave sintering or why the densification in enhanced in the initial and intermediate stage of sintering and seemingly reduced in the final stage. Possible theories to explain this are discussed in the next section.

2.5.4 Microwave Effect

The “microwave effect” is generally understood to mean the enhancement of the mass transport and solid-state reaction rates during the processing of ceramics, glass and other organic or inorganic materials. The effect includes also lower sintering or reaction temperatures, accelerated kinetics for a wide range of processes in these materials, and reduction of the activation energies. Therefore, this review will focus on the effect of microwave on density and grain size, spinel production in the microwave field and theories about the course of the “microwave effect”.

Effect of microwaves on density

The most common and observed effect of the microwaves is the enhancement of densification. The sintering of alumina by Janney et al. [91] was one of the first to demonstrate enhanced densification. They sintered alumina in a temperature range from 900°C up to 1600°C with a holding time from 1 to 60 min. For the conventional sintering (Brew) they used a tungsten element furnace form R. D. Brew, Inc. The furnace for the microwave sintering (MW) was self-constructed by the Oak Ridge National Laboratory. These sintering runs demonstrated the required sintering temperature was lower for microwave sintered samples. For a holding time of 1 min the temperature difference was 250°C and for 60 min was it 300 - 400°C, Figure 64.

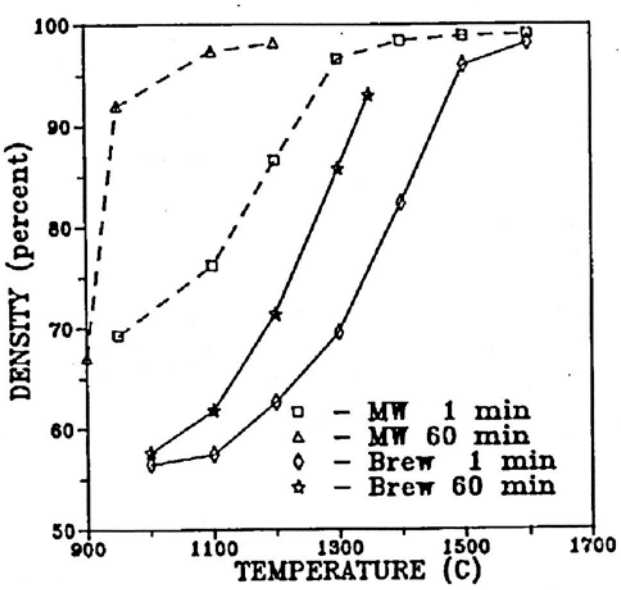

Figure 64 Microwave (MW) vs. conventional (Brew) sintering of high-purity alumina for 1 min and 1 h holds [91]

However, for their experiments Janney et al. [91] did not used the common microwave frequency of 2.45 GHz; they used 28 GHz, because it is very difficult to sinter alumina without a susceptor in a microwave field at the lower frequency and the higher frequency enabled them to sinter alumina with microwaves, because the increase in the microwave frequency also led to an increase of the power absorbed per unit volume, see section 2.4.2.

Samuels and Brandon [92] investigated the densification of four different compositions, viz. alumina, alumina + 20 wt% YSZ, alumina + 50 wt% YSZ and YSZ. In comparison to Janney et al. they used the more common microwave frequency of 2.45 GHz. However, they confirmed the finding of enhance densification for alumina. Further, the investigation demonstrated also the enhancement depends on the material as the effect increased with the content of YSZ, Figure 65.

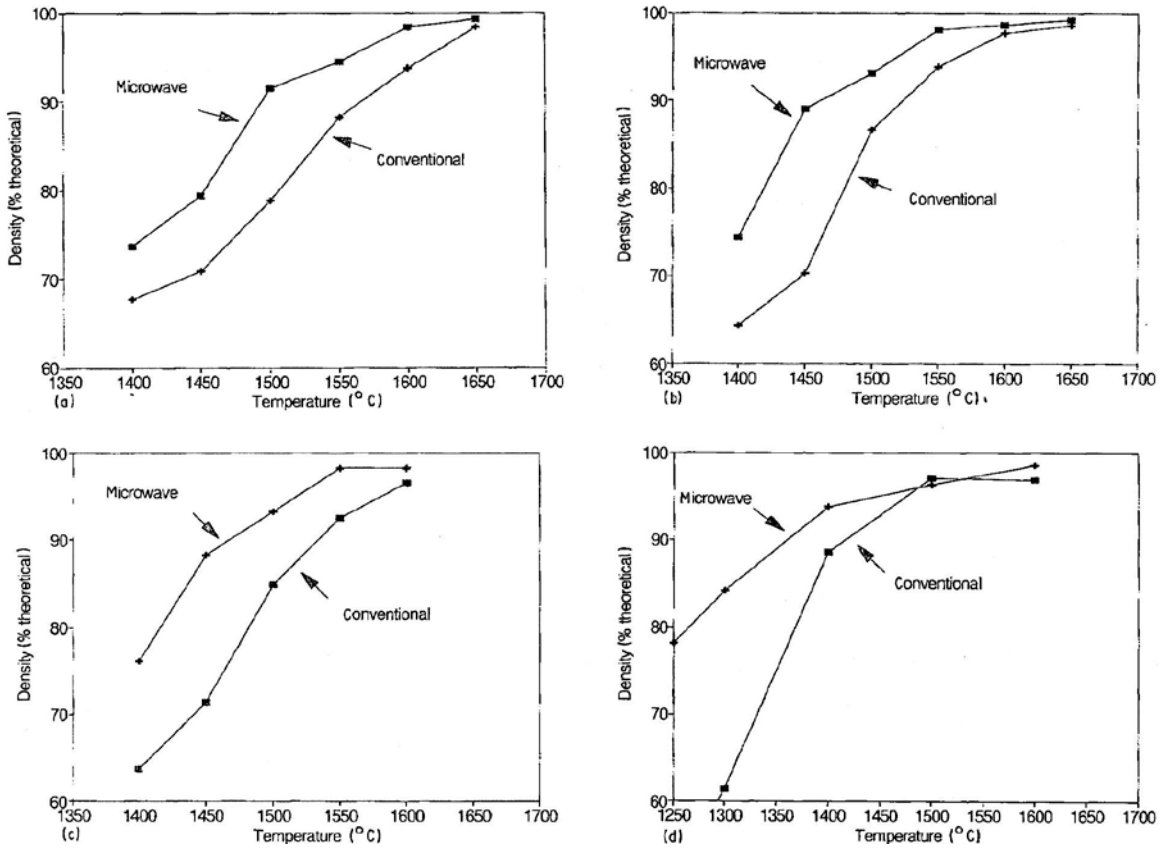

Figure 65 Variation of final density with sintering temperature for both microwave and conventional sintering, showing the microwave enhancement. (a) Alumina; (b) alumina + 20 wt % YSZ; (c) alumina + 50 wt % YSZ; (d) YSZ [92]

Fang, et al., [93] demonstrated the enhancement of the densification for zirconia-containing ceramic-matrix composites. They found that the densification of all their tested materials, viz. alumina, mullite, calcium strontium zirconium phosphate (CSZP) and barium zirconium phosphosilicate (BA25), was enhanced, but with higher zicronia content this enhancement was reduced, Figure 66 and Table 5.

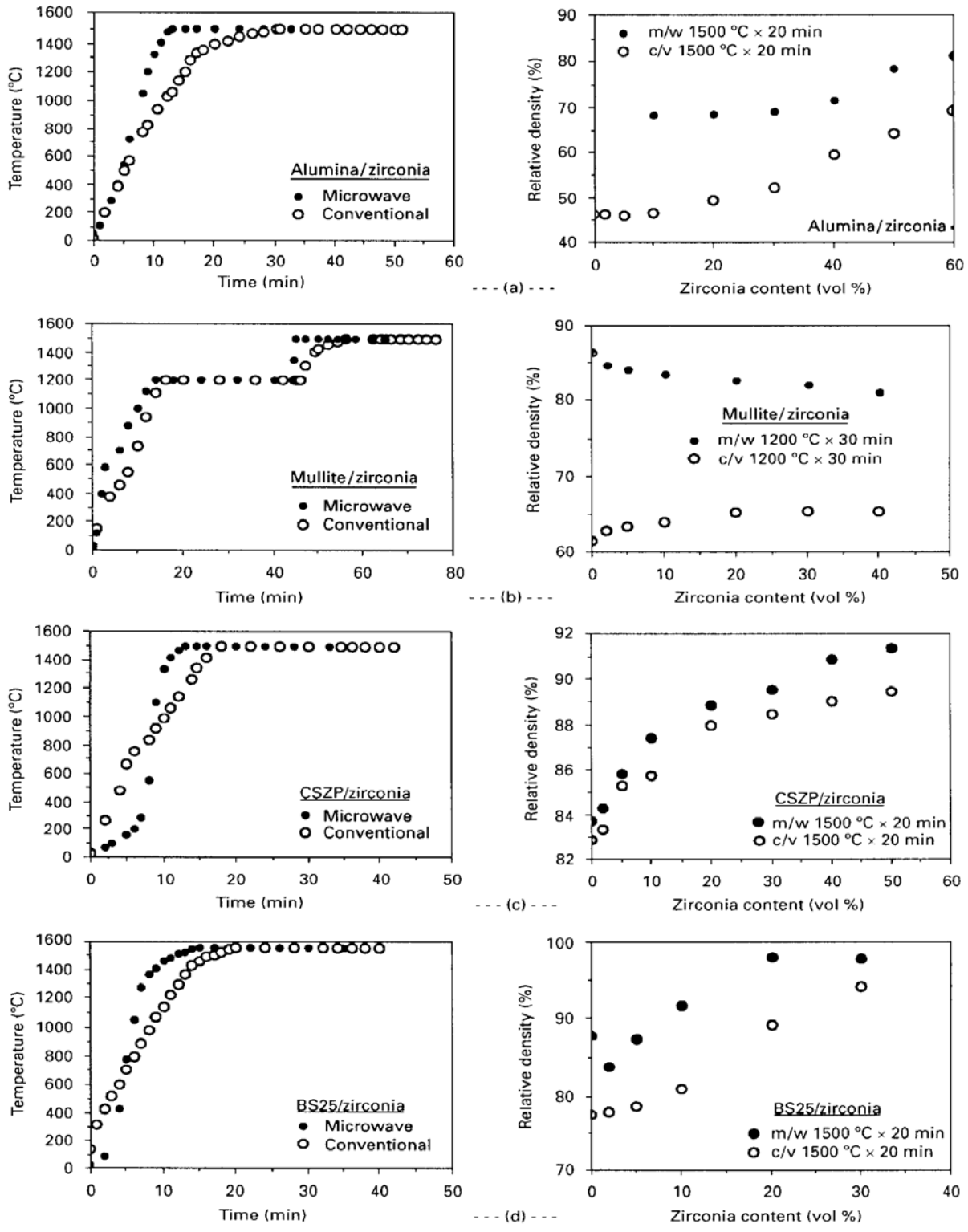

Figure 66 Heating curves and sintering densities of zirconia-containing composites based on (a) alumina, (b) mullite, (c) CSPZ, and (d) BS25 [93]

No.	ZrO_2 (vol %)	Alumina (1500 °C/20 min)	Mullite (gel) (1200 °C/30 min)	CSZP (1500 °C/20 min)	BS25 (1550 °C/20 min)
1	0	48.69	40.29	1.00	13.36
2	2	—	34.46	1.12	7.68
3	5	—	32.45	0.64	11.16
4	10	46.40	30.52	1.97	13.40
5	20	38.55	26.85	1.00	9.91
6	30	32.41	25.61	1.23	3.86
7	40	19.82	23.75	2.04	—

Table 5 Microwave enhancement in densities over the conventionally sintered samples, % [93]

Xu et al. [80] focused their densification experiments on how the heating rate effects the densification in the microwave field. They found that rapid microwave sintering has a different densification behaviour compared to slower heated samples, below 500°C min^{-1}, Figure 60. Xu et al. concluded that ultra-rapid microwave heating results in enhanced densification rate for ZnO compared to slower microwave heating. The reason for the lower density in Figure 60 was the short time available for densification at these high heating rates.

Mazaheri et al. [24] used conventional (CS), microwave and two-stage (TSS) sintering to sinter 8YSZ. For the microwave sintering, they used 2 different heating rates, one low heating rate (LMS) of 5°C min^{-1}, which was the same heating as for the conventional sintering, and a high heating rate (HMS) of 50°C min^{-1}. Their experiments showed that the lower heating rate for microwave sintering reduces the sintering temperature, Figure 67.

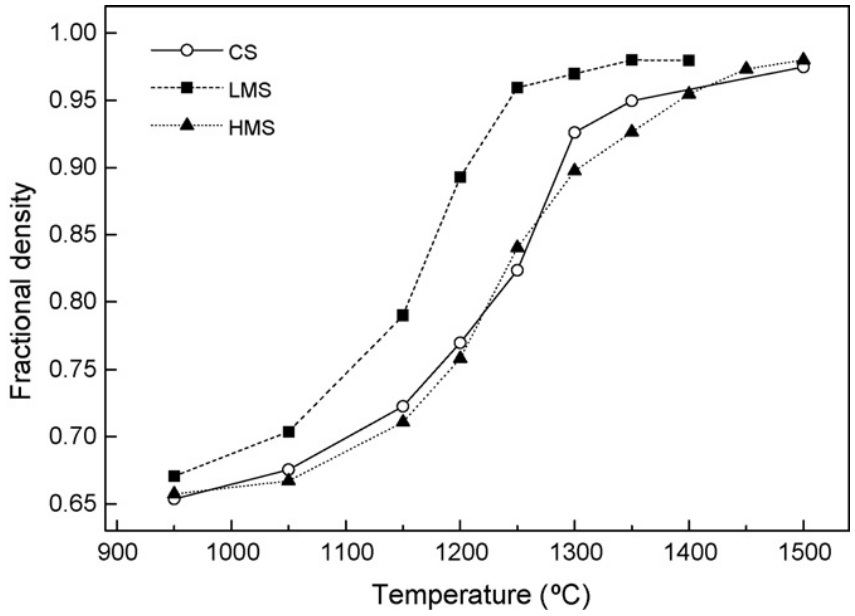

Figure 67 Fractional density variations of the specimens sintered by CS, LMS and HMS as a function of sintering temperature [24]

Mazaheri et al. [24] explained the difference between LMS and HMS with the high heating rate of HMS, because of the high heating rate the densification mechanism did not had the time to be activated. On the other side, this heating rate helped to reduce the sintering time, Figure 68.

If the densification mechanism had not be activated then the densification should demonstrated a similar behaviour as densification for the ultra-rapid heated samples (500°C min^{-1} and higher) demonstrated by Xu et al., Figure 60. The results in Figure 67 are presented in intervals of 100°C. The different heating rates would result in a difference that samples would need to reach a new temperature level (HMS = 2 min and LMS = 20 min). Since LMS spent more time in a temperature interval, the microwaves had more time to increase the densification.

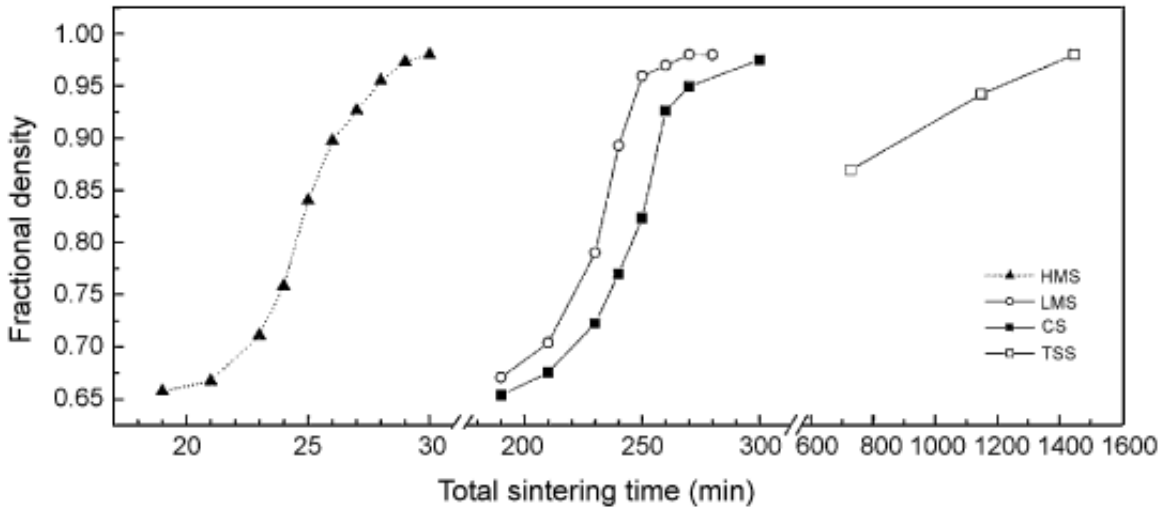

Figure 68 Fractional density versus total sintering time for specimens sintered via CS, LMS, and HMS routes [24]

Charmond et al. [94] used direct microwave sintering (D) and hybrid microwave sintering (H) in a single-mode cavity to investigate the densification and microstructure of nano 2 mol% yttria-doped zirconia. Hybrid heating was achieved by placing a SiC susceptor around the sample. A conventional furnace was used for the calibration runs (C). The sintering details are shown in Table 6.

Name	FP (W)	Sintering temperature (°C)	Density (g/cm^3)	Relative density (%TD)	Average grain size (nm)
Conventional sintering—2 °C/min					
C0	–	1550	6.05	100.0	450
Conventional sintering—25 °C/min					
C1	–	1360	5.53	91.4	220
C2	–	1550	5.74	94.8	430
Direct microwave sintering—25 °C/min					
D3	500	1275	5.75	95.1	200–250
D4	500	1360	5.75	95.0	240–270
D5	500	1500	5.86	96.8	380–450
Hybrid microwave sintering—25 °C/min					
H6	1000	1200	4.89	80.7	120–140
H7	1000	1275	5.48	90.5	140–190
H8	1000	1340	5.80	95.8	210–230
H9	1000	1350 (1 h)	5.96	98.6	230–270
Hybrid microwave sintering—250 °C/min					
H10	1000	1225	5.26	86.9	130–180

Table 6 Miscellaneous data on sintering experiments [94]

As others before, they achieved higher densities at lower temperature for direct and hybrid microwave heating, Figure 69.

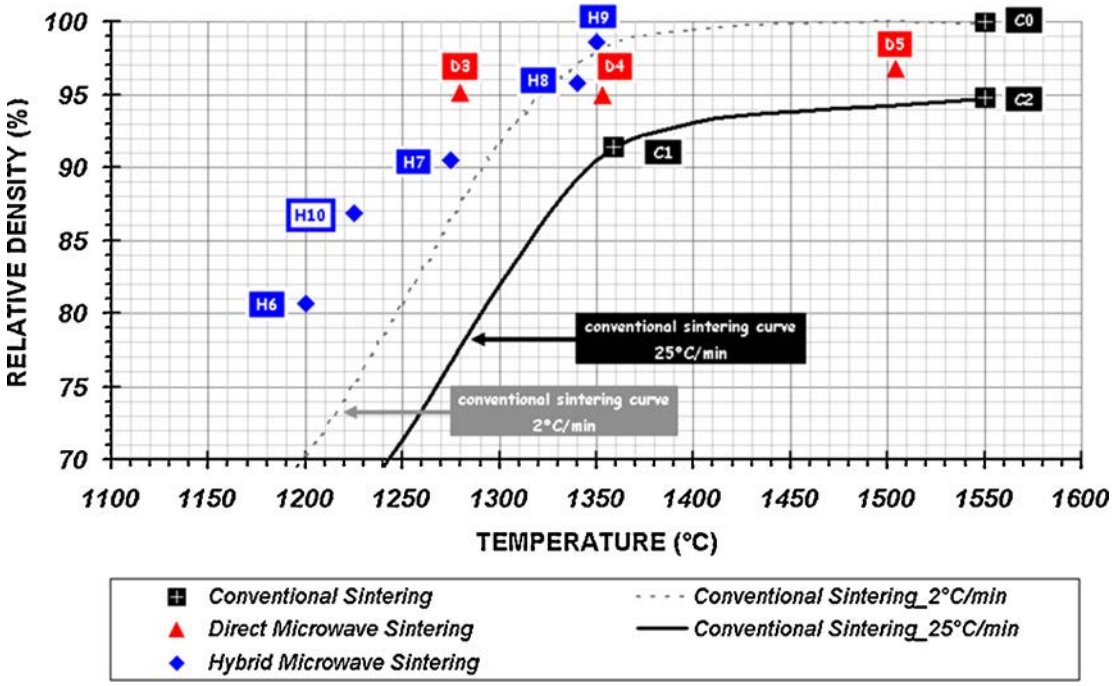

Figure 69 Variation of the relative density vs. maximal temperature for conventional (C), direct microwave (D) and hybrid microwave (H) sintering test [94]

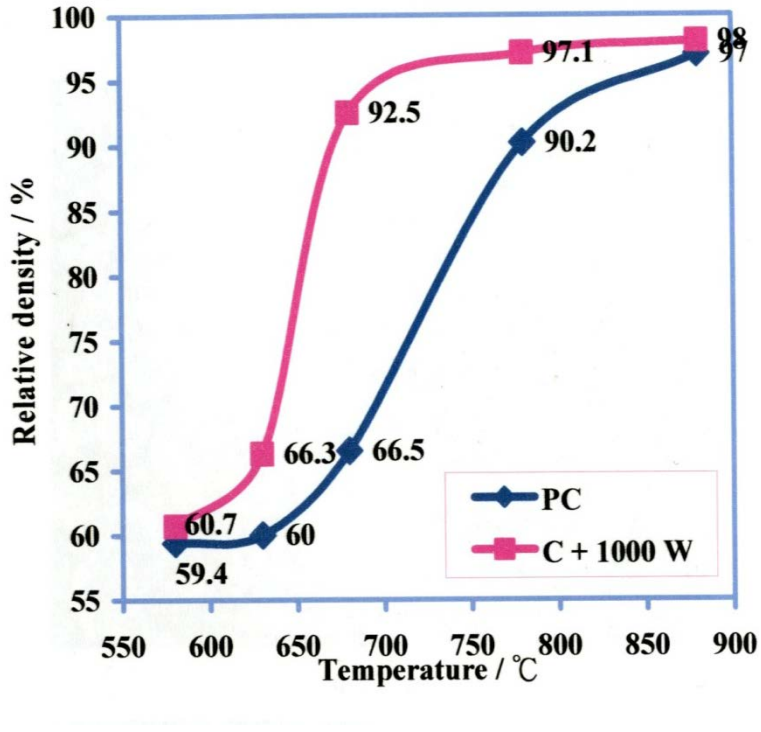

Figure 70 Density curves of submicron ZnO sintered for 1 h at different temperatures during pure conventional heating and hybrid heating with 1000 W microwave power [29]

During his investigation to find out if the “microwave effect” was genuine effect or not, Wang [29] used a hybrid furnace, which allows simultaneous conventional and

microwave heating, sinter ZnO, YSZ and alumina at various temperatures. His results for sintering submicron ZnO for 1 h at different temperatures during pure conventional heating and hybrid heating with 1000 W microwave power confirms the findings of previous authors about the enhancement of the densification for microwave sintering in the initial and intermediate stage, Figure 70.

Further, as he sintered ZnO for 1 h at 680°C with various amounts of microwaves, he found that microwave sintering required a minimum amount to have a significant effect on the densification, Figure 71 [29].

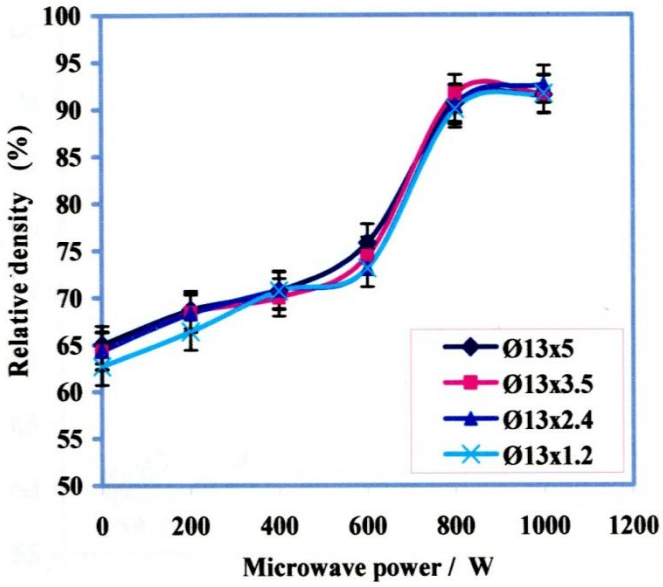

Figure 71 Density curves of submicron ZnO pellets with equal diameter and different thickness hybrid sintered at 680°C [29]

The use of a hybrid furnace for all the experiments requiring heating allowed that the temperature-time profile to be exactly the same for the conventional and microwave sintering processes since the same furnace was used the furnace parameters and the temperature measurement system were the same. This meant that the observed differences were all directly linked to the use of microwaves [29].

Effect of microwaves on grain size

During their experiments at Oak Ridge National Laboratory, Janney et al [95] sintered 8YSZ and found that microwave sintering samples (~2.2 µm at 99.47% TD) had a finer grain size than conventional sintered samples (~3.5 µm at 99.35% TD).

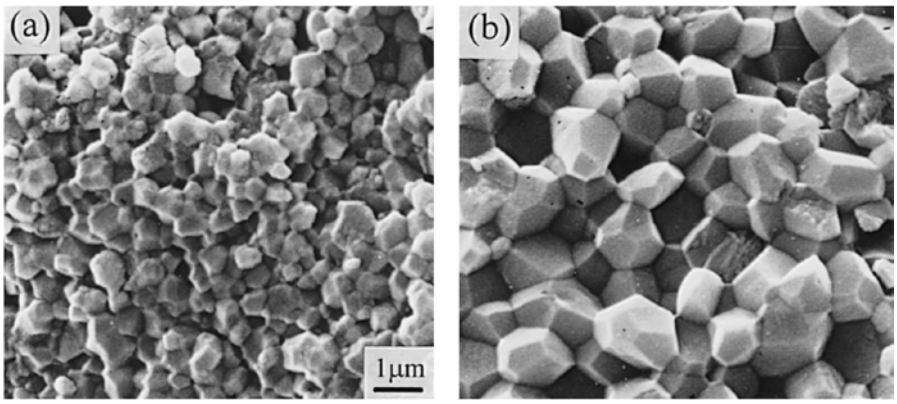

Figure 72 Microstructure of 8YSZ samples with 99.5% of TD by (a) microwave and (b) conventional sintering [96]

Xie et al. [96] sintered Ce-Y-ZrO2 with conventional and microwave heating to a theoretical density of 99.5% and measured the grain size of the samples fracture surface from scanning electron micrographs. The measure grain size was smaller and more uniform for the microwave sintered samples (0.65 μm) than for the conventional sintered samples (1.15 μm), Figure 72. They concluded that finer grain size resulted from a combination of the usage of microwaves and the shorter holding time at sinter temperature.

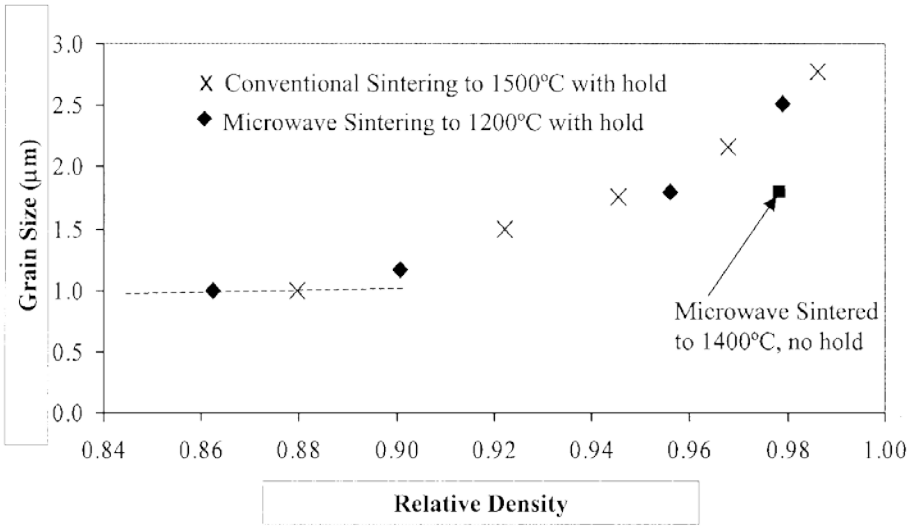

Figure 73 Grain growth trajectories of microwave-sintered and conventional sintered alumina samples [97]

Brosnan et al. [97] investigated the sintering of alumina in a temperature range from 900 - 1600°C. They measured the grain size of their samples and plotted the grain

size versus the relative density of the measured sample, Figure 73. This revealed that the grain growth follows the same trajectory for conventional and microwave sintering.

Binner et al. [70] used single-stage and two-step sintering to sinter 3YSZ samples with conventional and hybrid microwave/radiation heating. Hybrid heating produced a much finer and more homogenous grain size, Figure 74. However the use of hybrid heating allowed a higher initial heating rate (20°C min^{-1}) than for conventional sintering (7°C min^{-1}). Therefore they believe that the primary reason for the finer grain size was the increased initial heating rate.

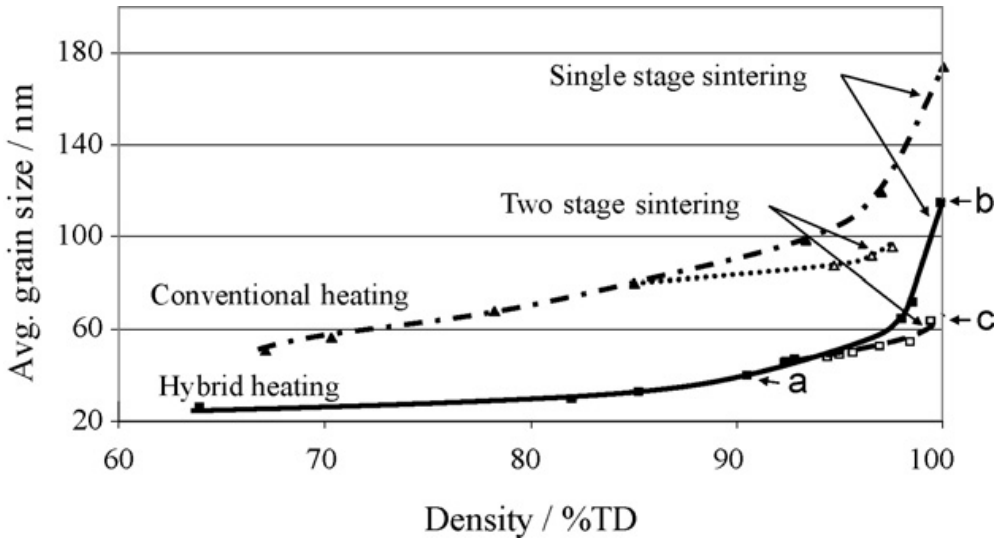

Figure 74 Grain size vs. density plots for nanostructured 3YSZ ceramics produced by single-step and two-step sintering using both conventional radiation heating and hybrid-microwave heating [70]

Mazaheri et al. [24] not only report the effect LMS and HMS on the densification of 8YSZ, they also compared their effect on the grain size development with CS and TSS for 8YSZ. They found that the grain size was smallest for TSS (295 nm) < HMS (0.9 µm) < CS (2.14 µm) < LMS (2.35 µm), Figure 75 andFigure **76**.

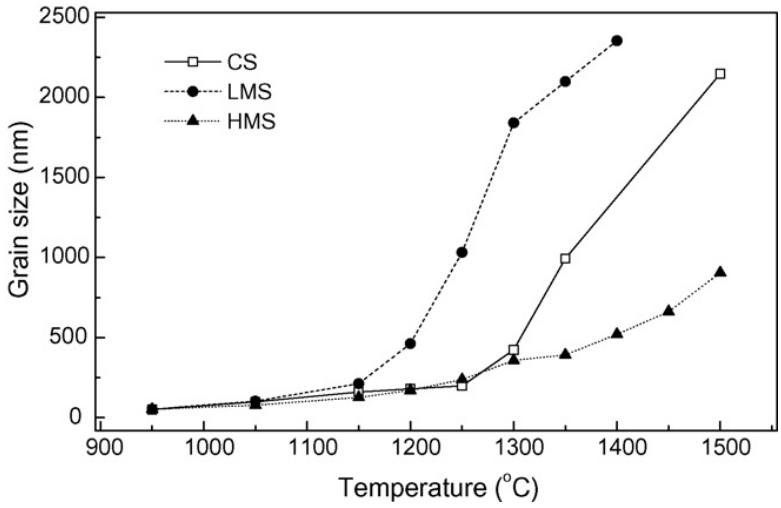

Figure 75 Grain size variation of CS, LMS and HMS 8YSZ samples as a function of temperature [24]

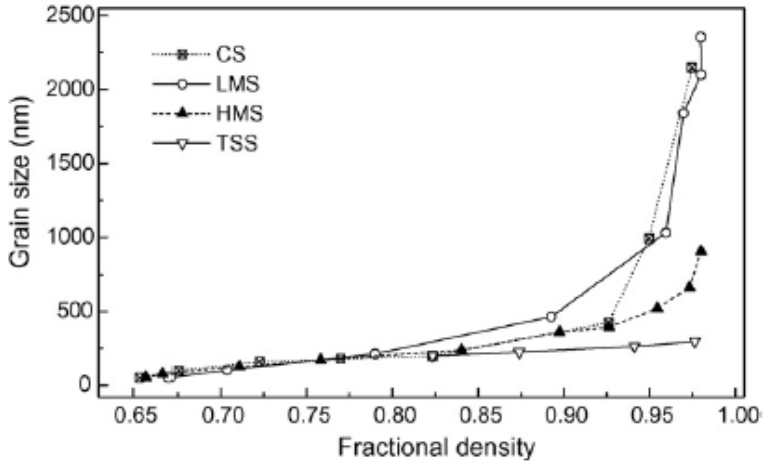

Figure 76 Grain size/fractional density trajectory obtained by CS, LMS, HMS and TSS for 8YSZ [24]

Charmond et al. [94] also compared the grain size with density for their work on sintering YSZ, Figure 77a, and showed that microwave-sintered samples had finer grains compared to the conventional sintered samples. On the other hand, conventional sintering produced a more homogenous microstructure.

For Charmond et al. [94] the maximum sintering temperature was the main parameter governing grain growth, which is indicated by Figure 77b. Therefore, they concluded microwaves do not accelerate the grain growth in the final sintering stage. They explain the reduced grain size for microwave sintering with the positive effect of microwaves during the densification.

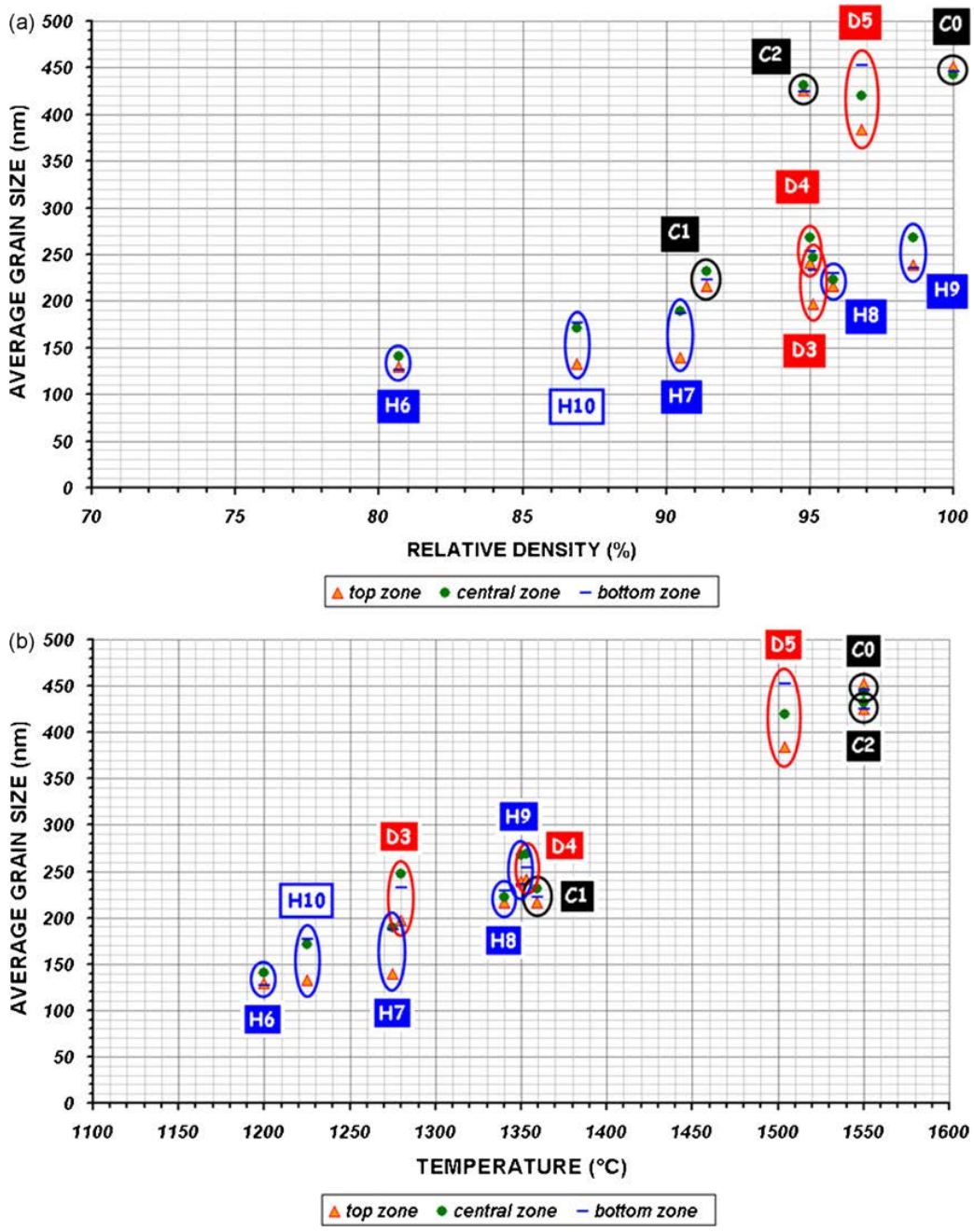

Figure 77 Variation of average grain size in the top, central and bottom zones vs. (a) the final relative density and (b) the sintering temperature for conventional (C), direct microwave (D) and hybrid microwave (H) sintering tests of YSZ, sample details see Table 6 [94]

Spinel production in a microwave field

Aguilar et al. [98] studied the possibility to use microwaves to produce magnesia-alumina spinel. For their experiments, they investigated powder bed samples and compressed pellets. Further, they used a carbon bed, as susceptor with this they

were able to produce spinel with microwaves. The samples were heated in an 800 W microwave field for 20, 40 and 60 min. They found that it was possible to produce spinel with microwaves when the samples were heated for at least 40 min.

Peelamedu et al. [99] successfully produced $NiAl_2O_4$ in the microwave field with the help SiC rods as susceptor. Compared with conventional reactions, the microwave reactions were considerably faster, Table 7. They concluded that the enhanced diffusion was caused by “anisothermal conditions” within the samples when heated by microwaves.

Sample	Reaction temperature (°C)	Sinter time		Sintered density (g/cm^3)		Phase analysis (%)	
		MW	CON	MW	CON	NIR[a]-MW	NIR[a]-CON
Set-1	1200	15	20	3.77	4.48	NiO—>8 Al_2O_3—<1 $NiAl_2O_4$—91	NiO—27 Al_2O_3—23 $NiAl_2O_4$—50
Set-2	1300	15	20	4.00	4.33	NiO—2 Al_2O_3—0 $NiAl_2O_4$—98	NiO—15 Al_2O_3—12 $NiAl_2O_4$—73
Set-3	1400	15	20	3.81 (95% T.D.)	4.15	NiO—<1 Al_2O_3—0 $NiAl_2O_4$—>99	NiO—6 Al_2O_3—>5 $NiAl_2O_4$—>88

[a] NIR—normalized intensity ratio. NIR of the x phase can be calculated using the formula $NIR_x = \frac{I_x - I_{back}}{I_x + I_y + I_z - 3I_{back}} \times 100$, where I_x, I_y and I_z are the absolute intensity values and I_{back} is the background intensity.

Table 7 Reaction conditions and the sintering results in both microwave (MW) and conventional (CON) processing [99]

Ganesh et al. [100] compared microwave assisted solid-state reactions with conventional solid-state reactions. For the microwave experiments, they mixed carbon black with their reaction material. The placement of the sample on top of a SiC plate helped to achieve a stable and instantaneous reaction in the microwave field. They found that the use of microwave reaction sintering helped to save processing time and power.

Zhang et al. [101] used a mixture of $BaCO_3$ and $Al(OH)_3$ to produce $BaAl_2O_4$ successfully in a microwave field. Further, they found that microwave reaction sintering reduced the sintering time and temperature (900°C for 5 min) compared to conventional sintering (1300°C for 90 min).

Theories

Janney et al. [102] investigated the effect of microwave on a number of ceramic processing steps, including sintering, annealing (to encourage grain growth) and diffusion of $_{18}O$ in a single crystal. In every case they found that microwaves enhanced different processes. Further they found the activation energy was reduced in all cases, although the amount of the reduction differed. For the densification, the reduction of the activation energy was most significant, decreasing from 575 kJ/mol for conventional sintering to 160 kJ/mol for microwave sintering. For the annealing it dropped from 550 to 480 kJ/mol whilst for diffusion it changed from 710 to 410 kJ/mol. They explained that high reduction in the activation energy for microwave sintering was not only caused by a differences in the diffusions process as for the other processes during conventional and microwave heating. Further, they concluded that the structural evolution was different in the case of microwave sintering of materials because the pores had a greater tendency to stay open in the later sintering stages, leading to a finer mean grain size and contributing to the increased reduction of the activation energy. Their conclusion was that this difference in structural evolution was achieved by an enhancement of bulk or grain boundary diffusion over surface diffusion. They proposed 3 hypotheses for the origin of their observation, via

1) Free surface effects, similar to the effects found in plasma sintering
2) Grain boundary coupling
3) Coupling to the lattice defects and other bulk effects

They rejected their own hypothesis of the free surface effects because when plasma sintering is interrupted the surface hydroxyl groups are stripped off, making it impossible to restart plasma sintering. However microwave sintering can be interrupted and restarted without any problems. Further, with microwaves the sintering atmosphere has little effect on the ability to heat or sinter materials compared to plasma sintering which requires a vacuum as the processing atmosphere [102]. For hypotheses 2 and 3 they acknowledged the importance of grain boundary coupling for the potential to enhance grain boundary, volume and surface diffusion and its potential importance for the distribution and action of additional phases in multi-phase systems. The importance of the coupling of the

microwaves to the lattice defects and other bulk effects was demonstrated by Janney et al.'s diffusion experiments involving single crystals, because they achieved a microwave effect in a material that does not contain free surfaces or grain boundaries. However they could not determine which mechanism is responsible for the enhanced diffusion-controlled processes [102].

During their investigation of the exchange reaction for four sodium-aluminasilicate compositions using conventional and microwave heating, Fathi et al. [103] found that microwave heating created a high interdiffusion, which resulted in a greater penetration depth of the ions exchanged during microwave heating. They thought the electric field of microwaves increased the vibrational frequency of an ion within a potential well. Further that a rapid reversal of the electric field would increase the local temperature and made it easier for the ion to leave the well.

Booske et al. [104] rejected the idea that microwave heating reduces the activation energy, because they argued that the activation energy is approximately equal to the enthalpy, which is determined by intrinsic material characteristics such as structure and atomic bonds. If enthalpy is equal to the activation energy then a reduction of the activation energy has to change the atomic bond, which according to Booske et al. unlikely. They suggested their own mechanisms for the effects caused by microwaves:

1) Localized resonant coupling to weak bond surface modes or point defects modes
2) Zero-frequency mode coupling requiring localized concentrations of charge imbalances
3) Three-wave mixing involving either 2 closely spaced microwave frequencies and 1 low frequency elastic wave or 2 high frequency elastic waves and 1 microwave frequency electromagnetic wave

According to mechanism 1, it is possible to create a source of excitation when the frequency of microwaves matches the resonating frequency of ions in weak bonds such surfaces or point defects. Further in accordance with mechanism 2, a charge imbalance as at free surfaces, grain boundary or vacancies can create localized

excess charges in the lattice which could couple with microwave. In the charged lattice area, a relative small change in the ion kinetics by inducing microwaves lead to substantial change to ion jump probabilities and ion mobility. For the previously described mechanisms, especially mechanism 1, not only the right frequency but also the phase (or wavelength) has to match to create the resonance. Therefore, it is difficult to match the microwaves to the right conditions for the resonance. However the finite bandwidth of microwave sources coupled with the scattering of the microwave are able to create electromagnetic k-spectrum which enables the resonate photon-to-phonon coupling as the microwave satisfy the conditions for the resonance through the necessary scattering angle. This opens the possible that microwave engery can be transferred via resonant (nonthermal) transfer to the crystal lattice between 2 high intensity electromagnetic waves (microwaves) to a low frequency (radio waves or lower) [104].

Further they suggested that mechanism 1 and 2 would have a higher impact at lower temperature on polycrystalline materials compared to single crystal forms. At higher temperatures they thought that mechanisms 2 and 3 would be dominant in single as well as in poly crystals [104].

Binner et al. [26] investigated the differences in the synthesis of titanium carbide using conventional and microwave heating. They found that synthesis was 3.3 - 3.4 times faster with microwave heating. They thought an increase of the Arrhenius pre-exponential factor by the factor of the increased reaction was the more likely reason for the enhance reaction compared to a reduction in the activation energy. They argued that the pre-exponential factor depends on the vibration of the atoms at the reaction interface and those could be influenced by microwaves.

Another theory was suggested by Nightingale et al. [105]. They found a small, but significant shift in the density – grain size relationship below 96% TD during their sintering of 3YSZ in conventional and microwave sintering. This lead to the conclusion, that in the initial and intermediate sintering stages the enhancement of the lattice diffusion is higher than for surface and grain boundary diffusion. However as soon as grain growth dominates in the final sintering stage this difference disappear.

As can be seen, a wide range of theories has been proposed in the past. However one theory that was suggested by Rybakov and Semenov [106] dominates. The basic idea behind this theory is that microwaves create a directed flow of charges, as vacancies, because grain boundaries act as semi-penetrable barriers and with no way of return, the charges are on a one way route.

This is best explained in terms of vacancy diffusion. Here, electrically charged vacancies in a solid have the potential to receive the action of the microwave field which enhances the vacancy flux, *J*, by a field-induced drift part:

$$J = -D\nabla N + DN_q E/kT \qquad (2.56)$$

Where *D* is the diffusion coefficient, *N* is the concentration, *q* is the effective electric charge of vacancies and *E* is the vector of the electric field. This drift part of the vacancy flux exceeds the diffusion part even if only a relative weak electric field is present. However, in a microwave field the vacancy drift is oscillating and would have on average no effect on the vacancy flux unless field induced space charge distortions interrupt the linear rectification of the currents.

Hence, in a defect free single crystal the oscillating microwaves would have no effect on the vacancy concentration because the drift of the vacancy would be equal in all directions of the oscillating microwave field and result in an average zero drift effect. However, if grain boundaries or interfaces are present they will cause disturbances in the vacancy concentration in their vicinity. These disturbances are in phase with the microwave field and create a non-zero net (average over the field period) drift flux. This net flux has the same directionality of positive and negative vacancies and would result into a neutral mass transport, where no extra force is created and only “normal” mass transport is present. However a charged transport is created because the mobility of positive and negative vacancies is different to each other. Therefore the product of the effective mobility and average volumetric force:

$$\langle J \rangle = \frac{D_+ D_-}{D_+ + D_-} \langle \rho_{sc} E \rangle \qquad (2.57)$$

results in a net drift vacancy flux responsible for mass transport. This is of the same physical nature as the ponderomotive force known in plasma physics. This ponderomotive force is measured by the magnitude of the pressure of the electromagnetic field, $E^2/8\pi$. However its radiation pressure (0.1 Pa) for a field strength of 10^3 Vcm^{-1} is low and not enough to influence the mass transport, which would require higher field strengths. Nevertheless, the microwave action is amplified by several factors. Firstly, the direct influence of the ponderomotive force on the mobility of vacancies in ionic crystalline solids results in an equivalent stress, which is by a large factor greater than the radiation pressure, $N_0/N \geq 10^5$ (N_0 is the concentration of atoms in the solid). Further, the tangential component of the microwave electric field leads to an enhanced ponderomotive mass transport at surfaces and grain boundaries and cause a net flux of vacancies only in the near-surface layer of each grain, where the space charges are localized and the mobility of vacancies is higher than in the bulk. The resulting additional mass transport factor $(D_v/D_s + a/R)^{-1}$ can reach several orders of magnitude (D_s is the diffusion coefficient in the near-surface amorphized layer, D_v is the diffusion coefficient in the bulk crystal, *a* is the thickness of the amorphized layer and *R* is a characteristic size of crystal). This way, the ponderomotive force has a significant influence on the mass transport in ionic crystalline solids, though the magnitude of the effect depends on the correlation of between microwave frequency and the ionic conductivity of the solid [106].

The influence of the ponderomotive force is shown in Figure 18 and Table 8. In principle it should increase every diffusion mechanism in the solid-state. This would mean for the sintering mechanisms described in section 2.2.3 that the surface, lattice and grain boundary diffusion would be influenced and increased. The increase in the lattice diffusion, from the grain boundary, and grain boundary diffusion are welcomed, because they contribute to the densification of ceramics and would lead to faster sintering and/or a lower sintering temperature. However, the increase in the surface diffusion would not be helpful, because this diffusion mechanism only promotes coarsening and not densification. Therefore, it can be said that the ponderomotive forces are a double-edge sword, because if a ceramic is easily densified under conventional conditions then microwaves will generally accelerate sintering, however

if the material is difficult to sinter by solid-state sintering, then microwave sintering could lead to additional coarsening, Table 8.

Table 8 Overview of sintering mechanisms [42, 106]

Mechanism	Source of matter	Sink of mater	Densifying	Nondensifying	Influenced by Ponderomotive Effect
Surface diffusion	Surface	Neck		X	X
Lattice diffusion	Surface	Neck		X	X
Vapour diffusion	Surface	Neck		X	
Grain boundary diffusion	Grain boundary	Neck	X		X
Lattice diffusion	Grain boundary	Neck	X		X
Plastic	Grain boundary	Neck	X		

As shown earlier the densification is only increased when using microwaves in the initial and intermediate stages of sintering. In the final sintering stage microwave sintering slows down significantly so that conventional sintering is able to catch up. There are 2 possible explanations for this behaviour. The first lies within the theory of the ponderomotive forces, because this force need interfaces, grain boundaries to be affected. This means a smaller grain size will result into higher number of interfaces and with it a greater effect of the ponderomotive forces. Therefore in the final sintering stage, where grain growth is taking place, the number of interfaces decreases and so does the ponderomotive forces.

The second possible explanation lies within the reports of reduced grain size for microwave sintering, described by Mazaheri et al. [24] and Charmond et al. [94]. Here, microwave sintering creates a similar difference in the kinetics between grain-boundary diffusion and grain-boundary migration as described by Chen et al. [107]. They found that the sintering of samples with two stage-sintering to achieve a smaller grain size reduced kinetics. However there was no evidence that the reduced kinetics were caused by a change in the diffusion mechanism as the density increased. Further they described the sintering in a ‘frozen microstructure’ as an ‘exhaustion process’ in which densification rate is reducing dramatically as the density increases.

They concluded that to achieve densification without grain growth, the grain-boundary migration needs to be suppressed while the grain-boundary diffusion is active.

The ponderomotive forces have the potential to yield the level of enhanced diffusion required to achieve the enhancements seen during microwaves sintering. Further, in the final stage microwave sintering can also be described as an exhaustion process as its densification rate is dramatically reduced as the density increases. If microwave sintering is reducing the grain size then it is possible the enhancement of the diffusion could leads to enhanced grain-boundary diffusion as suggested by Wroe and Rowley [33]. This could create a difference in the kinetics between the grain-boundary diffusion and grain-boundary migration. Since the grain-boundary migration is not suppressed the effect of the difference in the kinetics would not be as significant as described by Chen et al. [107]. However it could influence the grain size of microwave sintered samples and could explain why after a strong enhancement of the densification in the initial and intermediates sintering stages microwave sintering has a dramatically reduced densification rate in the final sintering stage.

Experiments to “prove” the ponderomotive effect

In the time since the theory was first suggested [27] two independent research projects have used hybrid heating, which allows the simultaneous use of microwave and conventional heating and minimized the problem of inaccurate temperature measurement and different furnace parameters. Both studies indicated that the ponderomotive force could be an additional driving force for the solid-state sintering [32, 33].

Freeman et al. [32] measured the current in sodium chloride (NaCl) crystals in the absence of microwaves and when microwaves were pulsed through the crystal. Their experiment was carefully designed so that the use of microwaves did not change the temperature of the sample so that all the sample parameter as carrier concentration and defect mobility remained constant. Further, they used a bias voltage as the driving force for the current and heated the applicator with heating tapes to keep a constant temperature. For the effect of the microwaves on the current passing

through the crystal they used a 14 GHz microwave pulse for 400 microseconds. This pulse was enough to influence the diffusion inside crystal, but it was too short to increase the temperature of the sample. The current that passed through the NaCl crystal was registered in a sensitive, high-gain amplifier.

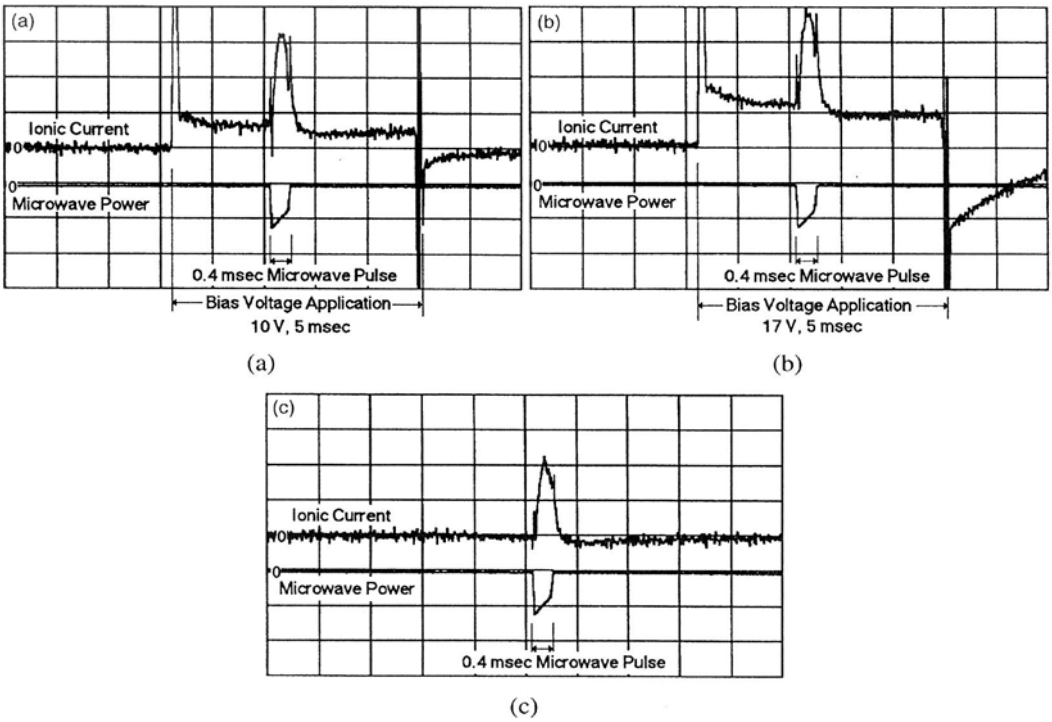

Figure 78 Oscilloscope traces showing the effect of microwave irradiation on ionic current in a NaCl crystal at 150°C. In (a) an ionic current results from application of a10 V bias pulse and is enhanced during microwave irradiation (≈ 2 kW). In (b) the bias voltage is 17 V. In (c) no bias voltage. In all 3 plots, the horizontal scale is 1 ms/div, and the vertical is 0.1 nA/div for the current. [32]

Figure 78a + b shows the current that went through the 150°C hot sample when the bias voltage was present and when microwaves were pulsed through. As can be seen, the microwaves increased the flow the current. However, when the bias voltage was increased the magnitude of the microwave response remained the same as for the lower bias voltage. More intriguing is the behaviour when no bias voltage was present, Figure 78c, because even here microwaves produced a resulting current and its magnitude was identical to that resulting from the other experiments. This and the fact that the effect was same when the crystal was removed and reinstalled lead Freeman et al. to the conclusion that the microwave acted as additional driving as described by the theory of the ponderomotive effect [32].

Freeman et al. experiments clearly demonstrated that microwave increase or created the flow of the current. This increased flow of a current is the main basis of the ponderomotive effect, which states that microwave increase the flow of charges and that the grain boundary create a directional flow as semi-penetrable barriers.

Wroe and Rowley [33] used a hybrid furnace that allowed simultaneous microwave and conventional heating for dilatometer measurements of YSZ. They heated the samples at 10°C min^{-1} to 1500°C for 1 h before reducing the temperature at a rate of 20°C min^{-1} to room temperature. The initial experiment showed the expected enhanced densification with microwaves, because the shrinkage started ~80°C earlier for the hybrid sintering and remained at a lower temperature throughout the whole process. It was even more interesting when the microwaves were switched on or off during the densification phase. When the temperature switched off at 1080°C the shrinkage rate was almost reduced to zero until the sample temperature reached the level for the conventional sintering and when it continued to follow the conventional shrinkage curve, Figure 79a. For the case when the microwaves were switched on at 1080°C, the shrinkage rate of the previous conventional sintered sample increased until it “caught up” with the hybrid shrinkage curve to follow it for the remainder of the experiment, Figure 79b. These experiments lead Wroe and Rowley to the conclusion that the enhancement of microwave sintering were of a non-thermal nature and that the microwaves created an additional driving as described in the theory of the ponderomotive force.

As Wroe and Rowley demonstrate, microwaves have a direct influence on the shrinkage of ceramics. The cause of shrinkage is a matter transport via diffusion, see section. 2.2.1, and as the ponderomotive effect suggests the shrinkage and with it the diffusion was increased when microwave were used.

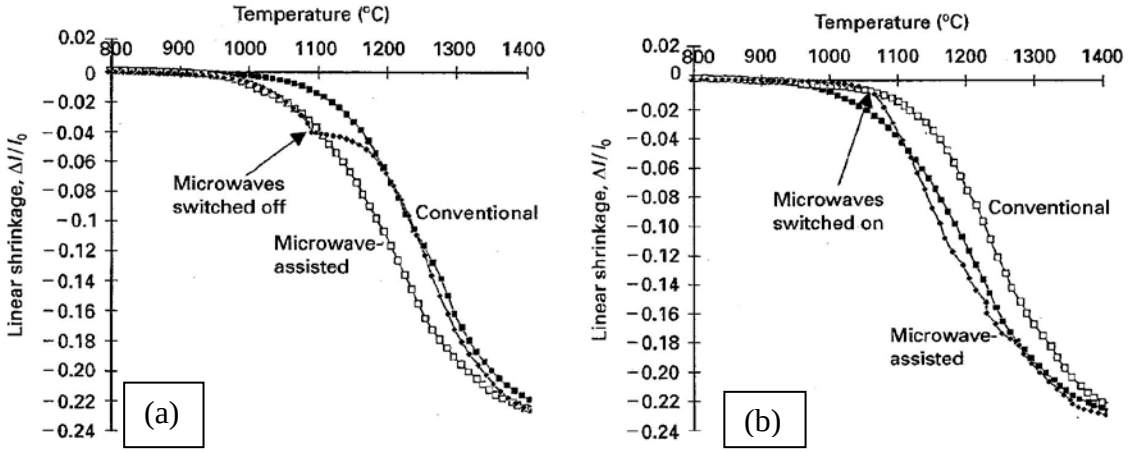

Figure 79 Normalized linear shrinkage of zirconia plotted as a function of sintering temperature for conventional and microwave-assisted sintering showing the effect of switching (a) off and (b) on the microwaves during the process (~ 1080°C). [33]

Whittaker [34] used a 3 mm diameter pellet of $YbBa_2Cu_3O_{7-\delta}$ embedded in a 13 mm diameter pellet of $YBa_2Cu_3O_{7-\delta}$ to investigate if the direction of the elemental diffusion was influenced by the use of microwaves. For this experiment Yb^{3+} would diffuse into $YBa_2Cu_3O_{7-\delta}$ and its diffusion was investigated by the use of X-ray fluorescence analyses on a scanning microscope after microwave and conventional heating. The samples were heated between 2 and 12 days in a single mode cavity and for microwave heating the samples were placed centrally in the wave guide of the microwave. The results showed, as expected, the conventional diffusion has no preferred direction, Figure 80a, However the microwave diffusion showed a preferred diffusion direction, because the diffusion parallel to the microwave field vector was increased by 10 times compared to the perpendicular direction, Figure 80b and c. Whittaker concluded that this is “the first and unequivocal evidence that microwaves may directly influence ion transport in a high temperature sintering process”.

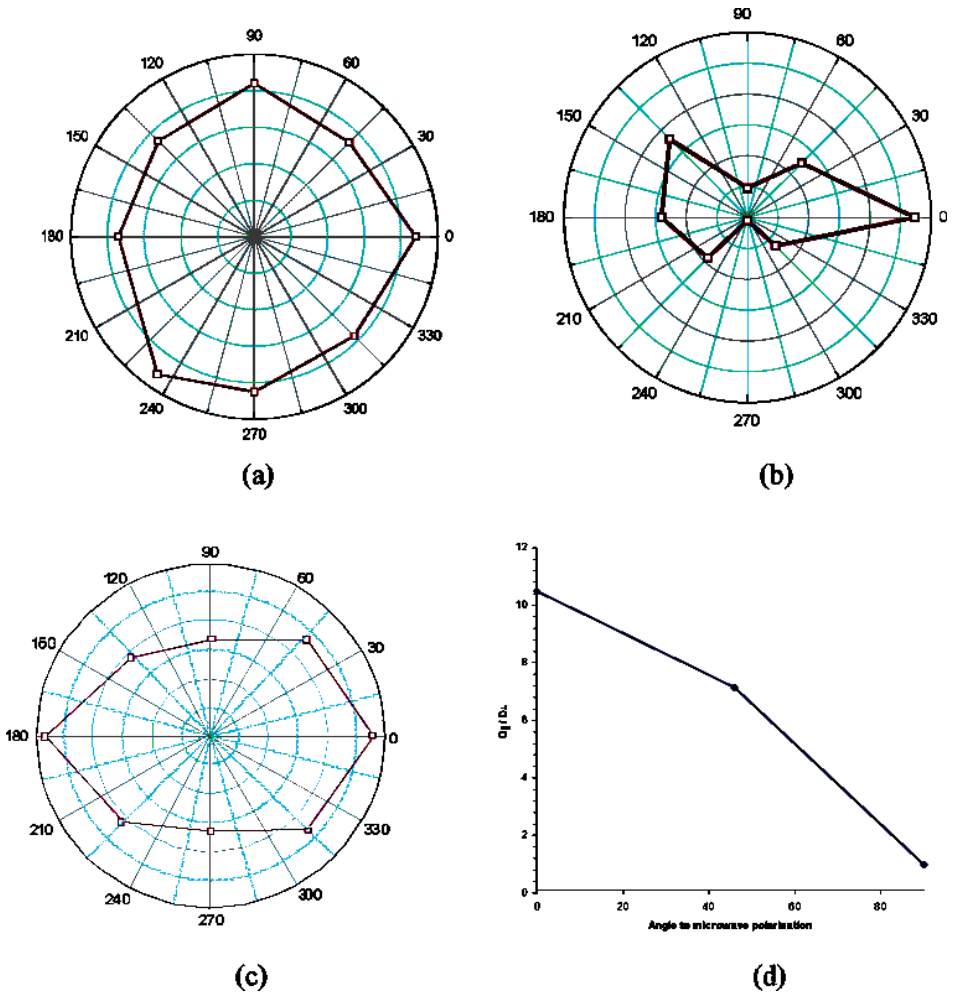

Figure 80 Polar plot of the relative diffusion coefficient (radial axis) for Y^{3+} diffusing into $YbBa_2Cu_3O_{7-\delta}$ as a function of the angle to the microwave polarisation. The radial axis represent the apparent diffusion coefficient: (a) conventional heated sample, 10 days at 800°C; (b) sample heated by microwaves polarized along the 0 - 180° axis, 5 days at ca. 700°C; samples by microwave polarized along the 0 - 180° axis, 13 days at ca. 700°C. (d) Alternative presentation of in part b, allowing for symmetry sample. [34]

Link et al. [108] undertook an investigation into a refined theory of the ponderomotive force suggest by Booske et al. [109], because, in this refined model, it was suggested that mass flow created by the ponderomotive forces of an enhanced (antisymmetric) electric field would lead to matter flow from the interior of the intergrain boundary towards and along the grain surfaces. This pattern would result in easier shrinkage of the closed porosity, because atoms would be extracted from the grain boundary and transported towards the grain surface. According to this theory Link et al. [108] suggested that pores would have a greater shrinkage in the direction of the microwave field, Figure 81.

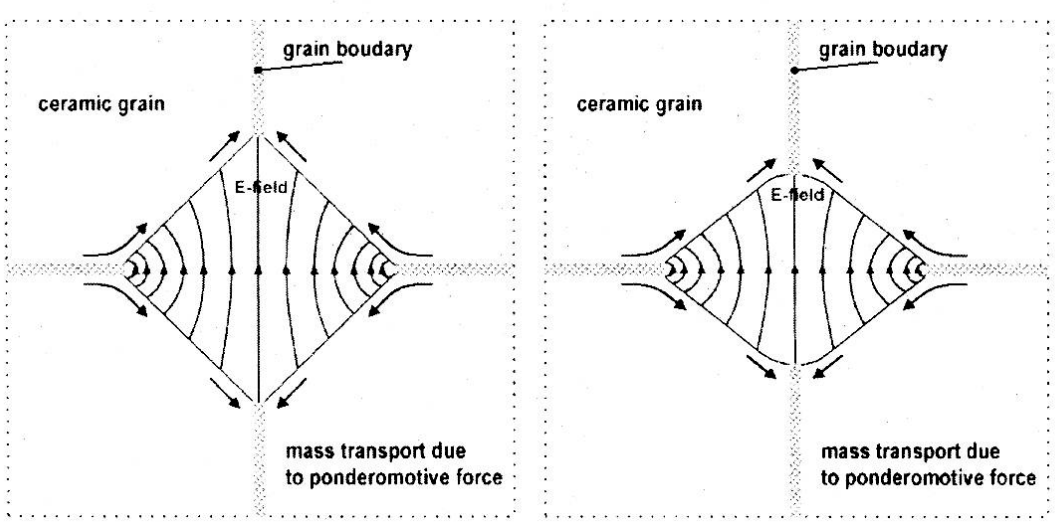

Figure 81 Scheme of a ceramic pore indicating field distribution and non-thermal mass transport according to Booske et al. [109] at an initial (left) and medium (right) stage of sintering [108]

To prove their hypothesis they placed 3YSZ into a single-mode waveguide applicator to achieve a maximum linearly polarised electrical field. These samples were soaked in the field at temperatures from 1230°C up to 1300°C until reaching 95 – 99 %TD. After heat treatment the samples were cut, polished and thermally etched before being examined by SEM. Data from the latter Link et al. to measure the maximum extension of the pores in the direction parallel $d_{\parallel E}$ and perpendicular $d_{\perp E}$ to the orientation of the electric field. After this they fitted an equivalent ellipse of the pores and measured the angle between a horizontal line perpendicular to the electric field and the large axis of the ellipse. They found the ratio $d_{\perp E}/d_{\parallel E}$ increased with sintering temperature, which was equal to an increase microwave power used, i.e. a higher E field. Further, for their microwave sintered samples they found a higher number of pores aligned perpendicularly towards the electric field compared to the conventionally sintered sample, where no trend was visible. This they concluded to be a strong evidence of the non-thermal effects of microwaves and the anisotropic shrinkage of pores [108].

2.6 Conclusion of the microwave effect theories and objective of the present work

The above experiments all indicate that the theory of the ponderomotive forces is the explanation for the “microwave effect”. However during their experiments at Oak Ridge Laboratory, Janney et al. [102] not only suggested that a reduction of the activation energy is accountable for the effects of the microwaves. They also found that the use of microwaves lead to a different structural development, where the open porosity remained open longer. As described above, the idea that microwave heating reduces the activation energy was quickly rejected. However until now there has been no confirmation or disproval of the different structural development described by Janney et al. The refined model of the ponderomotive force by Booske et al. [109] and the anisotropic pore shrinkage demonstrated by Link et al. [108] indicate that there could be an effect of microwaves on the closed porosity, which could lead a difference in the structural development. In this structural development, microwaves would affect the closed porosity and could lead to shrinkage of the closed porosity at the same time as the open porosity. Further the open pores could shrink more within the ceramic and less towards its surface. This would mean the open pores remain open longer during the sintering process but the open pores would be only to a shallower depth. The shrinkage of the total pore volume at the same time could create a similar effect as observed for the “microwave effect”.

Objective of this work:

1) Sintering ZnO samples under conventional and hybrid heating with various amounts of microwaves and different sintering times until a maximum density is reached of ~90% of the theoretical density
2) Measuring sample density and determine the samples’ open porosity using nitrogen adsorption and mercury porosimetry
3) SEM investigation of the samples’ microstructure (surface and cross-section)
4) Compare results with hypotheses

Hypotheses for the effect of microwave on the development of the porosity:

1. The sintering behaviour is the same for conventional and hybrid sintering and the difference in the densification is caused by an enhanced matter transport via

diffusion. This enhancement can only be caused by an external driving force, such as the ponderomotive forces described by Bykov et al. [106]. The development of the porosity would be not affect by the microwaves.

2. Since the microwaves heat the sample from the inside and conventional heating from the outside, the whole sample could sinter at the same time. This would mean that no heat transport is required to sinter the centre of the samples and the closed porosity would be reduced at the same time as the open porosity. This means a greater volume of open porosity would remain at higher densities.

If diffusion enhanced, confirmation by solid-state reaction of ZnO and alumina

3 Experimental

3.1 Experimental Procedure

3.1.1 Selected Materials

The primary material selected for both the sintering and solid-state reaction experiments was a submicron zinc oxide from Sigma-Aldrich with a high dielectric loss. It was 99.5% pure, had a theoretical density of 5.606 gcm^{-3} and an average particle size of 0.12 µm. Since the ZnO powder was the same as Wang [29] used for his experiments, his measured value for the dielectric loss could be used and was tan δ~0.24 at 2.45 MHz. The second material for the solid-state reaction experiments was α-alumina from Baikalox. It had a theoretical density of 3.96 gcm^{-3}, an average particle size of 0.17 µm and a high purity, high enough to be used for production of transparent ceramics as the main application according to the manufacturer (purity min. 99.99%). A nano magnesia form Sigma-Aldrich, which had particle size of <50 nm and theoretical density of 3.58 gcm^{-3}, was also used for the solid-state reactions.

3.1.2 Porosity experiments

Sample preparation

The ZnO powder was placed in an oven at 60°C over night to minimise the moisture content, because ZnO is a natural desiccant and the amount of moisture has an effect on the sintering properties of ZnO. Subsequently, the powder was placed in a desiccator to cool down, before it weighted and pressed with a hydraulic press without any additives such as lubricants into 3 mm thick pellets using a hardened steel die with a diameter of 6 mm. For each pellet, 0.28 g powder and a pressure of 61.8 MPa were used. The green density of these samples was calculated from the sample size and mass using the equation

$$\rho = \frac{4m}{\pi d^2 t} \qquad (3.1)$$

Where *m* is the sample weight, *d* is the diameter of the sample and the thickness of the sample is *t*. Using the value for the theoretical density of zinc oxide of 5.61 gcm^{-3}, the relative density of all of the pellets produced was 51±1%.

Sintering

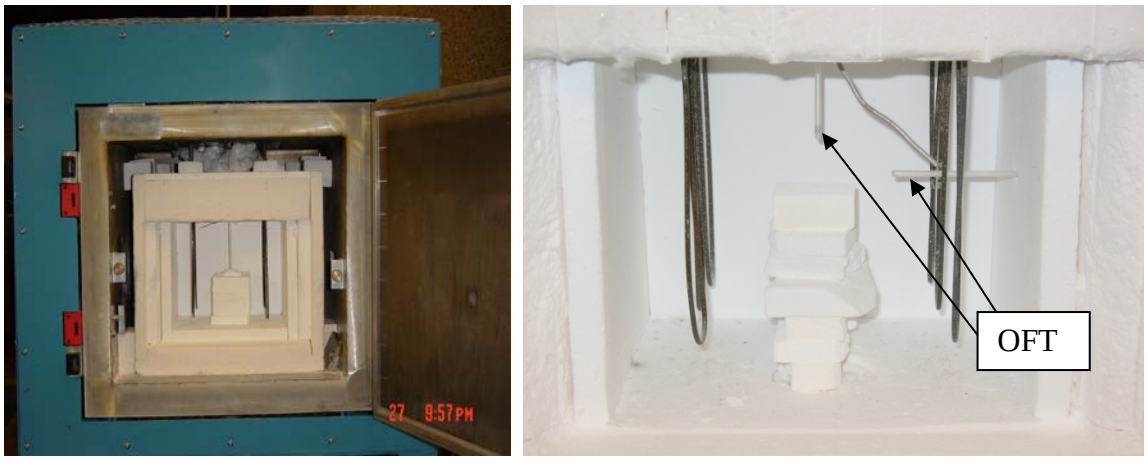

(a) (b)

Figure 82 Hybrid furnace showing (a) front view and (b) furnace space with placement of the OFT (mode stirrer is obstracted by the alumina fibre insulation)

The furnace used for the sintering, Figure 82a, was a hybrid furnace from C-Tech Innovation Ltd UK, which was specially designed to operate simultaneously with microwave and conventional heating. It consisted of a magnetron, waveguide, cooling system, circulator, microwave tuner and hybrid microwave cavity. The cavity was made of a metallic box, a mode stirrer and alumina fibre insulation material. The conventional heating was provided by 6 $MoSi_2$ heating elements. The magnetron produced up to 1.2 kW of 2.45 GHz microwave power. A separate Eurotherm controller controlled the conventional and microwave heating. The control over the heating and that it followed the programmed temperature was achieved by the Eurotherm controller for the conventional, which could automatically change the level of the used furnace and with it indirectly the sample temperature. For the microwave

power, a constant level microwaves were applied from a given point until it was switched off.

Optical fibre thermometers (OFT), Figure 82b, (M10 and M100, Luxtron, USA), which measured the surface temperature of the samples in two locations, viz the top and side, were used for temperature measurement.

Initially for a sintering run, 3 pellets were placed in a diagonal line with the centre pellet directly under the OFT. Unfortunately, the magnetron broke down part-way through the series of experiments, after this the experimental setup was changed into a stack of 4 pellets directly under the OFT. This change of the experimental procedure was required to keep the densities of sintered samples equal because after change of the magnetron the density for samples sintered using the first experimental procedure did not reach the densities from before the change. A reason for the change in the sintering behaviour can be change in the magnetron frequency since magnetrons are produced with a tolerance within their operating frequency. As discussed in section 2.4.2, the frequency of the microwaves has an effect on the on the power absorbed per unit volume and can cause a change in the heating/sintering behaviour.

All samples were initially held at 500°C for a period of 1 hour as the first stage in the sintering cycle. This was necessary to ensure thermal equilibrium was reached before the significant part of the experiment began. The second reason for this procedure is that the OFT's did not monitor temperatures below 450°C.

After the 500°C dwell time, the samples were heated at 20°C min^{-1} to the sintering temperature. The first test sintering temperature was 700°C for 3600 s as used in previous works at Loughborough University. Later the sintering temperature was increased to 800°C and held for periods of 6, 900, 1800, 2700 and 3600 s before the samples were cooled through the natural heating loss in the furnace to room temperature. Initially the heating was also stopped during the heating stage at 600°C and 700°C, because the previous dilatometer investigations of Wroe and Rowley [33] and at Loughborough University [29, 30] indicated that microwaves had a direct and immediate effect on the shrinkage, see Figure 79 in section 2.5.4. Since the

shrinkage increased as soon as the microwaves were used it is possible that the porosity would also be affected since the reduction of the porosity is the cause for the shrinkage and densification of ceramics.

After the break down and replacement of the magnetron and the change of the experimental setup, a new holding time of 1350 s was introduced, because the density difference at 1800 s was too different from the achieved at 900 s and the extra holding time allowed a more detailed investigation of porosity in the intermediate sintering stage.

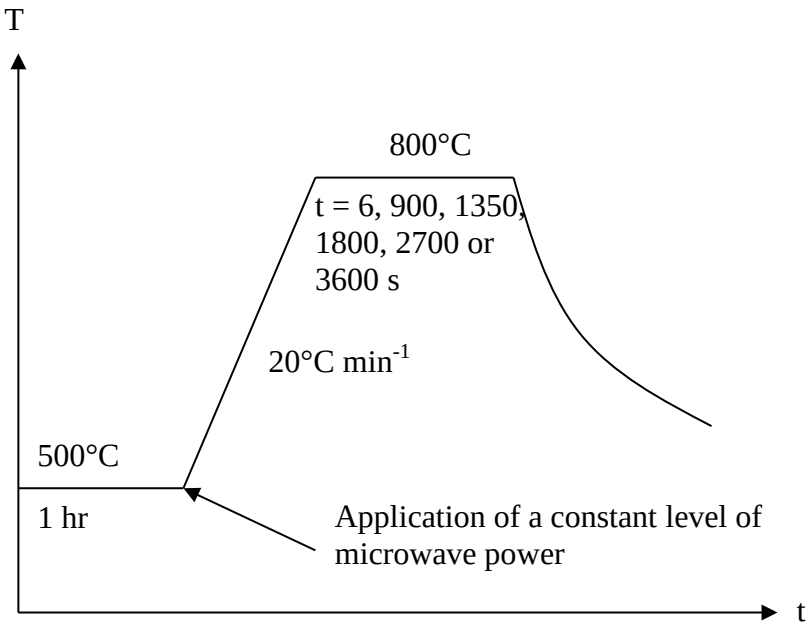

Figure 83 Heating cycle used

Throughout all of the sintering experiments, hybrid heating was used in which 0, 200, 400, 600 and 800 W of microwave power were used, combined with sufficient conventional heating to achieve the time-temperature profile illustrated in Figure 83 and 84.

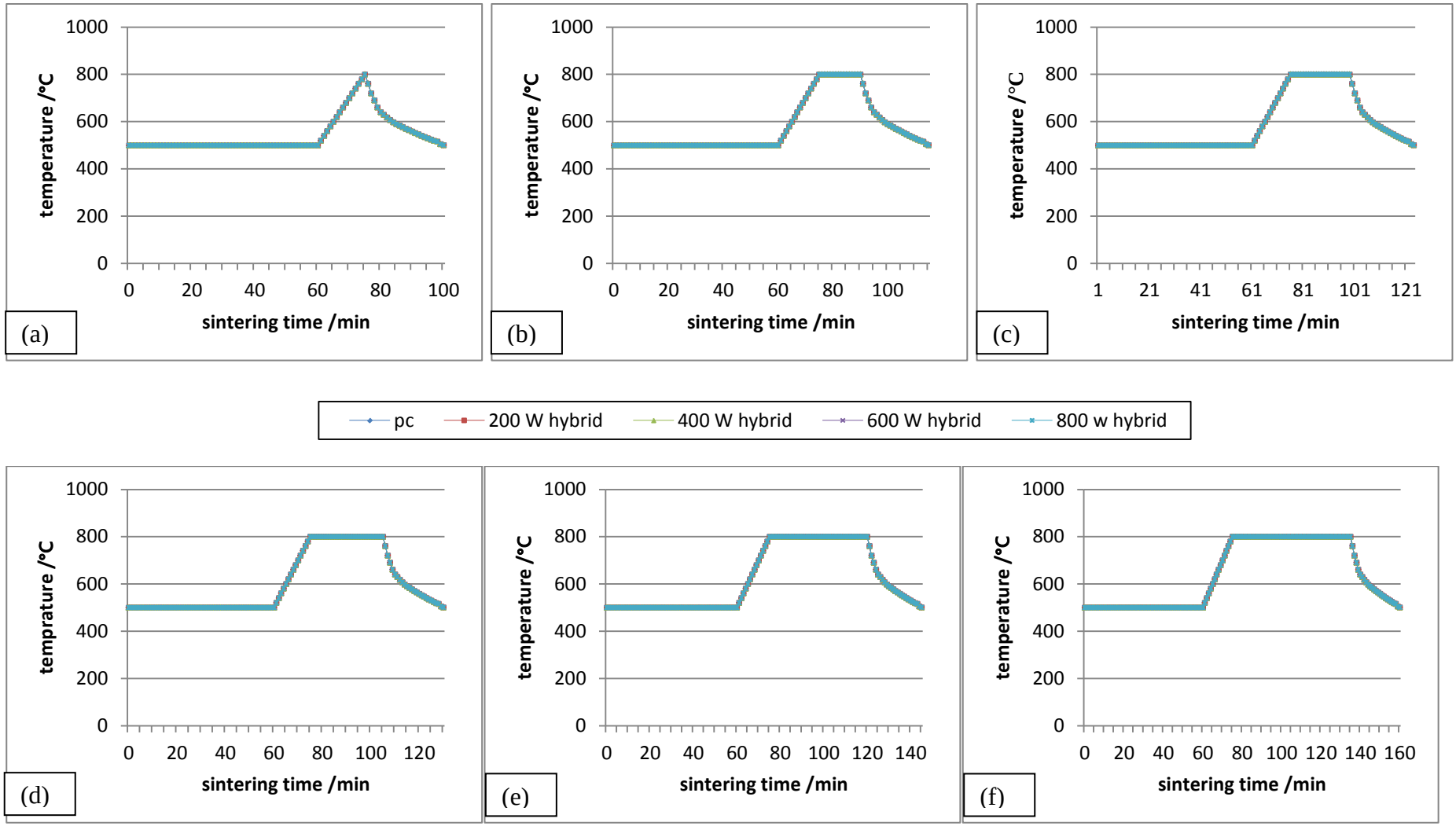

Figure 84 Heating cycle used to sinter ZnO for (a) 6 s, (b) 900 s, (c) 1350 s, (d) 1800 s, (e) 2700 s and (f) 3600 s

Characterisation

At the end of each sintering cycle, the density and the open porosity were measured. The density values were calculated from the sample size and mass using equation 3.1.

The open porosity in the samples was measured using a Micromeritics TriStar 3000 nitrogen adsorption unit for porosity <200 nm in diameter; a Micromeritics Poresizer 9310 mercury porosimeter at Loughborough University and a Micromeritics AutoPore IV 9510 mercury porosimeter at Nottingham University for the larger pore sizes (up to 360 μm). For the latter, the penetrometer was chosen by assuming that the total porosity was equal to the open porosity. This overestimation of the porosity ensures that the intrusion volume was large enough for the measurement. Thus, the penetrometer selected had an intrusion volume of 0.366 cm^3 and a sample cap of 5 cm^3, because of the small volume and size of samples.

Nitrogen adsorption

For the nitrogen adsorption testing all the samples for a given set of sintering runs were used, because the test is non-destructive and the higher number of samples increased the measurable pore volume and with it the accuracy. A test tube was initially placed with its holder on a balance and tared; the samples were then placed into the test tube and their mass recorded.

Before inserting and sealing the test tube in a measuring port, a fill rod was inserted into the tube and a thermal jacket was placed around it and pushed down until it contacted the ball, which contained the samples. Then the tube was sealed tight by hand in the measuring port and the required information for the samples were input into the program for the corresponding measuring port. Further, it was important to confirm if the gas support/bottles were open. At this point the program could be started and unless there was problem it ran automatically until the measurement was finished and the results were presented as a report (for detail see appendix).

Mercury porosimetry

Since the samples could not be used after the mercury porosimetry test, because they were contaminated with mercury, at lower densities only a maximum of 2 pellets per sintering run were used for testing. This ensured that at least 1 pellet remained for further testing. At r densities 80% of theoretical, all the pellets had to be used to avoid that the available pore volume dropped below the measurable pore volume.

Initially the Micromeritics Poresizer 9310 mercury porosimeter was used at Loughborough University. The test samples were weighed and filled into the penetrometer and sealed inside it. Then is the penetrometer was placed in the low pressure chamber of the porosimeter and evacuated. As soon as the machine showed that the required vacuum (~0.005 MPa) was reached the evacuation was switched off and the button for filling of the penetrometer with Hg pressed. This button was held until the machine indicated that enough Hg was filled into the penetrometer. At this point the first readings (pressure and intrusion as capacity) were recorded. Then the pressure was increased in steps until it reached a pressure of ~0.15 MPa. At every step the pressure and the intrusion were recorded.

After the pressure was reduced back to atmospheric pressure the penetrometer was placed in the high pressure port. There the pressured was increased via switching on and off a switch in steps, where the same readings as before were recorded, until the measurement was finished or the high pressure warning was signalled by the machine. After reducing the pressure back to atmospheric level the penetrometer was removed from the high pressure port and cleaned according to the manual and the test samples safely disposed of. Finally, the recorded values could be converted into pore size and pore volume, see Appendix.

After the Micromeritics Poresizer 9310 mercury porosimeter at Loughborough University could no longer produce the required pressure for the test the test series was continued at Nottingham University with the Micromeritics AutoPore IV 9510 mercury porosimeter. The results of both machine can be seen as equal, because the both the same measuring principal was used and only the degree of automation

was different. For this equipment it was required to run a blank run, without samples, of the penetrometer as a calibration/control run before every measurement series.

After the blank run the penetrometer was cleaned, dried and filled with the weighted samples. Then the penetrometer was sealed and placed in the low pressure chamber and the program started. As soon the penetrometer was filled with Hg, the program required that the filled penetrometer was removed from the low pressure chamber and weighed again. After the penetrometer was placed back into the low pressure chamber and the weight entered into the program the measurement continued automatically until the penetrometer had to be shifted to the high pressure chamber. As soon as it was confirmed that the penetrometer was in the high pressure chamber the automatic measurement resumed. As the measurement was finished the results were presented as a report (for detail see appendix).

Because both pore size measurements are based on the assumption that the pores were spherical, the Field Emission Gun Scanning Electron Microscope (FEGSEM) (LEO 1530VP, Carl Zeiss SMT, Oberkochen, Germany) was used to investigate the pores at the sample surface. In addition to the surface analysis, the FEGSEM was used to investigate cross-sections of the samples and with it the internal microstructure.

3.1.3 Solid-State Reaction

$MgO\text{-}Al_2O_3$

Sample preparation

Wet forming route

For the slip casting 15 wt% ethanol suspensions of MgO and Al_2O_3 prepared and mixed together. A block of plaster of Paris was prepared and a disk of polyvinylchloride with 6 mm diameter holes inside was place on top of the flat surface of the plaster block and fixed with bar clamps, Figure 85. After this the suspension

was poured carefully into the mould to avoid air bubbles. After the cast was hardened it was dried at 110°C until it's mass did not change.

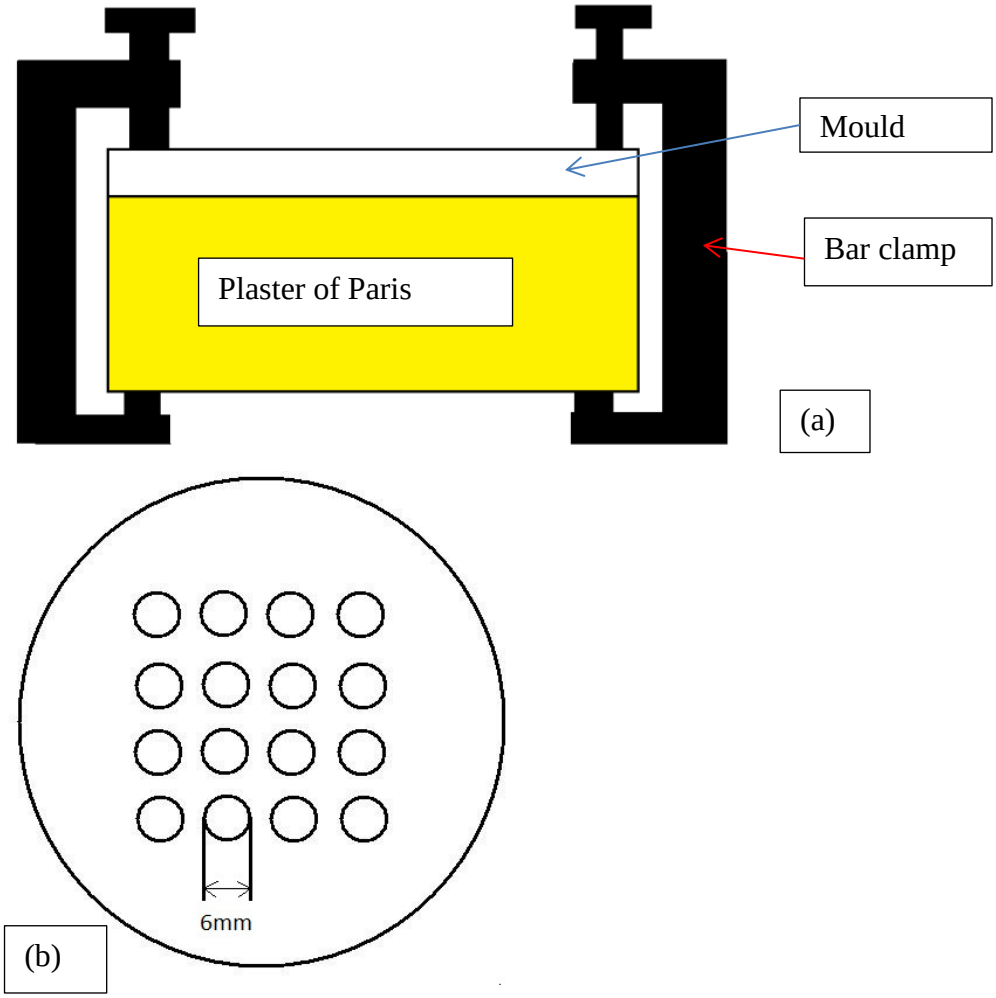

Figure 85 Arrangement (a) and mould surface (b) for slip casting

Zeta potential

The Zeta potential is a measure for the electrical double layer around dispersed particles in liquids. This double layer can be generated by excess charges on the particles surfaces due to the electrostatic forces between the particles. The zeta potential of the suspension was measured to determine if the suspensions were stable or not. For this a 5 wt% ethanol suspension of MgO and Al_2O_3 were produced and the zeta potential measured with an AcoustoSizer II (Colloidal Dynamics, Sydney, Australia). The measurement was undertaken by Mr. Lau at Loughborough University. During this measurement the pH was changed by dosing in small quantities of either

HCl or NaOH solutions to achieve the desired value by decreasing or increasing the pH respectively. An equilibration time of 180 seconds was used to ensure that the pH modifier was mixed homogeneously within the system before every zeta potential measurement at the different pH values

Dry route

For the dry route, 1.434 g of Al_2O_3 and 0.566 g of MgO powders were mixed with 6 g of hexane. This mixture was filled, together with ZrO_2-balls into a 25 ml plastic bottle and ball milled for 21 h. After ball milling the mixed powder was dried and die pressed with a pressure of 70 MPa into 10 mm diameter pellet.

Creating an interface

For the experimental involving interfaces 0.3 g of MgO powder were die pressed using 12.7 MPa into 10 mm diameter pellets. As the powder caused problems during the filling of the die, it was agglomerated by mixing it with hexane and drying prior to pressing. Since some of the die pressing problems continued as a solution for these 0.1 g of alumina powder was placed into the die before the agglomerated MgO and then a further layer of 0.1 g alumina powder was placed on top. The die pressing was done with same pressure as before and this resulted into the production of MgO powder pellets with a layer of alumina powder on each side.

This MgO pellet was placed centrally on a powder bed of 2 g of alumina in a 25 mm diameter die. After the placement a further 4 g of alumina was poured into the die to cover the core sample and a pressure of 40.74 MPa was used press the powder to yield the shell-based structure shown in Figure 86b.

ZnO-Al_2O_3

Sample preparation

The solid state reaction investigation required a reaction interface at which the reaction between ZnO and Al_2O_3 took place. Possibilities to create the interface were:

- ZnO and Al_2O_3 layer pressed together
- Shell and core
- Green ZnO and Al_2O_3 pellets stacked on top each other
- Sintered and polished ZnO and Al_2O_3 pellets stacked on top of each other

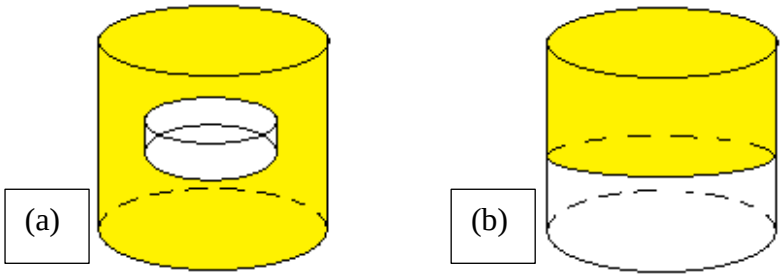

Figure 86 Sample arrangement for (a) shell and core and (b) stacking or layer pressed sample arrangement

The die pressing for these samples were done with a hydraulic press without any additives, such as lubricants. The ZnO powder was dried overnight as for the porosity experiments.

ZnO and Al_2O_3 layer pressed together

For this 1 g of ZnO was placed into 10 mm diameter die and 1 g of alumina was placed on top of the ZnO. After both materials were in the die a pressure of 70 MPa was used to compact them.

Shell and core

For the shell and core interface, see Figure 86a for the MgO- Al_2O_3 systen one of the materials, ZnO or Al_2O_3, was die pressed into a 10 mm diameter pellet as the ‘core’. For this 1.5 g of ZnO and pressure of 70 MPa or 1 g of alumina and pressure of 76.4 MPa was used. For the shell, 2 g of powder of the material that was not used for the core was placed in a 25 mm diameter die as a powder bed. After this the core sample

was place as centrally as possible on the powder bed and covered by 4 g of powder of the shell material. After these preparations were finished everything was pressed with pressure of 40.7 MPa.

Green ZnO and Al_2O_3 pellets stacked on top each other

In this case the sample preparation was the same as for the core sample by the shell and core samples. The green density of these samples was calculated from the sample size and mass using equation 3.1.

The densities of the samples were 52±1% of the theoretical density for Al_2O_3 and 54±1% for ZnO. The sample density was calculated by the use of the measured sample geometry and mass via equation 3.1.

Sintered and polished ZnO and Al_2O_3 pellets stacked on top of each other

In this case the green bodies of the previous idea were sintered to high densities. For the sintering both materials were heated in the hybrid furnace to 500°C, where the temperature was held for 1 h. After the holding time ZnO was heated at 20°C min^{-1} to 800°C and the temperature held for 1 h. For the Al_2O_3 a heating rate of 5°C min^{-1} was used to increase the temperature to 1400°C. This temperature was held for 2 h.

The densities of the samples were 98±1% of the theoretical density for Al_2O_3 and 95±1% for ZnO. The sample density was calculated by the use of the measured sample geometry and mass via equation 3.1.

Sintering

The equipment to heat the samples to the required temperature for the reaction was the same as for the porosity experiments.

MgO-Al_2O_3

The shell-core sample was heated to 500°C. There temperature was held for 1 h. After the holding time the temperature was increase by 10°C min^{-1} to 1450°C and held for 2 h. However it was found that when using pure conventional heating, the desired heating rate could not be maintained at temperatures higher than 1300°C. Therefore the heating rate was reduced to 5°C min^{-1}. This setup was used the sinter samples with pure conventional and 800 W hybrid heating.

ZnO-Al_2O_3

All test samples designed with internal interfaces were placed with the ZnO on top, Figure 87, in the furnace. The reason for this is that ZnO is a very good microwave absorber, which makes it possible to heat it only with microwaves at room temperature. However this characteristic also has a risk, at higher temperature the absorption properties increase for ZnO and its heating rate will increase and can lead to thermal runaway, see section 2.4.3. Therefore the ZnO was placed on top so that the OFT monitored the temperature of the ZnO so that the control program was able to avoid thermal runaway by controlling the furnace power. The alumina side of the samples was marked so that it was ensured that the ZnO always faced the OFT. The sample stage was made of porous alumina, to minimize the effect of microwaves on the stage and limit the heat transfer form or into the samples. After the placement, the samples were heated, as for the porosity experiments, to 500°C and held at this temperature for 1 hour as the first stage in the sintering cycle.

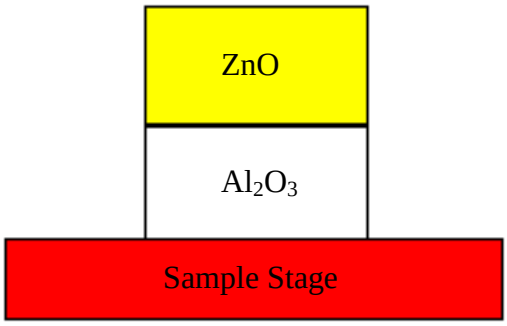

Figure 87 Sample arrangement for solid-state reaction

After a thermal equilibrium was ensured, the samples were heated at 10°C min^{-1} to 1200°C and held for a period of 2 h before the samples were cooled through the natural heating loss in the furnace to room temperature.

For the continuation of this investigation it was decided to use the idea of stacking green pellets of the raw materials for the reaction. Further the heating rate from 500°C to the reaction temperature was reduced to 5° C min^{-1}. The reaction temperature was increased to 1300°C and 1400°C. The holding times of these temperatures were for 5 h at 1300°C and 4.5h at 1400°C.

After it was found that previous reaction sintering were solid-vapour and not solid-state reactions, the heating rate was increased to 10°C min^{-1} and the reaction temperature was reduced to 1100°C. This temperature was held for periods of 1, 2.5, 5, 10 and 15 h before the samples were cooled through the natural heating loss in the furnace to room temperature.

Throughout all of the reaction experiments, hybrid heating was used in which 0, 800 or 1200 W of microwave power were used, combined with sufficient conventional heating to achieve the time-temperature profile illustrated in Figure 88 and 89

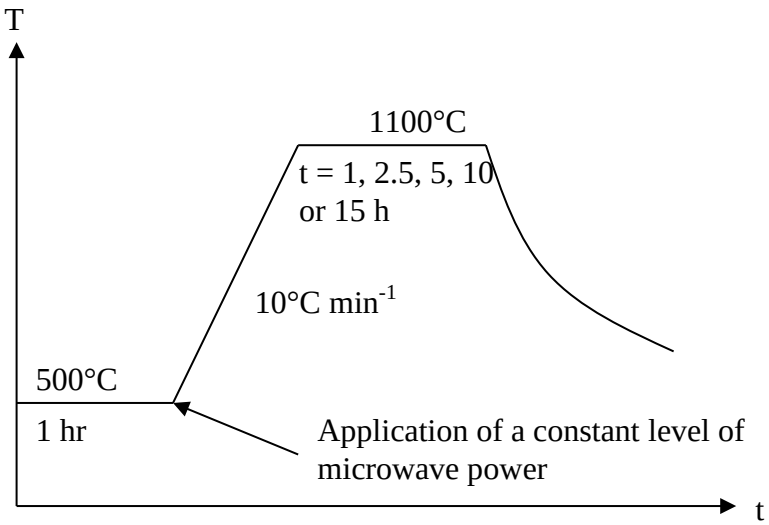

Figure 88 Heating cycle used

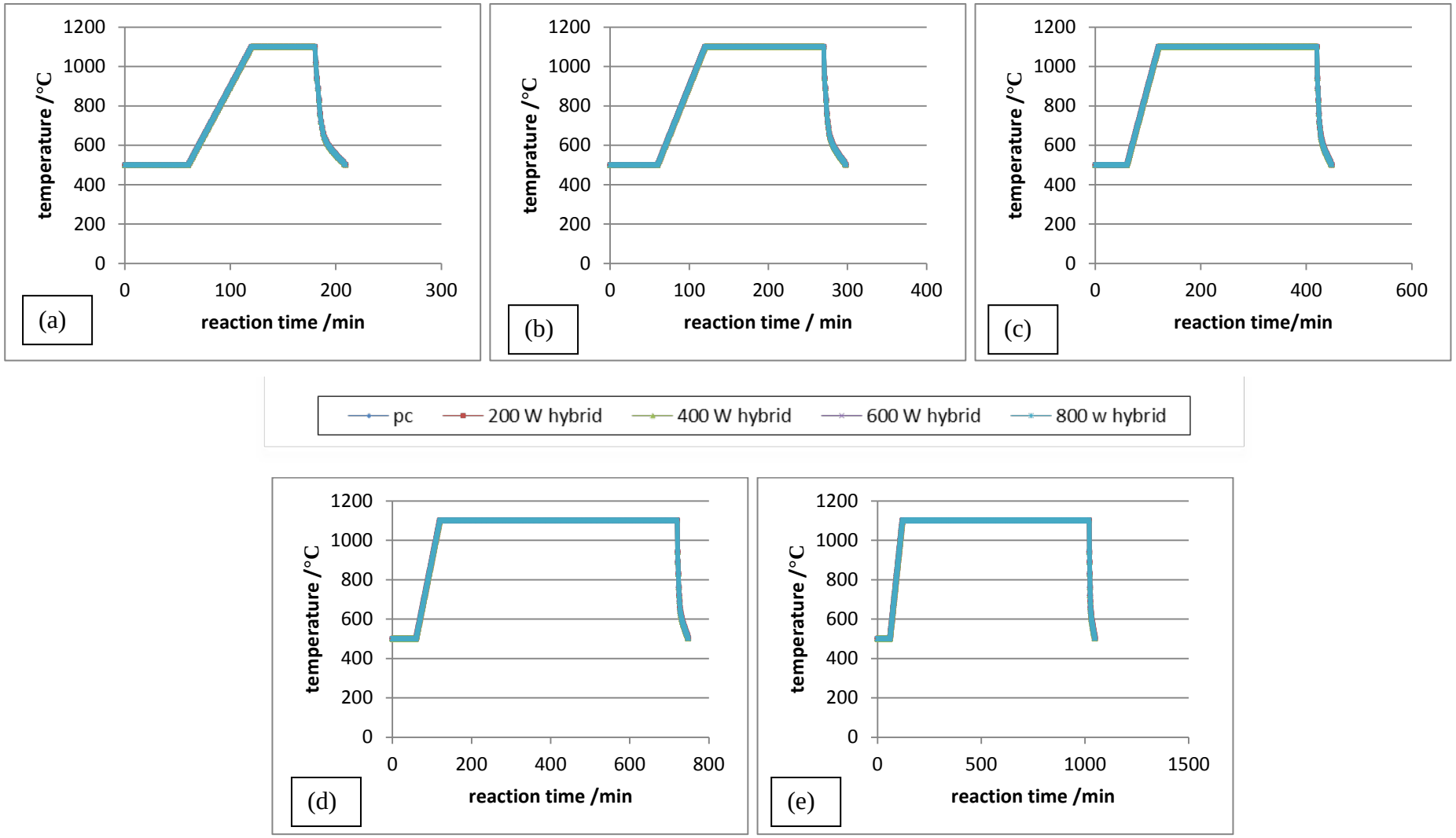

Figure 89 Heating cycle for the solid-state reaction of ZnO and alumina for (a) 1h, (b) 2.5 h, (c) 5 h, (d) 10 h and (e) 15 h used for investigation of the effect of microwaves on the solid-state reaction

Characterisation

For the electron microscope investigation, the samples were cross-sectioned perpendicular to the interface by a diamond cutting blade.

Back-scattered electrons scanning electron microscopy (BSE-SEM)

The use of back-scattered electrons (BSE-SEM) allowed easy identification if a different material was created. This is possible because the intensity of the signal of the back-scattered electrons primarily depends on the average of the atomic number of the material. The strong back scattering of heavy elements creates a bright area whilst the darker areas indicate lighter elements. For the system ZnO- Al_2O_3 for example, the use of BSE-SEM creates a very bright area, almost white, for ZnO, a dark grey area for Al_2O_3 and a light grey area for the reaction product.

Energy-dispersive X-ray spectroscopy (EDS)

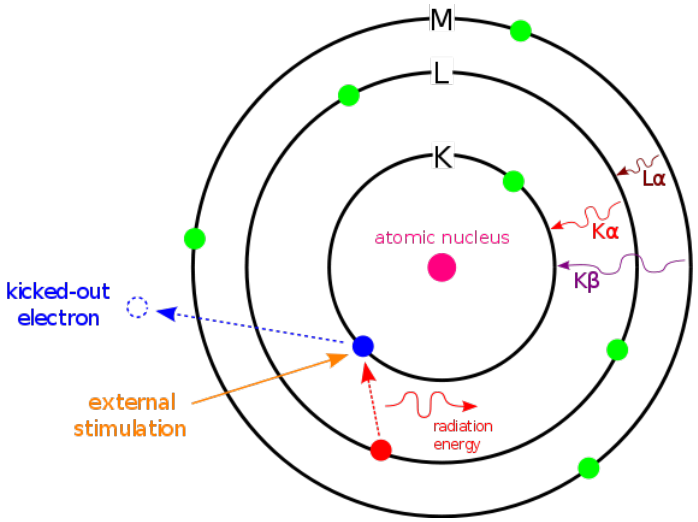

Figure 90 Principle of EDS [110]

Energy-dispersive X-ray spectroscopy (EDS) mapping was used to confirm the formation of the spinel. This technique uses the effect that the electron beam in the FEGSEM ejects an electron from an inner atomic shell. The resulting vacancy is occupied by an electron from a higher shell and in doing a characteristic X-ray is emitted that a detector can register. This characteristic X-ray radiation can be used

determine the presence and position of elements in a sample. For the spinel Zn/Mg, Al and O must present in a single area.

After the identification that a reaction layer was created, the thickness of the layer was measured with the help of printed back-scattered electrons pictures. The results of these measurements allowed the calculation of the experimental reaction rate constant K by using formula 2.6 and transposing it to yield:

$$K = \frac{y^2}{t} \tag{3.2}$$

where y is the thickness of the reaction layer in m and t is the reaction time in s.

The average of these reaction rates was used to calculate an average experimental reaction rate.

4 Results and Discussion

This chapter is separated into 2 major parts. The first is about the densification of ZnO and is divided into 3 smaller sections; the first covers the properties of the green bodies, the second is about the influence of microwaves on the sample density during sintering, whilst the last part is the investigation of pore development during sintering. The investigation of the effect of microwaves on the solid-state reaction between ZnO and alumina forms the second major part for this chapter.

Green body characterisation

Figure 91 and 92 show the typical porosity distribution for the open pores within the as-formed green bodies, as measured using nitrogen adsorption and mercury porosimetry respectively.

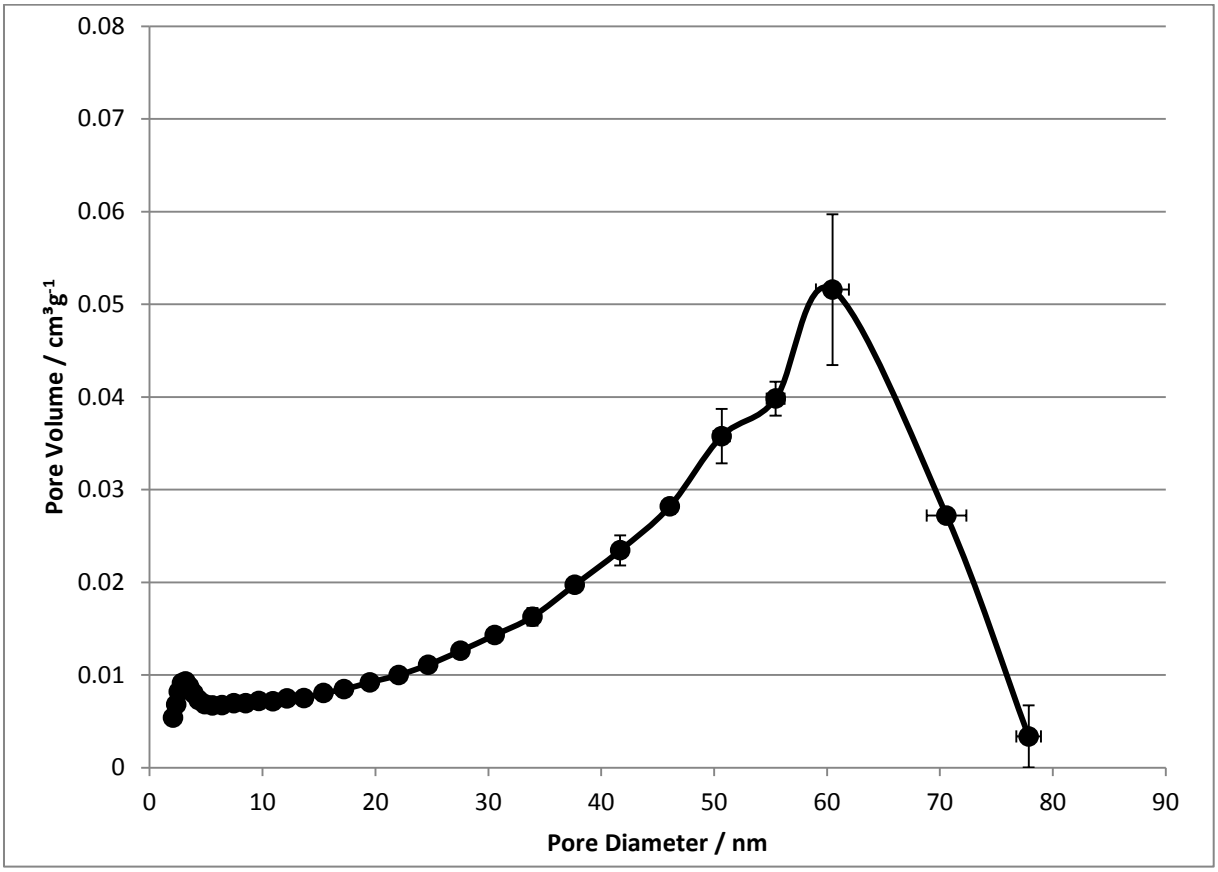

Figure 91 nitrogen adsorption porosity curve for green ZnO samples

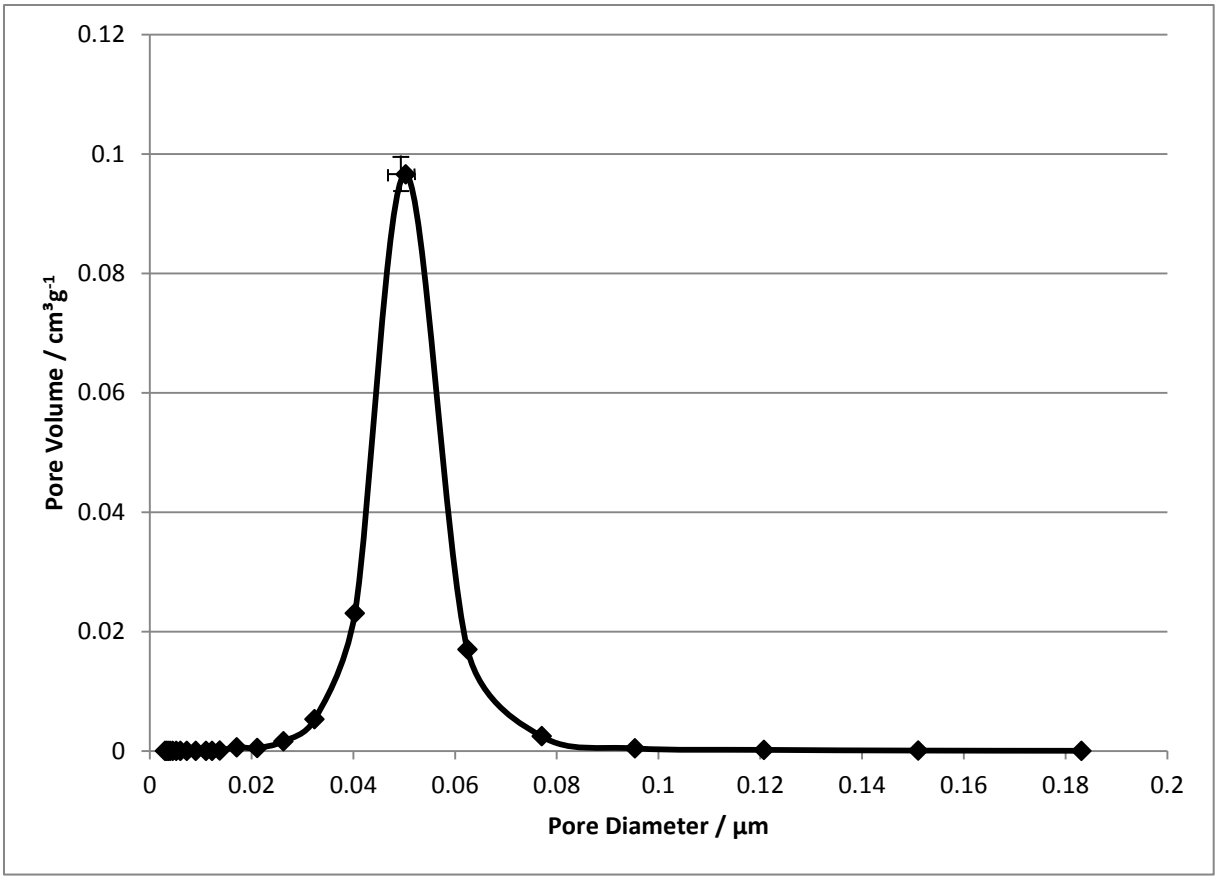

Figure 92 Mercury porosimeter porosity curve for green ZnO samples

There are 2 maxima in the pore size distribution. The smallest in size and amount occurred at around 3 nm with a volume of 0.01 cm^3g^{-1}; these are mesopores, they were only detectable using the nitrogen adsorption technique. The second and much larger, maxima occurred at around 50 - 60 nm with a volume of 0.05 - 0.1 cm^3g^{-1}. Both techniques detected these macropores, though the absolute volumes measured differed between the two techniques due to the different principles involved, see section 3.1.2.

Effect of microwaves on the densification

One aim of this project was it to keep the approach as close as possible to the previous work at Loughborough University [29, 30], although the sintering temperature for this investigation was increased to 800°C. There several reasons for this increase. One was that the pure conventional sintering of the 6 mm diameter and 10 mm diameter samples, which were equal in size and density to the previous samples [30], at 700°C for 60 min led to a lower sintering density ~60% of theoretical

density than during the previous investigations, which were ~66% [29] and ~70% of theoretical density. The most possible causes of this difference is the aging of the furnace.

The main reason for the increased temperature, however, was the need to achieve a higher density for the samples that were sintered using pure conventional heating, A sample that was about 60 – 70% dense would be just at the beginning of the intermediate sintering stage, which has a higher influence on the porosity than the initial sintering stage. Therefore, the density to be achieved needed to be at around 90% of theoretical density, where the intermediate sintering stage changes into the final stage. The increase in density could be achieved by two different approaches. The first was to keep the temperature constant and increase the sintering time so that densification could progress further. The risk of this method is that if the chosen sintering temperature is too low than the densification would stop before the desired density is reached because the induced driving forces were too low for further densification and so only coarsening would be achieved. The second method is to increase sintering temperature and with it the degree of diffusion. This leads to higher densities in a shorter time, see section 2.2.1. However, if the sintering temperature is too high, it could lead to volatilization for ZnO, or to abnormal grain growth due to oversintering.

In consideration of the usage of the hybrid furnace it was decided to increase the sintering temperature to 800°C. At this temperature the purely conventionally sintered samples had a density of ~88%. This was considered as acceptable, because it is at the end of the intermediate stage however the open porosity would still be measureable; open porosity is typically eliminated at somewhere around 95% of the theoretical density.

For the variation of the microwave power, it was initially planned to raise it from 0 to 1000 W in steps of 200 W. In practice, the maximum used was stopped at 800 W, because after 60 min sintering at this power the density of these samples was 94% of the theoretical density. This was very close to the point where the residual porosity becomes closed, with such porosity it would be very difficult to analyse the changes occurring.

After these initial problems were solved the required samples for the investigation of the effect of microwave on the porosity were sintered and their density was recorded for all heating conditions and sintering times to confirm that microwaves influenced the samples and increased their densities as the microwaves power level increased. This would ensure that anything observed during the investigation of the porosity could be linked back to the use of microwaves. The results are displayed in Figure 93a.

As the investigation was in the phase of repeating and confirming results the hybrid furnace suffered a breakdown of the magnetron. As the magnetron was replaced the sintering of the remaining samples was resumed. However the density of the new sintered samples was suddenly lower for the 800 W hybrid heated samples, from ~94% to ~82% of theoretical density. At first the existing experimental arrangement was continued and the height of the samples in the furnace was varied in case the location of the maximum electric field changed. However during all of these experiments the density of the sintered samples remained lower than before the magnetron change. Therefore it was decided to change the experimental procedure. Now the samples were positioned as a single stack below the OFT and the number of the samples used was increased to 4. After this the densities of the sintered samples were equal or at least very similar to the values as before the change of the magnetron, see Figure 93b.

Since the experimental procedure was changed, even when the densities were equal it could not be assumed the effect of the microwaves on the porosity was the same. Therefore the whole experimental series had to be repeated. During the repetition of these experiments an addition sintering time of 22.5 min was introduced. The decision had already been made before the technical problems, because the density results and initial porosity data suggested that an extra data point at around this time would help to reveal the shape of the curves.

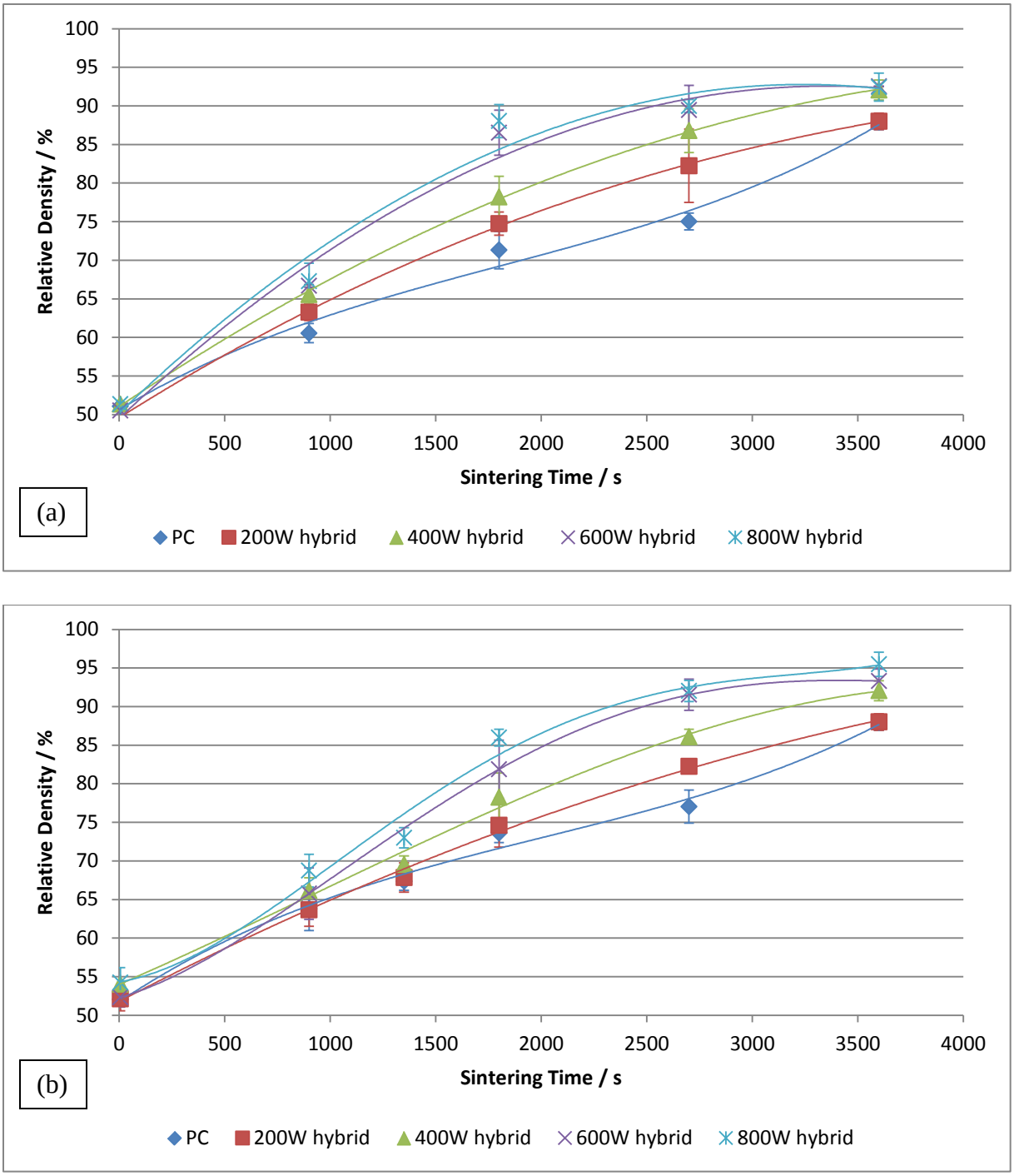

Figure 93 Densification curves at 800°C for ZnO under a range of microwaves power levels but the same heating profiles, (a) before and (b) after change of the magnetron and experimental procedure

As already indicated, Figure 93 compares the densification curves for pure conventional and hybrid heating with different levels of microwave power before and after the change of the magnetron and experimental procedure. The measured densities are in the most case within the margin of error. The only major deviation was the density for the 600 W hybrid sintered samples after 1800 s. For an unknown

reason, the samples sintered with the newer experimental procedure had a 5% lower density at this point of the sintering.

Nevertheless in both cases the behaviour of the densification was similar and as the temperature-time profile was the same, ±2°C, for all samples for each experimental procedure; this leaves only the amount of microwaves used during these sintering runs as being responsible for the differences in density. After 6 s the density difference between the sintering conditions was very small, as expected. Densification had hardly begun and the samples were all, effectively, still green bodies. As the sintering time increased, a density difference between the samples sintered with different microwave power level appeared. This increase resulted in the largest density differences at 1800 s and 2700 s, where the pure conventional sintered samples had just entered the intermediate sintering stage whilst the 800 W hybrid sintered samples had almost reached the final sintering stage. At even longer sintering times the trend in the densification rate changed and the difference in the densities between the different sintering conditions decreased again.

This enhancement of the densification in the initial and intermediate stage of sintering has been observed before by Samuels and Brandon [92], Brosnan et al. [97], Wang [29] and others. In particular, the density curves are very similar to those reported by Wang, Figure 70, who used the same sintering equipment and approach. Both sets of results, Figure 70 and 93 , show a rapid increase in the density for samples sintered with significant amounts of microwaves until around 90% of theoretical density, when the rate of sintering decreased significantly as the final sintering stage was reached.

In addition to the enhancement of the densification, a comparison of the densification curves also confirms Wang`s observation [29] that a minimum amount of microwave energy is required to enhance the densification, Figure 71. In Wang's project, the critical amount of microwaves was 600 W. However in this project even 200 W microwaves achieved an increase in densification at the intermediate stage. This decrease down from 600 W is easily explained even though the equipment was the same, since Wang used a sintering temperature of 680°C whilst the present work

800°C was used. This increase in sintering temperature by 120°C leads to an increase in tan δ, i.e. the materials' ability to absorb microwaves is increased. Therefore in the present work even a relatively small amount of microwaves had an effect on the densification.

All this confirms that these samples were affected by the use of microwaves; however, the question that remains is why the densification is increased during microwave sintering in the initial and especially intermediate sintering stages but less so in the final stage.

During the initial phase, Figure 28, the particles are rearranged and necks between particles are formed. The change in the density of the body during this stage is small compared to during the intermediate stage, when the grain boundaries grow rapidly, Figure 29. The results in Figure 93 indicate that the microwaves are clearly predominately affecting the growth of the grain boundaries, rather than their formation. The 200 W hybrid sintered samples are a good example for this, because after 900s their curve in Figure 93 follows that for the pure conventional sintered samples. However, once the intermediate stage was reached, the curves for the pure conventional and 200 W samples separate and the effect of the microwaves becomes noticeable. At higher microwave levels, the effect is noticed sooner, Figure 93, since the process of densification is accelerated. Evidence for the latter is that the temperature-time profile for all the samples was the same, ±2°C, throughout the sintering process. Towards the end of the sintering schedule, however, the magnitude of the 'microwave effect' decreases, Figure 93, as has been observed before [27, 92, 97].

There are 2 possible explanations for the behaviour outlined above, though they are not mutually exclusive. The first is based on the need for interfaces if the ponderomotive forces are to achieve a significant effect. If the grains grow, as happens in the final sintering stage, then the number of interfaces decreases and hence so does the ponderomotive forces. The other possible explanation is the potential that microwaves create an effect similar to two stage-sintering in which the final sintering stage is seen as an exhaustion process. Wroe and Rowley [33] have

suggested that the use of microwaves enhances grain boundary diffusion this could create a difference in the kinetics between the grain-boundary diffusion and grain-boundary migration, although the magnitude of the effect would not be as significant as that described by Chen et al. [107] for two stage sintering because grain-boundary migration is not suppressed. However, it could influence the grain size of microwave sintered samples (keeping it finer) and hence could explain why, after a strong enhancement of the densification in the initial and intermediates sintering stages, microwave sintering has a dramatically reduced densification rate in the final sintering stage.

Earlier, two hypotheses for what might be happening were introduced, see section 2.6. If hypothesis 1, enhanced diffusion via an additional driving force, is right, then there would be no difference in the microstructure and the porosity would be the same at given density. For hypothesis 2, different sintering behaviour, the closed porosity would be reduced at the same time as the open porosity. This means that a greater volume of open porosity would remain at higher densities and the internal microstructure would be different for conventional and hybrid sintering at a given level of densification.

Pore size changes during densification

Figure 94 through 99 show the measured pore development during sintering under the different sintering conditions. The mercury porosimetry results for the sintering before the change of the magnetron and experimental procedure are incomplete, because of technical problems the porosimeter and after the magnetron change only the new samples were investigate. To increase confidence in the measured results the total specific pore volume, V_p, of the samples was calculated using:

$$V_p = \frac{V_s(1 - \mathrm{TD})}{m_s}$$

Where V_s is the sample volume, TD is the theoretical density of the sample and m_s the sample's mass.

The calculated V_p is equal to the total specific pore volume (open and closed porosity) of each sample at each point during sintering. Since the total specific pore volume is used for the comparison, the measured specific pore volume should be lower, because the measurement techniques used were only capable of measuring the open porosity. Between the techniques used, the nitrogen adsorption is expected to yield a higher value for the pore volume than the mercury porosimetry, since the latter is based on the use of pressure to force mercury into the pores. The latter can lead to so called bottle neck pores that have a narrow opening concealing a large pore, displaying an artificially small apparent pore diameter. Figure 100 shows the comparison of the calculated specific pore volume with the measured specific pore volumes for the conventionally sintered samples for both experimental arrangements from the start of the sintering time, 6s, up to the end after 3600 s as a function of the sample's density. As expected the measured pore volumes are smaller or at least equal to the calculated. Therefore it can be said that the measured porosities were reliable and can be used for further analysis.

The difference between the measured porosity results before and after change of the magnetron and experimental procedure, see Figure 94 through Figure 99, was in the most cases small; because the densities were similar the amount of the porosity had to be similar. The greatest difference for the results was the measured pore volume for 600 W hybrid sintering after 1800 s. Here the porosity of the samples after the change had a higher amount of open porosity. This was not a surprise because the density for these samples was lower than for the samples before the change and therefore their porosity was higher.

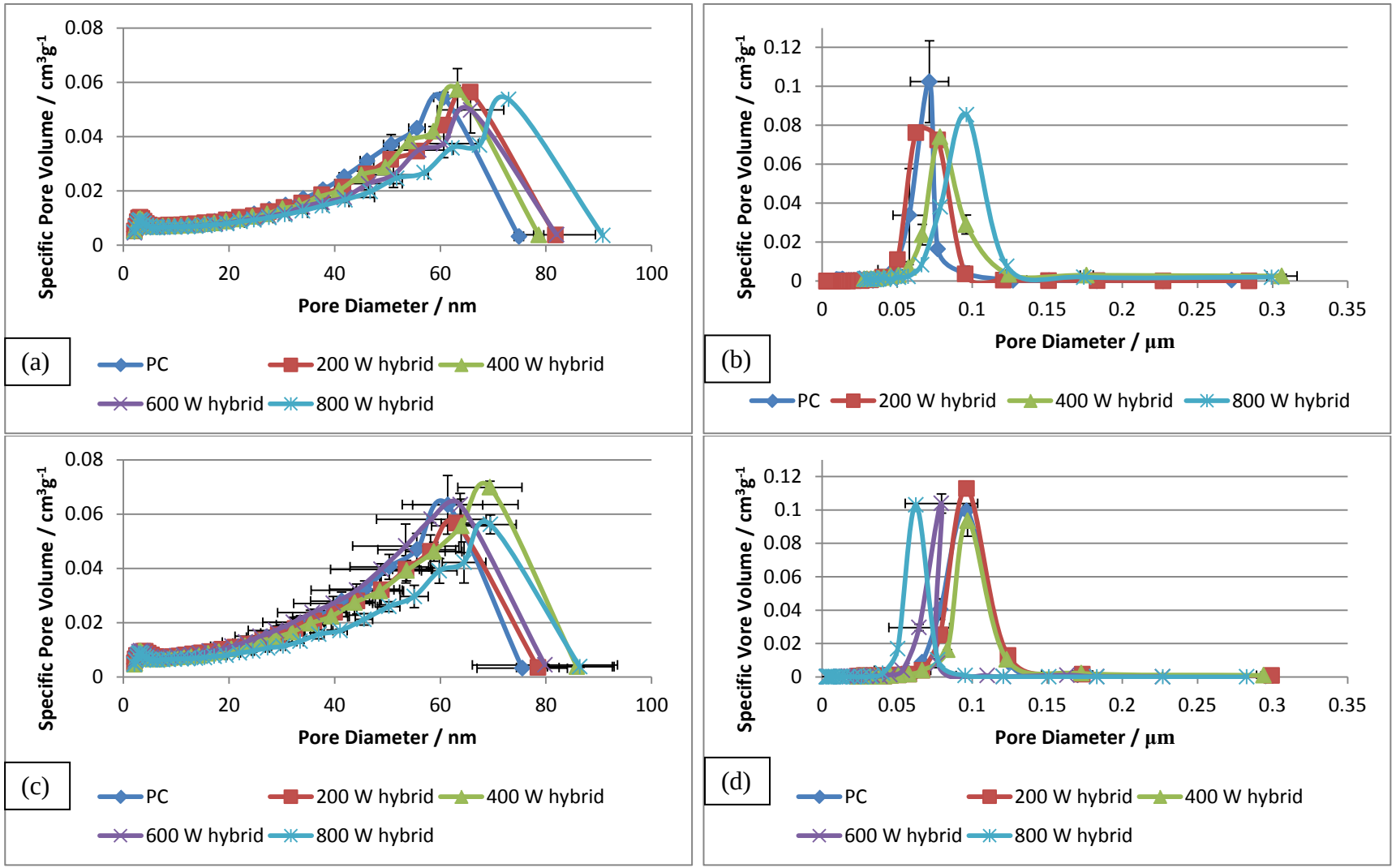

Figure 94 nitrogen adsorption porosity (a, c) and Mercury (b, d) porosity curve for ZnO samples sintered at 800°C for 6 s (a, b) before (samples used for nitrogen adsorption: 1-2; Hg: 1-2) and (c, d) after (samples used for nitrogen adsorption: 3; Hg: 3) change of the magnetron and experimental procedure

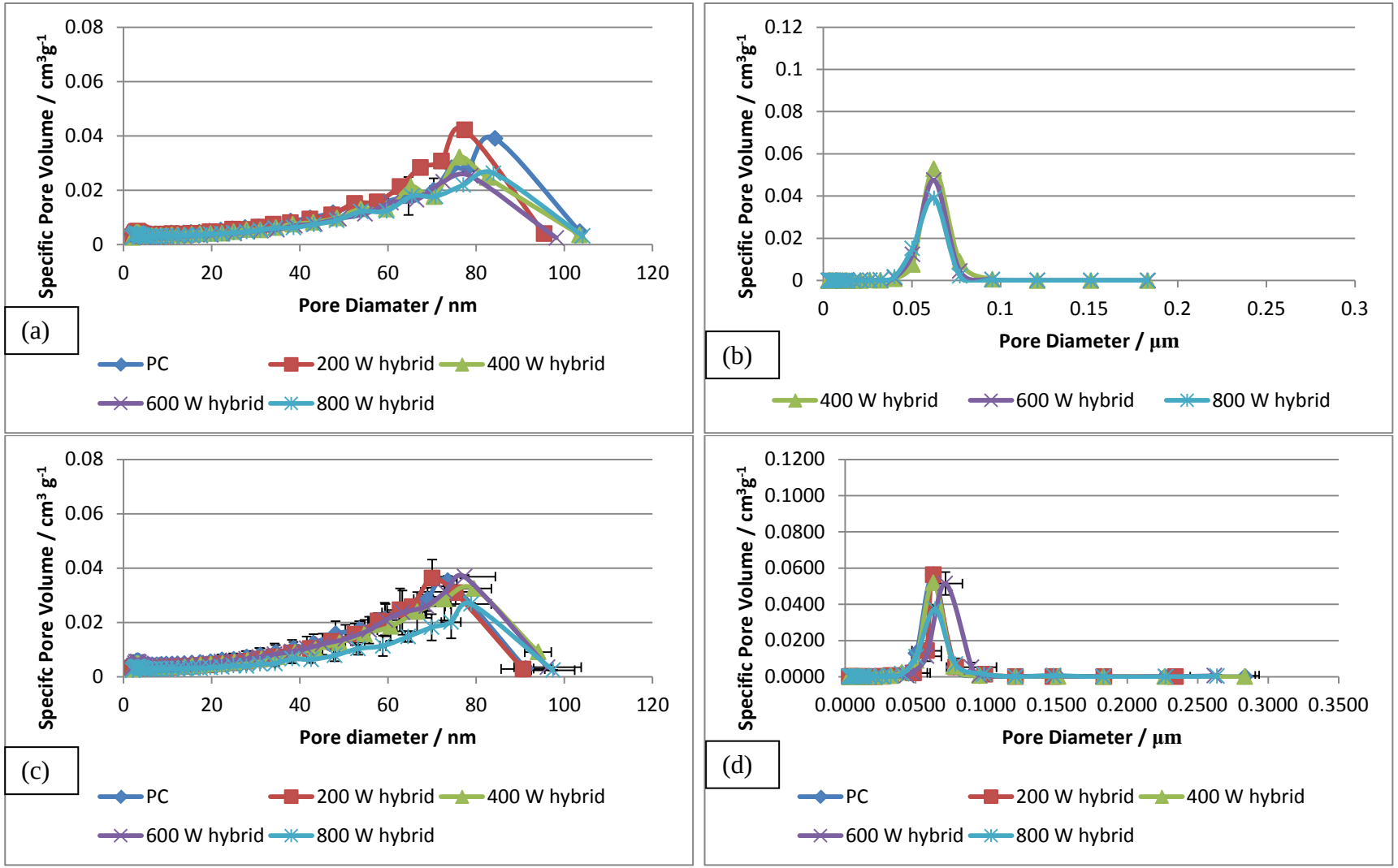

Figure 95 nitrogen adsorption porosity (a, c) and Mercury (b, d) porosimeter curve for ZnO samples sintered at 800°C for 900 s (a, b) before (samples used for nitrogen adsorption: 1-2; Hg: 1) and (c, d) after (samples used for nitrogen adsorption: 4; Hg: 3) change of the magnetron and experimental procedure

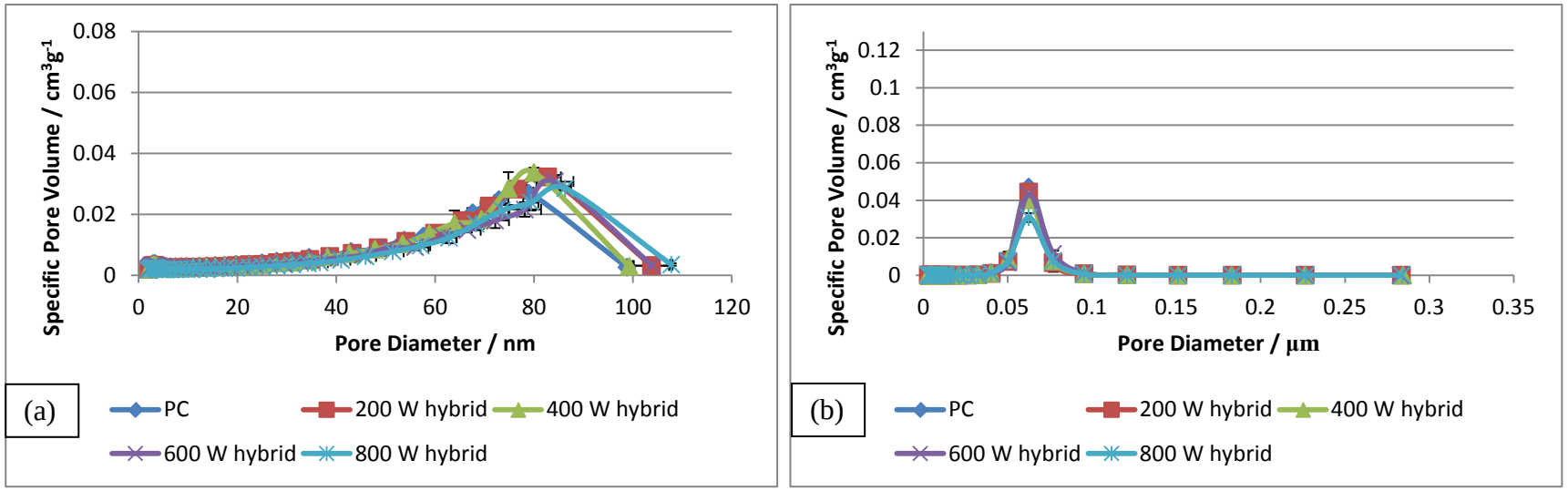

Figure 96 nitrogen adsorption porosity (a) and Mercury (b) porosity curve (samples used for nitrogen adsorption: 3; Hg: 3) for ZnO samples sintered at 800°C for 1350 s after change of the magnetron and experimental procedure. Comment about 1350 s introduced with experimental change.

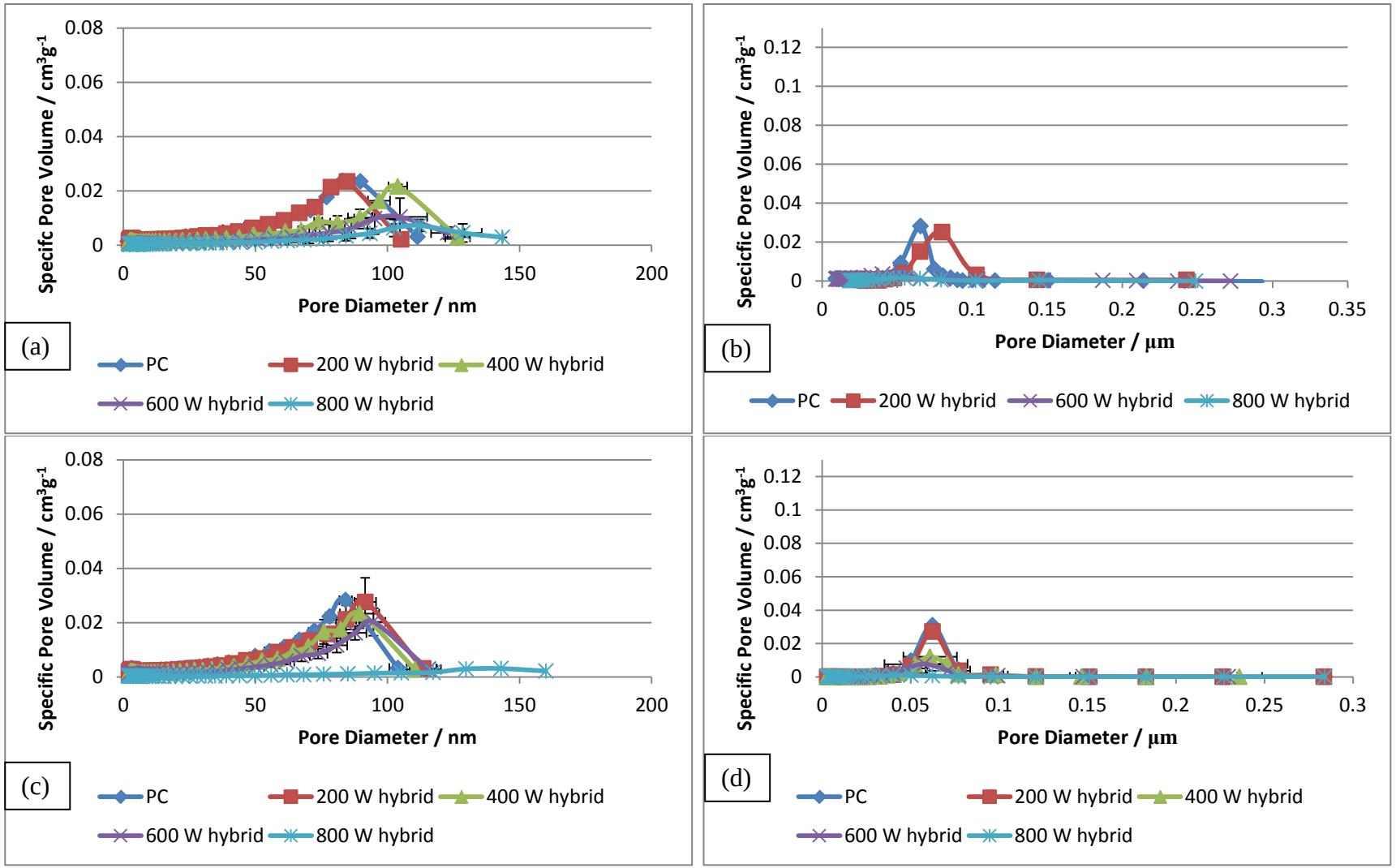

Figure 97 nitrogen adsorption porosity (a, c) and Mercury (b, d) porosity curve for ZnO samples sintered at 800°C for 1800 s (a, b) before (samples used for nitrogen adsorption: 2-3; Hg: 1) and (c, d) after (samples used for nitrogen adsorption: 6; Hg: 3) change of the magnetron and experimental procedure

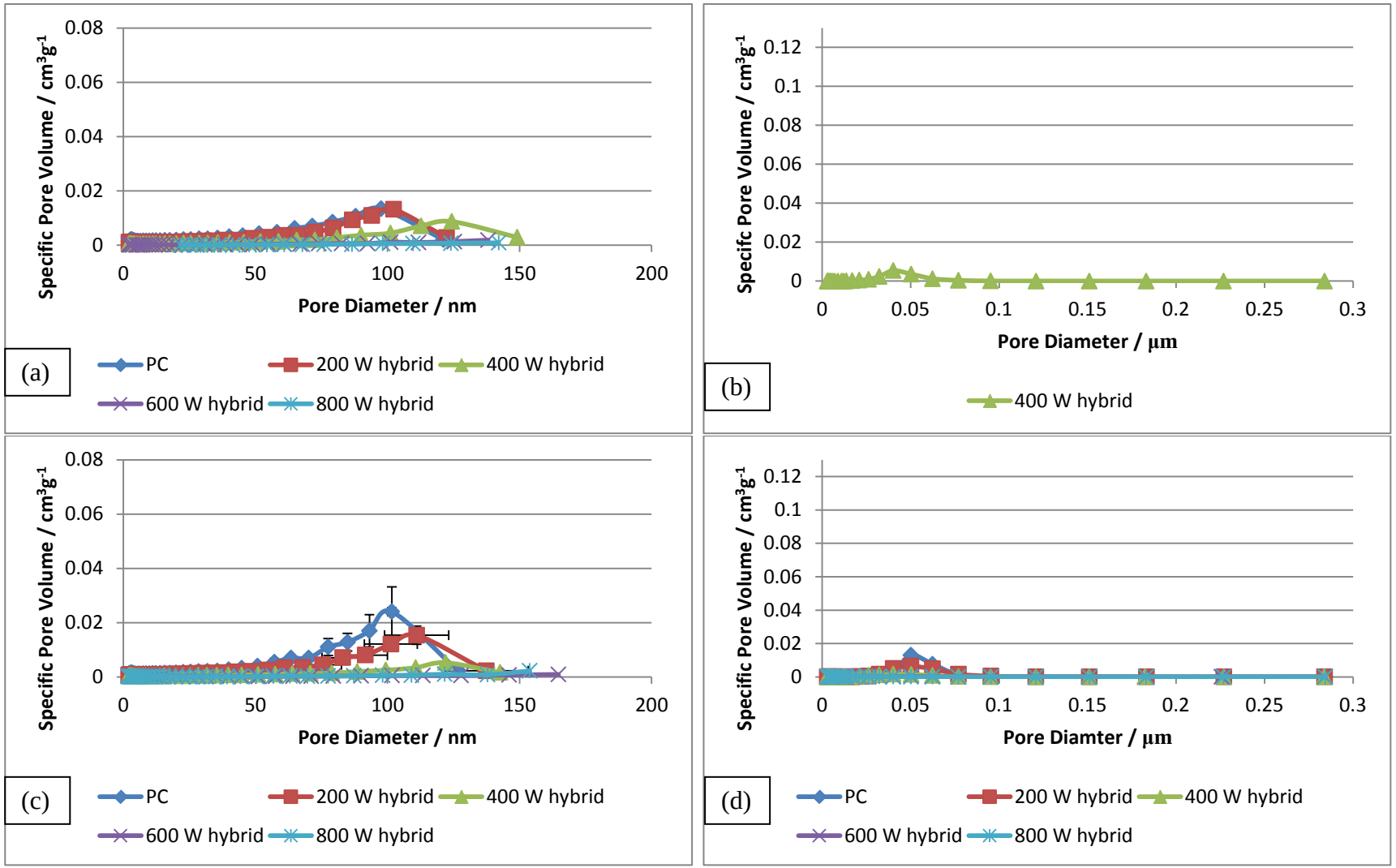

Figure 98 nitrogen adsorption porosity (a, c) and Mercury (b, d) porosity curve for ZnO samples sintered at 800°C for 2700 s (a, b) before (samples used for nitrogen adsorption: 1; Hg: 1)and (c, d) after (samples used for nitrogen adsorption: 3; Hg: 3) change of the magnetron and experimental procedure

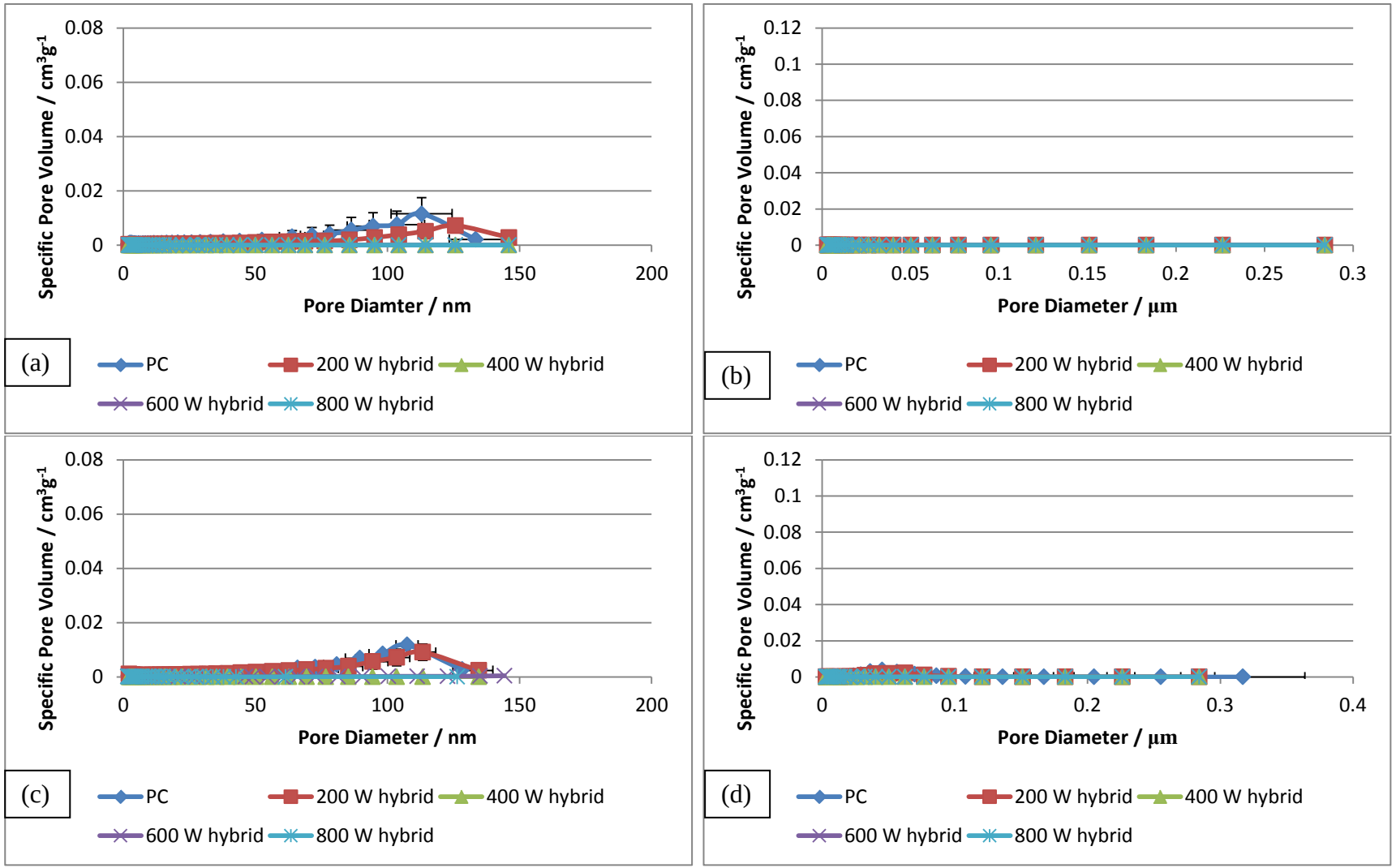

Figure 99 nitrogen adsorption porosity (a, c) and Mercury (b, d) porosity curve for ZnO samples sintered at 800°C for 3600 s (a, b) before (samples used for nitrogen adsorption: 1-2; Hg:1-2) and (c, d) after (samples used for nitrogen adsorption: 4; Hg: 2-3) change of the magnetron and experimental procedure

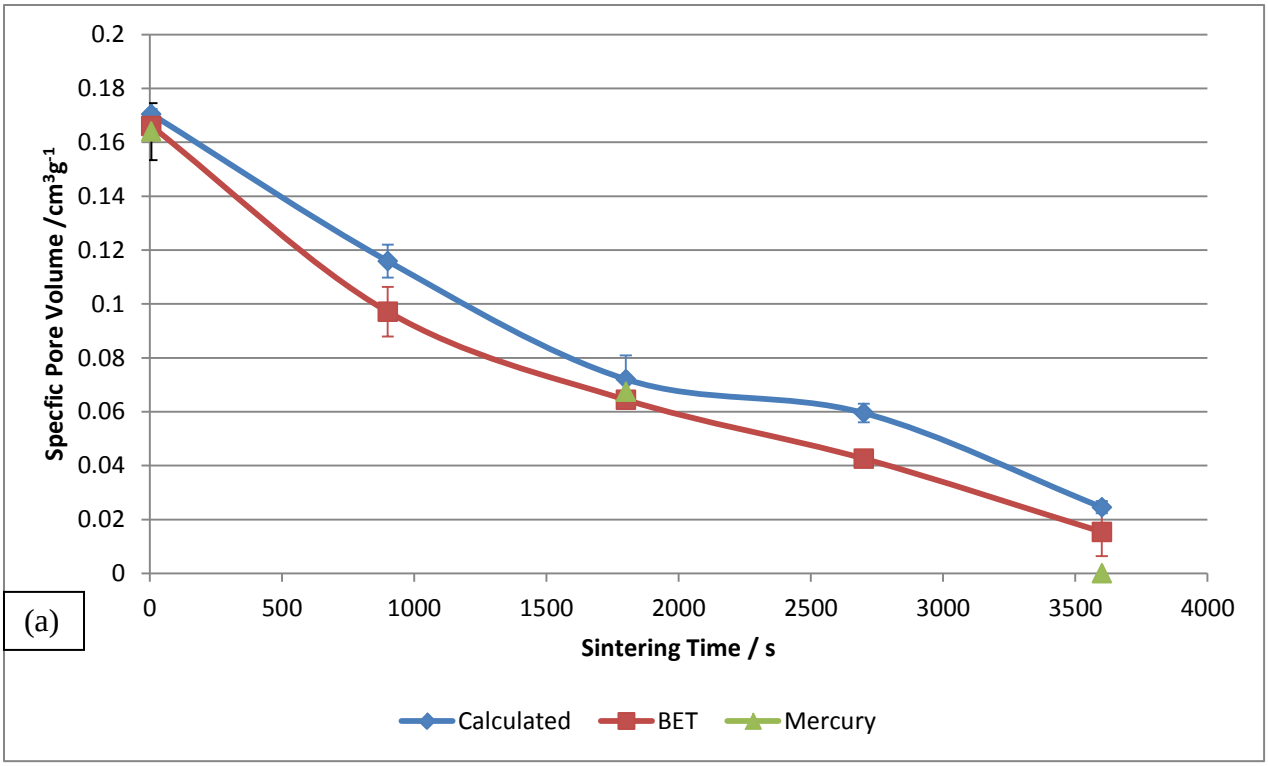

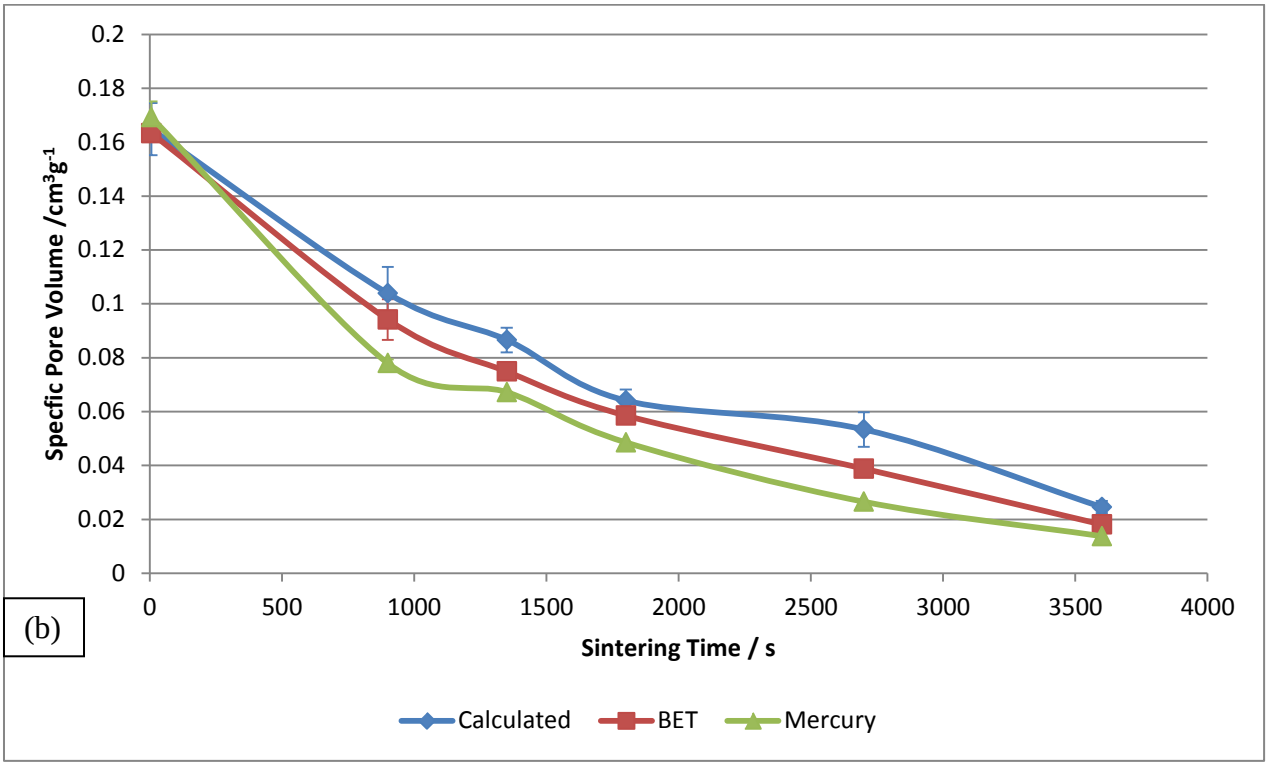

Figure 100 Comparison between the estimated pore volume for the samples sintered with pure conventional heating and the measured pore volume with nitrogen adsorption and mercury porosimetry (a) before and (b) after change of the magnetron and experimental procedure.

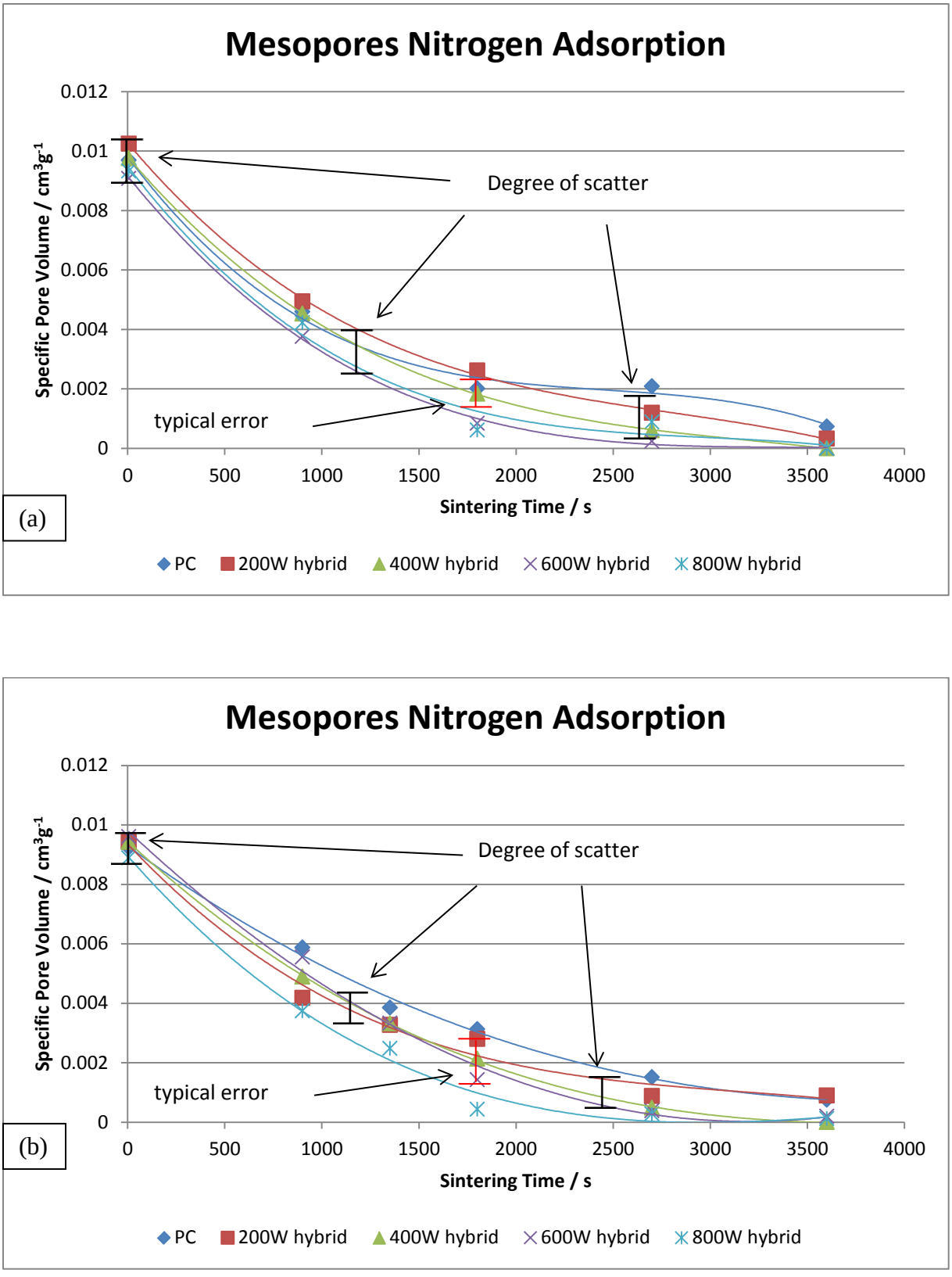

Figure 101 Maximum volumes for nitrogen adsorption porosity mesopores (a) before and (b) after change of the magnetron and experimental procedure

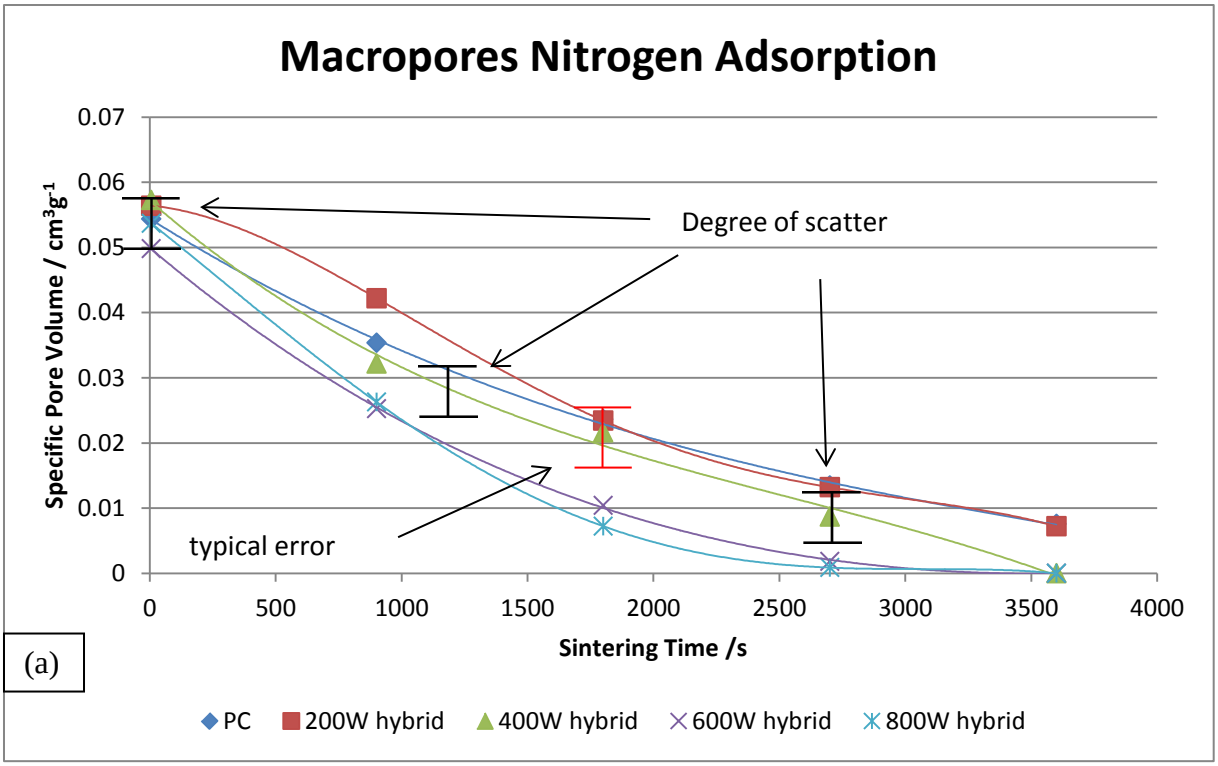

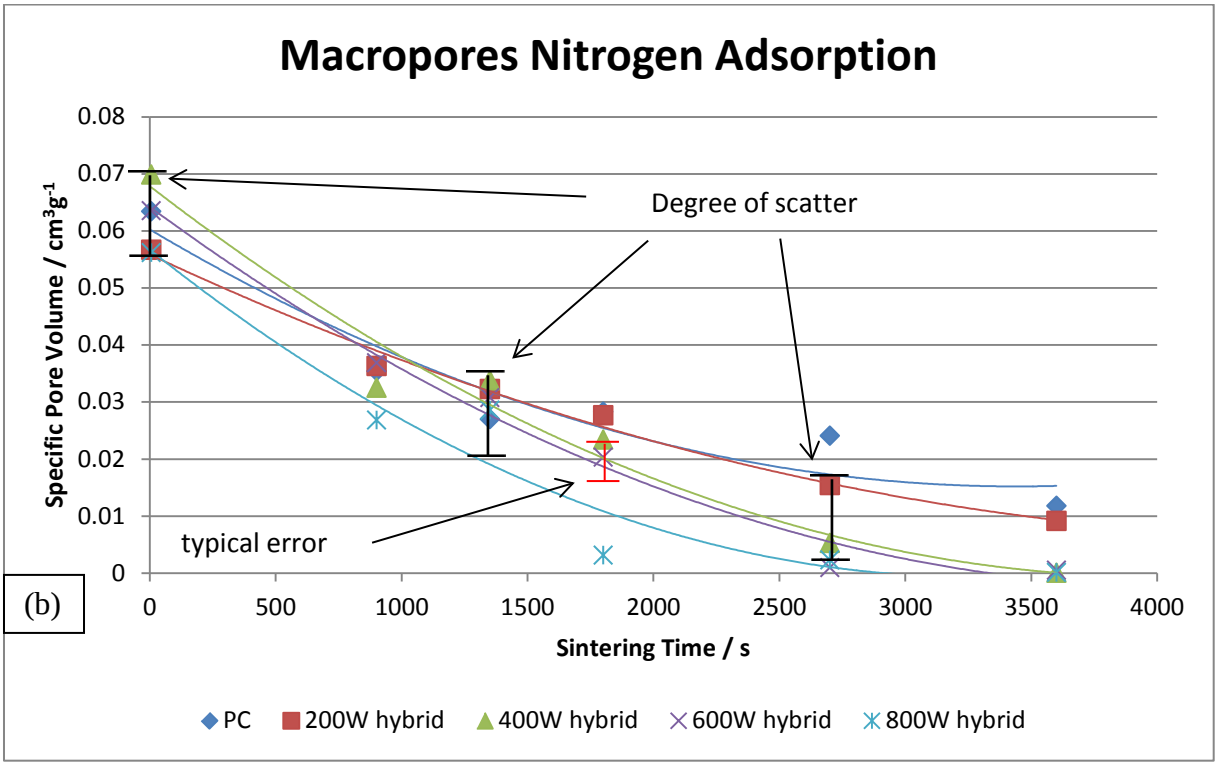

Figure 102 Maximum volumes for nitrogen adsorption porosity macropores (a) before and (b) after change of the magnetron and experimental procedure

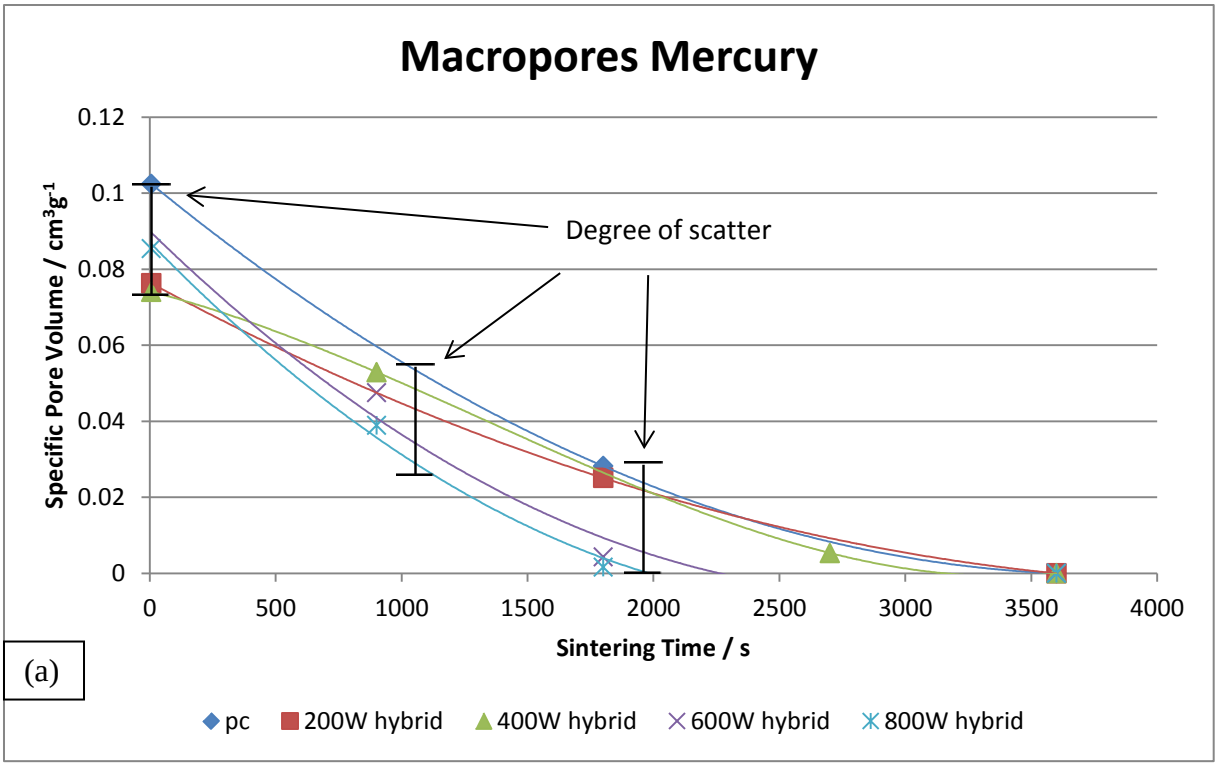

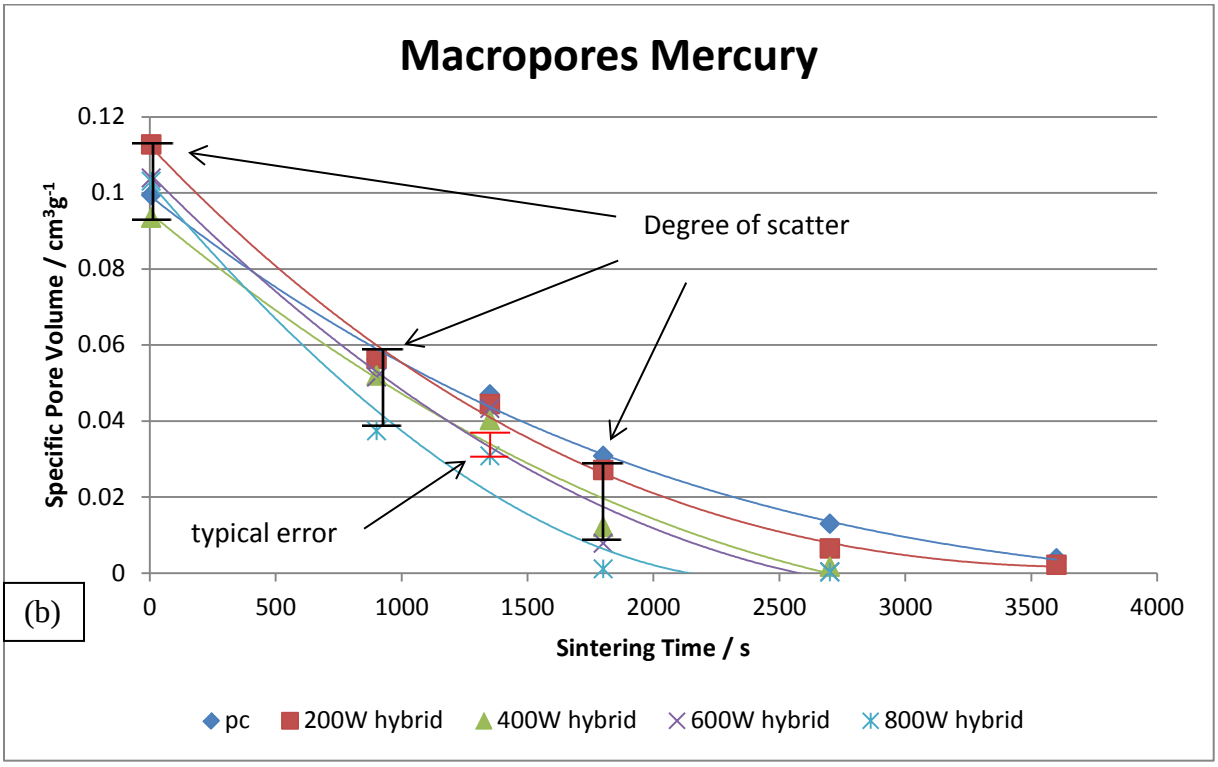

Figure 103 Maximum volumes for Mercury porosity (a) before and (b) after change of the magnetron and experimental procedure

The measured maximum pore volumes, see Figure 101 through, show an increased reduction in the porosity for samples when higher amounts of microwaves were used during sintering. This is only logical because the reduction of the porosity is an integral part of the densification. However the techniques used have their limitations. As soon as the sintered samples achieved a density that was greater than 90% of the TD none of the techniques were able to measure the remaining open porosity at all accurately, however the latter should not disappear before the samples achieved a value of ~96% of the theoretical. Mercury porosimetry was not able to measure the porosity of these samples because the volume of the open porosity was reduced below the accuracy of the measuring equipment. The latter was 1% of the full intrusion volume of the penetrometer used (0.366 cm^3). Since the nitrogen adsorption technique relies on the absorption of gas layers to measure to porosity, it should have been able to detect the pores. However, the pore diameter measured increased during sintering and nitrogen adsorption technique can only measure porosity up to a pore diameter of ~200 nm; this limit was exceeded and so the data in Figure 101 through 103 is incomplete, particularly for the samples sintered using the higher microwave power levels.

Figure 101 through 103 nevertheless shows the development of the measured maximum pore volumes; however a degree of caution must be exercised when interpreting the data. It will be noted that after 6s the variability in the porosity is very great; this is due to the inherent variability in the green bodies since next to no sintering had occurred at this point in time. As sintering progressed, the individual variability of the porosity for the sintering conditions can reach very small levels in some cases. However, since all the sintered samples inherited the initial variation in the porosity of the green bodies, a significant degree of scatter in the data must be accepted. Nevertheless, the overall trend is clear and it can be said that a higher level of microwaves lead to a faster reduction of the porosity.

The argument that higher amounts of microwaves lead to a smaller amount of porosity over time is logical because the densification is only achieved by the reduction of the porosity. As discussed in section 2.2.6, the initial effect of the rearrangement of the particles is small compared to the reduction of the porosity after

the necks are formed and neck and grain boundary growth have started. The forming of necks and the growth of necks and grain boundaries are all diffusion controlled processes. Therefore, one reason for the increased reduction of the open porosity is an enhanced diffusion caused by the microwaves, because the temperature and other process condition were the same for all sintering conditions. The only difference left is the amount of microwaves used. If this is the cause, it would indicate that microwaves would acted as an additional driving force, as suggested by Rybakov and Semenov [27], in the initial and particularly the intermediate sintering stage.

Nevertheless, even allowing for the general trend that a higher microwave power level lead to increased porosity reduction over time, it could also be observed that before the experimental procedure was changed the microwaves had a greater effect on the open porosity especially in the time range between 6 s and 1800 s. A possible explanation for this could be a greater temperature difference between the sample core and centre. Before the magnetron change, three samples were laid in a line during sintering, whilst after the change the four samples used were stacked. The reason for the change has been already explained, a reduction in the power from the new magnetron leading to lower densities with the original arrangement. However, the new arrangement will have resulted in greater influence of one samples on another and hence a lower temperature gradient across each individual sample was anticipated.

The temperature difference was calculated by using the heat flow equation:

$$\dot{Q} = \frac{\lambda A T_1 - T_2}{\delta} t$$

where $\dot{Q}$ is the heat flow, λ is the thermal conductivity, A is the surface area, t is the time and δ is the thickness.

For cylinder the heat flow equation is

$$\dot{Q} = \frac{2\pi l \lambda (T_1 - T_2)}{\ln(\frac{R_2}{R_1})} t$$

Where l is the cylinder length, R_2 is the outer radius and R_1 is the inner radius of the cylinder, see Figure 104.

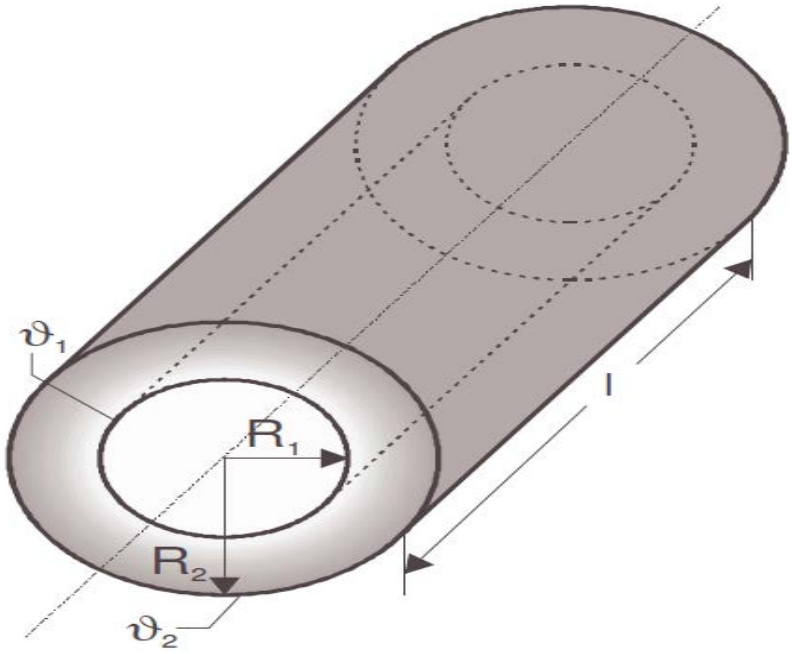

Figure 104 thermal conductivity of a cylinder ($\vartheta_1 = T_1$, $\vartheta_2 = T_2$) [111]

The equation was used to calculate the temperature difference:

$$T_1 - T_2 = \frac{\dot{Q}\ln(\frac{R_2}{R_1})}{t2\pi l\lambda} = \Delta T$$

For the calculations a few assumptions were made:

1) The surface temperature is equal around the samples
2) The sample is pure ZnO without any porosity
3) No shrinkage of the sample

For the calculation the outer diameter was the diameter of the pellet 3 mm. Since a division through 0 is not possible the inner diameter was 0.1mm. Regardless of the chosen inner diameter, which increases the temperature the smaller it is, the temperature for the samples after the experimental procedure change will be only a ¼. Since all other values were constant and only the length changed, which was 4

times higher after the change than before. The thermal conductivity was taken from Figure 105;

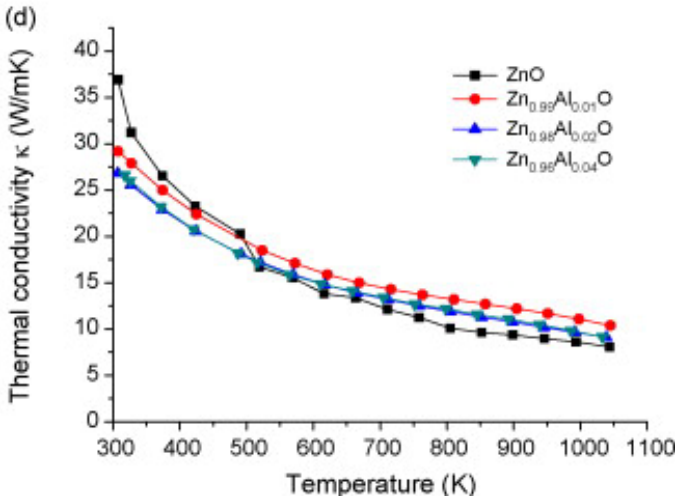

Figure 105 Temperature dependence of thermal conductivity of (hot-pressed) ZnO [112]

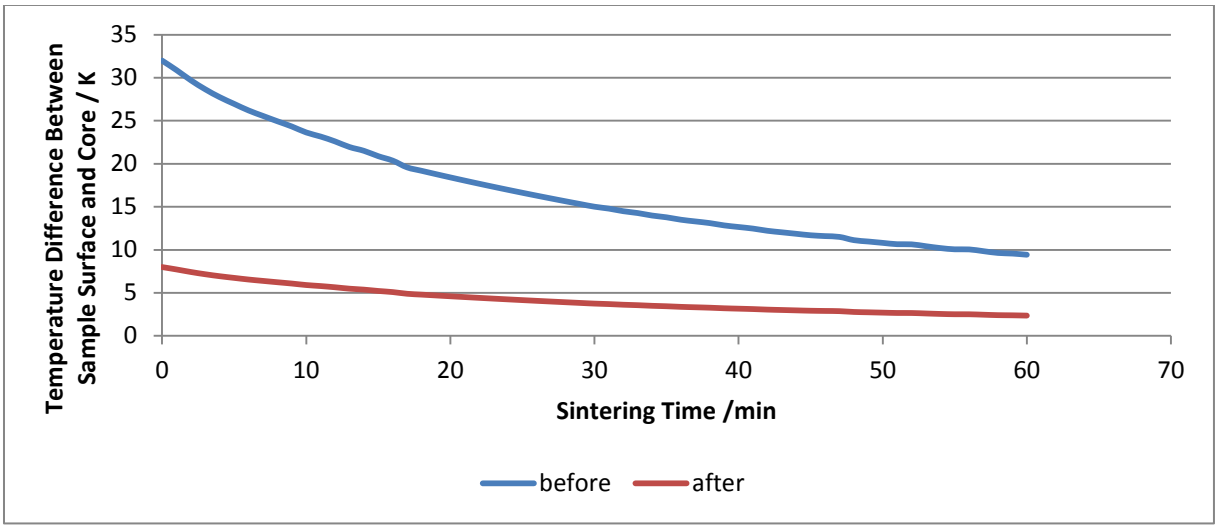

Figure 106 Calculated temperature gradient across samples for 800 W hybrid heating at 800°C as a function of holding time at temperature for an inner radius of 0.1 mm before and after the change of the experimental procedure

As it can be seen from Figure 106 the temperature gradients across the samples before and after the change of the magnetron and experimental procedure. However these differences were probably larger in the original sample arrangement.

Figure 107 to 112 show the FEGSEM images of the surfaces of the samples sintered under different hybrid conditions and the different experimental procedures. The

images in Figure 107 and 108 of the samples at the beginning of the densification process show, as expected, similar structures.

Figure 109 and 110 show the situation after 1800 s for both experimental conditions and the difference in the pore structure shows the different stages of the densification at this stage. The images of pure conventional (a) and 200 W (b) hybrid sintered samples show samples close to the beginning of the intermediate stage; the density for both sintering conditions is just above 70% of the theoretical. The rearrangement of the particles and neck forming are finished and neck growth and the grain boundary lengthening has just started. However both images look less porous than in Figure 107 and 108, this supports the results of the porosity measurement where the amount of porosity was at least half of the initial value. In contrast, the ceramics shown in Figure 109 and 110 d (600 W) and e (800 W) look much denser. This is not a surprise since the samples of these sintering conditions have a density of above 80% of the theoretical. Grain boundary lengthening is well underway.

The surface of all the samples that had been sintered for 3600 s, Figure 111 and 112, show open porosity, this is expected since all the sample densities at this point of the sintering cycle were below 95%. Only at a density closer to full density will all the open porosity be eliminated, Figure 30. However the volume of the remaining open porosity was too low for any of the measuring techniques used so that, except for pure conventional and 200 W hybrid sintering, no measured results could be obtained at this sintering time.

Note that another possible reason for the open porosity at later sintering times is the volatilization of the ZnO. This can influence the surface of samples to make them look like they have greater porosity because some of the material evaporates and increases the surface roughness.

The sample in Figure 112 d and e shows less sign of condensation and look denser with a greater grain size than their counterparts in Figure 111 d and e. A reason for this could be that these samples were in the middle of their stack during sintering. In this place they were more shielded by the other pellets from the furnace atmosphere. This shielding could lead to less volatilization and less condensation.

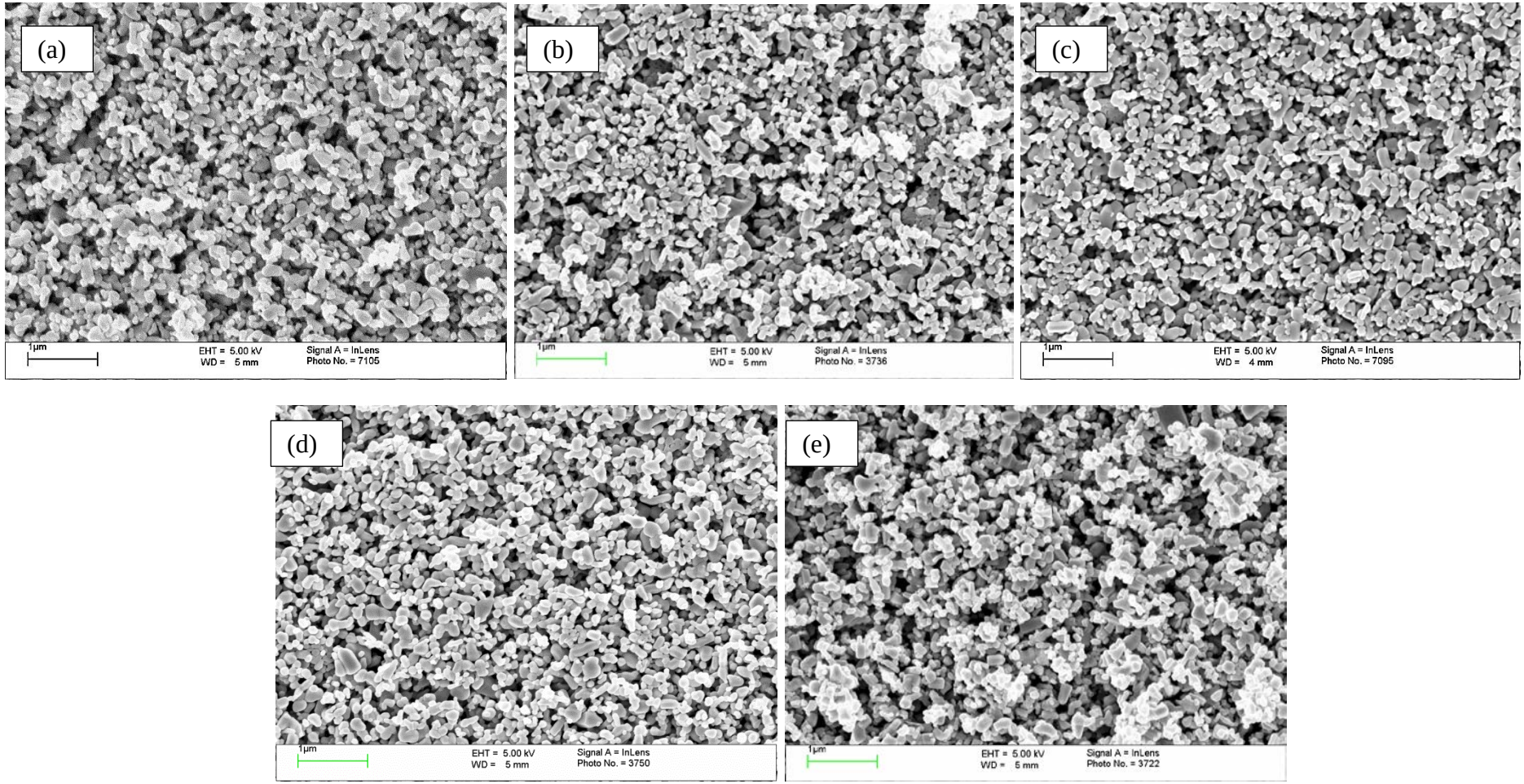

Figure 107 Surfaces of ZnO samples sintered for 6 s at 800°C using (a) pure conventional heating, (b) 200 W hybrid heating, (c) 400 W hybrid heating, (d) 600 W hybrid heating and (e) 800 W hybrid heating before change of the magnetron and experimental procedure

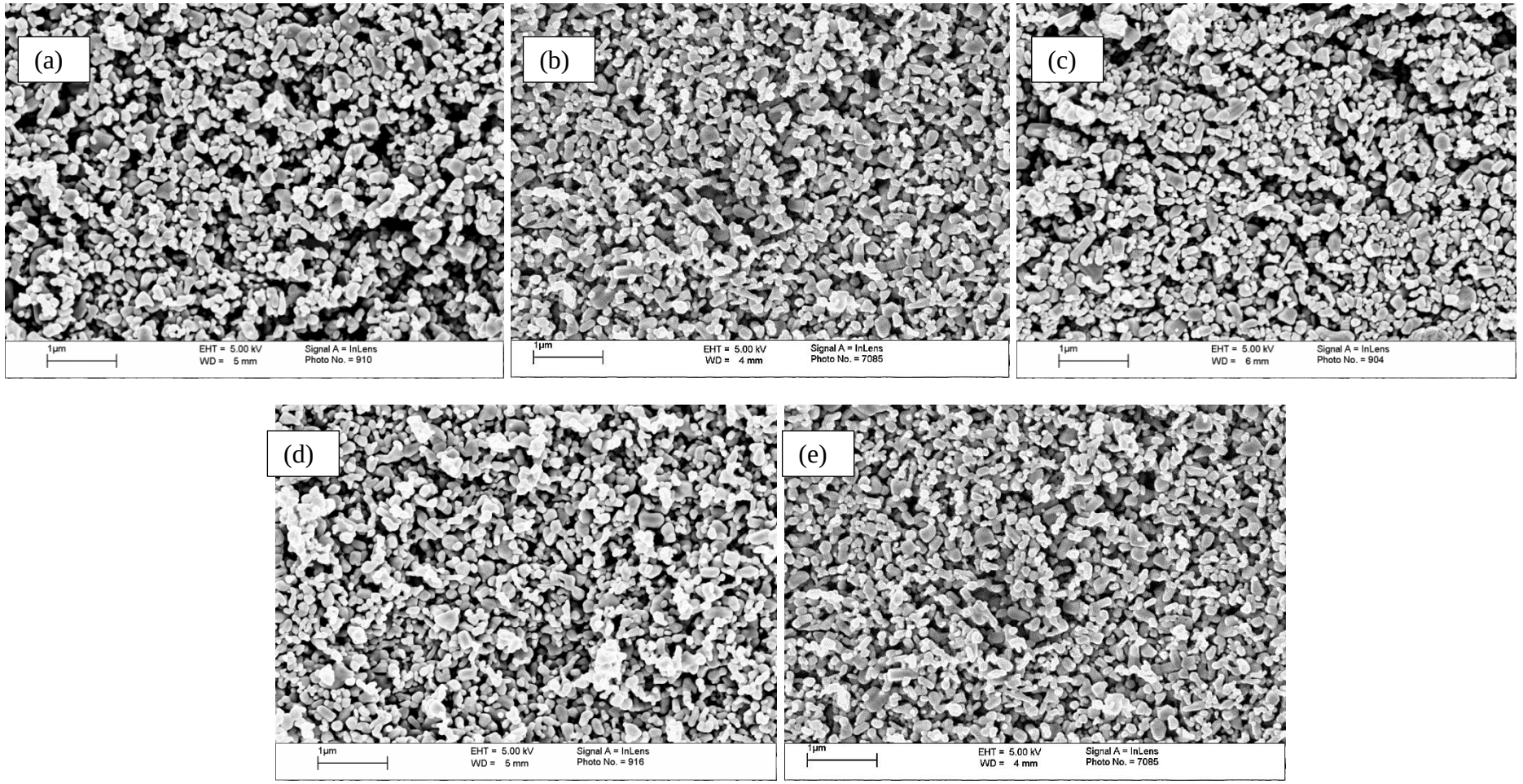

Figure 108 Surfaces of ZnO samples sintered for 6 s at 800°C using (a) pure conventional heating, (b) 200 W hybrid heating, (c) 400 W hybrid heating, (d) 600 W hybrid heating and (e) 800 W hybrid heating after change of the magnetron and experimental procedure

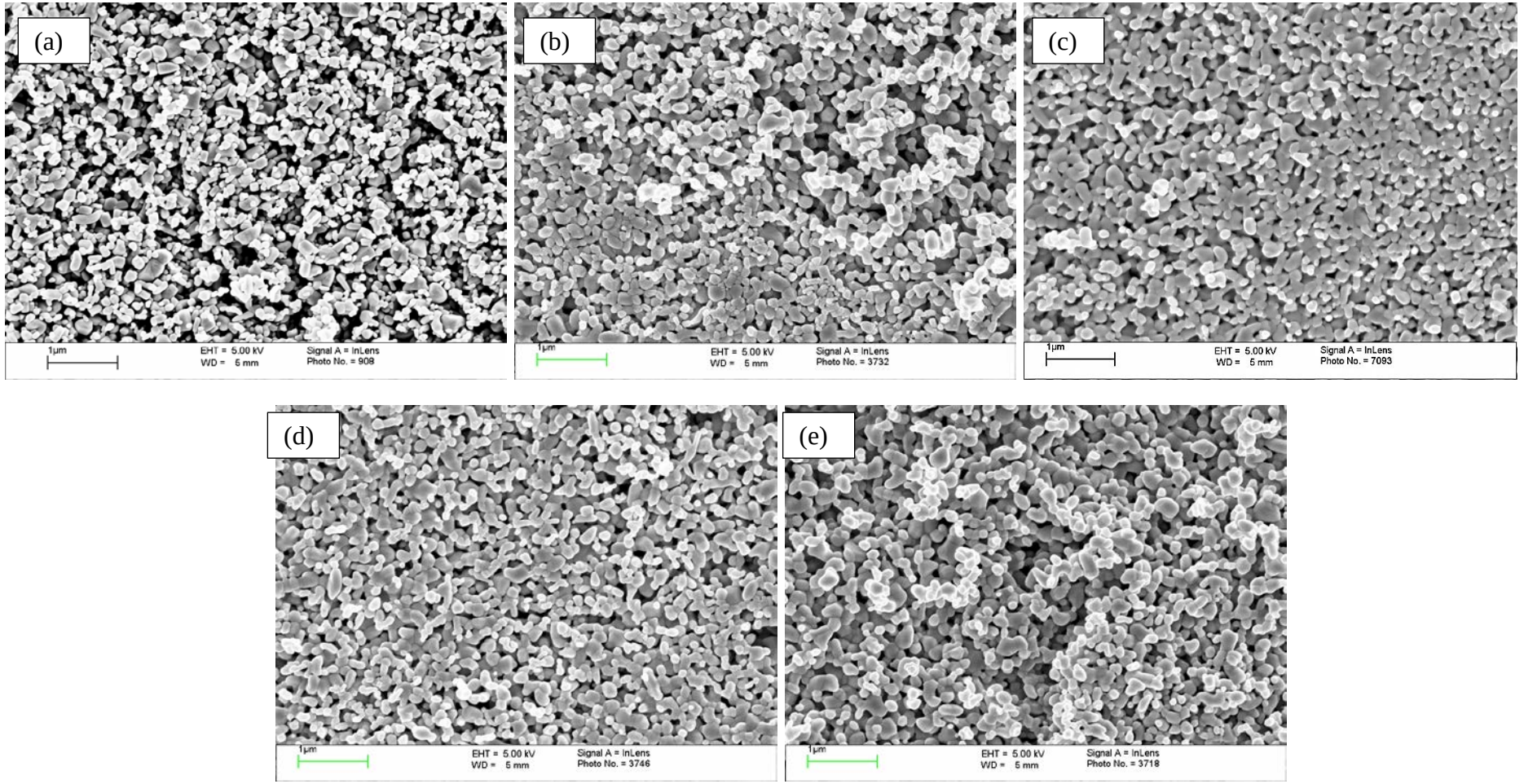

Figure 109 Surfaces of ZnO samples sintered for 1800 s at 800°C using (a) pure conventional heating, (b) 200 W hybrid heating, (c) 400 W hybrid heating, (d) 600 W hybrid heating and (e) 800 W hybrid heating before change of the magnetron and experimental procedure

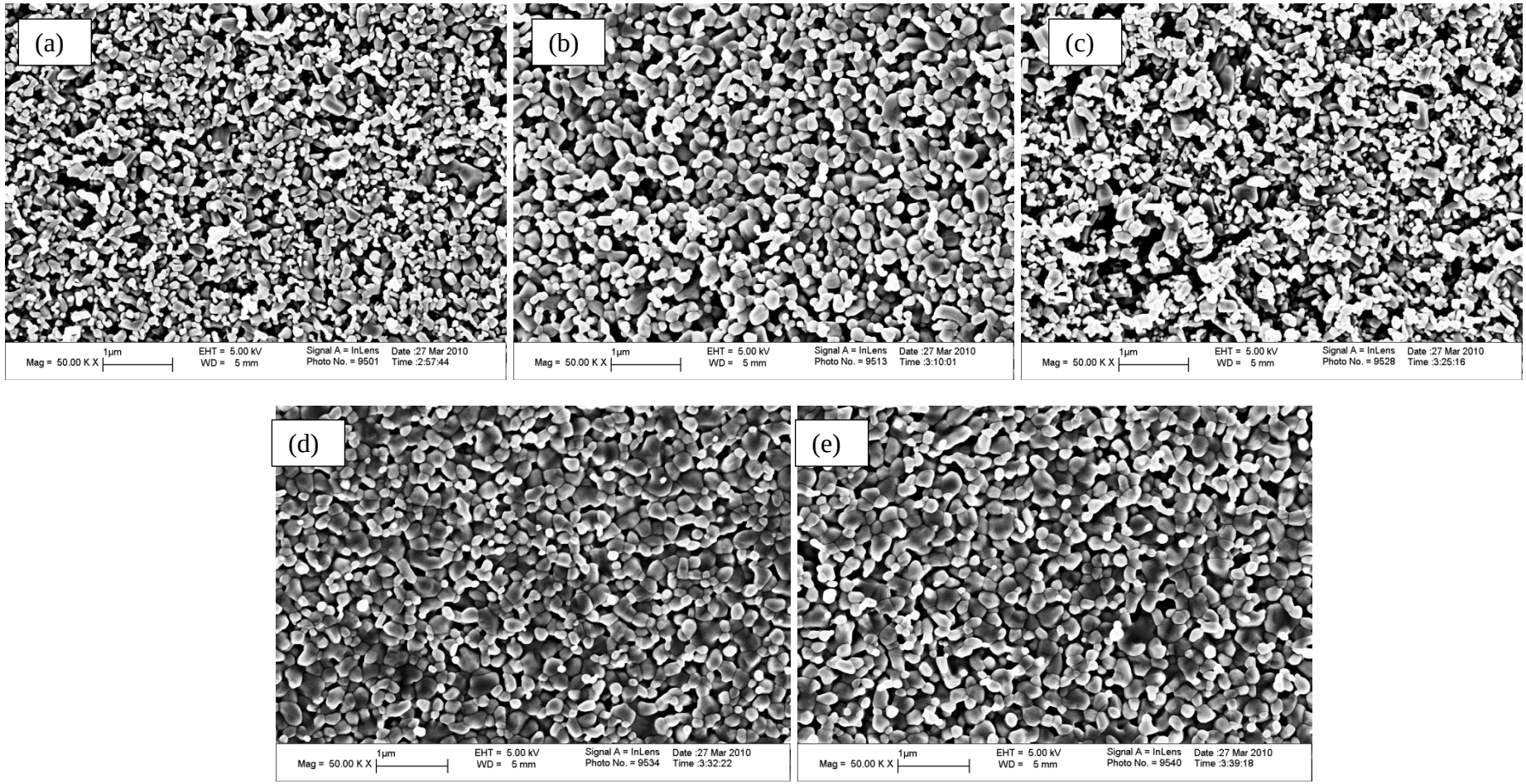

Figure 110 Surfaces of ZnO samples sintered for 1800 s at 800°C using (a) pure conventional heating, (b) 200 W hybrid heating, (c) 400 W hybrid heating, (d) 600 W hybrid heating and (e) 800 W hybrid heating after change of the magnetron and experimental procedure

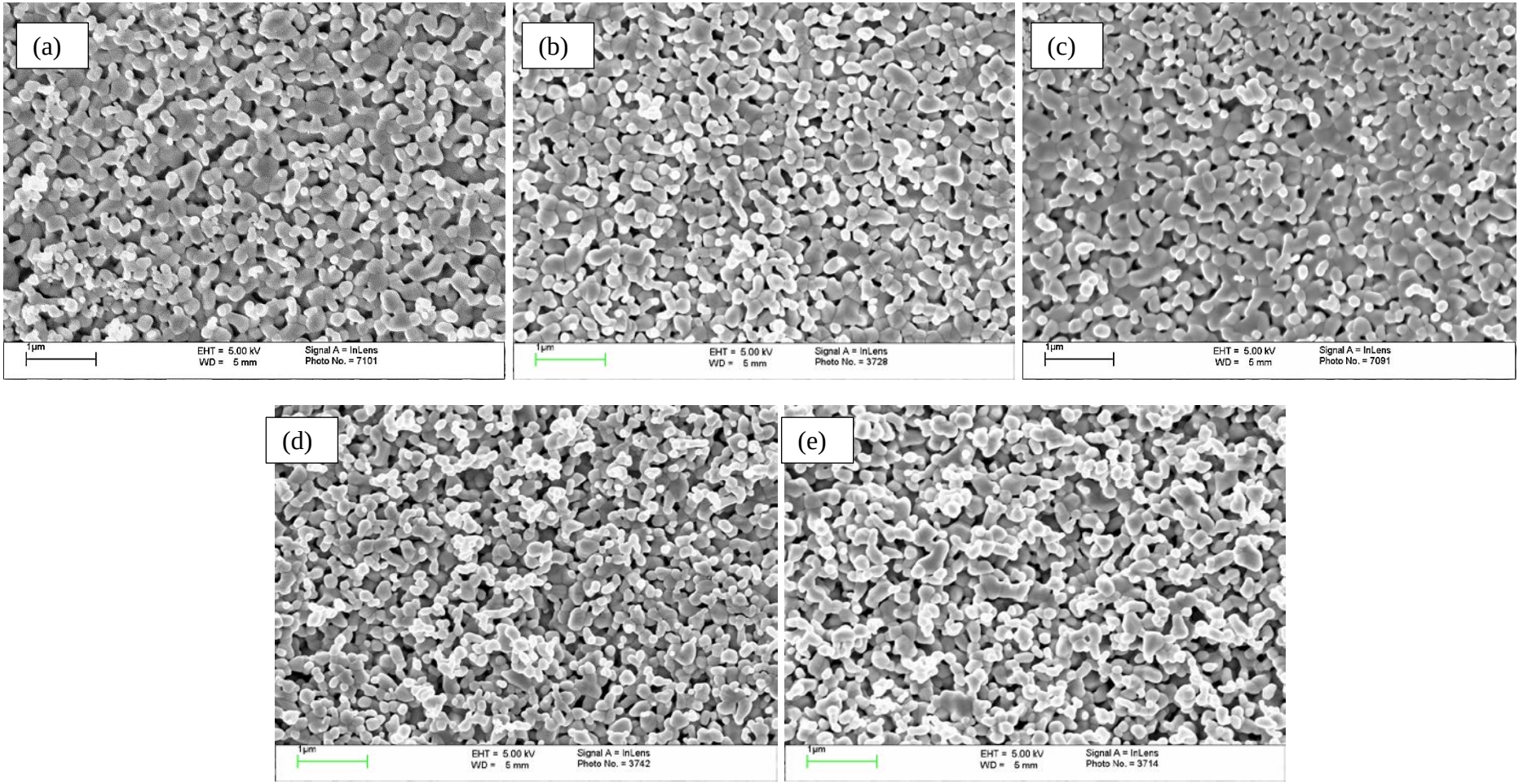

Figure 111 Surfaces of ZnO samples sintered for 3600 s at 800°C using (a) pure conventional heating, (b) 200 W hybrid heating, (c) 400 W hybrid heating, (d) 600 W hybrid heating and (e) 800 W hybrid heating before change of the magnetron and experimental procedure

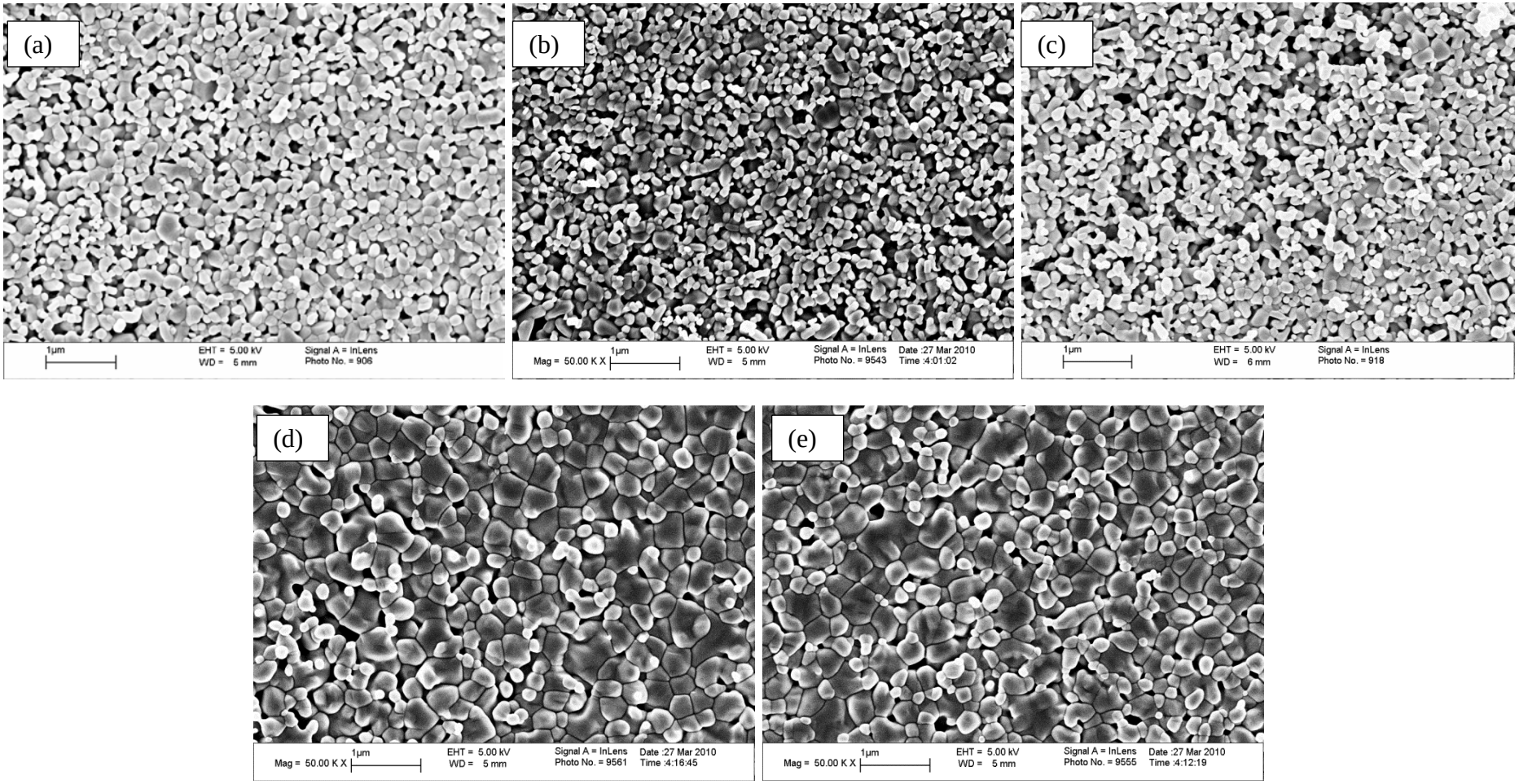

Figure 112 Surfaces of ZnO samples sintered for 3600 s at 800°C using (a) pure conventional heating, (b) 200 W hybrid heating, (c) 400 W hybrid heating, (d) 600 W hybrid heating and (e) 800 W hybrid heating after change of the magnetron and experimental procedure

When the reductions of the measured maximum specific pore volumes were compared in relation to the sintering time, Figure 101 to 103, it seemed that there were significant differences between the conventional and 800 W hybrid sintered samples. Before it can be definitively said that there is an effect of the microwaves on the porosity, it is better to compare the maximum specific pore volume with the sample density, Figure 113 to 115, because only if the porosity is different when the samples have the same density can it be said that the porosity is affected by the microwaves and with it the structural development. If this is not the case then the microwave effect is most like an enhancement of the existing sintering behaviour.

Figure 113 to 115 show the comparison of the specific pore volume and pore diameter vs. sample density. All the diagrams show that the reduction of the pore volume follows the same path. Therefore it can be concluded that the open porosity is the same for each sample independent of its sintering conditions at a given density. If the open porosity is the same at a given density, and the total porosity is the same, then the closed porosity is the same and it can be concluded that the porosity is not affected by the use of microwaves. The earlier difference found for the pore reduction vs. sintering time was due to the difference in the sample density at the given sintering time.

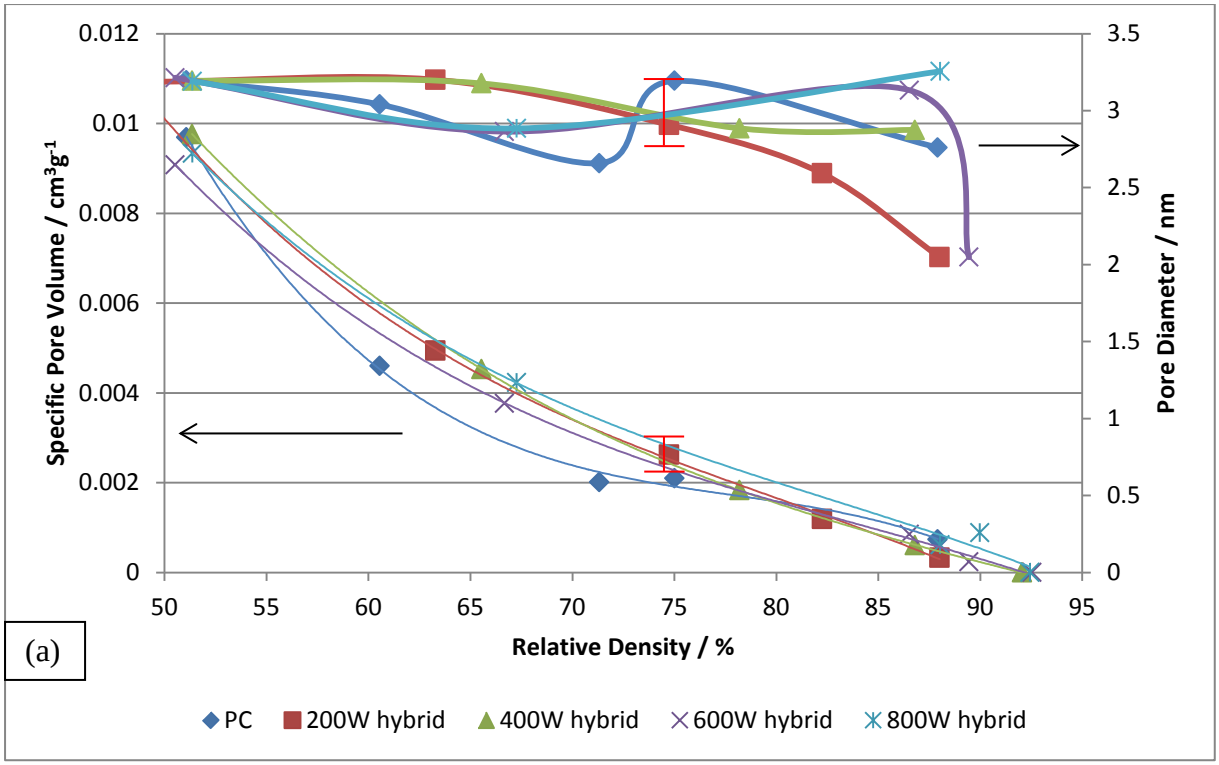

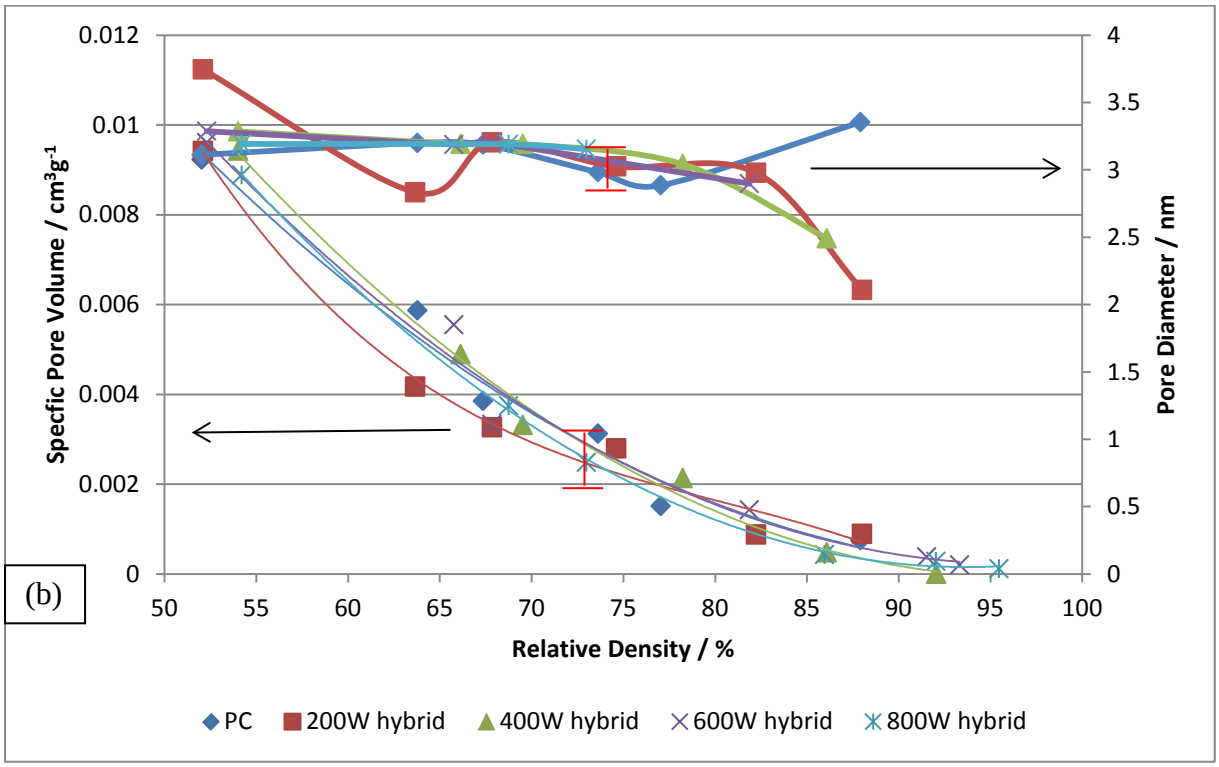

Figure 113 Comparison of pore volume and diameter vs. sample density for nitrogen adsorption mesopores (a) before and (b) after change of the magnetron and experimental procedure

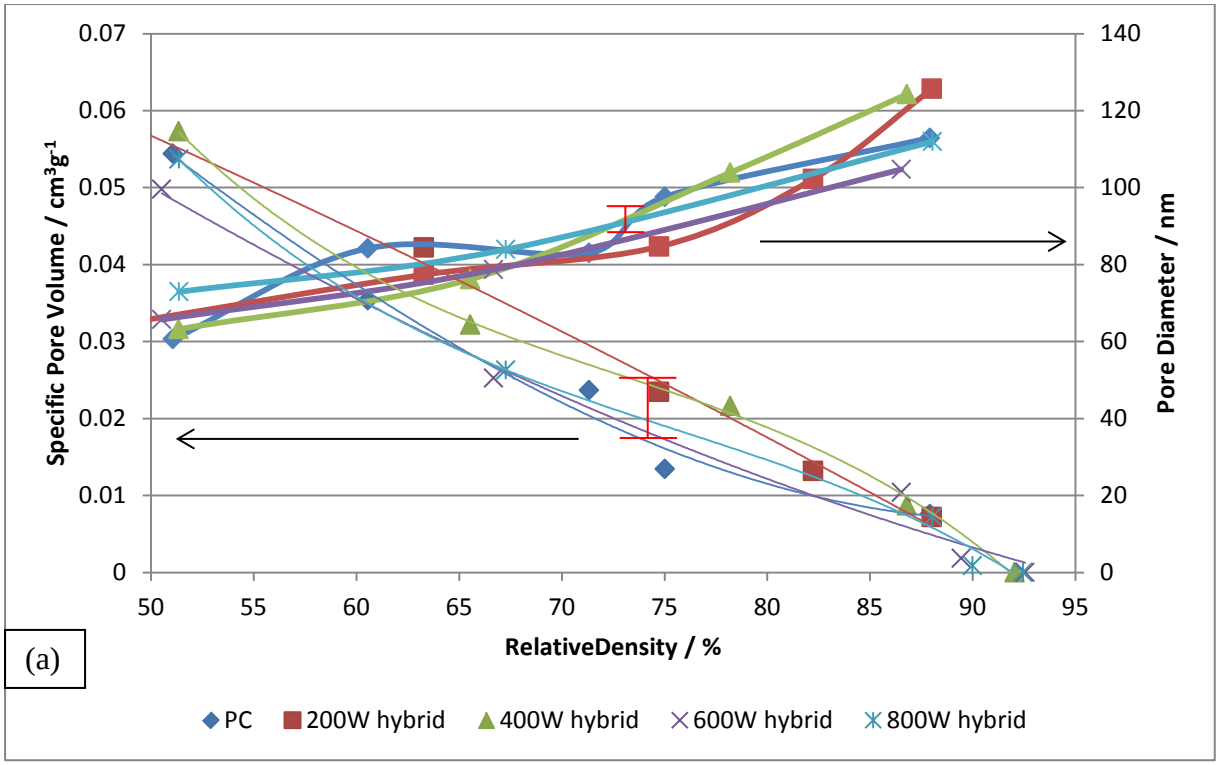

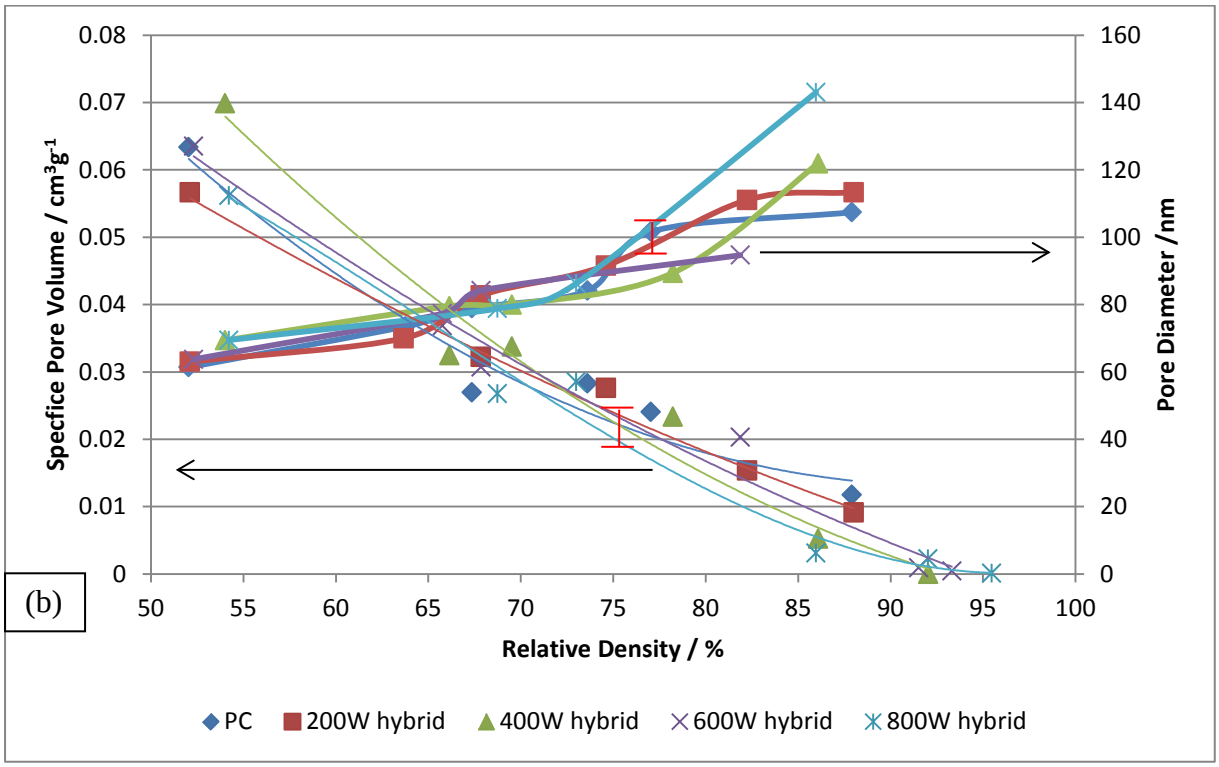

Figure 114 Comparison of pore volume and diameter vs. sample density for nitrogen adsorption macropores (a) before and (b) after change of the magnetron and experimental procedure

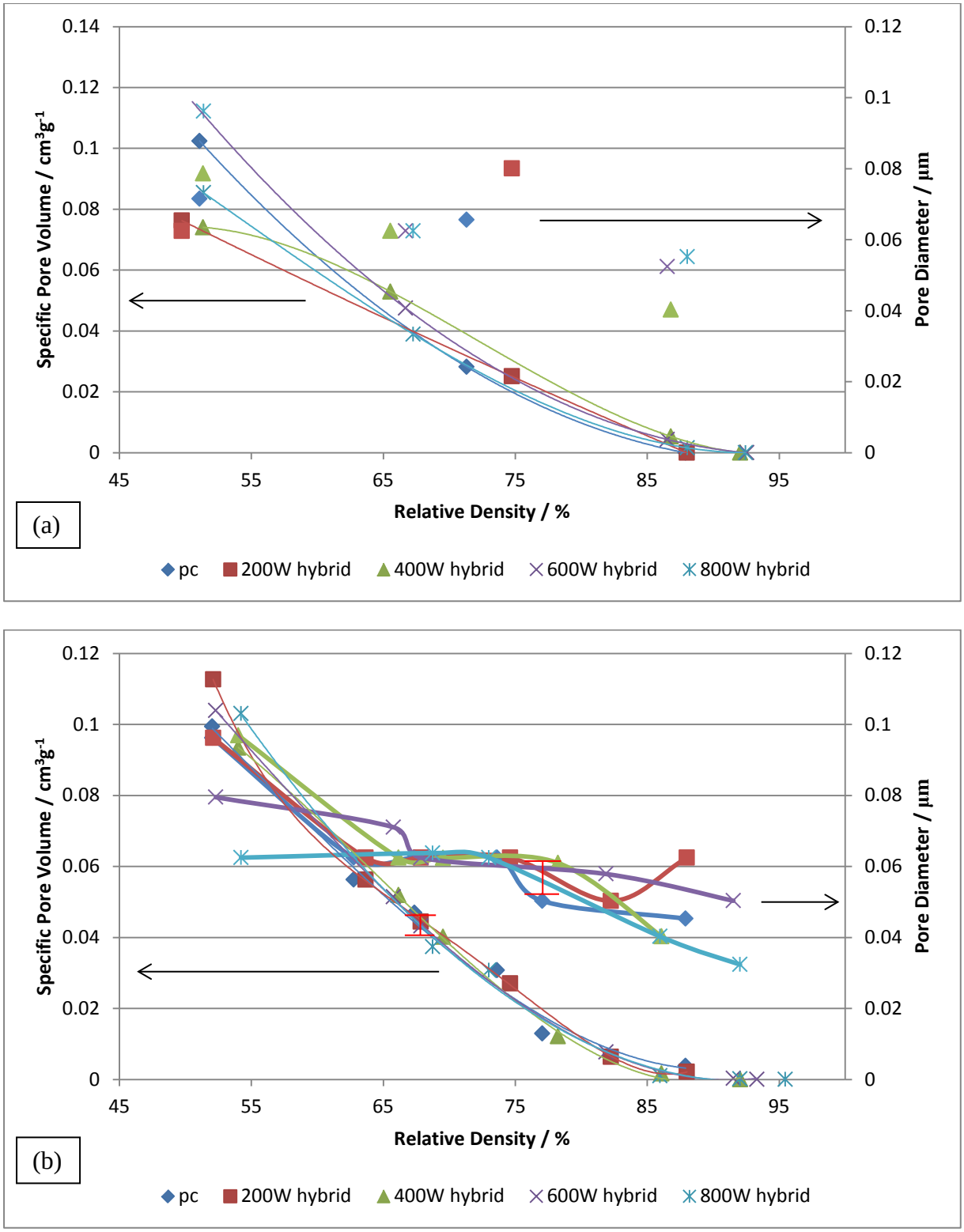

Figure 115 Comparison of pore volume and diameter vs. sample density for mercury porosemetry (a) before and (b) after change of the magnetron and experimental procedure

Between the two different experimental procedures, the samples after the change in experimental procedure followed this trend more closely. For the samples before the change the results show greater variation but, nevertheless, with their error bar as far it could be determined. Therefore it can be said that the general trend was the same for both experimental conditions.

The different trends in the comparison of the pore diameter vs. sample density, Figure 113 to 115, can be explained by the different measurement techniques. Mercury porosimetry determines the pore diameter by the pressured required to force mercury into the pores. This can lead to false results from so called ‘bottle neck’ pores that have a narrow opening into the pore as discussed earlier. Therefore measurements can show a larger pore volume than expected for a given pore diameter and a trend of an apparent reduction of the pore diameter. However, all trends show that the pore diameter is not affected by the microwaves. At a given density, the pore diameter is the same for every sintering condition; only the measured value varies with the measuring technique used.

After these finding, the development of the internal microstructure was compared, Figure 116 to 118, for conventional and 800 W hybrid sintered samples at different densification stages. Note that only samples produced using the experimental procedure adopted after the magnetron change could be cross-sectioned, because for the earlier samples none were left for this investigation.

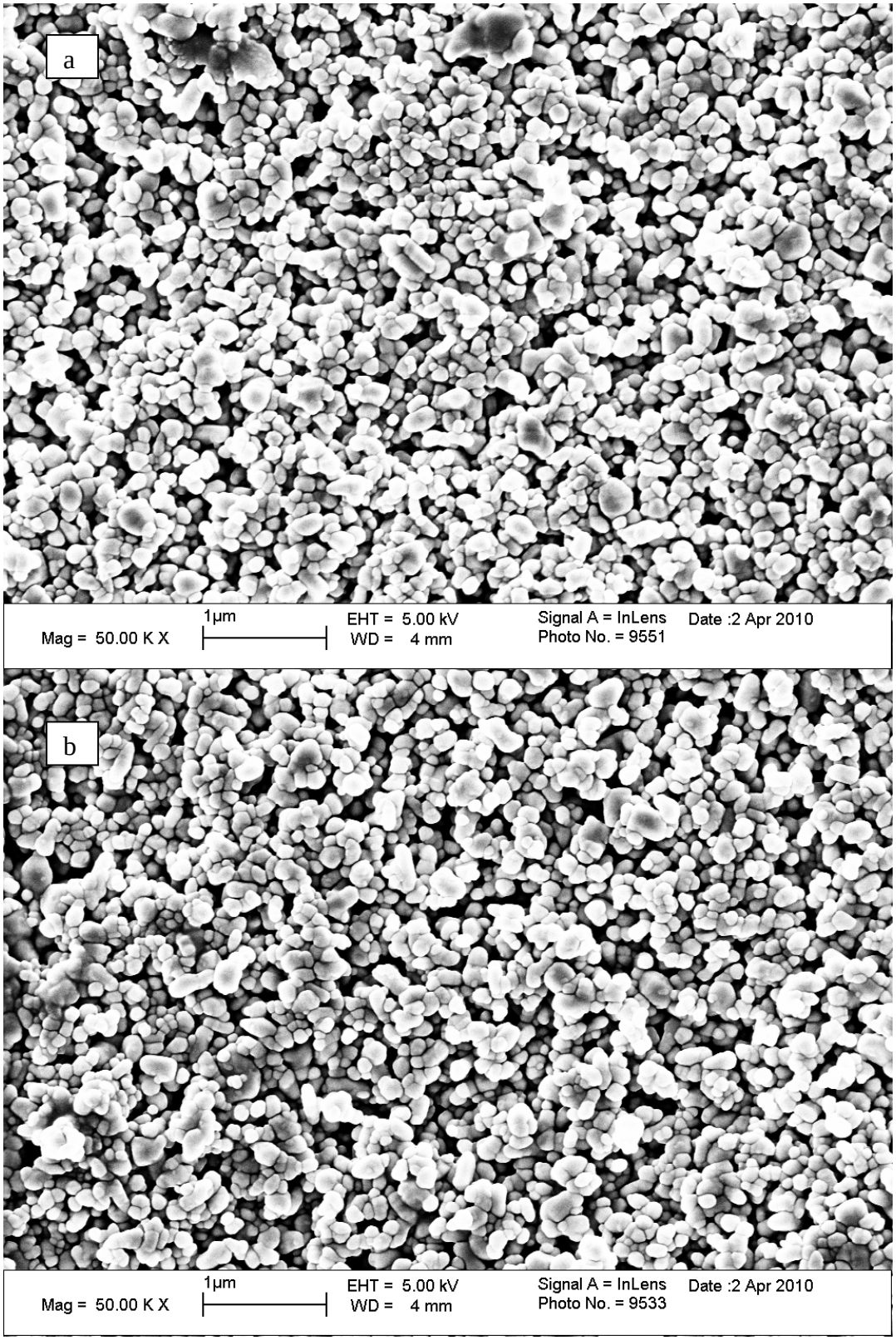

Figure 116 Internal microstructure of submicron ZnO samples sintered at 54% theoretical denstiy (a) Conventional (800°C 0.1 min), (b) Hybrid 800 watts (800°C 0.1 min)

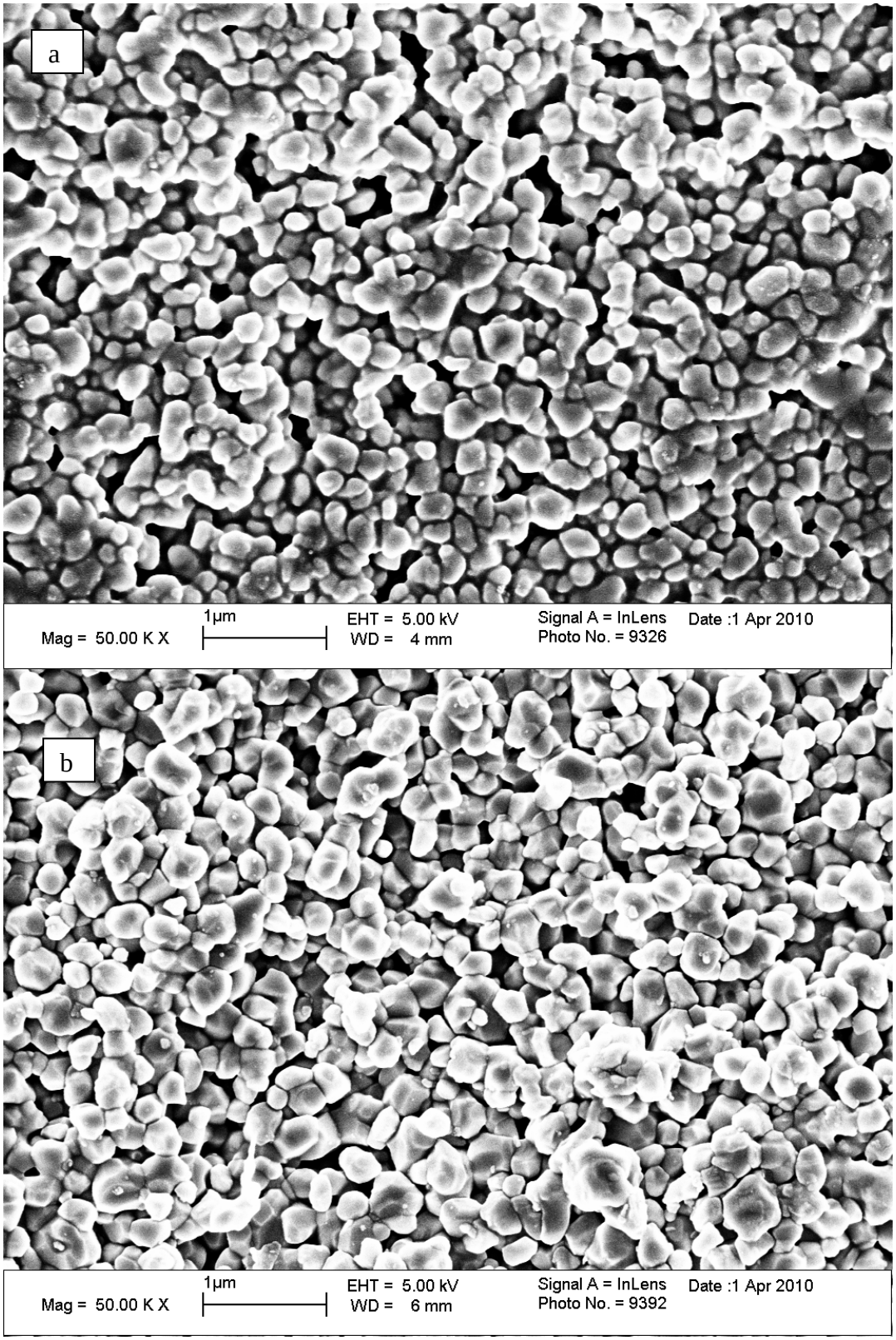

Figure 117 Internal microstructure of submicron ZnO samples sintered at 70% ± 1% theoretial density (a) Conventional (800°C 30 min, 71 % TD), (b) Hybrid 800 watts (800°C 15 min, 69 % TD)

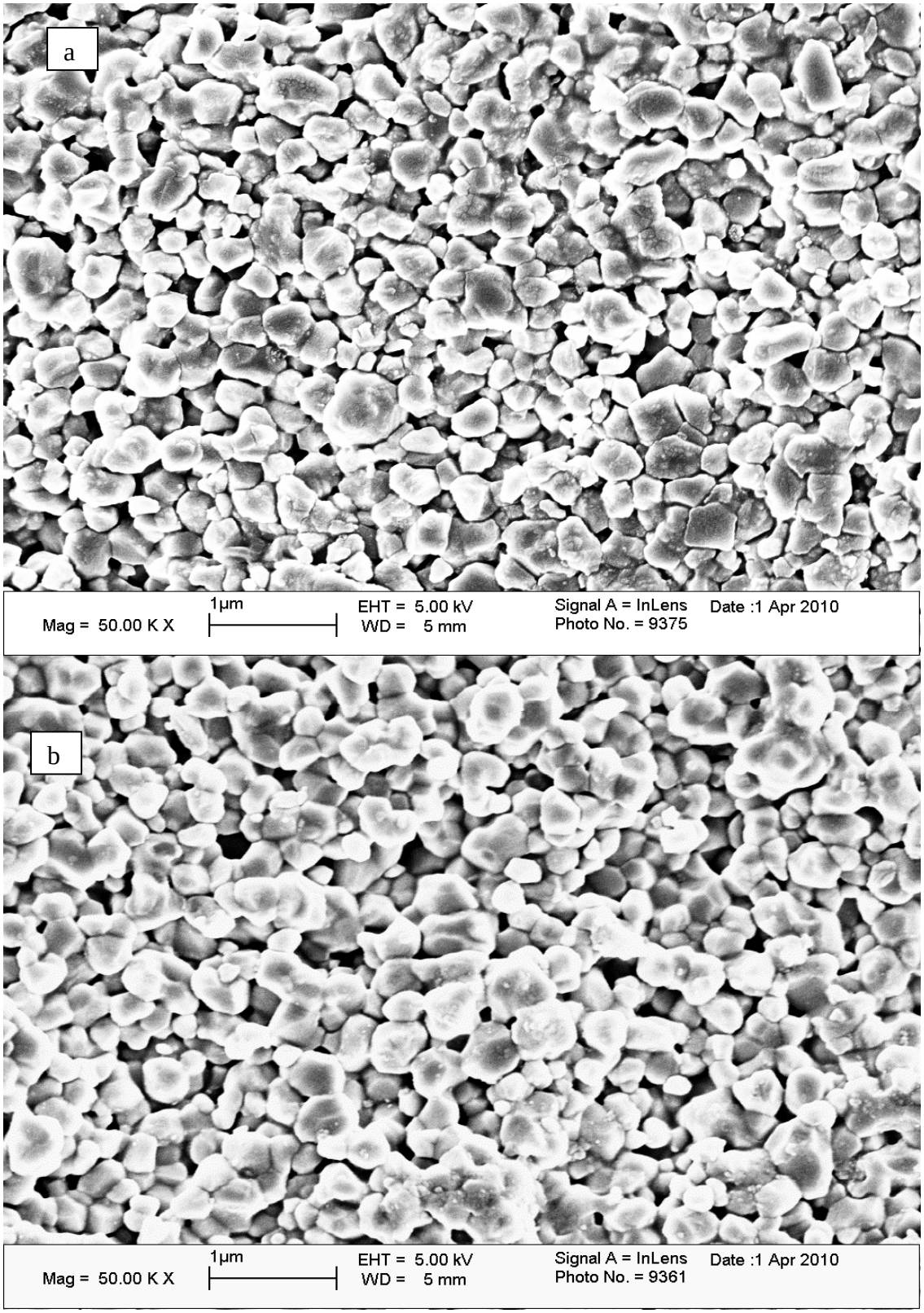

Figure 118 Internal microstructure of submicron ZnO samples sintered at 88% theoretical density (a) Conventional (800°C 60 min), (b) Hybrid 800 watts (800°C 30 min)

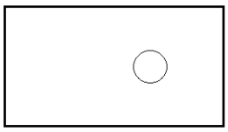

Figure 119 Area for the investigated internal microstructure

Figure 116 shows both samples after 6 s; densification had not really started. Therefore both samples look the same and both are still just packed particles with a large amount of porosity present. Figure 117 show both samples with a density of around 70% of the theoretical and, as expected, they look denser than before. For both, the rearrangment of the particles and neck forming has finished and neck growth and grain boundary lengthening is underway. This all leads to the denser impression, because all these processes lead to pore reduction and densification. Figure 118 show the samples at 88% of theoretical. In this stage of the densification the intermediate stage of sintering is slowly coming to a close. The neck growth and grain boundary lengthening have continued. This reduced the porosity further and increased the size of the grains. That no difference in the internal microstructure was found, confirmed the finding of the comparison of the pore volume/diameter vs. samples density.

Janney et al. [113] claimed that microwaves keep the pores of ceramic samples more open in the later stages of sintering. Therefore they thought the structural development for microwave sintering was different compared to conventional sintering. However these results show a completely different picture. This investigation demonstrated that the structural development is the same for conventional and hybrid sintering. A reason for the difference in the results could be in the experimental arrangements. The main difference was the furnaces used. Here a hybrid furnace was used compared to Janney's experiments where separate conventional and microwave furnaces were utilised, this brings the influence of different furnace parameters, such as temperature distribution, into play. This makes a comparison between conventional and microwave sintering difficult. In comparison, the use of a hybrid furnace has allowed the use of conventional and microwave heating at the same time. This has enabled the use of exactly the same temperature-time profile, where only the amount of the microwaves used is different. Further, Janney used different temperatures for conventional (1350°C) and microwave

sintering (950°C), which created a different thermal history for the samples and will have had an effect on the porosity. In addition, they used thermocouples for temperature measurement. Although they claimed that the thermocouple did not influence their microwave sintering, as Wang [29] demonstrated the use of a thermocouple can result in large differences between the actual sample temperature and the measured temperature. This could mean that the Janney et al. measured a false temperature for their microwave sintered samples.

The finding of these experiments, that hybrid sintering is “only” an enhancement of the existing structural development, does not disprove the theory of the ponderomotive effect suggested by Rybakov and Semenov [27]. It explains that microwaves increase the flux of near-surface charges, which can pass only in one direction through grain boundaries and hence create a directional flow. This has been demonstrated by Whittaker [34], Figure 80 section 2.5.4. Therefore microwaves can have an effect on the matter transport during sintering and with it on the densification, as demonstrated by Wroe and Rowley [33], Figure 79 section 2.5.4. In their work, as soon as they switched the microwaves off, the sintering curve dropped from the level of microwave sintering to conventional sintering and moved in the opposite direction as soon as microwaves where switched on. However all this can only happen if the sintering behaviour is the same because the ponderomotive force is best described as an additional driving force for sintering and not a radical change in the sintering behaviour. Therefore the conclusion of these porosity experiments was that the microwaves did not affect the development of porosity and that therefore the structural development was the same for conventional and microwave sintering. This indicates the theory of the ponderomotive effect could be the explanation for the “microwave effect” and microwaves act as additional driving force to increase the matter transport via diffusion.

Additional porosity investigation

In the early stage of the porosity investigation the sintering was also stopped during the heating from 500°C to 800°C at 600°C and 700°C to measure the porosity even at these points of the sintering. The idea for this came for the dilatometer experiments of Wroe & Rowley [33], Wang [29] and Lorenz [30], because all of these

investigations showed that the shrinkage increased as soon as the microwaves were switched on. This could have an effect on the porosity. However the measured porosity at 600°C and 700°C was not different to the measured porosity at 800°C for 6 s, see Figure 120. Therefore it could be said that the porosity was not affected by the microwaves before the samples reached the sintering temperature of 800°C. Hence porosity measurements at 600°C and 700°C were discontinued.

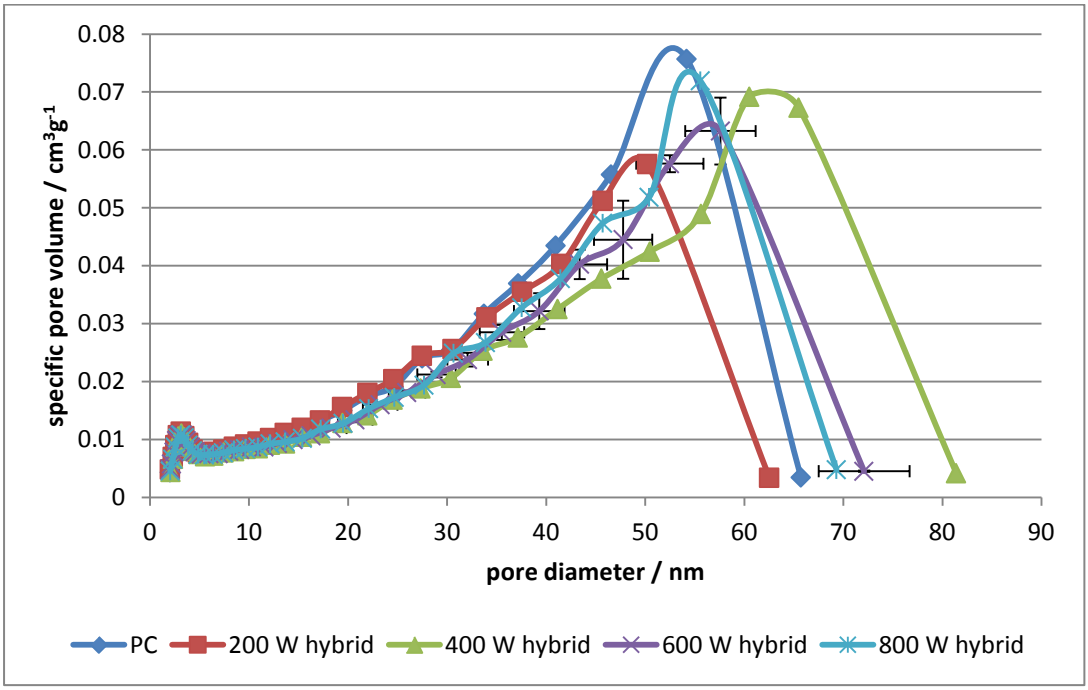

Figure 120 nitrogen adsorption porosity curve for ZnO samples sintered at 700°C for 6 s

Solid-state reactions

The porosity experiments indicated that the enhancement in the densification was caused by enhanced diffusion, the investigation into the solid-state reaction between MgO/ZnO and alumina was designed to show whether enhanced diffusion would be found from solid-state reactions. If microwaves enhance diffusion then it should result in a higher reaction rate and hence thicker spinel layer. This chapter is subdivided into the different spinels, magnesium aluminate spinel ($MgAl_2O_4$) and zinc aluminate spinel ($ZnAl_2O_4$).

Magnesium aluminate spinel

For the solid-state reaction experiments it was decided to use MgO and Al_2O_3 to create $MgAl_2O_4$. The reasons behind this decision were that most of the spinel reactions via microwave reaction sintering were demonstrated with this spinel, see section 2.5.4. In an attempt to reduce the reaction temperature nano-material for both reaction partners were used. The first idea for mixing the material in a ratio of 1:1 was to produce a suspension of each and mix them together. The suspension liquid for the raw materials would be ethanol, because MgO would react with water to form magnesium hydroxide. Before the mixing was attempted, the zeta potential of the MgO- and Al_2O_3-suspension had to be measured to determine whether the suspensions would be stable and if they would agglomerate or stay dispersed after mixing. For this reason the zeta potential of the two suspensions was measured with the Acoustosizer.

The Acoustosizer test revealed that the initial pH for both suspensions was around 9 and the isoelectric point was pH = 8.5 for the alumina suspension and pH = 6 for the magnisa suspension. However the stable zeta potential was positive for MgO and negative for alumina. Therefore without any treatment the two materials would agglomerate after they are mixed together since different charges will be pulled together. A potential dispersant would be tetramethylammonium hydroxide (TMAH) or acetic acid [114, 115].

However before any dispersant could be tested the Acoustosizer broke down and it was unknown how long the repair would take. Therefore a slip casting attempt, a proof of concept, with the untreated mixture was undertaken. After the slip casting it was found that the surface of the casting mould was damaged in the form of softening of the surface of the plaster of Paris block and was most likely caused by dehydration of the plaster due to the used ethanol. Due to the problems with the Acoustosizer and the slip casting it was decided to abandon the wet preparation route and use a dry route.

For the dry green forming the MgO and Al_2O_3 powder were mixed in ethanol and ball milled with ZrO-balls for 21 h. After the ball milling the wet powder was dried and used for die pressing. After die pressing the mixture, the pellets were cross sectioned and investigated with EDS. There it was found that Al and Mg were in close contact and nicely distributed, see Figure 121. At this time it was realized that the sample preparation was on a false track, because this kind homogenous mixture of the raw material would good for a proof of concept study. This kind of study had already been done, see section 2.5.4. Also outcome of the reaction of this homogenous mixture would be transformation of the raw materials into spinel. Since the reaction partner were in close contact with each other it would be likely that the transformation would none or 100%. Therefore it would be difficult to gain information about the reaction rate. The safer and easier way to gain information about the reaction/diffusion rate is the creation of a reaction interface. The spinel reaction would take place at this interface and the thickness of the reaction phase could be directly linked to the reaction/diffusion rate.

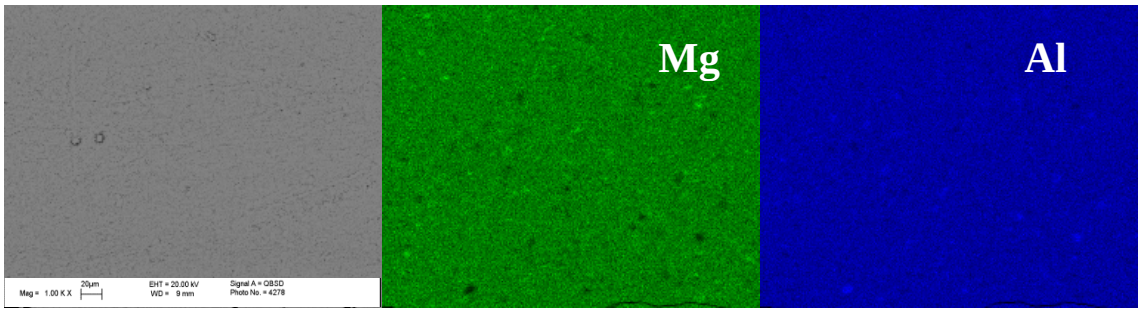

Figure 121 EDS map of die pressed MgO and Al_2O_3 mixture sample (scale for SEM picture: 20 µm)

The first idea to create an interface was to die press pellets of MgO and Al_2O_3 and place them at top of each other during the reaction sintering. The die pressing of Al_2O_3 was done without any problems. However the MgO powder was not ideal for die pressing, because even a few grams of powder were voluminous and the powder in the die had to be slightly compressed by inserting the upper die into the die several times before the whole powder load was in the die, see Figure 122. During the pressing, the powder creeped everywhere and stuck to the die, which resulted into problems to get the pellet out of the die and the pellet circular surfaces were

damaged every time, which made the production of a pure and undamaged MgO sample impossible.

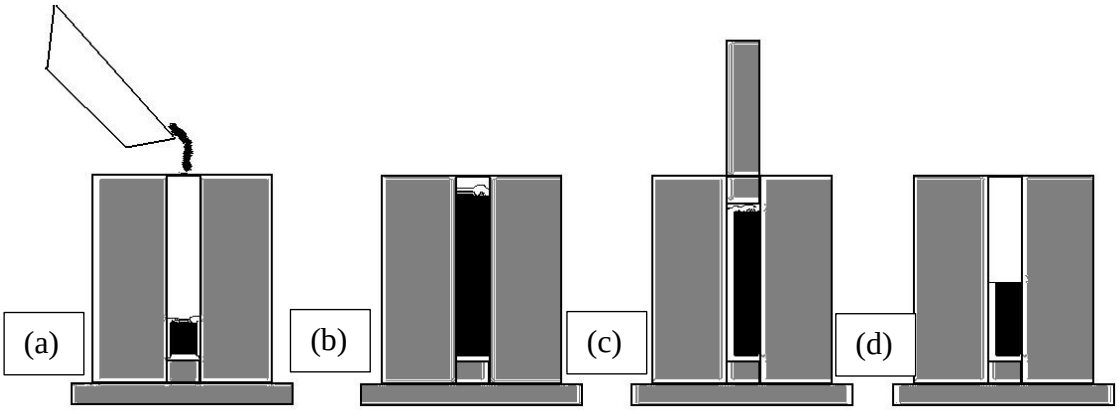

Figure 122 schematic of die pressing of nano alumina to create reatcion couples (a) filling the die, (b) stop filling when powder reach the top of the die, (c) insert upper die and use gravity to compress powder in die, (d) remove upper die and restart cycle until all powder is filled into the die

The first idea to solve the die pressing problems with MgO was to agglomerate it with hexane. For this the powder was mixed with hexane and dried. However this did not solve the problem, in that the pellet stuck to the die punches so that the circular surfaces were damaged when the pellet was removed from the die.

The problem of the stickiness was solved by placing a layer of Al_2O_3 powder at the bottom of the die and on the top of the MgO powder in the die. This enabled the production of 10 mm diameter MgO pellets with a layer of the Al_2O_3 on the two circular surfaces. For the reaction couple the MgO pellet was placed on an Al_2O_3 powder in a partially filled 25 mm diameter die. After the placement the rest of the Al_2O_3 powder was filled into the die and the Al_2O_3 with the MgO core was die pressed, see Figure 86.

After the die pressing the combined pellet was heated using a similar heating cycle to the porosity investigation. At first the samples were heated to 500°C and hold at this temperature for 1 h. At the end of the holding the temperature was increased by initially 10°C min^{-1} to the reaction temperature, here 1450°C. The heating rate was

reduced compared to the porosity experiments, because at temperature of 1000°C or above the conventional part of the furnace has not the ability to achieve such high heating rate. After the first heating cycle the heating rate was reduced further to 5°C min^{-1}, because the pure conventional heating could maintain the heating rate beyond 1300°C. At 1450°C the temperature was held for 2 h. The heating conditions used to prepare samples were pure conventional and 800 W hybrid heating. After the heating the samples were cross-sectioned and investigated by FEG-SEM. There it was found that no reaction had taken place and that the MgO pellet was cracked. Further it was found that Al_2O_3 pellet was not connected to its MgO core and that between the two materials was a considerable gap, which was big enough for MgO core to fall out when the pellet was tilted. A factor for the gap could be shrinkage during the sintering.

After the difficulties to prepare a reaction couple of MgO and Al_2O_3 with a reaction interface and unable to bring them to a solid-state reaction, it was decided to stop with the system MgO- Al_2O_3 and changed to the system ZnO- Al_2O_3.

Zinc aluminate spinel

The first task was to create an interface between the reaction partners. As the means to create the interface and the reaction couples, die pressing was chosen, because it could be done for both materials without any greater difficulties. Ideas for the creation of an interface were:

- Sintered and polished ZnO and Al_2O_3 pellets stacked on top of each other
- Shell and core
- ZnO and Al_2O_3 layer pressed together
- Green ZnO and Al_2O_3 pellets stacked on top each other

Test samples for all the interface ideas were produced. These samples were heated to 1200°C for 2 h by pure conventional and 800 W hybrid heating. All the samples

were cross-sectioned and checked to see if a reaction product had been created. Further, the cross-section of the green bodies for the shell/core and layer pressing ideas were investigated with the FEGSEM to check the quality of the interface between ZnO and Al_2O_3.

Sintered and polished ZnO and Al_2O_3 pellets stacked on top of each other

The powder of ZnO and Al_2O_3 was die pressed into pellets and sintered to high density (ZnO =95% of theoretical density, Al_2O_3 =98% of theoretical density). After sintering one of the circular surfaces was polished to a smooth finish for each material and as perfect as possible contact between the surfaces of ZnO and Al_2O_3 created. These treated samples were stacked into the hybrid furnace. The stack was arranged such that the polished surfaces were in contact with each other and that ZnO pellet was on top of the Al_2O_3 sample and faced the OFT. The reason for the latter has been explained (see p. 118); in brief it was to avoid the potential risk of a thermal runaway at temperatures above 1000°C. With the OFT monitoring the temperature of the more microwave absorbing pellet, the control program of the hybrid furnace was better able to regulate the temperature.

After the pure conventional and 800 W hybrid heating cycle to 1200°C for 2 h the samples were cross sectioned and prepared for FEG-SEM. The results revealed that no reaction had taken place; no trace of any reaction product was found.

Shell and core

In this case one of the materials, ZnO or Al_2O_3, was pressed into a 10 mm diameter pellet that was placed on a powder bed of the other material in a 25 mm die. After the remaining powder of the powder bed material was poured into the die to

surround the core sample, it was compacted into the shell for the combined sample. This provided a good contact between the two phases, see Figure 123.

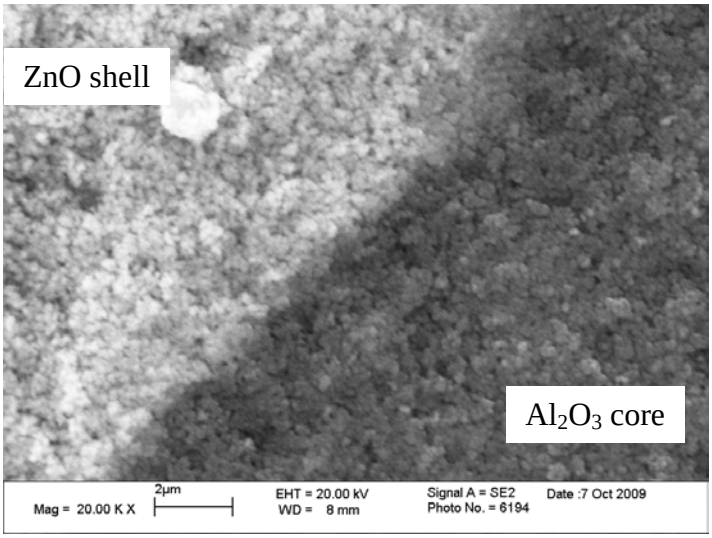

Figure 123 Interface between ZnO shell and Al_2O_3 core in the green body

Because of the potential of a thermal runaway at temperature above 1000°C, a shell of ZnO was the better setup to help the control of the sample temperature. Otherwise without careful temperature control it could be possible to melt the ZnO core inside the Al_2O_3 shell. Figure 124 shows that a reaction product was created. This FEG-SEM investigation revealed another problem with this arrangement, however. The solid-state reaction would take place all around the core sample, because the entire core surface would be the interface for the reaction. This would make the identification of the reaction mechanism, solid-state or solid-vapour, almost impossible, because a solid-vapour could take place even at a distance from the contact interface.

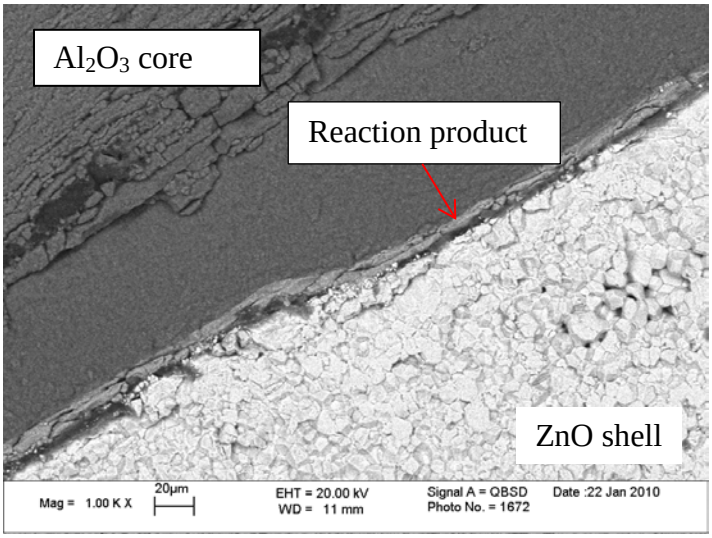

Figure 124 Interface between ZnO shell and Al_2O_3 core after 800 W hybrid heating at 1200°C for 2 h

ZnO and Al_2O_3 layer pressed together

In this case ZnO and Al_2O_3 powders were poured on top of each other into a die and pressed. The cross section of this pellet showed a very good contact between the reaction partners. However it was be very difficult to identify the interface, see Figure 125.

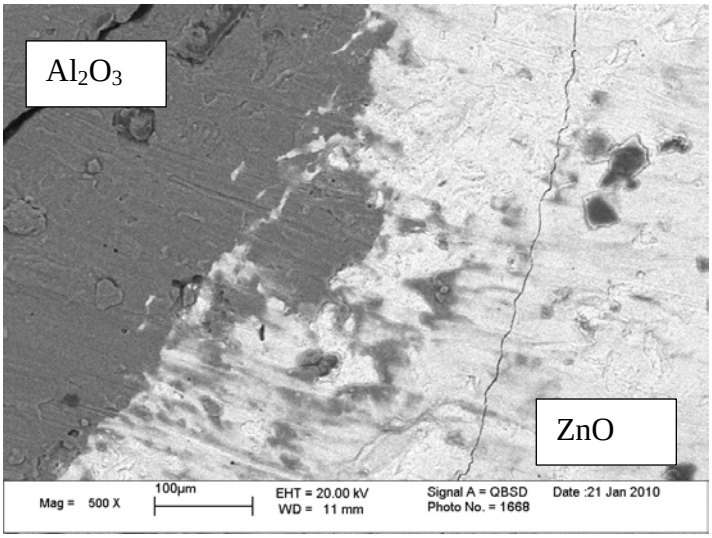

Figure 125 Interface for the ZnO and Al_2O_3 layer pressed together in green boy

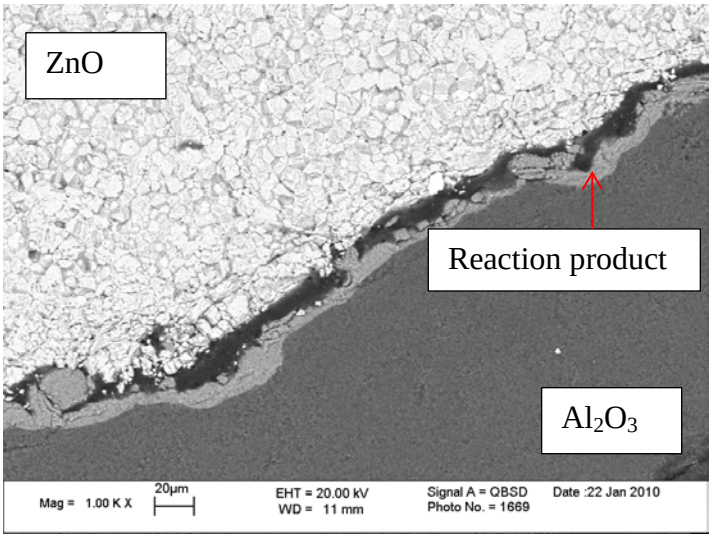

Figure 126 Interface for the ZnO and Al_2O_3 layer pressed together after 800 W hybrid heating for 2 h

After the heat treatment it was found that a reaction product was formed, see Figure 126. However the reaction layer was very uneven and had large thickness variations. All this resulted in problem with measuring the reaction layer.

Green ZnO and Al_2O_3 pellets stacked on top each other

For this arrangement the pellets of ZnO and Al_2O_3 were pressed and placed on top of each other, again with ZnO at the top. After heating to 1200°C it was found that the samples remained separate bodies but a reaction product had been created. The reaction product adhered to the alumina but separated from the ZnO on cooling due to the difference in the thermal expansion of the materials. Nevertheless, the advantages of this setup were that both reaction partner could be easily produced by die pressing and the potential interface was easy to define since the contact area was the between the two samples was the only possible place for the reaction as long the reaction was a solid-state reaction. A solid-vapour reaction could be identified by the creation of a reaction product outside of the contact area such as the sides of the samples.

Therefore the approach with the stacked green samples was used for the full investigation. The initial reaction temperatures were increased to 1300°C and 1400°C to create a larger reaction product layer. Due a mistake in the furnace programming the holding times were different for 1300°C it was 5 h and 4.5h for 1400°C. The cross section of the Al_2O_3 part of the samples revealed the reaction product layer, Figure 127. Interestingly, the thickness of this layer was equal for both sintering conditions and the cross section revealed a layer of ZnO on top of the reaction product layer. This had not been observed in the samples heated at 1200°C. Due to the presence of this layer and lack of a difference in the reaction layer thickness at 1300°C and 1400°C the investigation of the cross section was continued and a reaction layer outside of the contact area was found, Figure 128. As there was no direct way for the material to be transported via diffusion the ZnO had to be transported as vapour. Therefore the reaction mechanism for these heating cycles at 1300°C and 1400°C was solid-vapour; this also explained that the ZnO layer on top of the reaction product was the condensate of the ZnO vapour. This would also explain why there was no difference in the thickness of the reaction product layer. Since a sloid-state reaction was desired, so that it had a change of being influenced by the used of microwaves. The reaction temperature was reduced to 1100°C and the reaction time varied to change the thickness the reaction layer.

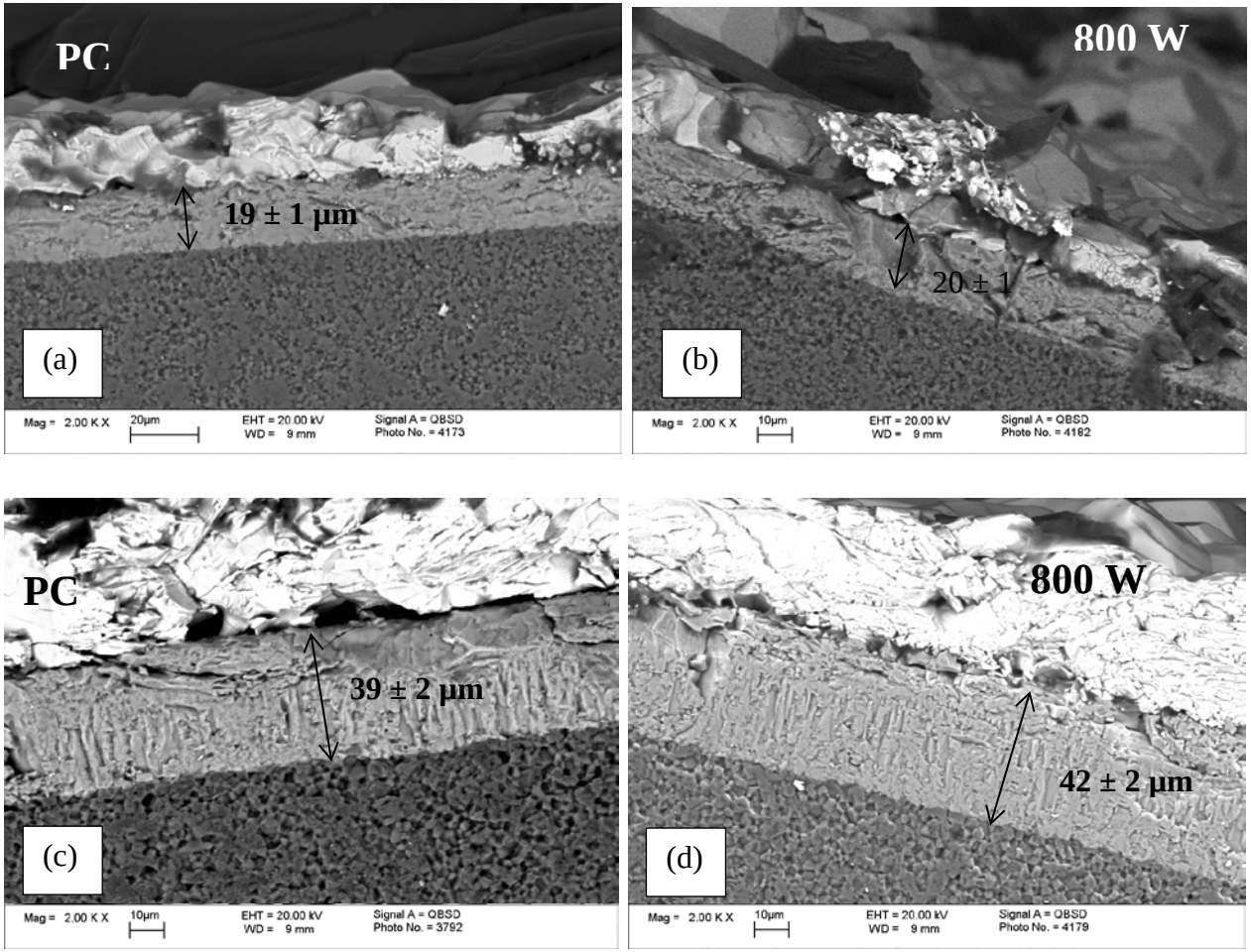

Figure 127 BSE micrograph of (a,c) pure conventional and (b,d) hybrid reaction sintered samples after 5 h at 1300°C (a,b) and 4.5 h at 1400°C (c,d)

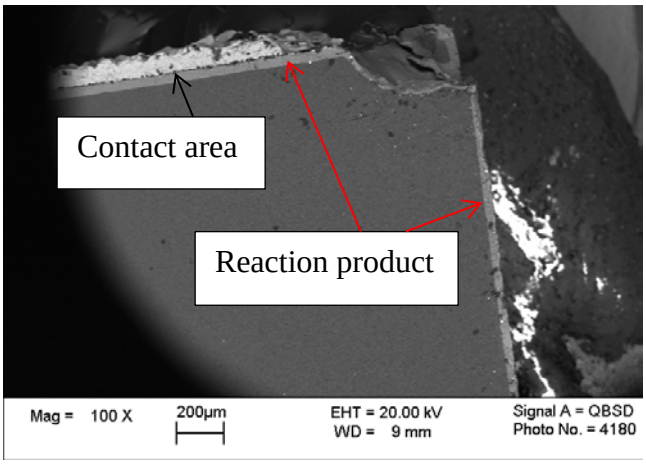

Figure 128 BSE micrograph of 800 W hybrid reaction sintered samples 4.5 h at 1400°C

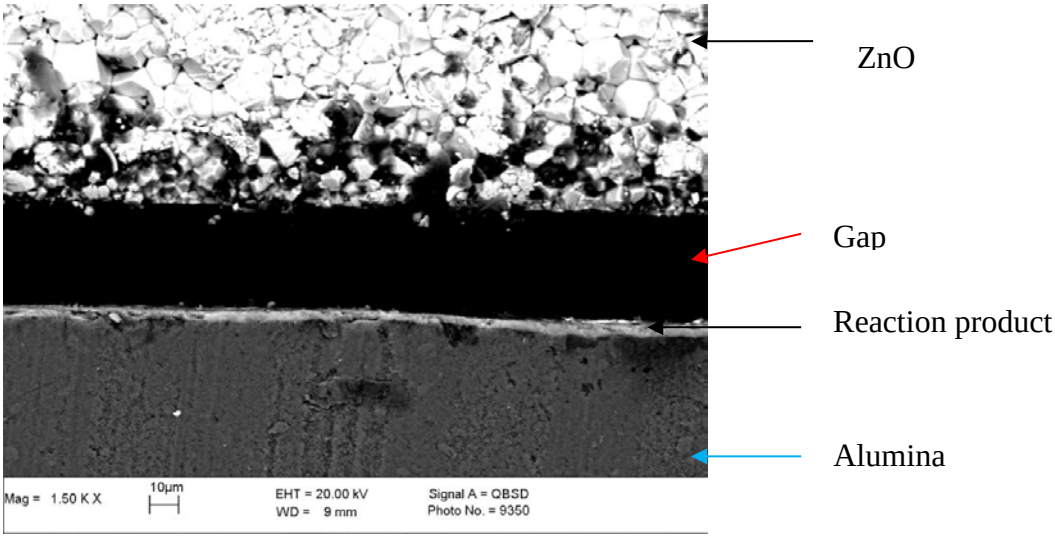

Figure 129 BSE micrograph of 800 W hybrid reaction sintered samples after 2.5 h at 1100°C

The BSE pictures, Figure 129, show clearly that the reaction product, i.e. the spinel layer, adhered to the alumina but separated from the ZnO on cooling to leave a gap. Ignoring the dark region of the gap, the BSE detector recognized 3 different back scattered electrons intensities, these intensities, white, bright grey and dark grey, represent different materials, see section 3.1.3.

In addition to the BSE imaging, EDS mapping was used to investigate local compositional variations.

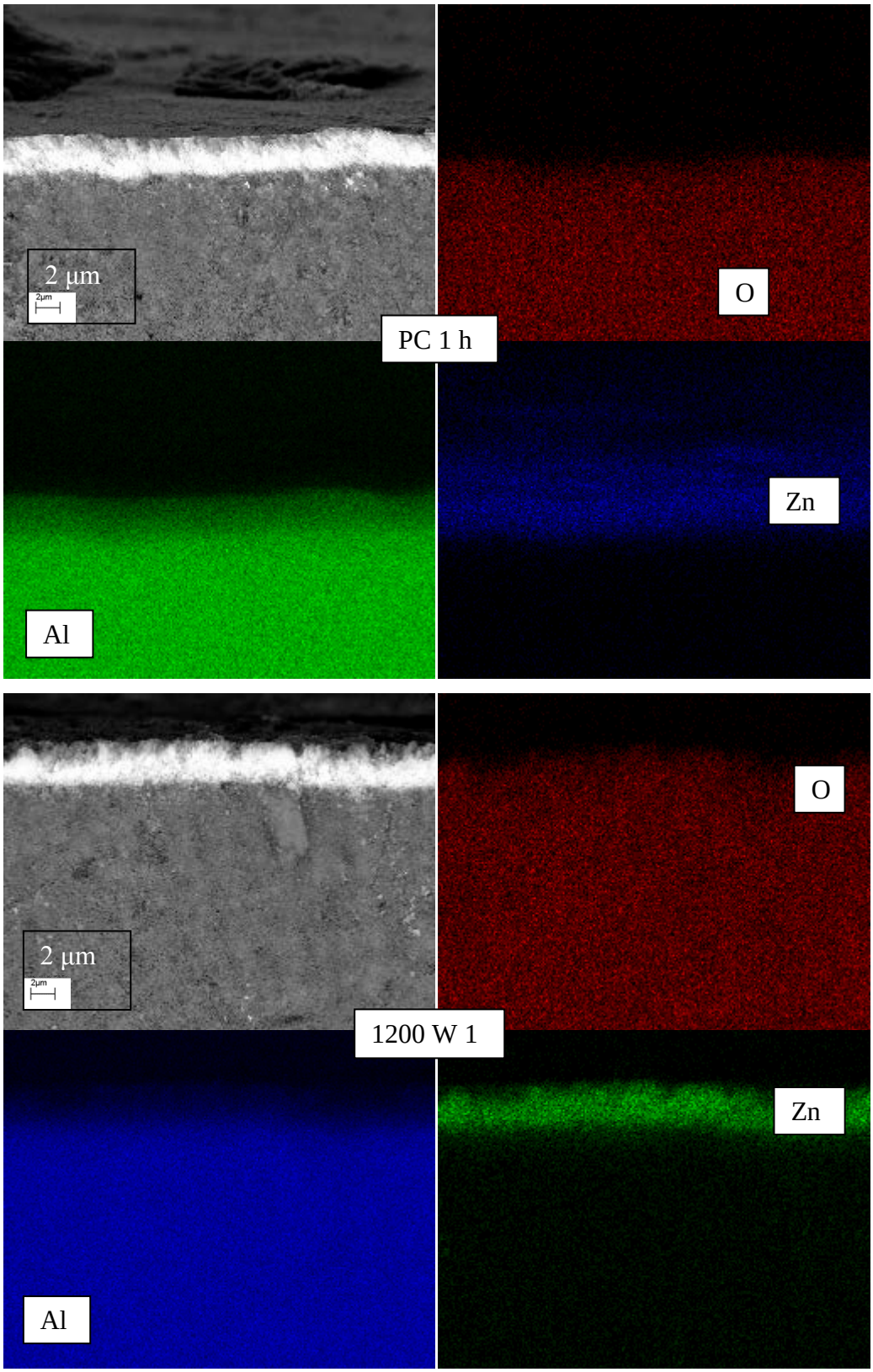

Figure 130 EDS map of alumina sample with reaction layer after a reaction time of 1 h using pure conventional and 1200 W hybrid heating

Since the reaction product was only present on the surface of the alumina sample on the side which had been in contact with the ZnO, the EDS mapping was focused on the alumina/reaction product interface. The results may be seen in Figure 130. The mapping of O, Al and Zn demonstrate that O and Al were present in both phases, though the level of the latter was reduced in the reaction layer compared to the rest of the sample. Zn was only present in the reaction layer, since the ZnO phase was separated by a gap and hence not examined. It is known that the only phase in the $ZnO\text{-}Al_2O_3$ system is $ZnAl_2O_4$, which suggests strongly that the spinel was produced. This was further confirmed by the similar EDS spectra for the reaction layer after the reaction of 2.5 h for pure conventional and 1200 W hybrid heating, Figure 131.

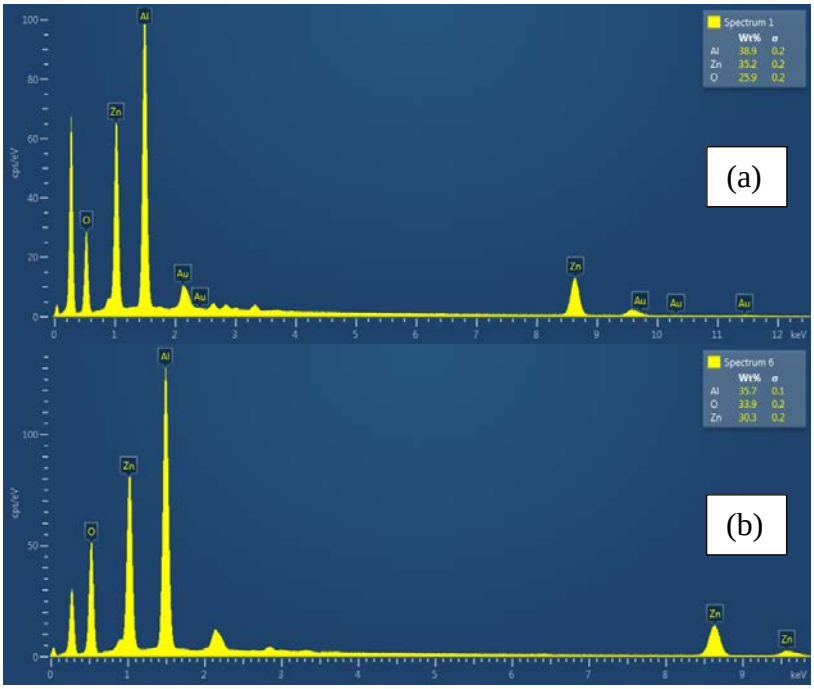

Figure 131 EDS spectrums for reaction product layer after the reaction time of 2.5 h using (a) pure conventional and (b) 1200 W hybrid heating

After it was confirmed that spinel was produced, the reaction layer thickness was measured from the BSE images, some of these images are shown in Figure 132. It can be seen that the use of microwaves increased the thickness of the spinel layer compared to the conventionally heated solid-state reaction.

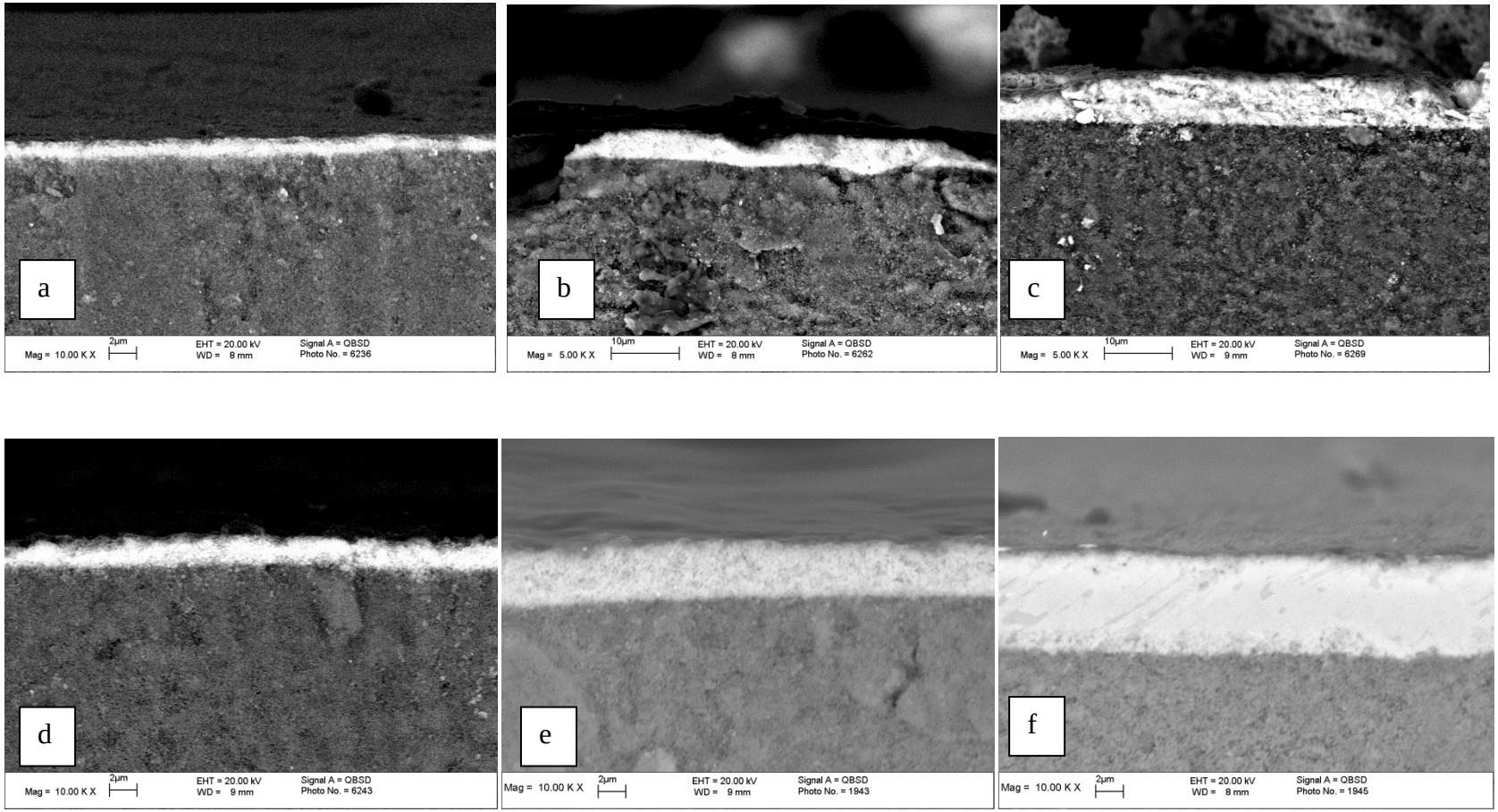

Figure 132 BSE of the spinel layer for pure conventional (a-c) and 1200 W hybrid (d-e) solid-state reacted samples for 1 h (a, d), 5 h (b, e) and 15 h (c, f)

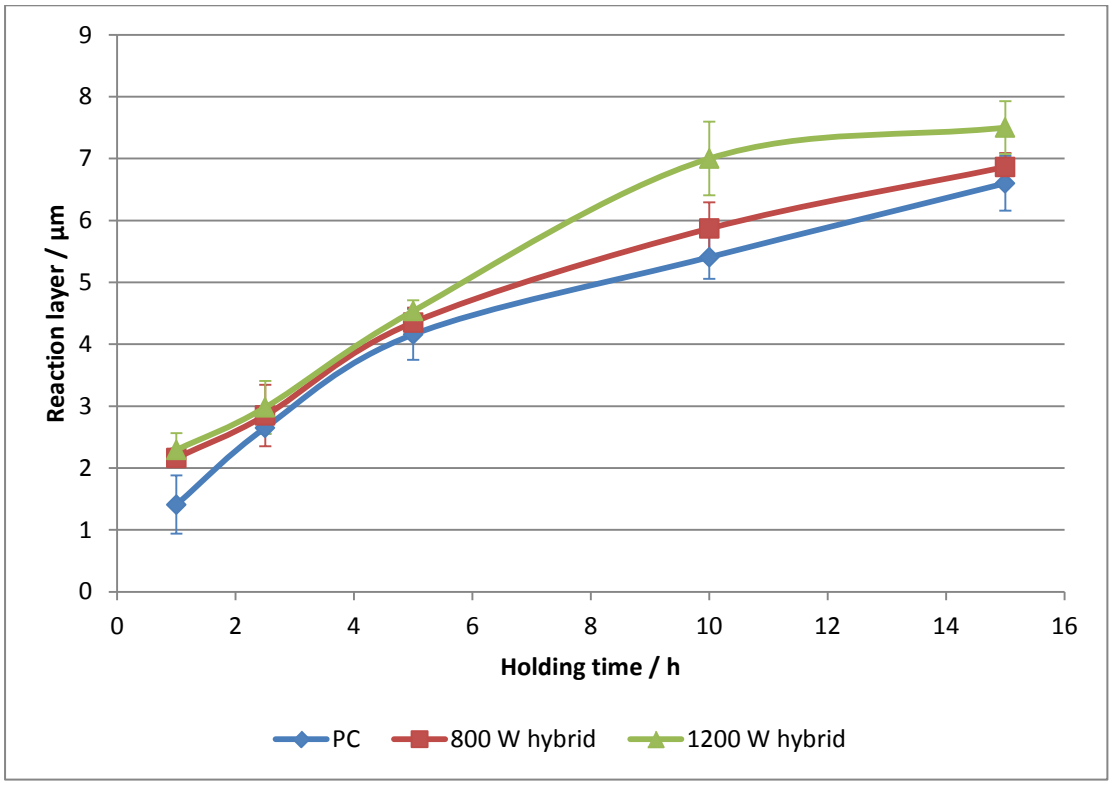

Figure 133 Reaction layer thickness vs. holding time

Figure 133 shows that the thickness of the reaction layer increased with both time and a greater microwave contribution to the heating. The growth of the layer for all reaction conditions followed a square root function; this confirms that the reaction was diffusion-controlled and, therefore, it can be concluded that the hybrid heating enhanced the diffusion of the reactants, because matter transport by diffusion is the limiting factor for the reaction rate in a solid-state reaction, see section 2.3.1. In contrast to the densification work, the effect of microwaves was quite small compared to the conventional reaction. One reason for this is that in the latter stage, from 2.5 h onwards, the samples, especially the ZnO, reached high densities. This would reduce the potential for diffusion because the free energy in the system was already at a low level. Further, the higher density increased the resistance for diffusion and the effect of microwave was further reduced by the ZnO grains being quite large, see Figure 129. These large grains will have reduced the number of interfaces. If the ponderomotive effect suggested by Rybakov et al. [27] and

supported by the densification experiments, is true then a reduction in the number of interfaces leads to a smaller effect for microwaves, because the interfaces are needed as a semi-penetrable barrier for the directional flow of the charges. Therefore, relatively high amounts of microwaves were required to achieve a significant difference in the growth of the spinel layer. After 2.5 h and 5 h the difference between the reaction product layers was only marginal, because the difference in the reaction time was too short to show any difference between the different reaction conditions. As the solid-state reaction continued, the 1200 W hybrid solid-state reaction created a thicker reaction layer than the other conditions. However at 15 h the difference between the measured spinel layers was much smaller than after 10 h.

A possible explanation for the difference in the thickness of the reaction layer obtained from the hybrid-heated solid-state reaction compared to the pure conventional conditions after 1 h is the fact that green bodies were used for the diffusion couples, thus there will have been an initial densification prior involved. It has already been demonstrated that microwaves can enhance densification and hence it is not surprising to see an enhanced initial effect for the microwave hybrid heated samples. Initially fully sintered ZnO and alumina samples had been tried for solid state reaction, but after a reaction time of 4 h no trace of a reaction layer was detected. However after 1 h the rate of growth of the reaction layer for the conventional and hybrid heated samples became more or less the same up to at least 5 hours. This may be for a similar reason that the microwaves enhance densification most during the intermediate stage compared to either the initial or final stages; there are more interfaces present for the ponderomotive effect to interact with. It would have been interesting to extend the reaction time beyond 15 hours to see if the conventionally heated samples ‘caught up’ with the microwave hybrid heated samples, however this was not realistic since the hybrid furnace could not be left running on its own overnight and it was not allowed to conduct experiments throughout the night. There is possibly a hint in the 1200 W hybrid data of a decrease in the rate of formation between 10 and 15 hours, but it is dangerous to over analyse what is just two data points.

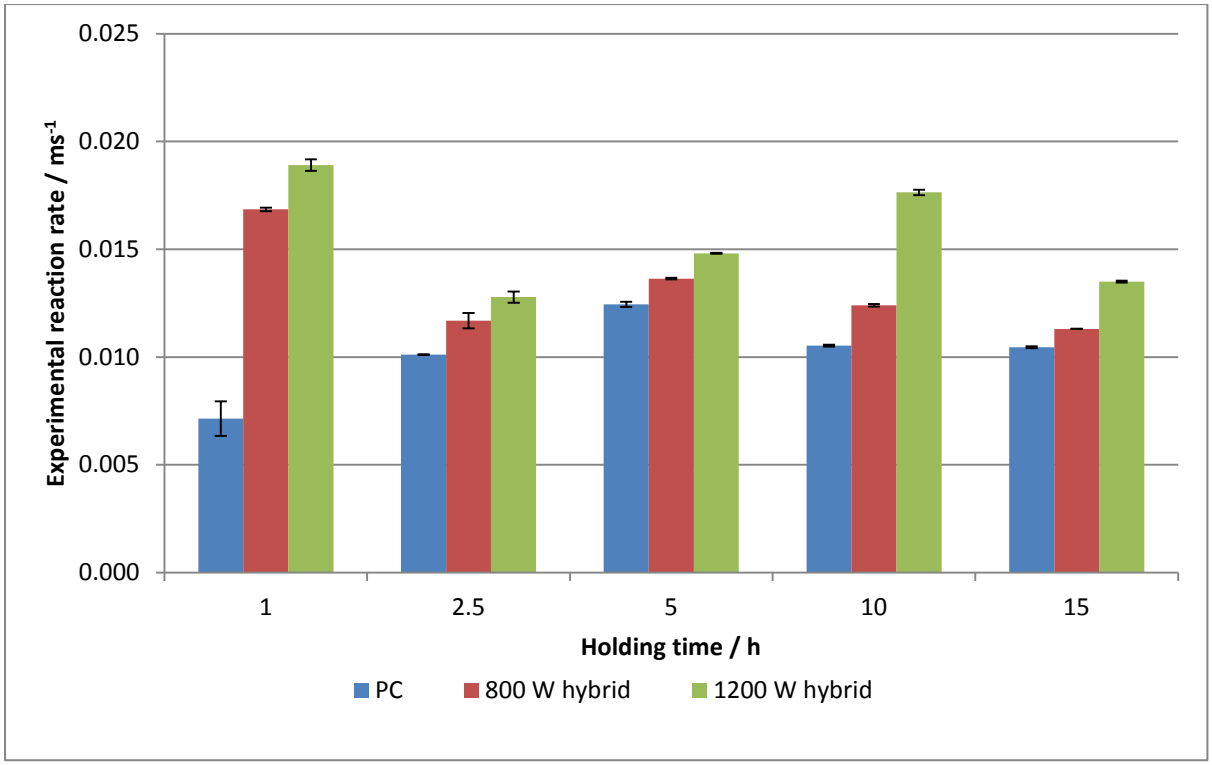

Figure 134 Experimental reaction rate constant

The impression that 800 W hybrid heating behaves in similar manner to pure conventional heating is confirmed when the calculated experimental reaction constants are compared, see Figure 134. After the reaction in the 800 W hybrid heated sample dropped from its highest level, the reaction rates for both reaction conditions rose from 2.5 h to 5 h. After this, the reaction rate was reduced for both. This drop was expected because with the growth of the spinel layer the distance between reactants increased and the density of the layer increased as well. This led to the reduction of the reaction rate. However, the reaction rate reduction was different for the two heating regimes since the conventionally heated samples saw a decrease in their reaction rate to a lower level where it then stayed constant. In contrast, the 800 W hybrid heated solid-state reaction reduced its reaction rate over time and the decrease in the reaction rate was not as big as for pure conventional heating. The experimental reaction rate underlines that the 1200 W heated solid-state reaction was influenced by the use of microwaves, because the reaction rate increased from 2.5 h until 10 h and then dropped again to a lower level at 15 h. If the reaction rate would have continued to decrease as for 800 W or stayed constant

cannot be said because no experiment beyond 15 h has been undertaken. The increased reaction rate for the microwave assisted solid-state reaction could be only caused by an enhanced diffusion for the Zn-ions, because the diffusional transport is the limiting factor for the solid-state reaction. Since no additives and the same temperature-time profile was used only the usage of microwave could be the cause for this. Therefore microwaves had created an additional driving force to increase the diffusion and with it the reaction rates. This additional driving force is also the reason that the 1200 W hybrid solid-state reaction rate was still increasing until 10 h whilst the reaction rate for the other heating conditions was reduced to a lower value than after 5 h.

It can be summarised that microwaves have an effect on the solid-state reaction to form spinel, however to achieve it, large fractions of microwaves are required. May be enhancement of the solid-state reaction requires a minimum amount of microwaves, as seen by the densification. However here it seems that the minimum amount of microwaves is above 800 W. 1200 W of power might be the “transition” amount. However without experiments using higher amounts of microwaves it cannot be said at which point in the function between the effect on the reaction rate and the amount of microwaves the use of 1200 W lies.

What is responsible for the increased reaction rate observed for the 1200 W hybrid-heated samples? Figure 133 demonstrates that all sintering conditions follow a square root function, which means all of them are diffusion based solid-state reactions. Methods to increase the reaction rate are to increase the reaction temperature, or time, or to use additives. Since no additives were used and the temperature-time profile was the same for sintering condition, the only remaining difference is the amount of the microwaves used. The possibilities for microwaves to influence the solid-state reaction are the inverse temperature field or an increase of the matter transport as suggest by the ponderomotive effect. The inverse temperature field that microwaves can create is unlikely to influence the solid-state reaction, because if the hottest point in the samples was in the centre than their surface temperature would be decreased and the reaction rate would be reduced, if

not completely halted. The only possible explanation left is that microwaves increase the matter transport, because only if increased amounts of ZnO were transported would the reaction rate increase. The reason for this is that the rate of matter transport via diffusion is the limiting factor in the solid-sate reaction and the chemical reaction is much faster than reaction material can be transported to the reaction zone. Therefore to increase the reaction rate more material has to be transported to the reaction zone. How can microwaves increase the matter transport? The previous investigation of the reduction of the porosity demonstrated that the sintering behaviour was the same for conventional and microwave sintering. Therefore it can be assumed that the reaction behaviour was the same between conventional and hybrid solid-state reaction. This assumption is underlined by the development of the reaction layer thickness, because all the reaction layers follow the function of a square root, which indicates the process for all is a diffusion-based process. Since all the matter in this reaction is transported via diffusion, hybrid solid-state reaction lead to an enhancement of the diffusion, or at least for an additional driving force to enhance it.

The comparison of these results with the microwave spinel reaction described by Peelamedu, Ganesh and Zhang [99-101] cannot be taken at face value, because in all of their experiments the solid-state reaction was done with a mixture of the reactants. In the experiments undertaken in this work, the reaction partners were 2 separate compacts. In comparison to a mixture where the reaction partners are in close contact with each, here the distance between the reaction partners increased with the duration of the reaction, which reduced the rate of reaction. However both sets of experiments demonstrated an enhancement of the reaction with the use of microwaves. Further, the present work did not involve the use of a carbon-based susceptor, which could have significantly changed the method of heating and hence the outcome of the experiments.

As discussed before, the only logical explanation for the enhanced microwave solid-state reaction is an enhancement of the diffusion. This matched the findings of Whittaker [34], who demonstrated that diffusion can be directed towards the direction

of the microwaves. If microwaves are able to influence the direction of the diffusion of ions, then they definitely have an influence on the diffusion. Therefore it can be concluded that for this solid-state reaction, the enhancement of the diffusion is the cause for the enhanced reaction rate and growth of the reaction layer for the hybrid solid-state reaction. This enhancement of the solid-state reaction confirms the assumption of the densification experiments that microwaves act as an additional driving force for diffusion, because an additional driving force is needed to achieve an increase in the level of matter transport. Since the processing parameters remained fundamentally the same except for the level of microwaves used, it can be concluded the microwaves provide the addition driving force for the enhanced diffusion. This conclusion strengthens the theory of the ponderomotive force suggested by Rybakov and Semenov [27], because they say that microwaves increase the flux of surface near charges and theses charges can pass grain boundaries only in one direction. This creates a directionality of the charges flux. As explained in section 2.1.3, diffusion is the transport of charges (electron, vacancies etc.) and the directionality of the diffusion has been proved by Whittaker [34] and microwaves have an effect on the diffusion and with it on the production of spinel. Therefore it can be said the increase in the spinel layer thickness is a further indication that the ponderomotive force is likely to be the cause for the “microwave effect”.

Further when the reaction between ZnO and Al_2O_3 is compared between the reactions at 1100°C for 5 h and 1300°C for 5 h, then it could be seen that the reaction layer at 1100°C was increased for the 800 W hybrid heating compared to pure conventional heating. In comparison the reaction layer had equal densities for both heating conditions. This indicates that microwaves can only influence the reaction as long it remains in the solid-state. However some caution is advised because at 1100°C the difference between reaction layers for pure conventional and 800 W hybrid heating was quite small at 5 h compared to other reaction times in this investigation.

5 Conclusions

After Wang [29] confirmed that the “microwave effect” was a genuine effect, this project was designed to find out if the “microwave effect” arises from an additional driving force, as described by the ponderomotive effect suggested by Rybakov and Semenov [27], or if it is something different, for example, as indicated by the different structural development for microwave sintering observed by Janney et al. [113].

To achieve this the development of the porosity during the densification was investigated for pure conventional and hybrid sintering with various amounts of microwaves but always ensuring that the time-temperature profile seen by the samples was *identical* to within ±2^{o}C at any given point. The initial results, which focused on the densification of the samples, confirmed that the samples followed the behaviour observed by Wang [29], Samuels and Brandon [92] and others. Therefore it was ensured that the samples were affected by the microwave and everything that would be observed by the investigation of the porosity was caused by the microwave.

The investigation of the effect of microwaves on the density and the porosity were complicated by the forced change of the magnetron and with it the experimental procedure. The measured densities remained at a similar level to before the change but the effect of the microwaves on the porosity was slightly decreased after the change. The cause for this is believed to be a higher temperature difference between the sample core and surface. However both experimental procedures produced the same general behaviour for microwaves on the porosity.

As the changes in the porosity were investigated over the course of the sintering process it initially seemed that microwave sintering enhanced the reduction of the porosity when higher amounts of microwaves were used. However when the porosities at any given density were compared it became clear that the microwaves were not changing the process by which the porosity was reduced. The results demonstrated that the microwaves had no effect on the *development* of the porosity, because at any given density the measured open porosity was the same for every

sample, regardless of the amount of microwaves involved. Therefore the closed porosity was not affected as well. Further confirmation of this fact was achieved by the investigation of the cross-section of pure conventional and 800 W hybrid sintered samples during the densification process until about 88% of theoretical density, the highest value investigated. This revealed that, when the densities were the same, the microstructures were the same. Therefore the initial enhanced pore reduction was only caused by the higher density of the microwave sintered sample at the given sintering time. The conclusion is that microwaves have no effect on the development of the porosity during sintering, meaning that microwave sintering follows the same structural development as conventional sintering. If this is true then it follows that an additional driving force has to be present, because the neck growth, the lengthening of the grain boundaries, the grain growth and reduction of the porosity all depend on diffusion and all of the samples were sintered with exactly the same temperature-time profile. Therefore, this enhanced diffusion was caused by an additional driving force induced by the microwave field.

These results were confirmed by the solid-state reaction between ZnO and Al_2O_3. The reaction rate was increased with the use of hybrid heating and the amount of the microwaves used. Since the same temperature-time profile was again used for all reaction sintering conditions, only the microwaves affected and enhanced the solid-state reactions. These reactions were again diffusion-controlled, therefore the enhancement of reaction rate was achieved by an enhancement of the diffusion caused by an additional driving force induced by the microwave field.

The effect of the samples densification is the most likely explanation for the small but significant increase in the reaction rate for hybrid sintering compared to conventional sintering after the reaction time of 1 h. However, it is then noted that there is relatively little difference in the reaction layer thickness over the period 2 to 5 hrs. This may be for a similar reason that the microwaves enhance densification most during the intermediate stage compared to either the initial or final stages; there are more interfaces present for the ponderomotive effect to interact with. It would have been interesting to extend the reaction time beyond 15 hours to see if the

conventionally heated samples ‘caught up’ with the microwave hybrid heated samples, however this was not realistic since the hybrid furnace was a shared furnace and could not be monopolised. There is possibly a hint in the 1200 W hybrid data of a decrease in the rate of formation between 10 and 15 hours, but it is dangerous to over analyse what is just two data points.

If the diffusion is enhanced in the earlier sintering stages why does this effect seem to get lost during the final sintering stage? There are 2 possible explanations. The first is due to the reduced grain size, described by Mazaheri et al. [24] and Charmond et al. [94], and which itself occurs due to the use of microwaves. The argument is that the use of microwaves enhances the diffusion paths that lead to densification, viz. lattice and grain boundary diffusion (and probably particularly the latter as suggested by Wroe and Rowley [33]), but not the diffusion paths that enhance grain growth such as surface diffusion. This leads to differences in the kinetics between grain-boundary diffusion and grain-boundary migration, in a similar manner to those described by Chen et al. [107] for two stage sintering and, as for that process, there is an exhaustion effect. Although the effect would not be as significant it could explain why after a strong enhancement of the densification in the intermediate sintering stage, microwave sintering has a dramatically reduced densification rate in the final sintering stage.

The second possible explanation for the reduction of the “microwave effect” in the final sintering stage lies within the theory of the ponderomotive effect, because according to this theory the effect of microwaves is greater when the number of interfaces to interact is high, which means for ceramics samples a high number grains with the smallest possible grain size. Therefore when the grain growth in the final sintering stage starts then the size of the grains increase and their number decreases, it will reduce the magnitude of the “microwave effect”.

6 Future work

The effect, or better said, non-effect of microwaves on the development of the porosity has only been demonstrated for ZnO. Since ZnO is a very good microwave absorbent, and therefore very easily affected by microwaves, it cannot be taken for granted that it would be same every other material. Therefore this investigation needs to be extended to other ceramics such as zirconia or alumina and other materials systems, such as polymers, glasses and powder metals to check if similar result can be achieved.

To find out if microwave sintering leads in the final sintering stage to an effect similar to two stage-sintering, the grain growth during the sintering should be investigate. The grain size for the different sintering condition should be compared in relation to the actual sample density as demonstrated by Mazaheri et al. [24], Figure 76.

The solid-state reaction of ZnO and alumina should be extended beyond the 15 hours reaction time in this experimental series. This would allow finding out if the microwave-assisted reaction rate remains at a higher level or drops down to the level of the pure conventional reaction. If this is the case, then clear explanations for why it occurs will need to be proved. Further, the solid-state reaction should be repeated with different amounts of microwaves to see if microwaves have a similar non-linear effect on the solid-state reaction as Wang found for the densification of ceramics. The amount of microwaves between 800 and 1200 W could define what the critical amount of microwaves to create a significant difference in the reaction rate is. The increase of microwave to higher level then 1200 W could define the amount of microwaves to maximise the effect microwaves on the solid-state reaction. An investigation of the solid-state reaction in the first hour would be difficult, because the potential effect of the densification and reduced activation energy could overlap each other and the measurement of the spinel layer thickness will be more difficult as it will be very thin, making accurate measurement difficult.

7 Appendix

Nitrogen adsorption

The thermodynamic fundamental for measuring the pore size distribution with the nitrogen adsorption system is the use of the adsorption isotherm [116]:

$$\Delta G_{ads} = RT(\ln P_{ads} - \ln P_0) \qquad (A.3)$$

Where ΔG_{ads} is the free energy change during the adsorption, R is the gas constant, T is the absolute temperature, P_{ads} is the equilibrium vapour pressure of the liquid contained in a narrow pore during the adsorption and P_0 is the equilibrium pressure of the same liquid exhibiting a plane surface. For the adsorption of nitrogen at its normal boiling point of 77 K, the following Kelvin equation can be written [116]:

$$r_k = \frac{4.15}{\log P_0 / P} \text{ (Å)} \qquad (A.4)$$

Where r_k is the Kelvin radius and P is equal to P_{abs}

The Kelvin radius or critical radius is not the actual pore radius because some adsorption has already occurred on the pore wall by condensation, leaving a centre core of radius r_k. A similar process occurs during desorption when the evaporation of the centre pore takes place and some of the adsorbed film remains on the pore wall.

So that the actual pore radius is calculated by [116]:

$$r_p = r_k + t \qquad (A.5)$$

Where r_p is the actual pore radius and t is the depth of the adsorbed film. By using the assumption that the absorbed film depth in a pore is the same as that on a plane surface for any value of the relative pressure, t is given by [116]:

$$t = \left(\frac{W_a}{W_m} \right) \tau \qquad \text{(A.6)}$$

Where W_a and W_m are the quantity absorbed at a particular relative pressure and the weight corresponding to the monolayer respectively and τ is the thickness of one layer of the adsorbed material. τ can be calculated by considering the area S and volume $\overline{V}$ occupied by one mole of the liquid nitrogen if it were spread over a surface to the depth of one molecular layer [116]:

$$S = (16.2)(6.02*10^{23}) = 97.5*10^{23}\ \text{Å}^2 \qquad \text{(A.7)}$$

$$\overline{V} = (34.6*10^{24})\ \text{Å}^3 \qquad \text{(A.8)}$$

Then

$$\tau = \left(\frac{W_a}{W_m} \right) 3.45\ \text{Å} \qquad \text{(A.9)}$$

Now the equation, (A.5), can be written as [116]:

$$t = \left(\frac{W_a}{W_m} \right) 3.54\ \text{Å} \qquad \text{(A.10)}$$

The common curve is described closely by the Halsey [117] equation for which nitrogen can be written as

$$t = 3.54 \left(\frac{5}{2.303 \log P_0 / p} \right)^{\frac{1}{3}} \qquad \text{(A.11)}$$

For nitrogen at standard temperature and pressure can be written:

$$\Delta V_{liq} = \frac{\Delta V_{gas}}{22.4*10^{3}} 34.6 = \Delta V_{gas}(1.54*10^{-3}) \text{ cm}^3 \quad \text{(A.12)}$$

Where ΔV_{gas} is the change in absorbed volume between successive P/P_0 values and ΔV_{liq} is the volume of liquid corresponding to ΔV_{gas}.

The actual pore volume, V_p, is evaluated by recalling that the volume of liquid is composed of the volume evaporated out of the centre cores plus the volume desorbed from the film left on the pore walls.

Then,

$$\Delta V_{liq} = \pi \overline{r_k} l + \Delta t \sum S \quad \text{(A.13)}$$

and since,

$$V_p = \pi \overline{r_p} l \quad \text{(A.14)}$$

Where l is the pore length, by combination of the above two equations,

$$V_p = \left(\frac{\overline{r_p}}{\overline{r_k}} \right)^2 [\Delta V_{liq} - (\Delta t \sum S)(10^{-4})] \text{ cm}^3 \quad \text{(A.15)}$$

The surface area of the pore walls is calculated from the pore volume by [117]:

$$S = \frac{2V_p}{\overline{r_p}} *10^4 \text{ (m}^2\text{)} \quad \text{(A.16)}$$

Mercury porosimetry

The recorded values by the mercury porosimetry were the actual measuring pressure *P* in psi and the intrusion in pF (Pico Farads). The measured pore size was calculated by:

$$D = \frac{-4\gamma \cos\Theta}{P} \qquad \text{(A.17)}$$

Where *D* is the pore size, *γ* is the surface tension, Θ is the contact angle and *P* is the measured pressure.

In the high-pressure chamber, it is necessary to calculate the correct pressure on the mercury head, because the penetrometer is placed in a vertical position in the high-pressure chamber and this leads to an additional pressure through the weight of the mercury column. This pressure increment decreases if the sample is intruded by the mercury and the mercury height in the penetrometer stem decreases. These head corrections were calculated by

$$P_c = P_0 \frac{h}{h_0} \qquad \text{(A.18)}$$

Where P_c is the correct pressure, P_0 is the maximum head pressure, *h* is the actual mercury height and h_0 is the maximum stem height.

The actual height, *h*, cannot be observed directly, but can be calculated from the total intruded volume.

$$P_0 = 0.1934\ h_0 \qquad \text{(A.19)}$$

The total system volume of penetrometer is given by

$$V_0 = \frac{\pi}{4} d^2 h_0 \qquad \text{(A.20)}$$

Where V_0 is the total system volume, d is the inner diameter of penetrometer.

The intruded volume is given by

$$V = \frac{\pi}{4} d^2 (h_0 - h) \qquad \text{(A.21)}$$

Where V is the intruded volume.

The combination of equation A.17, A.19 and A.20 lead to

$$P_c = P_0 - \frac{P_0}{V_0} V \qquad \text{(A.22)}$$

So that the head correction can be calculated as a function of the intrusion volume, V.

For the pore volume, first, the intrusion reading is calculated into cumulative changes in capacitance (initial value taken as zero) by:

$$dC = \sum \Delta I \qquad \text{(A.23)}$$

Where dC is the changes in capacitance and I is the intrusion reading.

These changes in capacitance are calculated in to the cumulative pore volume per gram by

$$V_P = \frac{dC * SCF}{m_s} \qquad \text{(A.24)}$$

Where V_p is the pore volume, *SCF* is the conversion factor (supplied for the penetrometer) and m_s is the sample mass.

8 References

1. **Galema, S. A.**, Chemical Society Review, 1997, Vol. 26, pp. 233-238.
2. **Wiebrock, F., Hoogenboom, R. and Schubert, U. S.**, Macromol. Rapid Commun., 2004, Vol. 25, pp. 1739-1764.
3. **Hoz, A. d. l., Diaz-Ortiz, A. and Moreno, A.**, Chemical Reviews, 2005, Vol. 34, pp. 164-178.
4. **Panda, S. S., Singh, V., Upadhyaya, A. and Agrawal, D.**, Scripta Materialia, 2006, Vol. 54, pp. 2179-2189.
5. **Upadhyaya, A., Tiwari, S. K. and Mishra, P.**, Scripta Materialia, 2007, Vol. 56, pp. 5-8.
6. **Prabhu, G., Chakraborty, A. and Sarma, B.**, International Journal of Refactory Materials & Hard Materials, 2009,Vol. 27, pp. 545-548.
7. **Fathi, Z., Ahmad, I., Simmons, J. H., Clark, D. E. and Lodding A. R.**, Ceramic Transactions, 1991, Vol. 21, pp. 623-629.
8. **Siligardi, C., Leonelli, C., Bondioli, F. Corradi, A. and Pellacani, G. C.**, Journal of the European Ceramic Society, 2000, Vol. 20, pp. 177-183.
9. **Faeghi, A. and Ebadzadeh, T.**, Ceramics International, 2012, Vol. 38, pp. 2653-2658.
10. **Sutton, W. H.**, American Ceramic Society Bulletin, 1986, Vol. 68, [2], pp. 376-386.
11. **Vaidhyanathan, B., Singh, A. P., Argwal, D. K., Shrout T. R. and Roy R.**, Journal of the American Ceramic Society, 2001, Vol. 84, [6],pp. 1197-1202.
12. **Akpinar, S., Kusogulu, I. M., Ertugrul, O. and Onel K.**, Journal of the European Ceramic Society, 2012, Vol. 32, pp. 843-848.
13. **Shen, B., Kang, L. and Yao, X.**, Journal of Electroceramics, 2008, Vol. 21, pp. 448-451.
14. **Marinel, S. and Savary, E.**, Journal of Materials Processing Technology, 2009 Vol. 209, pp. 4784-4788.
15. **Park, S. S. and Meek. T. T.**, Journal of Material Science, 1991, Vol. 26, pp. 6309-6313.
16. **Janney, M. and Kimray, H. D.**, Materials Research Society Symposium Proceedings, Microwave Processing of Materials, 1991, Vol. 189, pp. 215-227.

17. **Bykov, Y. V., Egorov, S. V., Eremeev, A. G., Rubakov, K. I., Semenov, V. E., Sorokin, A. A. and Gusev, S. A.**, Journal of Materials Science, 2001, Vol. 36, pp. 131-136.
18. **Guo, L., Luo, H., Gao, J. and Yang, J.**, Materials Letters, 2006 Vol. 60, pp. 3011-3014.
19. **Thakur, O. P., Prakash, C. and Agarwal, D. K.**, Journal of Ceramic Resources, 2002, Vol. 3, [2], pp. 75-79.
20. **Felgnera, K. H., Mullerb, T., Langhammera, H. T. and Abicht, H. P.**, Materials Letters, 2004, Vol. 58, pp. 1943-1947.
21. **Yang, R.-Y., Chen, H.-Y., Hsiung, C.-M. and Chang, S.-J.**, Ceramics International, 2011, Vol. 37, pp. 749-752.
22. **Agrawal, S., Cheng, J., Guo, R., Bhalla, A. S., Islam, R. A. and Priya, S.**, Materials Latters, 2009, Vol. 63, pp. 2198-2200.
23. **Wang, J., Binner, J., Pang Y. and Vaidhyanathan, B.**, Thin Solid Films, 2008 Vol. 516, pp. 5996-6001.
24. **Mazaheri, M., Zahedi, A. M. and Hejazi, M. M.**, Materials Science and Engineering A, 2008, Vol. 492, pp. 261-267.
25. **Xie, Z., Yang, J. and Huang, Y.**, Materials Letters, 1998, Vol. 37, pp. 215-220.
26. **Binner, J. G. P., Hassine, N. A. and Cross, T. E.**, Journal of Material Science, 1995, Vol. 30, pp. 5389-5393.
27. **Rybakov, K. I.. and Semenov, V. E.**, Physical Reiew B, 1995, Vol. 52, [5], pp. 3030-3033.
28. **Pert, E., Carmal, Y., Birnboim, A., Olorunyolemi, T., Gershon, D., Calame, J., Llyod, I. K. and Wilson Jr., O. C.**, Journal of the American Ceramic Society, 2001, Vol. 84, [9], pp. 1981-1986.
29. **Wang, J.** *Determination of the physical basis behind the 'microwave effect'.* Loughborough Unversity, UK, PhD Thesis, 2005, pp. 5,6,80-178
30. **Lorenz, A.** *Ivestigation of microwave effect using a dilatometer.* TU Freiberg, Germany, pratice semester report, 2006, pp. 30-38
31. **Hossbach, K.** *In situ dilatometer measurement of ZnO and YSZ und microwave and hybrid heating conditions.* TU Freiberg, Germany, pratice semester report, 2005, pp. 30-38

32. **Freeman, S. A., Booske, J. H. and Coper, R. F.**, Physical Review Latters, 1995, Vol. 74, [11], pp. 2042-2045.
33. **Wore, R. and Rowley, A. T.**, Journal of Materials Science, 1996, Vol. 31, pp. 2019-2026.
34. **Whittacker, A.G.**, Chemestry of Materials, 2005, Vol. 17, [13], pp. 3317-3574.
35. **Reed, J. S.** *Priciples of Ceramic Processin.* 2nd . 1995. pp. 594-605.
36. **Rahaman, M. N.** *Ceramic Processing,* 2007
37. **Richeson, D. W.** *Modern Ceramic Engineeing,* 2006.
38. **Novich. B. E. and Pyatt, D. H.**, Journal of the American Ceramic Society, 1990, Vol. 73, [2], pp. 207-212.
39. **Lewis, J. A.**, Journal of the American Ceramic Society, 2000, Vol. 83, [10], pp. 2341-2359.
40. **Schlegel, E.** *Grundlagen der Sinter- und Schmelztechnik.* 1984.
41. **Barsoum, M. W.** *Fundamentals of Ceramics.* 2003, cap. 10.
42. **Rahaman, M. N.** *Ceramic Processing and Sintering.* 2nd ed. 2003. cap. 7-9.
43. **German, R. M.** *Sintering Theory and Practice.* 1996.
44. **Barsoum, M. W.** *Fundamentals of Ceramics.* 2003, cap. 14.
45. **Kingery, W. D., Bowen, H. K., Uhlman, D. R.** *Introduction to Ceramic.* 1976.
46. **Rahaman, M. N.** *Ceramic Processing.* 2007. cap. 9.
47. **Burke, J. E. and Rosolowski, J. H.** *Treatise on Solid State Chemistry.* 1976.
48. **Budworth, D. W.** *An Introduction to Ceramic science.* 1970.
49. **Schmalzried, H.** Reaction in the solid state. *Solid-state Reactions.* s.l. : Verlag Chemie, 1974, pp. 79-108.
50. **Arvid Hedvall, J.**, Zeitsschrift fuer anorganische und allgemeine Chemie, 1915, Vol. 92, pp. 301-312.
51. **Bunting, E. N.**, Bureau of Stabdars Journal of Research, 1932, Vol. 8, pp. 279-287.
52. **Bengtson, B. and Jagitsch, R.**, Arkiv foer Kemi, Mineralogi och Geologi., 1947, Vol. 24A, [18], pp. 1-15.
53. **Lindner, R.**,Zeitschrift fuer Elektrochemie, 1955, Vol. 59, [10], pp. 967-970.
54. **Branson, D. L.**, Journal of the American Ceramic Society, 1965, Vol. 48, [11], pp. 591-595.

55. **Otero Arean, C.; Fernandez Colinas, J. M. and Villa Garcia, M. A.**, Reactivity of Solids, 1986, Vol. 1, pp. 227-233.
56. **Bailey, J. T. and Russel JR., R.**, American Ceramic Society Bulletin, 1968, Vol. 47, [11], pp. 1025-1029.
57. **Ping, L. R., Azad, A.-M. and Dung, T. W.**, Materials Research Bulletin, 2001, Vol. 36, pp. 1417-1430.
58. **Sarkar, R. and Banerjee, G.**, Journal of the European Ceramic Society, 1999 Vol. 19, pp. 2893-2899.
59. **Li, J.-G., Ikegami, T., Lee, J.-H., Mori, T. and Yajima, Y.**, Ceramics International, 2001, Vol. 27, pp. 481-489.
60. **Carter, R. E.**, Journal of the American Ceramic Society, 1961, Vol. 44, [3], pp. 116-120.
61. **Smithsonian National Museum of Amercian History Behring Center.** invention at play. *inventors' stories.* [Online] [Cited: 28 2 2012.] http://www.inventionatplay.org/inventors_spe.html.
62. **National Inventors Hall of Fame Foundation, Inc.** *Hall of Fame/ inventor profile.* [Online] 2007. [Cited: 28 2 2012.] http://www.invent.org/hall_of_fame/136.html.
63. **Carlton Gallawa, J.** *WHO INVENTED MICROWAVES?* [Online] [Cited: 28 2 2012.] http://www.gallawa.com/microtech/history.html.
64. **Meredith, R.** *Engineers' Handbook of Industrial Microwave Heating,* 1998, cap. 3
65. **Metaxas, A. C. and Meredith, R. J.** *Industrial Microwave Heatin,* 1983, cap. 2
66. **Von Hippel, R.** *Dielectric Materials and Applications.* s.l. : The Massachusetts Institute of Technology, 1954, pp. 18 - 20.
67. **Hummel, R. E.** Electric Properties of Materials. 3rd. 2001, pp. 185-189.
68. **Tinga W. R. and Voss W. A. G.** *Microwave Power Engineering.* New York : Academic Press, 1968.
69. **Liu, Y., Min, F.-f., Zhu, J.-b. and Zhang, M.-x.**, Materials Science and Engineering: A, 2012, Vol. 546, pp. 328-331.
70. **Binner, J. and Vaidhyanathan, B.**, Journal of the European Ceramic Society, 2008, Vol. 28, pp. 1329-1339.

71. **Paul, A.** *Processing and Properties of Nanostructured Zirconia Ceramics.* Loughborough University, UK, PhD Thesis, 2009, pp. 92-189,.
72. **Kumar, R. S., Ryu, B. D., Chandramohan, S., Seol, J. K., Lee, S.-K. and Hong, Ch.-H.**, Materials Letters, 2012, Vol. 86, [1] pp. 174-177.
73. **Jones, M. I., Valecillos, M.-C., Hirao, K. and Yamuchi, Y.**, Journal of the European Ceramic Society, 2002, Vol. 22, pp. 2981-2988.
74. **Qi., S. and Yang, B.**, Catalysis Today, 2004, Vol. 98, [4], pp. 639-645.
75. **Menezes, R. R. and Kiminami. R. H. G. A.**, Journal of Material Processing Technology, 2008, Vol. 203, pp. 513-517.
76. **Xu, J., Chen, F. and Tan, F.**, Ceramics International, 2002, Vol. 38, pp. 6895-6898.
77. **Zhang, D. M., Zhuang, Z., Wang, X. P., Gao, Y. X. anf Fang, Q. F.**, Journal of the European Ceramic Society, 2012, [12], Vol. 32, pp. 3229-3247.
78. **Binner J.** *Microwave Processing of Materials.* Pittsburgh, PA : Materials Research Society, 1992, pp. 357-362.
79. **Pert E., Carmel Y., Birnbiom A., Olorunyolemi T., Gershon D., Calame J., Lloyd I. K. and Wilson Jr. O. C.**, J. Am. Ceram. Soc., 2001, Vol. 84, [9], pp. 1981-1986.
80. **Xu G., LLoyd I. K., Carmel Y., Olorunyolemi T. and Wilson Jr. O. C.**, Journal of Material Research, 2001, Vol. 16, pp. 2850-2585.
81. **Xie Z., Cheng J., Roy R., Roy D. M. and Argrawal D. K.**, Materials Letters, 1999, Vol. 38, pp. 190-196.
82. **Binner J. G. P., Hassine N. A. and Cross T. E.**, Journal of Materials Science, 1995, Vol. 30, pp. 5389-5393.
83. **Vaidhynathan B., Singh A. P., Argawal D. K. and Ganguly S.**, Journal of the American Ceramic Society, 2001, Vol. 84, [6], pp. 1197-1207.
84. **Vaidhyanathan B. and Rao K. J.**, Chemistry of Materials, 1997, Vol. 9, pp. 1196-1200.
85. **Vaidhyanathan B., Raizada P. and Rao K. J.**, Journal of Material Science Letters, 1997, Vol. 16, pp. 2022-2025.
86. **Bykov Yu., Eremeev A., Egorov S., Ivanov V., Kotov Yu., Khrutov V. and Sorokin A.**, Nanostructured materials, 1999, Vol. 12, pp. 115-118.

87. **Sheppard L .M.**, American Ceramic Society Bulletin, 1988, Vol. 67, 10, pp. 1656-1661.
88. **Katz J. D. and Blake R. D.**, American Ceramic Society Bulletin, 1991, Vol. 70, [81], pp. 1304-1308.
89. **Patterson M.** *Microwave processing of Materials III.* Pittsburgh, PA : Materials Research Society, Vol. 269, p. 291.
90. **Li J., Kong X., Xie Z. and Huang Y.**, Journal of the American Ceramic Society, 1999, [6], Vol. 82, pp. 1576-1578.
91. **Janny, M. A. and Kimrey, H. D.**, Ceramic Transactions, 1988, pp. 919-924.
92. **Samuels, J and Brandon, J. R.**, Journal of the Materials Science, 1992, Vol. 27, pp. 3259-3265.
93. **Fang, Y., Cheng, J., Roy, R., Roy, D. M. and Agrawal, D. W.**, Journal of Materials Science, 1997, Vol. 32, pp. 4925-4930.
94. **Charmond, S., Carry, C. P. and Bouvard, D.**, Journal of the European Ceramic Society, 2010, Vol. 30, pp. 1211-1221.
95. **Janney, M. A., Calhoun, C. L. and Kimrey, H. D.**, Journal of the American Ceramic Society, 1992, Vol. 75, [2], pp. 341-346.
96. **Xie, Zh., Wang, Ch., Fan, X. and Huang Y.**, Materials Letters, 1999, Vol. 38, pp. 190-196.
97. **Brosnan, K. H., Messing, G. L. and Agrawal, D. K.**, Journal of the American Ceramic Society, 2003, Vol. 86, [6], pp. 1307-1312.
98. **Aguilar, J. A.; Gonzalez, M. and Gomez, I.**, Journal of Microwave Power and Electromagnetic Energy, 1997, Vol. 32, [2] pp. 74-79.
99. **Peelamedu, R. D.; Roy, R. and Agrawal, D. K.**, Materials Latters, 2002, Vol. 55, pp. 234-240.
100. **Ganesh, I.; Srinivas, B.; Johnson, R.; Saha, P. and Mahajan, Y. R.**, Journal of the European Ceramic Society, 2004, Vol. 24, pp. 201-207.
101. **Zhang, N.-B.; Bai, Ch.-G.; Ma, M-Y and Li, Z.-Y.**, Transactions of Nonferous Metals Society of China, 2010, Vol. 20, pp. 2020-2025.
102. **Janney, M. A. and Kimray, H. D.**, Materials Research Society Symposium Proceedings, Microwave Processing of Materials, 1991, Vol. 189, pp. 215-227.

103. **Fathi, Z., Ahmad, I., Simmons, J. H., Clark, D. E. and Lodding, A. R.**, Ceramic Transactions, 1991, Vol. 21, pp. 623-629.
104. **Booske, J. H., Cooper, R. F. and Dobson, I.**, Journal of Material, 1992, Vol. 7, [2] pp. 495-501.
105. **Nightingale, S. A., Dunne, D. P. and Worner, H. K.**, Journal of Materials Science, 1996, Vol. 31, pp. 5039-5043.
106. **Bykov, Y. V., Rybakov, K. I. and Semenov, V. E.**, Journal of Physics D: Applied Physics, 2001, Vol. 34, pp. R55-R75.
107. **Chen, I.-W. and Wang, X.-H.**, Nature, 2000, Vol. 404, pp. 168-171.
108. **Link, G., Miksch, S., Thumm, M. and Takayama, S.**, Ceramic Engineering and Science Proceedings, 2008, Vol. 28, [7] pp. 55-66.
109. **Booske, J. H., Copper, R. F., Freeman, S. A., Rybakov, K. I. and Semenov, V. E.**, Physic of Plasmas, 1998, Vol. 5, [5], pp. 1664-1670.
110. Energy-dispersive X-ray spectroscopy. *Wikioedia.* [Online] [Cited: 10 12 2013.] http://en.wikipedia.org/wiki/Energy-dispersive_X-ray_spectroscopy.
111. **TU. Ilmenau,** Theoretische Grundlagen. [Online] [Cited: 10 12 2013.] http://www.maschinenbau.tu-ilmenau.de/mb/wwwtd/m2twin/images/grund.pdf.
112. **Cheng, H., Xu, X. J., Hng, H. H. and Ma, J.**, Ceramic International, 2009, Vol. 35, [8] pp. 3067-3072.
113. **Janney, M. A. and Kimrey, H. D.** Microwstructure Evolution in Microwave Sintered Alumina. [book auth.] C. A. Handwerker, Blendell, J. E. and W. Kaysser. *Sintering of Advances Ceramics.* 1990, pp. 382-390.
114. **Wernet, J. H. and Wernet, M. P.,** 1994, Symposium on Laser Anemomentry: Advances and Applications, NASA Technical Memorandum 106591.
115. **Ferrari, B., Moreno, R., Sarkar, P. and Nicholson, P. S.**, Journal of the European Ceramic Society, 2000, Vol. 20, pp. 99-106.
116. **S. Lowell, J. E. Shields.** *Powder surface area and porosity,* 1991, pp. 55-64.
117. **D.Halsey, G.**, Journal of Chemical Physics, 1948, Vol. 16, pp. 931-937.